Development of ultrathin Cu(In,Ga)Se –based solar cells with reflective back contacts

Louis Gouillart

université PARIS-SACLAY

Development of ultrathin $Cu(In,Ga)Se_2$–based solar cells with reflective back contacts

Thèse de doctorat de l'université Paris-Saclay

École doctorale n° 575 : electrical, optical, bio : physics and engineering (EOBE)

Spécialité de doctorat : électronique et optoélectronique, nano- et microtechnologies

Unité de recherche : Université Paris-Saclay, CNRS, Centre de Nanosciences et de Nanotechnologies, 91120, Palaiseau, France

Référent : Faculté des sciences

Thèse présentée et soutenue à Palaiseau, le 20 Janvier 2020, par

Louis Gouillart

Composition du Jury

Jean-Paul KLEIDER Directeur de Recherche, GeePs-CNRS, France	Président
Ludovic ESCOUBAS Professeur, Aix-Marseille Université, France	Rapporteur & Examinateur
Martina SCHMID Professeure, Université de Duisburg-Essen, Allemagne	Rapporteur & Examinatrice
Romain CARRON Chercheur, Empa, Suisse	Examinateur
Roland SCHEER Professeur, Martin Luther-Universität Halle-Wittenberg, Allemagne	Examinateur

Stéphane COLLIN Chargé de Recherche, C2N-CNRS, France	Directeur de thèse
Negar NAGHAVI Directrice de Recherche, IPVF UMR 9006-CNRS, France	Co–directrice de thèse
Andrea CATTONI Chargé de Recherche, C2N-CNRS, France	Co–encadrant
Marie JUBAULT Ingénieur Chercheur, IPVF-EDF, France	Co–encadrante
Marika EDOFF Professeure, Université d'Uppsala, Suède	Invitée

Thèse de doctorat

NNT : 2020UPASS007

"All my life the early sun has hurt my eyes, he thought. Yet they are still good. In the evening I can look straight into it without getting the blackness. It has more force in the evening too. But in the morning it is painful."

Ernest Hemingway, *The Old Man and the Sea* (1952).

Acknowledgements

The work reported in this thesis manuscript is the result of several interactions between me and researchers that I had the opportunity to meet, both before and during my PhD studies. Hence, I would like to acknowledge and thank them for their valuable contributions, not only from a professional viewpoint but also from a personal one.

Back in 2016, Frederique Donsanti and Marie Jubault allowed me to carry out my final-year internship at the *Institut de Recherche et Développement sur l'Énergie Photovoltaïque* (IRDEP). For 6 months, I worked on the development of magnesium fluoride-based antireflection coatings for CIGS solar cells, under their supervision as well as the one of Fabien Mollica, PhD student at that time. Thanks to the three of them, I benefited from ideal conditions to discover the research world, to learn about the field of CIGS-based solar cells and to blend in with the IRDEP research group. Throughout my internship, you remained supportive and always managed to help me when necessary. I enjoyed working with you so much that despite the substantial downtime of the magnesium fluoride evaporator, I decided to keep on working at IRDEP and to apply to a PhD position!

This would not have been possible without the help of Frederique Donsanti and Negar Naghavi, who recommended me as a PhD student on the topic of ultrathin CIGS solar cells. Given that this PhD position was a collaboration between IRDEP and the *Centre for Nanoscience and Nanotechnology* (C2N), I also want to warmly thank two researchers from this lab for trusting me to carry out these PhD studies: Stéphane Collin and Andrea Cattoni.

All in all, this PhD led me to work under the supervision of Stéphane, with the co-supervision of Negar, Andrea and Marie. Working with such a large team of supervisors was a unique opportunity to broaden my knowledge in the field of photovoltaics and material science, and I am very grateful for the time and energy that each of my supervisors has put in this project in order to help me. Each of you brought valuable contributions to my work, either at the laboratory or with fruitful discussions during meetings. It was a real pleasure to work with you, in a serious yet casual atmosphere. I am also glad that each of you remained involved in my PhD work and kept track of my progress, especially as we were most of the time working in different places, far from each other. In summary, you made this possible.

During the past three years, both the IRDEP and C2N laboratories closed in order to move to Palaiseau. Fortunately, I had the opportunity to continue my experimental work at the *Ångström Solar Center* in Uppsala, Sweden. It allowed me not only to work on the fabrication of complete solar cells, but also to discover the Swedish culture. For this, I kindly thank Prof. Marika Edoff who welcomed me within her research group twice, for periods of three and two months. Despite your busy schedule it was always easy to reach you as you managed to make time for discussion. Your permanent enthusiasm and optimism kept me highly motivated during my stays in Sweden.

I would also like to express special thanks to the jury members of my PhD defense. To Prof. Martina Schmid and Prof. Ludovic Escoubas, who accepted to review my thesis, and to the other jury members as well: Prof. Roland Scheer, Dr. Romain Carron and Dr. Jean-Paul Kleider. I am very grateful that you accepted to take part in the evaluation of my thesis, and I thank you for the interest you showed regarding my work.

The results reported here would not have come to life without the help of several coworkers. Hence, I am very grateful to Frederique Donsanti and Marie Jubault, who trained me to use the CIGS co-evaporator tool at IRDEP. I would also like to thank Damien Coutancier, Jessica Legendre, Samuel Rives and Thibaut Hildebrandt for taking part in the fabrication of my CIGS solar cell samples at IRDEP, as they helped with the deposition of back and front contact layers. I thank Enrique Leite too, for helping me with the characterization tools of the IRDEP laboratory, as well as Sophie Gaillard and Valérie Daniau for their help regarding the chemical processes I used at the *Institut Photovoltaïque d'Île-de-France* (IPVF). Also, I would like to thank Claire Vialette, who was of a great help when dealing with administrative procedures, and who remained patient under any circumstances.

While working at the IPVF (formerly IRDEP) laboratory, I also met a lot of other students and made several friends. First as an intern, I was happy to meet Fabien Mollica, Harold Le Tulzo, Mishael Stanley and Valentin Achard, with whom I would go jogging during lunch time or play tennis in the evening. I am glad that we still have many opportunities to see each other! During my PhD studies I also met several other students and researchers like Fabien Lafond, Adrien Bercegol, Cécile Molto, Sophie Bernard, Margot Kozolinsky, Olivier Fournier, Katherine Alvino, Arpit Mishra, Salim Mejaouri, Baljeet Goraya, Anatole Desthieux, Emilie Raoult, Paul-Alexis Pavard and many others. It was a pleasure to get to know you, to share ideas, but also to play table football during lunch breaks and to hang out with you after work!

During my PhD studies, I spent most of my time at the C2N, which is why I would also like to acknowledge the researchers I met there. First, I thank Xavier Lafosse and Alan Durnez for their help with the deposition of dielectric materials and transparent conductive oxides, and for the useful advice they gave me. I thank Laetitia Leroy and Laurent Couraud too, who trusted me while I was extensively using the evaporation tool to deposit silver layers. Many thanks to Gilles Patriarche as well, for his valuable help with the STEM/EDX study performed at the C2N. I also warmly thank Christophe Dupuis, Stéphane Guilet and Abdelmounaim Harouri, for their precious advice but also for their friendliness, which made working with them very enjoyable.

As a member of the sunlit team at the C2N, I also met a lot of students from this team. I was happy to work on the ARCIGS-M project with Julie Goffard, who has an impressive knowledge of cleanroom processes and is also great at organizing BBQ parties! I thank Joya Zeitouny too, who helped me a lot on this project. The Lebanese farewell dinner you prepared was awesome! In addition, I would like to thank you and Thomas Bidaud, as both of you significantly contributed to the cathodoluminescence study reported in this work. This PhD was also the opportunity to meet several students working on different projects. I'm thankful to Jérôme Michallon, Benoît Behagel, Maxime Giteau and Pierre Rale, who I met during the first few months of my

PhD and who welcomed me to the sunlit team. I also thank Hung-Ling Chen, Daniel Pelati, Federico Petronio, Amadéo Michaud, Thomas Bidaud and Romaric De Lépinau, as I really enjoyed working with you during my PhD studies. I am also glad that we had the opportunity to get a demo from our "Master of Pasta", to run away from boars in Marcoussis, and that I could regularly come across one of you late at night in Paris! I would then like to thank Andrea Scaccabarozzi, thanks for your great sense of humour and for teaching me essential Italian words like *coniglietto*. Also, many thanks to Ahmed Ben Slimane, you certainly know how to make the most of conferences! I thank Amaury Delamarre too, in particular for helping me to prepare my defense. I wish you the best at CNRS! I'd also like to thank François Chancerel and Linh Nguyen; even if we did not work a lot together at the lab it was a pleasure to spend some time with you during events with the rest of the team. Lastly, I was happy to get to know the recently arrived PhD students Bérengère Frouin and Capucine Tong. Good luck for the next 2 years and a half!

I also met wonderful people while working at the *Ångström Solar Center*. I was really impressed by the very efficient way of working I found in this laboratory; despite the short duration of my stays in Sweden, I could quickly get to work in the cleanroom. For this, I deeply thank Amit Patel, Rimantas Brucas and Jonathan Scragg, who trained me to use the various cleanroom tools I needed to achieve my experiments. I warmly thank Ramy Salameh and Pia Lansåker for their help with administrative procedures, their kindness and their availability to answer my questions.

I rapidly felt integrated within the thin film solar cell group of the *Ångström Solar Center*, in particular thanks to Wei-Chao Chen as we worked in close collaboration at the lab. Thank you for teaching me everything I had to know about the CIGS co-evaporator, I appreciated working with you and getting to know you during coffee breaks or at the restaurant. I would also like to thank Adam Hultqvist for his significant and kind help on several fabrication steps of my samples, as well as Lars Riekehr for the STEM/EDX analyses and the fruitful discussions we had on the topic. I thank Jan Keller, Lars Stolt and Uwe Zimmerman too, for the numerous discussions we had on the topic of CIGS solar cells and the highly valuable advice they gave me. Lastly, I thank the other researchers from the *Ångström Solar Center* that I had the opportunity to meet and to discuss with during lunch time or on Friday evenings.

To conclude this section of acknowledgements, I thank my family, who never stopped supporting me throughout my PhD studies. Besides, I would like to express one *snoop* thank-you, and to dedicate special thanks to all my friends who have been by my side during those three years of PhD.

Contents

List of Symbols

FF	Fill Factor
J_{SC}	Short-circuit current density
V_{OC}	Open-circuit voltage
ACIGS	Silver Copper Indium Gallium Diselenide – $(Ag,Cu)(In,Ga)Se_2$
ALD	Atomic Layer Deposition
ARC	Antireflection coating
CBD	Chemical Bath Deposition
CGI	[Cu]/([Ga]+[In]) atomic ratio
CIGS	Copper Indium Gallium Diselenide – $Cu(In,Ga)Se_2$
CL	Cathodoluminescence
C2N	*Centre for Nanoscience and Nanotechnology*
EDX	Energy Dispersive X-ray spectroscopy
EQE	External Quantum Efficiency
GD-OES	Glow-Discharge Optical Emission Spectroscopy
GGI	[Ga]/([Ga]+[In]) atomic ratio
I(V)	Current-Voltage
IR	Infrared
IRDEP	*Institut de Recherche et Développement sur l'Énergie Photovoltaïque*
ITO	Tin-doped indium oxide
LCOE	Levelized Cost of Electricity
NP	Nanoparticle
OVC	Ordered Vacancy Compounds
PDMS	Poly(dimethylsiloxane)
PDT	Post-Deposition Treatment
PV	Photovoltaic
QNR	Quasi Neutral Region
RBC	Reflective Back Contact
RCWA	Rigorous Coupled Wave Analysis

SCR	Space Charge Region
SEM	Scanning Electron Microscopy
STEM	Transmission Electron Microscopy in scanning mode
TCO	Transparent Conductive Oxide
TEM	Transmission Electron Microscopy
XRD	X-Ray Diffraction
XRF	X-Ray Fluorescence

General introduction

During the last three decades, the Intergovernmental Panel on Climate Change (IPCC) has been analyzing the impacts of human activities on climate. In particular, the influence of anthropogenic emissions of greenhouse gases on global warming and climate change has been established and widely described [1], [2]. The international community is aware of this issue, as it recently ratified the Paris Agreement negotiated during the 2015 United Nations Climate Change Conference (COP 21) [3]. It allowed for the first time to set a common goal that consists in maintaining the global average temperature to less than 2°C above pre-industrial levels.

In order to achieve this objective, it is essential that the sector of electricity production includes a higher proportion of renewable sources in the upcoming decades. In this regard, solar photovoltaic systems have a major role to play as the solar resource is abundant and in general less polluting and dangerous than fossil fuels and nuclear power [2], [4]. The photovoltaic market has been largely dominated by the silicon technology, but thin-film technologies have emerged as an alternative. In particular, the $Cu(In,Ga)Se_2$ (CIGS) technology accounted for about 2% of the photovoltaic module production capacity in 2017 [5]. Using a standard absorber thickness of 2 – 3 µm, CIGS devices have reached record efficiencies of 23.4% at the laboratory scale and of 17.4% for a module [6].

It is possible to further increase the industrial competitiveness of CIGS-based modules by reducing the thickness of the CIGS absorber while maintaining a similar photovoltaic efficiency [7]. This would represent a triple advantage, thanks to (1) an increase of the industrial throughput due to a shorter CIGS deposition time [7], (2) a lower consumption of indium and gallium which are listed as critical raw materials by the European Commission [8] and (3) a higher power conversion efficiency with reduced electrical losses in the thinner absorber layer [9], [10].

However, the record efficiency for a CIGS-based solar cell with an ultrathin absorber (*i.e.* ≤ 500 nm) is limited to 15.2% [11]. Ultrathin CIGS solar cells on conventional molybdenum back contacts suffer from low efficiencies because of 2 main loss mechanisms [12]: the higher probability of charge carrier recombination at the back contact, and the insufficient light absorption in the CIGS layer due to the poor reflectivity of the CIGS back interface with Mo. The present PhD thesis reports different strategies to overcome the efficiency limitations of ultrathin CIGS-based solar cells.

Part I: first, the context of this work is provided by a brief description of the energy and photovoltaic markets. The role of the CIGS technology within the photovoltaic industry is then detailed. The physics of the CIGS solar cell is presented, as well as the state-of-the-art of ultrathin CIGS solar cells. Finally, the materials and methods for the fabrication, characterization and simulation of CIGS solar cells are listed.

Part II: three approaches are studied in order to improve the V_{OC} and *FF* of CIGS solar cells with absorber thicknesses of ≈500 nm. On the one hand, the composition grading of ultrathin absorbers is optimized to create a back surface field that contributes to the CIGS rear passivation in complete solar cells [13]. This CIGS composition grading is created by reducing the substrate temperature during CIGS co-evaporation. The resulting CIGS layers are characterized, as well as complete solar cells. Then, the effects of the alloying of CIGS with silver (ACIGS) are reported, and the performances of complete cells are analyzed. These ultrathin CIGS and ACIGS films are also compared in a cathodoluminescence study. Finally, the impacts of an alumina passivation layer at the CIGS back contact with Mo are reported in the case of an ungraded CIGS composition. This passivation layer is fabricated using an upscalable process of nanoimprint lithography, and the impacts of the passivation on the photovoltaic performances are described.

Part III: a novel architecture of reflective back contacts for CIGS solar cells is successfully developed. It consists of a highly reflective silver mirror encapsulated in transparent conductive oxide (TCO) layers, and it is compatible with the direct co-evaporation of CIGS. The optical benefits of such a reflective back contact are first simulated with the Reticolo software. The properties of the fabricated reflective back contacts are reported, and ≈500 nm-thick CIGS layers co-evaporated on top of them are characterized. Thorough studies in transmission electron microscopy coupled with energy dispersive x-ray spectroscopy provided substantial information on the TCO/CIGS interface and helped to optimize the architecture of this reflective layer stack. As a perspective, light trapping strategies based on an additional dielectric layer with nanostructures were investigated numerically.

Part I. General context of ultrathin CIGS-based solar cells

Introduction to part I

In order to understand the stakes for the development of ultrathin CIGS-based solar cells, a brief overview of the energy and photovoltaic (PV) markets is given. The role of the CIGS technology within the PV industry is also discussed.

Next, a description of the architecture and physics of CIGS solar cells is provided, together with a short state of the art of CIGS devices with standard absorber thickness.

The benefits and challenges for the development of ultrathin CIGS solar cells are then listed, and the current status of ultrathin CIGS is detailed with a focus on the back contact properties.

Finally, the materials and methods used for the fabrication, characterization and simulation of CIGS devices in this study are presented.

Chapter 1. Industrial aspects of the photovoltaic technology

1.1.Introduction

This work is focused on the CIGS semiconductor technology and its application to PV devices. Hence, to get a clear picture of the context of this study, it is essential to first describe the sector of electricity production, its current issues, and the role of PV. The distribution of the PV market between the different existing technologies is also analyzed, and some of the notable assets of CIGS devices are listed.

1.2.A brief overview of the PV market

1.2.1. The global production of electricity and the share of PV

The world total supply of primary energy reached 13 647 million tons of oil equivalent in 2015 [14], and by the end of 2018 the global capacity of electricity production was 7 110 GW [15].

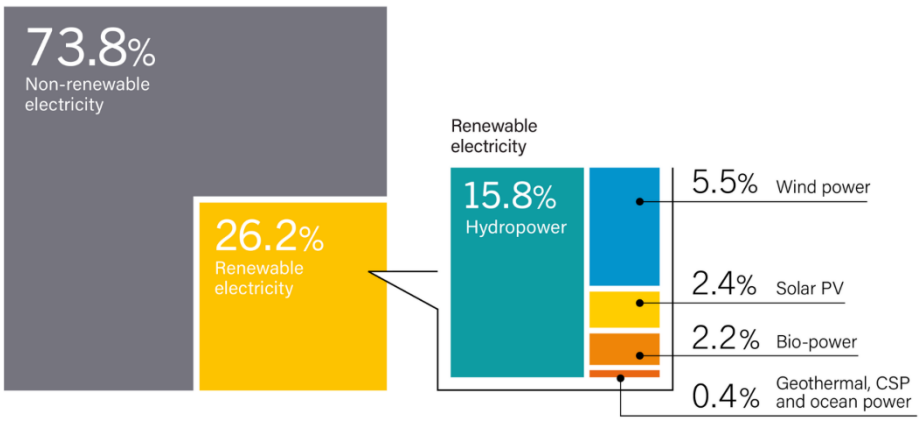

Figure I. 1. Estimated renewable energy share of global electricity production, end-2018. Totals may not add up due to rounding. From [15].

In 2018, 65.6% of the installed power capacity and 73.8 % of the generated electricity relied on non-renewable energy sources [15]. But the share of electricity generated from renewable energy has increased over the years [15], amounting to 26.2% of the global electricity production in 2018 (see Figure I. 1). The sector of renewable electricity is dominated by hydropower with 60.3% of the production, while the share of PV only accounts for 9.2%. Still, the PV market has a significant growth potential.

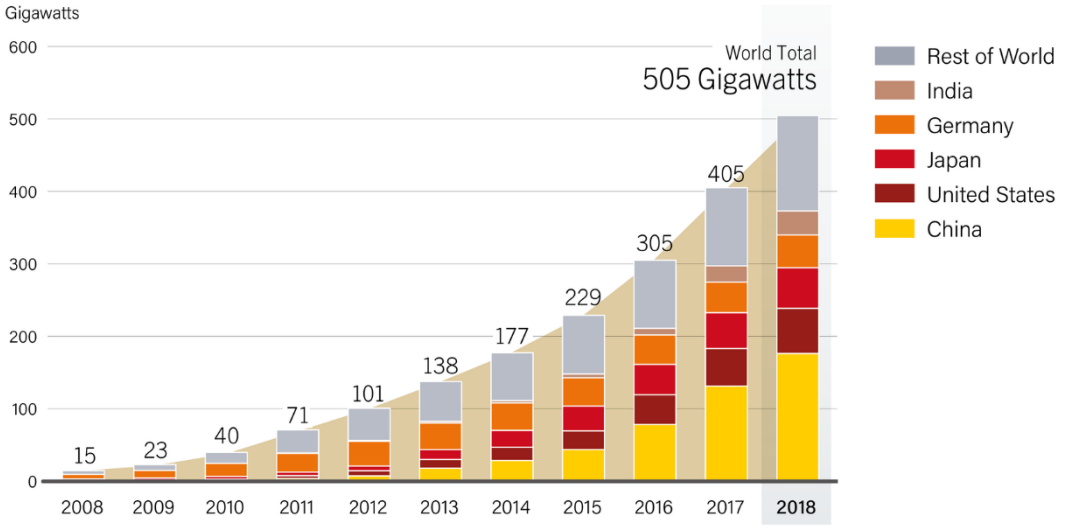

Figure I. 2. Solar PV global capacity by country and region, 2008 – 2018. Data are provided in direct current (DC). From [15].

The evolution of the installed solar PV global capacity over the last decade can be seen in Figure I. 2. It reveals that the PV market is rapidly growing, with a cumulative capacity of 505 GW in 2018 as compared to only 15 GW ten years earlier. The electricity production capacity of PV increased by 100 GW in 2018 owing to its improving competitiveness, which makes solar PV the fastest-growing energy technology [5], [15].

However, since 2016 the growth rate of the PV global capacity has stabilized. This results from a 15% decrease of China's annual addition to its PV capacity in 2018 following a substantial reduction of subsidies from the central government, which was compensated on the global scale thanks to an increasing demand in Europe and in emerging PV markets that is correlated to price reductions [15], [16]. This indicates that the development of the PV market is tied to its competitiveness as well as government policies. In this regard, the next sections will analyze the competitiveness of the PV technology, but also the global trends toward the energy transition and the reduction of greenhouse gases emissions.

1.2.2. Competitiveness of the PV electricity production

A consistent and widely used method to determine the price of electricity produced from different energy sources is to assess their levelized cost of electricity (LCOE). It consists in a calculation of the average total cost to install and operate a given power-generating system divided by its total energy production.

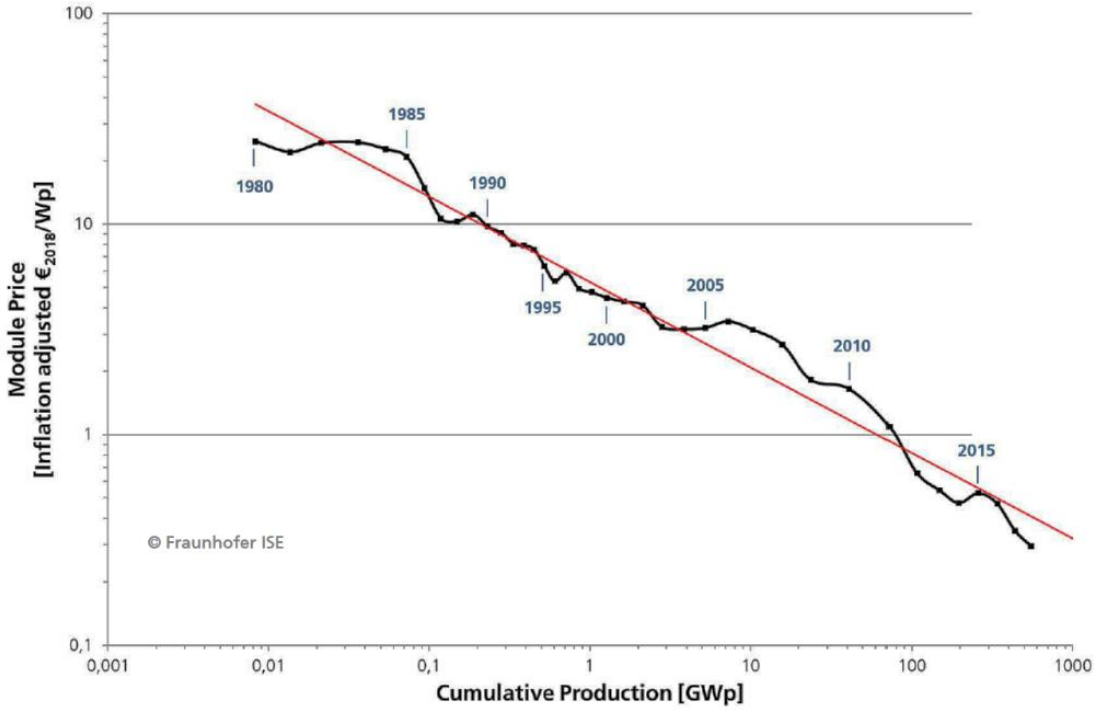

Figure I. 3. Price learning curve of solar PV modules, including all commercially available PV technologies. From [5].

In 2018, the cost of a PV system ranged from 600 to 1400 €/kWp, depending on the PV technology and the type of PV plant, and the LCOE for PV systems varied between 3.71 and 11.54 $€_{cent}$/kWh in Germany, based on the size of the PV installation and the average solar irradiance [17]. In comparison, the LCOE of coal lied between 4.59 and 9.96 $€_{cent}$/kWh in 2018, depending on the coal quality and the type of power plant [17]. This means that PV is already a competitive source of electricity production.

The LCOE of PV systems decreased over the last years, essentially thanks to a reduction of the module prices [5], [17], as shown in Figure I. 3. A learning rate of 24% can be deduced from the price learning curve of the last 38 years, *i.e.* each time the cumulative production doubled, the module price decreased by 24%. On top of that, the cost of electricity generated from PV systems is also expected to decrease in the upcoming years. Using a learning rate of 15%, the LCOE of PV systems in 2035 is predicted to range between 2.16 and 6.74 $€_{cent}$/kWh in Germany, while the LCOE of coal should be stable [17]. Thus, the competitiveness of PV should further improve over the years, confirming the strong growth potential of the PV market.

Nevertheless, the impacts of PV deployment are not limited to the economic field. Indeed, supplying energy and electricity from renewable sources has become a major challenge of the 21st century in order to reduce the emissions of greenhouse gases and to achieve a sustainable economy.

1.2.3. Climate change and greenhouse gases emissions

The issue of climate change has been gaining more and more attention over the past decades, and it can be considered as the next natural limit that our economy will have to face [2].

In this context, the Intergovernmental Panel on Climate Change (IPCC) has released five assessment reports since 1990, analyzing the impact of human activities on climate. The latest report underlines in particular the influence of anthropogenic emissions of greenhouse gases on climate change [1]. Figure I. 4 shows the upward trends in three greenhouse gases concentrations and in the annually and globally averaged surface temperature anomaly.

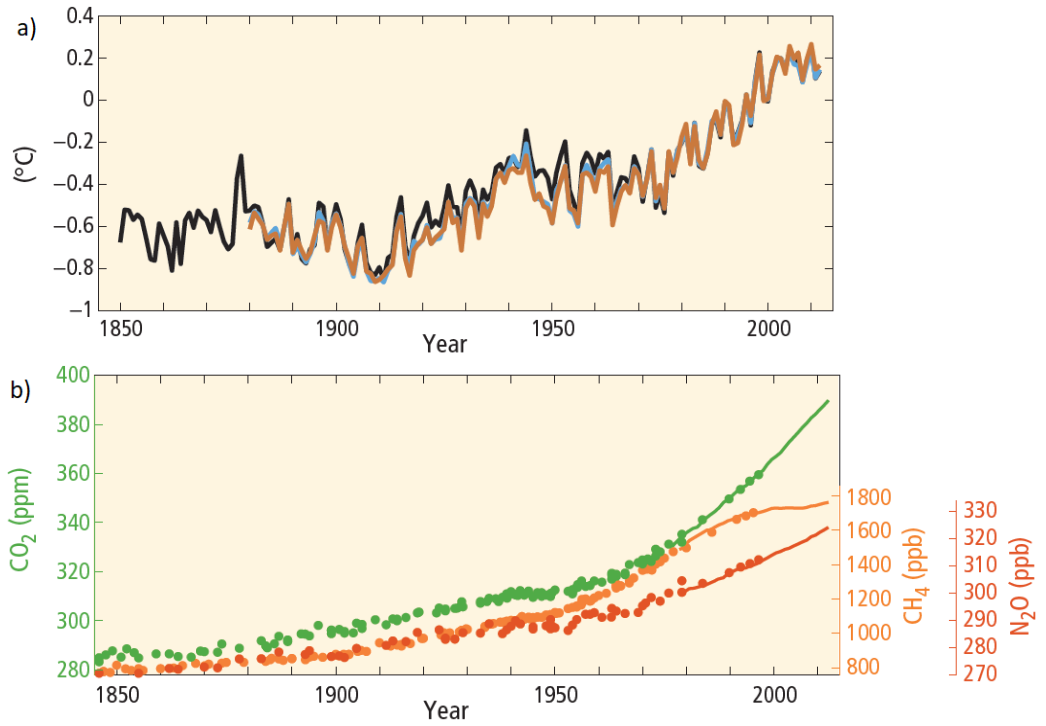

Figure I. 4. (a) Annually and globally averaged combined land and ocean surface temperature anomaly. The temperature anomaly is derived from the difference between a given annual average temperature and the average temperature over the period with best coverage (1961 – 1990). Colors indicate different sources of data sets. (b) Atmospheric concentrations of three greenhouse gases: carbon dioxide (CO_2, green), methane (CH_4, orange) and nitrous oxide (N_2O, red), determined from ice core data (dots) and from direct atmospheric measurements (lines). From [1].

Several factors allow to establish a relationship between human activities and climate change [2]:

- The use of fossil fuels and the deforestation due to mankind contribute to the increasing concentration of greenhouse gases in the atmosphere.
- Greenhouse gases are known to increase the average surface temperature on Earth by reflecting a part of the infrared light emitted from the ground.
- An uncontrolled global warming will have severe and irreversible impacts on both climate and economy.

Global awareness has raised on the topic of climate change. Government policies are more and more engaged toward the development of a sustainable economy and the reduction of greenhouse gases emissions, as shown recently with the ratification of the Paris Agreement negotiated during the 2015 United Nations Climate Change

Conference (COP 21) [3]. It provides guidelines and a notable quantitative objective that all signing parties are committed to fulfill, as described in article 2(a):

> Holding the increase in the global average temperature to well below 2°C above pre-industrial levels and pursuing efforts to limit the temperature increase to 1.5°C above pre-industrial levels, recognizing that this would significantly reduce the risks and impacts of climate change.

As of September 2019, the agreement was approved and signed by 185 countries [18], which is a major step toward the mitigation of climate change. To achieve the goal of a global average temperature increase limited to less than 2°C, the part of greenhouse gases emissions stemming from the production of electricity must be reduced.

Indeed, the sector of electricity production had the largest contribution to the emission of fossil fuel CO_2 in 2014 [19]. The IPCC has also investigated various future scenarios up to 2100 in order to keep the temperature change due to anthropogenic greenhouse gases emissions below 2°C as compared to pre-industrial levels. In those scenarios, an atmospheric concentration of about 530 ppm CO_2eq by 2100 is predicted to have a 50% chance of limiting the temperature change to 2°C [19]. The transition pathways of the electricity supply proposed in order to meet the goal of the Paris Agreement all show that the share of renewable electricity will strongly increase during the next decades, as seen in Figure I. 5. Interestingly, all scenarios exhibit a growth of the total electricity supply despite the decrease of the fossil fuel share in the production of electricity.

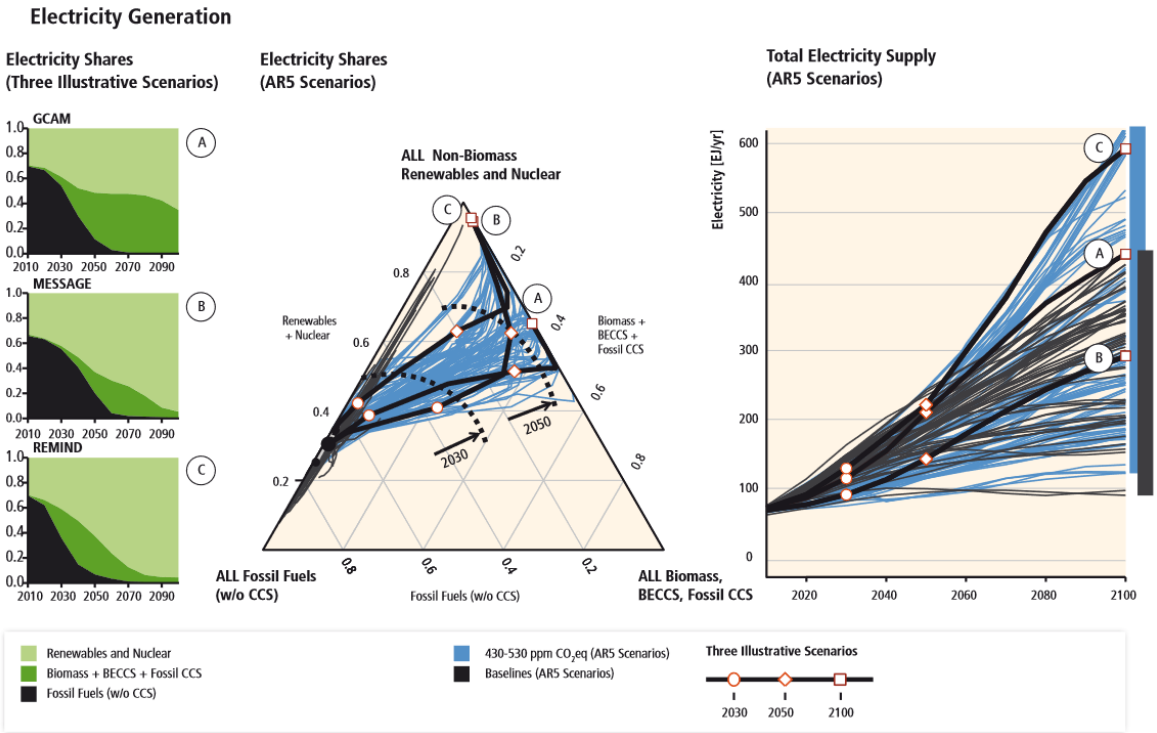

Figure I. 5. Transition pathways of electricity generation over the time span from 2010 to 2100 for mitigation scenarios that lead to atmospheric concentrations of greenhouse gases of 430–530 ppm CO_2eq. From [19].

It is clear that renewable sources of electricity, including the PV technology, will play a major role in the upcoming energy transition. It is worth mentioning that the deployment of PV will also face several challenges, *e.g.* the uneven geographical availability and the intermittency of solar resources, the need for energy storage systems, the limited flow of energy that can be supplied from PV systems, and the toxicity of materials necessary to produce some types of PV modules [2]. Still, renewable energy sources, sunlight in particular, remain a promising alternative to carbon energy as they are abundant, various, and in general less polluting and dangerous than fossil fuels and nuclear power [2], [4]. In addition, a variety of PV technologies are already available and commercialized, which should bring more flexibility and resilience to the PV market and its electricity production. The next section will briefly describe the distribution of the PV market among those technologies.

1.3.Commercial PV devices: CIGS and other technologies

The solar PV market consists of several different technologies. The annual global production has been historically dominated by the silicon PV technology [5], which can be distinguished between monocrystalline and multicrystalline Si, as shown in Figure I. 6.(a). The share of multicrystalline Si has grown over the years to become the major technology for module production and represented 60.8 % of the annual production in 2017. In comparison, monocrystalline Si and thin film technologies accounted for 32.2% and 4.5% of the market in 2017 [5]. The proportion of thin film technologies in the annual production of modules is thus quite limited, and it has been regularly decreasing during the last decade.

Still, among thin film technologies the market share of CIGS modules has been the only one not to decrease since 2010, as it oscillated around 2% of the total PV module production [5]. Hence, the share of CIGS in the field of thin film technologies has increased up to approximately 42% in 2017, see Figure I. 6.(b). The rest of the thin film market is shared between CdTe and amorphous Si, with respective shares of 51% and 7%. Besides, as a result of the growing total PV production over the years, the production of CIGS modules has also been increasing to reach 1.9 GWp in 2017.

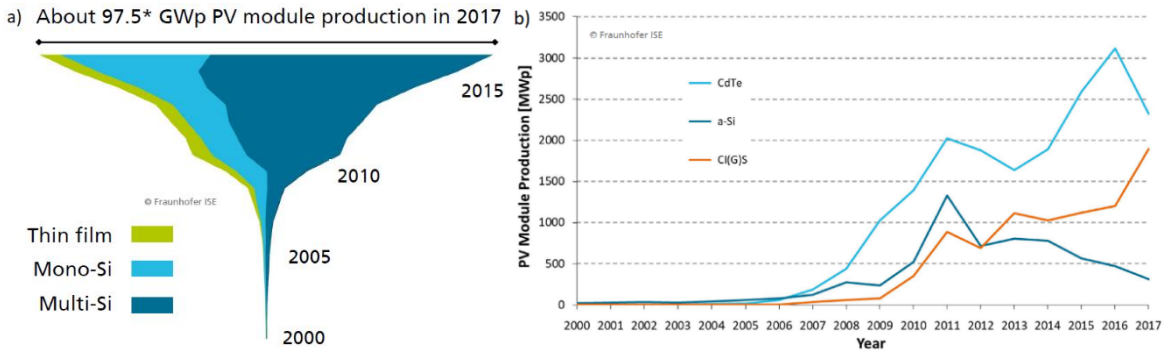

Figure I. 6. (a) Annual global PV production by technology (in GWp), from 2000 to 2017. *2017 production numbers reported by different analysts may vary, a realistic total PV module production is estimated to be 97.5 GWp in 2017. (b) Annual global PV module production of thin-film technologies between 2000 and 2017. Data: from 2000 to 2010: Navigant; from 2011: IHS. Graph: PSE GmbH 2018. From [5].

As of 2019, the record efficiency for a CIGS-based module is 17.4 ± 0.6 % (1.09 m^2, aperture area), below the best efficiencies of 19.9 ± 0.4 % (1.51 m^2, aperture area) for multicrystalline Si and 24.4 ± 0.5 % (1.32 m^2, designated illumination area) for monocrystalline Si modules [6]. Still, the CIGS technology has several advantages for industrialization, even as compared to Si PV modules which largely dominate the market and benefit from their advanced commercial maturity [20], [21]:

- Thin film technologies rely on semiconductors with a direct bandgap and thus have a much higher absorption coefficient than Si which is an indirect bandgap material. As a result, thin film PV devices have low materials consumption as they require about 1 hundredth of semiconductor material as compared to Si.
- CIGS modules exhibit a competitive LCOE as compared to multicrystalline Si, as they were both calculated to range between 0.10 to 0.14 $/kWh for various locations in the US (2016) [7]. The LCOE of CIGS devices could be further reduced with a lower module price, an increased efficiency with a similar module price, and a reduced degradation rate [22].
- Thin film PV is well suited for building-integrated photovoltaics, thanks to the possible use of flexible substrate and the monolithic integration of modules. In addition, the CIGS technology is more robust than other PV materials under non-standard conditions of diffuse light, high temperature and partial shading.
- Thin film PV has a carbon footprint of 12–20 g CO_2eq/kWh, much lower than Si with 50–60 g CO_2eq/kWh due to its energy intensive purification and processing steps for fabrication. This contributes to the shorter energy payback time of 0.78 year for CIGS-based PV modules, instead of 2.12 and 1.23 years for mono- and multi-crystalline Si, respectively (assuming that modules are produced in China and installed in a region with a solar irradiation of 1700 kWh.h.m^{-2} per year) [23].

The present PhD thesis is focused on the reduction of absorber materials usage for the fabrication of CIGS-based PV devices. Doing so while successfully maintaining their efficiency would result in an improved competitiveness. Before analyzing the consequences of a reduced CIGS absorber thickness, the architecture and the physics of standard CIGS-based solar cells will be described in the next section.

Chapter 2. Physics of CIGS solar cells

2.1.Introduction

In order to introduce the physics of CIGS PV devices, the typical architecture of CIGS-based solar cells will be presented together with a brief state of the art. The fundamental mechanisms for charge carrier generation and collection will be exposed. In addition, the main figures of merit that are commonly used to characterize and compare solar cells will be detailed.

2.2.CIGS solar cell architecture

The CIGS technology has been studied for more than 40 years. Back in 1975, the Bell laboratories reported an efficiency of 12%, which was measured outdoor under a solar intensity of ~92 mW/cm^2 [24]. Since then, CIGS-based solar cells have been continuously improved and reached efficiencies over 20% at the laboratory scale in 2011 [25]. The record efficiency at present is as high as 23.35%, and was achieved by SolarFrontier [26].

The standard architecture of a CIGS solar cell is depicted in Figure I. 7. CIGS photovoltaic devices are fabricated on a substrate, usually a slab of soda-lime glass, with a molybdenum layer as a back contact with the CIGS semiconductor. The front layers that complete the solar cell generally consist of a CdS buffer layer and ZnO-based transparent electrodes. In this configuration, light enters the solar cell stack from the top Al-doped ZnO layer. To reduce the total light reflection of the device, an additional antireflection coating made of MgF_2 can be deposited on top of ZnO:Al.

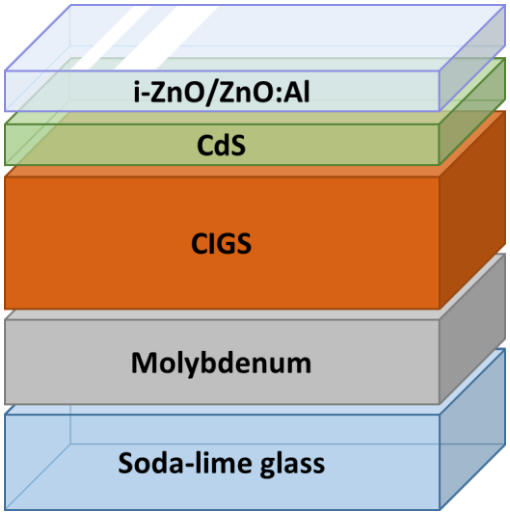

Figure I. 7. Schematic of a standard CIGS-based solar cell.

The main properties and historical improvements of each layer will now be discussed.

2.2.1. Substrates

Soda-lime glass (SLG) is a type of glass that contains significant amounts of sodium, calcium and aluminum oxides beside silicon oxide. It is well suited as a substrate for the fabrication of CIGS solar cells, essentially thanks to:

- its low cost. The manufacturing cost for using a SLG substrate as well as a front stack of EVA/SLG is estimated to amount to ~12 $\$_{2015}/m^2$ assuming a monolithic CIGS module fabricated by sputtering and sulfurization after selenization, for a 1 GW/year production volume in the U.S [7]. This represents only ~17% of the total module cost of 69 $\$_{2015}/m^2$.
- its glass transition temperature in the 550–600 °C range [27] that is compatible with the typical deposition temperatures of CIGS.
- its thermal expansion coefficient of 9.1–9.5 × 10^{-6} K^{-1} [27], [28], that matches the one of the CIGS layer.
- the diffusion of Na from the SLG to the CIGS layer during the fabrication process. The incorporation of Na was reported to be beneficial for the performance of CIGS solar cells back in 1993 [27]. This aspect will be discussed together with the CIGS absorber in section I.2.2.3.

Recently, flexible substrates have also gained attention as they allow for a wider range of applications and cost-efficient roll-to-roll manufacturing processes [29]. A high efficiency of 20.8% was recently reported for a CIGS solar cell with an area of 0.5-cm^2 on a polyimide substrate [30]. MiaSolé also reached an efficiency of 17.4 ± 0.6 % for a flexible CIGS module (1.09 m^2, aperture area) [6].

2.2.2. Molybdenum and other back contacts

Mo is widely used as a CIGS back contact, and CIGS solar cells with the highest efficiencies include a Mo back contact deposited by sputtering [26], [31], [32]. Indeed, Mo is one of the few metals that is inert during the deposition of CIGS [33], and permeable to Na diffusion [27]. It also forms an ohmic contact with CIGS, in particular thanks to the growth of a $MoSe_2$ [34] interfacial layer when Mo is exposed to Se vapor at temperatures ≥400°C [35].

The fabrication of CIGS solar cells with transparent back contacts has also been investigated, in particular for bifacial applications [36], [37] or in superstrate configuration [38], [39], where light enters the solar cell respectively from both sides or from the substrate/back contact side. Transparent back contacts are usually made of a highly doped, transparent conductive oxide (TCO). The challenges and potential benefits of a transparent back contact – especially in the case of ultrathin CIGS absorbers – will be detailed in section I.3.2.3.

2.2.3. CIGS-based absorber

$Cu(In,Ga)Se_2$ is a quaternary I-III-VI semiconductor. It can be regarded as an alloy of the $CuInSe_2$ and $CuGaSe_2$ ternary compounds, where In and Ga share the same atomic sites in the CIGS crystalline structure. The tetragonal chalcopyrite structure of CIGS is represented in Figure I. 8.

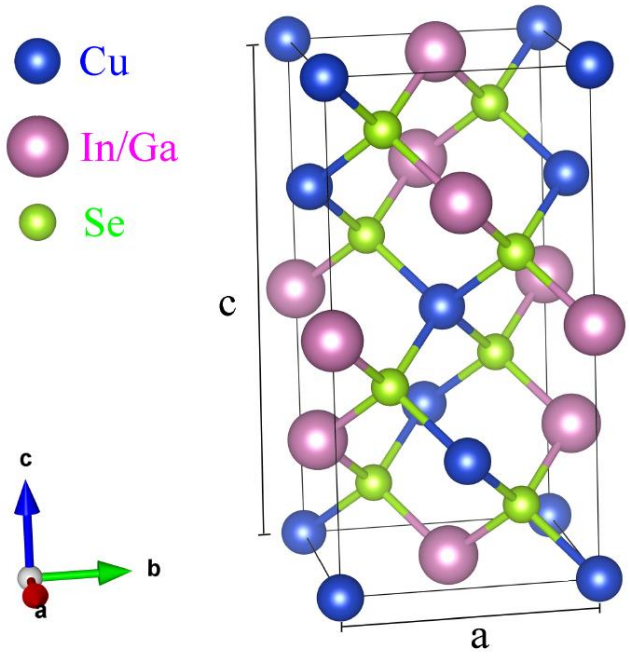

Figure I. 8. Schematic of the unit cell of the Cu(In,Ga)Se_2 chalcopyrite crystalline structure, where a and c refer to the lattice constants. From [40].

A distortion of the structure results in a ratio of lattice constants c/a ≠ 2, which depends on the composition in In and Ga. The lattice constants decrease from a = 5.780 Å and c = 11.604 Å for $CuInSe_2$, to a = 5.607 Å and c = 10.983 Å for $CuGaSe_2$ [41]. The atomic ratio of In and Ga in the CIGS composition, commonly denominated as GGI = [Ga]/([Ga]+[In]), also modifies the bandgap of CIGS following the formula [42]:

$$E_g = 1.01 + 0.626 \times GGI - 0.167 \times GGI(1 - GGI) \qquad \text{(I. 1)}$$

A valence band offset of ΔE_V = -0.04 eV and a conduction band offset of ΔE_C = 0.60 eV between $CuInSe_2$ and $CuGaSe_2$ were calculated and reported by Wei and Zunger [43]. Highest efficiencies of CIGS solar cells are obtained for bandgap values close to 1.15 eV [32], [44], *i.e.* for average GGI ratios close to 0.30.

The Cu stoichiometry of CIGS solar cells, which can be expressed as the atomic ratio CGI = [Cu]/([Ga]+[In]), is generally below unity [30], [45]. The Cu deficiency of CIGS solar cells results in the formation of a compensated pair of shallow defects: $(2V_{Cu}^{-} - In_{Cu}^{2+})$ [46], while Cu-rich CIGS films exhibit significantly lower concentrations of defects [45]. Still, a slight prevalence of the Cu vacancy defects leads to a *p*-type doping of CIGS layers with Cu-poor stoichiometry [46]. A Cu-poor stoichiometry also improves the performances of CIGS solar cells thanks to the formation of ordered vacancy compounds (OVC) at the front interface of CIGS, such as $Cu(In,Ga)_3Se_5$ or $Cu(In,Ga)_5Se_8$ [47]. Indeed, the OVCs show a wider bandgap due to a lower valence band maximum as compared to the chalcopyrite CIGS [48]. Besides, the OVCs favor the diffusion of Cd deposited by chemical bath deposition (CBD), which can lead to a *n*-type doping of the OVC layer if Cd atoms are sufficiently activated [47]. These combined effects in turn repel holes toward the CIGS bulk and reduce recombination of charge carriers at the CdS/CIGS hetero-interface [45], [47].

As the presence of the OVC layer is necessary to reach high CIGS solar cell performances, the most common processes for the deposition of CIGS were designed to achieve high quality films with Cu-poor compositions. Two methods in particular are used for commercial manufacturing of CIGS modules: the co-evaporation process where absorber elements are simultaneously evaporated, and the sequential process in which metallic precursor layers are selenized or sulfoselenized under annealing [49]. The co-evaporation process, which was used in this work, was initially based on the growth of a bilayer [50], [51], but then evolved into the so-called three-stage process [52], [53] that consists in a Cu-poor/Cu-rich/Cu-poor growth sequence. The main benefit of this co-evaporation process is to enable the formation of a double-graded Ga composition, and thus a double-graded conduction band, that is beneficial to photovoltaic performances [29], [52], [54]. The impacts of the CIGS band grading will be further discussed in section I.3.2.1.

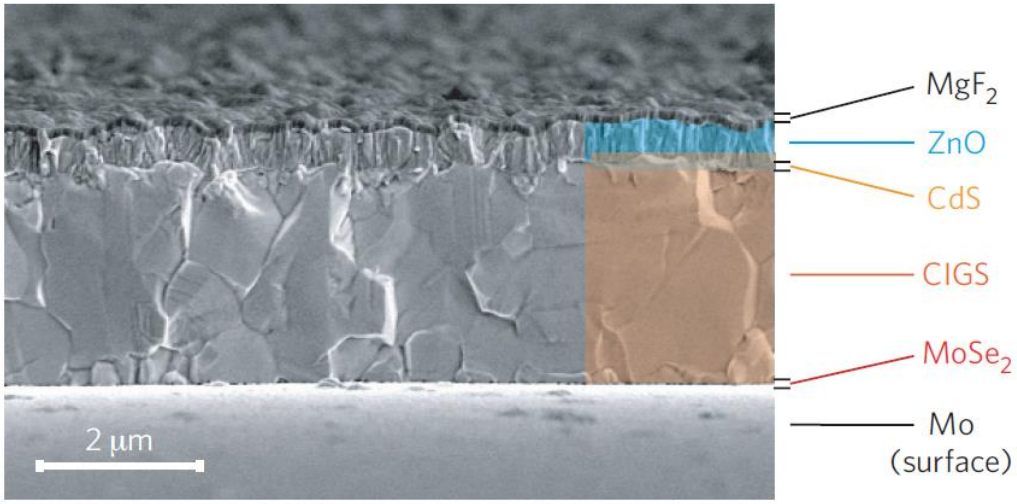

Figure I. 9. Cross-section image of a complete CIGS solar cell in scanning electron microscopy (SEM). The device was fabricated on a polyimide substrate and achieved an efficiency higher than 18%. From [29].

Recently, a lot of research efforts have been made toward the incorporation of alkali to the CIGS absorber, as the coincidental diffusion of Na from the SLG substrate to the CIGS absorber was discovered to boost solar cell efficiencies in 1993 [27]. Indeed, Na in concentrations of $\sim 10^{19}$ atoms/cm^3 was shown to substitute the detrimental In_{Cu}^{2+} donor defect, thereby increasing the effective hole density of CIGS and reducing the recombination of charge carriers [27], [55]. Various strategies for the intentional incorporation of Na to CIGS have then been reported, such as the deposition of a NaF precursor layer on the back contact prior to CIGS deposition [56], [57], the use of a NaF post-deposition treatment (PDT) after the CIGS growth [58]–[60] and the fabrication of CIGS solar cells on Na-doped Mo back contacts (Mo:Na) [61]. Similar or improved efficiencies are achieved when Na is intentionally added to CIGS as compared to when it is incorporated via its out-diffusion from the SLG [57], [60]. This allowed in particular the development of efficient CIGS solar cells fabricated on Na-free flexible substrates like polyimide (PI) [29], [30], [62] or stainless steel foils [63], [64].

The addition of heavier alkali elements has also gained a lot of attention since 2013, when the record cell efficiency was achieved on a polyimide substrate with a KF PDT [65]. Contrary to Na, the incorporation of K during the growth of CIGS was reported to lead to the formation of a deep defect level that results in a reduced minority carrier lifetime and a poorer collection of photogenerated charge carriers [66]. In contrast, adding K to the CIGS layer via a PDT was shown to modify the composition of the CIGS front interface: it forms a K-containing In_2Se_3 compound in the OVC layer [67]–[70], and it enhances the formation of Cd_{Cu} donor sites during the chemical bath deposition of the CdS buffer layer [65], [71]. As a result, the CdS buffer layer can be thinned to reduce its parasitic absorption, in turn improving the efficiency of CIGS solar cells [65]. The recombination rates at the heterojunction and in the depletion region were also shown to be reduced thanks to a K-treatment [72]. For a detailed summary of the effects associated with the PDT of KF, the reader can refer to the review from Muzillo [73]. Finally, heavier alkali elements like Rb and Cs were also studied recently, and led to the best CIGS efficiencies in particular thanks to improved carrier lifetimes. [26], [31], [32].

It is worth mentioning that alkali elements were reported to exhibit a heterogeneous distribution in CIGS, as they preferentially accumulate at grain boundaries and interfaces rather than in the CIGS grain interior [74]–[76]. However, the effects of alkali on the grain boundaries of CIGS are still debated, as recent studies reported either the existence or the absence of a grain boundary passivation effect due to the segregation of alkali [77], [78]. Nevertheless, CIGS layers generally exhibit micrometer-scale grains and thus a large amount of grain boundaries, as shown in the scanning electron microscopy (SEM) cross-section in Figure I. 9. The CIGS grain boundaries do not have a significant impact on solar cell performances [79] as they usually exhibit surface recombination velocities below 10^4 cm/s [78], [80], [81], which is estimated to be low enough to reach efficiencies over 20% [82].

Over the last 10 years, solar cells with high performance have also been achieved with absorbers based on silver-alloyed CIGS, *i.e.* (Ag,Cu)(In,Ga)Se_2 (ACIGS), where Ag and Cu share the same atomic sites in the chalcopyrite structure [83], [84]. Regardless of the GGI ratio, the substitution of Cu by Ag results in a decreased melting temperature, an enhanced grain size and an increased bandgap with lower valence band and conduction band edges [84]–[86]. The lower melting point of ACIGS can decrease the amount of structural disorder thanks to a sintering effect, which could possibly reduce the density of intra-grain defects [86], [87]. Besides, the efficiency of CIGS solar cells with high GGI ratios and bandgaps over 1.3 eV can be improved with Ag-alloying, mostly thanks to the electronic band structure of ACIGS that allows a better band alignment with CdS as compared to CIGS [84], [88], [89]. Owing to the promising properties of this semiconductor, the development of ultrathin absorbers made of ACIGS was also investigated in this work.

2.2.4. Cadmium sulfide and buffer layers

Standard CIGS solar cells are fabricated by deposition of an *n*-doped CdS buffer layer on top of the CIGS absorber, thereby forming a *p*-*n* heterojunction. The CdS layer is usually grown by chemical bath deposition (CBD) in an aqueous solution of ammonia

containing a cadmium salt and a sulfur precursor like Cd acetate and thiourea, respectively [90].

The CBD process leads to the growth of conformal CdS layers that avoid detrimental shunt paths and protect the absorber surface from plasma damage during the deposition of the front contact layers by sputtering [91]. It was also reported that the diffusion of Cd in the OVCs at the front surface of the absorber could contribute to the passivation of the heterojunction interface [47]. However, the CdS buffer exhibits two major disadvantages: the toxicity of cadmium, and its rather low bandgap (~2.4 eV) that results in parasitic absorption at wavelengths below ~500 nm [91].

This led to the recent investigations of Zn-based buffer layers like Zn(O,S) [91]. Zn-based buffer layers are non-toxic, and can be deposited with a variety of processes including CBD [91], [92]. In addition, Zn(O,S) has a higher bandgap than CdS that can be tuned between 2.8 eV and 3.8 eV, depending on its oxygen and sulfur composition [93]. This feature notably allows a better band alignment and a proper conduction band offset at the heterointerface of wide bandgap CIGS-based absorbers [94].

It is worth mentioning that the current record efficiency for laboratory-scale CIGS solar cells of 23.35% was achieved with a Cd-free architecture, where the buffer layer consists of a $Zn(O,S,OH)_X$ film prepared by CBD [26].

2.2.5. Transparent front contact

The transparent front electrode is made of TCO films that combine a high transparency with a sufficient lateral conductivity. It is commonly prepared by sputtering of a bilayer stack made of intrinsic and aluminum-doped ZnO (*i*-ZnO/ZnO:Al).

The main role of the high-resistance *i*-ZnO film is to passivate pinholes in the CdS layer and to avoid local shunt paths in complete devices [90], [95]. The highly doped ZnO:Al layer ensures the lateral conduction of free electrons thanks to its low sheet resistance, which is typically in the order of magnitude of 10 Ω/sq. However, the ZnO:Al layer is also responsible for parasitic absorption in the infrared region due to free carrier absorption. Hence, its thickness has to be optimized to achieve both a sufficient transparency and conductivity.

CIGS devices with best efficiencies (>22 %) are prepared with highly transparent front contact layers, where i-ZnO is replaced by (Zn,Mg)O as its wider bandgap results in an increased transparency and provides a better band alignment with Zn(O,S) [26], [72], [96]. In addition, the top ZnO:Al layer can be replaced by a more transparent boron-doped ZnO film [26], [32], [97].

2.2.6. State of the art for CIGS devices

Table I. 1 gives a brief overview of the best efficiencies that were reported for CIGS-based solar cells and modules. To compare the performances of CIGS devices with other photovoltaic technologies, one may refer to the record efficiency tables edited by Green *et al*. [6].

For a deeper understanding of the CIGS-based photovoltaic technology, the next section will detail the physics of CIGS solar cells.

Institute or company	Substrate & back contact	CIGS deposition method	Buffer layer	Front contact	Efficiency & area	Reference
Solar cells						
Solar Frontier	Glass/ Mo	Sputtering, selenization then sulfurization, and Cs post-treatment	$Zn(O,S,OH)_X$	$Zn_{0.8}Mg_{0.2}O$/ ZnO:B	23.35 % * (1.04 cm^2)	[26]
Solar Frontier	Glass/Mo	Sputtering, selenization then sulfurization, and Cs post-treatment	CdS	no intrinsic layer ZnO:B	22.9 % * (~1 cm^2)	[32]
ZSW	Glass/Mo	Co-evaporation, RbF PDT	CdS	(Zn,Mg)O or *i*-ZnO/ ZnO:Al	22.6 % * (~0.5 cm^2)	[31]
Uppsala University	Glass/Mo	Co-evaporation of ACIGS	CdS	*i*-ZnO/ ZnO:Al	20.9 % (~1 cm^2)	[84]
EMPA	PI/Mo	Co-evaporation at 450°C, RbF PDT and capping layer	CdS	*i*-ZnO/ ZnO:Al	20.8 % * (0.52 cm^2)	[30]
NREL	SLG/Mo	Co-evaporation	CdS	*i*-ZnO/ ZnO:Al	20.8 % * (~0.1 cm^2), 23.3 % * concentrated	[98]
Modules						
MiaSolé	Stainless steel/Mo:Na	Sputtering and selenization	CdS (sputtering)	? / ZnO:Al	17.4 % * (1.09 m^2)	[96], [99]
Solibro	Glass/Mo	Co-evaporation	CdS	*i*-ZnO/ ZnO:Al	17.5% * (0.94 m^2)	[96]
Avancis	Glass/SiN/Mo	Sputtering, rapid thermal processing, S and Se	Zn(O,S)	ZnO:Al	19.0% (0.67 cm^2)	[100]

Table I. 1. Selection of high-performing CIGS-based solar cells and modules that were recently achieved. *Independently certified efficiencies.

2.3.Charge carrier generation

The fundamental principle of a photovoltaic device is to generate electrical power by absorbing light in order to generate positive and negative charge carriers, and to selectively extract them at two distinct contacts [101]. In practice, this is usually achieved via a p-n junction of two semiconductor materials, though it is not an absolute requirement for an efficient solar cell [101], [102]. The sun provides an abundant, quasi-unlimited source of light that can be converted into power by photovoltaic systems [4], which is why they are generally designed to produce electricity from sunlight. Hence, the solar spectrum will first be described in this section, then the absorption of light and generation of charge carriers will be analyzed. Finally, the collection of charge carriers as well as the main loss mechanisms will be presented together with the common performance parameters.

2.3.1. The solar spectrum

Figure I. 10 shows the solar spectral irradiance received on Earth which was modeled with the SMARTS2 (version 2.9.2) software [103]. Two reference conditions are described, the spectral irradiances for an air mass of 0 and 1.5, respectively designated as AM 0 and AM 1.5 G:

- The AM 0 spectrum corresponds to the extraterrestrial spectral irradiance, at the surface of the Earth's atmosphere. It is close to the spectral irradiance of a black body at 5800 K, which describes quite accurately the light spectrum emitted by the Sun [102].
- The standard global AM 1.5 spectral irradiance is the fraction of the solar spectrum that reaches a surface on Earth under normal incidence conditions, for an elevation of the Sun of 41.8° above the horizon. More simply put, it is the solar spectral irradiance that impinges the terrestrial surface after crossing the atmosphere over a distance corresponding to 1.5 times its thickness [103]. The "global" spectrum (AM 1.5 G) takes into account the typical diffusion of the atmosphere. It exhibits absorption bands due to molecules found in the atmosphere, such as O_2, CO_2, H_2O and others. The standard testing conditions (STC) for one-sun illumination uses the AM 1.5 G spectrum as a reference. Its integrated irradiance leads to a power density of ~1000 $W.m^{-2}$.

The filled area represents the maximum solar power density of the AM 1.5 G spectrum that can be converted into electrical power by a CIGS-based solar cell with a standard bandgap of 1.15 eV, or ~1080 nm when expressed as a wavelength. In this respect, the two major loss mechanisms of photovoltaic energy conversion are unfolded: the non-absorption and the thermalization of photons whose energy is respectively lower and higher than the bandgap of the absorber, or alternatively photons with wavelengths above and below the wavelength corresponding to the bandgap, respectively. These unavoidable loss processes, as well as radiative recombination and isothermal dissipation losses occurring in photovoltaic devices can be described with the well-known Shockley-Queisser model [104], using the thermodynamic principle of detailed balance. A discussion of this theoretical efficiency limit can be found in [101]. For the typical bandgap range of CIGS solar cells (1.1–1.3 eV), a maximum efficiency of ~33% is predicted under STC [105].

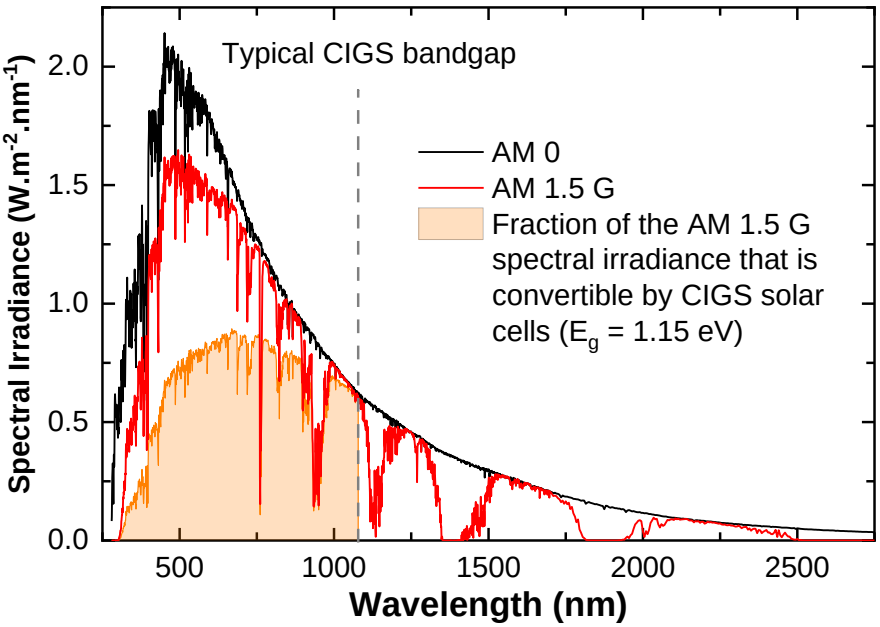

Figure I. 10. Solar spectral irradiance for an air mass of 0, *i.e.* outside the Earth's atmosphere (AM 0, black line), and standard global spectral irradiance reaching the Earth's surface for an air mass of 1.5 (AM 1.5 G, red line). The filled area is the sunlight power density (AM 1.5 G) that can be converted by a CIGS solar cell with a typical bandgap of E_g = 1.15 eV, taking into account thermalization losses.

In conclusion, the first requirement that must be considered to achieve an efficient photovoltaic device is the absorption of the incident light over a wide range of wavelengths.

2.3.2. Light absorption

Semiconductor materials, unlike metals, exhibit electronic band structures with a bandgap (E_g), which is an energy range where no electron states can exist. In the fundamental state, *i.e.* without any excitation, the electronic band at the lower energy edge of the bandgap is filled with electrons and is called the valence band. On the other hand, the electronic band at the upper energy edge of the bandgap is depleted of electrons and is referred to as the conduction band. The semiconductor can thus be considered as a two-level system. Figure I. 11 depicts how an incident photon can interact with this two-level system in three distinct ways depending on its energy $h\nu$:

1. $h\nu < E_g$, the photon energy is lower than the bandgap. In this case the photon is not absorbed by the semiconductor and will not be converted by the solar cell.

2. $h\nu = E_g$, the photon energy is equal to the bandgap. For this situation, the photon can be absorbed by the semiconductor, as it provides a sufficient energy to promote an electron from the valence band to the conduction band, leaving a positively-charged empty state in the valence band that is commonly called a hole. This mechanism results in the creation of an electron-hole pair without any energy loss.

3. $h\nu > E_g$, the photon energy is higher than the bandgap. In this configuration, the photon can also generate two carriers but the excess energy is relaxed on a sub-picosecond timescale due to the emission of phonons and the thermalization of the carriers to the band edges [101]. Hence, the maximum energy that can be converted from photons whose energy is higher than the semiconductor's bandgap is limited, see also Figure I. 11.

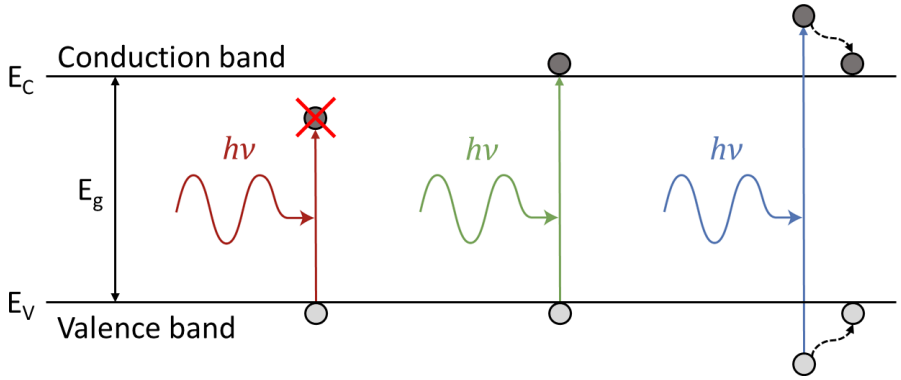

Figure I. 11. Schematic representation of the different interactions between a photon and a two-band system. If $h\nu < E_g$, the photon is not absorbed. If $h\nu = E_g$ the photon can promote an electron from the valence band to the conduction band with no energy loss in the process. If $h\nu > E_g$, the photon can also generate a pair of charge carriers, but the excess energy $h\nu - E_g$ is lost by thermalization of the electron and hole to the band edges E_C and E_V, respectively.

2.3.3. Generation of charge carriers

The simple presentation of the photon absorption in the previous section describes the relationship between light absorption of a semiconductor and its bandgap. In addition, the absorption coefficient of a semiconductor is a wavelength-dependent function that is related to the electronic band structure of the semiconductor. Semiconductors with a direct bandgap, like CIGS and other absorbers of the thin-film photovoltaic technology, exhibit a much higher absorption coefficient than Si, which has an indirect bandgap that requires phonon-photon interactions for light absorption. In practice, some of the incident photons with an energy higher than the semiconductor's bandgap are not absorbed, due to light reflection out of the device or parasitic light absorption in inactive layers for example.

Figure I. 12 shows the absorption coefficient of CIGS for a bandgap of 1.2 eV and the density of the generated charge carriers for a solar cell with a 1000 nm-thick CIGS layer under one-sun illumination. Most of the charge carriers are generated close to the CdS buffer layer, within a CIGS depth of about 500 nm. Some interferences with a small amplitude are observed at the CIGS back contact due to light reflection at the CIGS/Mo back contact. In this case, a non-negligible part of the incident light is transmitted to the metallic Mo back contact. It is absorbed in the Mo layer but it does not contribute to the generation of electron-hole pairs, because the charge carriers get completely thermalized in the continuous electronic band structure of the metal.

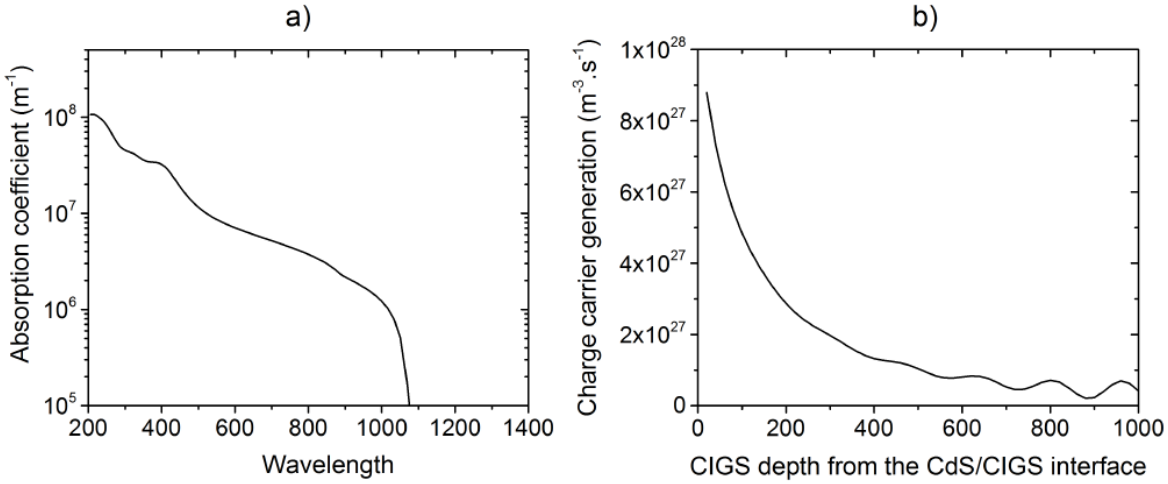

Figure I. 12. a) Absorption coefficient of CIGS for a bandgap of 1.2 eV derived from ellipsometric measurements and b) profile of the generated charge carrier density in a 1000 nm-thick CIGS layer, simulated for a CIGS solar cell under one-sun illumination with the ray transfer matrix method. From [12].

In order to produce an electrical power with a solar cell, the charge carriers generated in the semiconductor material need to be selectively collected before they recombine. The collection of charge carriers will be analyzed in the next section for the case of the CIGS/CdS heterojunction.

2.4.Charge carrier collection

2.4.1. The p-n junction

In most photovoltaic devices, a *p-n* junction is designed to achieve an efficient collection of the photogenerated charge carriers. In the case of the CIGS technology, the *p-n* junction consists in a heterojunction formed between 2 semiconductors of different bandgaps: CIGS and CdS. In Figure I. 13, the electronic band diagram of a typical CIGS solar cell under one-sun illumination at short-circuit condition was simulated with SCAPS (version 3.3.07, software created by Burgelman *et. al* from the university of Gent [106], [107]), with materials parameters described in [29].

Discontinuities, or offsets, of the valence band maximum and the conduction band minimum are observed due to the varying bandgap of each material constituting the solar cell. Besides, the contact between the *p*-doped CIGS and the *n*-doped CdS results in the formation of a built-in potential. For a detailed derivation of this potential and associated electric field, the reader may refer to the work of Prof. Würfel [102].

As the CIGS layer is poorly doped (acceptor density $N_A = 4 \times 10^{15}$ cm^{-3}) and the CdS is highly doped (donor density $N_D = 1 \times 10^{18}$ cm^{-3}), the neutrality condition at the CIGS/CdS interface results in a depletion of free carriers in the CIGS region over a depth of approximately 300 nm, which is called the Space Charge Region (SCR). In the rest of the CIGS layer, the density of majority carriers (holes) and the net doping density are almost equal ($p \approx N_A$). Hence, this portion of the CIGS film is almost neutral and is designated as the Quasi Neutral Region (QNR).

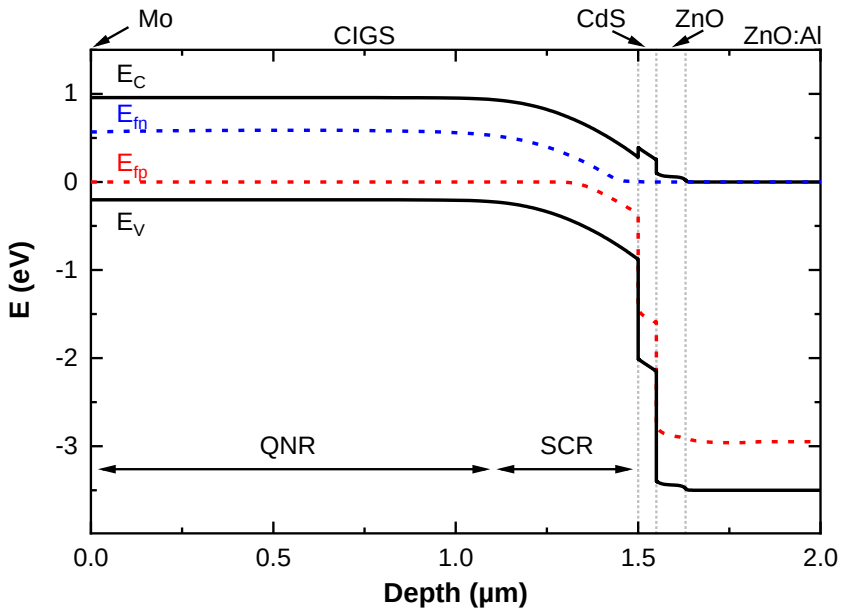

Figure I. 13. SCAPS simulation of the band diagram of a CIGS solar cell under one-sun illumination at short-circuit condition (V = 0). Materials parameters used for in the simulation model were taken from [29]. The CIGS composition is fixed at GGI = 0.3, corresponding to a bandgap of E_g = 1.16 eV.

The charge carriers generated in this structure migrate with respect to the diffusion and drift processes and can be selectively collected at each interface. The following section will present the mechanisms leading to charge collection.

2.4.2. Diffusion and drift mechanisms

Two distinct processes are responsible for the motion of photogenerated charge carriers in the CIGS solar cell:

- The diffusion mechanism tends to equilibrate the densities of free carriers. As a consequence, the majority carriers of CdS (electrons) diffuse to CIGS, and the majority carriers of CIGS (holes) diffuse to CdS. The resulting current densities are expressed as:

$$J_{n,diff} = +\, q\, D_n \frac{dn}{dx}$$
$$J_{p,diff} = -\, q\, D_p \frac{dp}{dx} \qquad \text{(I. 2)}$$

where x is the distance over single direction (one dimensional model), q the elementary charge, n and p the free carrier densities of electrons and holes, D_n and D_p are the diffusion coefficients of electrons and holes, respectively. The difference between the two populations of charge carriers can also be regarded as a chemical potential $\Delta\mu$ that corresponds to the quasi Fermi level splitting of electrons and holes, respectively E_{fn} and E_{fp} (see [102] for more information). The diffusion length of free carriers is linked to D and the carrier lifetime τ as follows:

$$L = \sqrt{D\tau} \qquad \text{(I. 3)}$$

- The electric field created across the junction drifts charge carriers, leading to the following drift current densities:

$$J_{n,drift} = q\, n\, \mu_n \boldsymbol{E}$$
$$J_{p,drift} = q\, n\, \mu_p \boldsymbol{E} \qquad \text{(I. 4)}$$

  where μ_n and μ_p are the mobilities of electrons and holes, respectively. The drift current dominates the motion of charge carriers in the SCR, sweeping electrons (respectively holes) toward CdS (respectively CIGS). As a result, an almost perfect collection of carriers can be assumed in the SCR thanks to its electric field. However, one must keep in mind that the width of the SCR is voltage-dependent, and is much reduced when a solar cell is operated at its maximum power point, as compared to the short-circuit condition (V = 0) [102]. The contribution of the drift currents is thus lower for operating solar cells.

The Gärtner model [108]–[110] can be used to describe the collection efficiency of a CIGS solar cell. In this model, the collection is assumed to be limited by the diffusion of minority carriers to the CdS layer. In addition, the back contact recombination of the CIGS layer is neglected, which is a valid approximation only for CIGS films much thicker than the electron diffusion length. The collection is considered to be perfect for carriers generated in the SCR region, as well as for carriers generated in the QNR region at a distance from the SCR that is below one electron diffusion length. This leads to a collection function of $f_c^{QNR} = \exp(-(x-w)/L_n)$, with w the space charge region width and L_n the electron diffusion length.

However, some of the photogenerated charge carriers recombine in the CIGS solar cell before being selectively collected, and recombination losses can in turn decrease the diffusion length of carriers. Hence, the various recombination processes need to be considered in order to accurately describe the collection of charge carriers in CIGS photovoltaic devices.

2.4.3. Recombination and other losses

CIGS solar cells undergo radiative band to band recombination (annihilation of an electron-hole pair with the emission of a photon) and non-radiative recombination. These recombination processes result in the following current-voltage or I(V) relationship for a solar cell in the dark:

$$J_{diode} = J_0(\exp(qV/kT) - 1) \qquad \text{(I. 5)}$$

with J_{diode} being the diode current density, also called dark current. J_0 is the saturation current, q the elementary charge, k the Boltzmann constant and T the temperature. This diode current is dependent of the applied bias and recombination mechanisms taking place in the photovoltaic device. In the ideal case of a solar cell without non-radiative recombination, the saturation current J_0 is only due to the radiative recombination of the solar cell with an emission spectrum that corresponds to a black-body with the temperature of the solar cell.

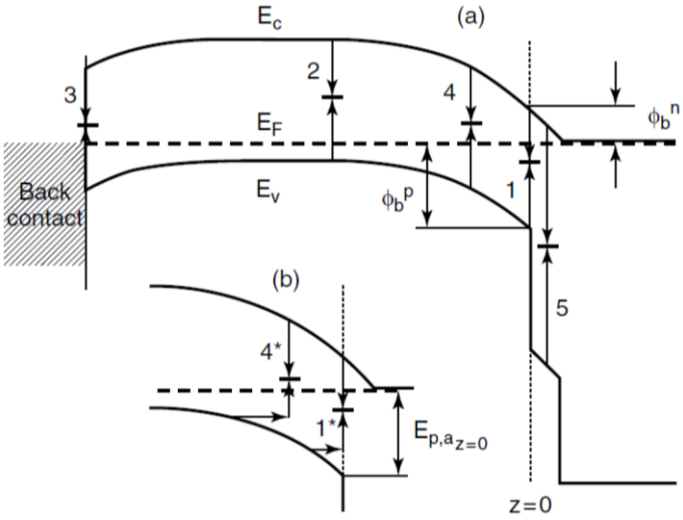

Figure I. 14. a) Schematic representation of the main recombination processes occurring in CIGS solar cells: (1) recombination at the CIGS front contact, (2) in the CIGS bulk, (3) at the CIGS back contact, and (4) in the SCR. b) The tunneling enhanced recombination mechanism is also depicted in the cases of (1*) front contact and (4*) SCR recombination. From [111].

Figure I. 14 shows the various types of non-radiative recombination that occur in non-ideal solar cells. The recombination mechanisms that are considered here are due to the presence of impurities or defects in the CIGS structure and create energy levels inside the CIGS bandgap (Shockley-Read-Hall recombination). The energy released by the non-radiative recombination of an electron-hole pair is released by emission of phonons. These non-radiative recombination processes have different activation energies. This effect can be implemented to the diode current in equation (I. 5) with an ideality factor n:

$$J_{diode} = J_0(\exp(qV/nkT) - 1) \qquad \text{(I. 6)}$$

The main characteristics of the non-radiative recombination depend on their location:

1. *SCR*: a mid-gap defects in the SCR exhibits an activation energy of $E_g/2$ and can thus be described by an ideality factor of 2. The physical reason for this ideality factor of 2 is that in the SCR, the application of a bias leads to a symmetric variation of the quasi-Fermi levels with respect to the mid-gap defect level [111].
2. *QNR*: the diode current depends on the density of minority carriers and their collection function. For sufficiently low voltages, only the electron quasi-Fermi level varies with an applied forward bias, and the ideality factor for recombination in the QNR is 1. For thin CIGS absorbers, a sufficient electron diffusion length can allow electrons to diffuse to the CIGS back contact, where they recombine.
3. *Front contact*: the ideality factor depends on the conduction band offset between CIGS and CdS (ΔE_C). For $\Delta E_C < 0$, also called a spike-like band offset, the activation energy of recombination is equal to the CIGS bandgap, and thus $n = 1$. For $\Delta E_C > 0$, or cliff-like band offset, the activation energy is decreased by ΔE_C, leading to an ideality factor value between 1 and 2. A Fermi level pinning occurring at the front interface will also lead to an ideality factor larger than 1.

4. *Tunneling enhanced recombination*: the band bending at the heterojunction favors the tunneling of holes to defects in the SCR or at the CIGS front interface. This type of recombination was speculated to occur in highly doped CIGS layers with a strong band bending in the SCR [45]. In this case the ideality factor is higher than 1.

In addition to recombination processes, parasitic resistance losses also occur in CIGS solar cells. A high total series resistance (R_S) of the device results in a voltage loss. The existence of shunt paths leads to a low parallel resistance (R_P or R_{SH}) and allows the carriers to move laterally with respect to the *p-n* junction, limiting their extraction out of the solar cell.

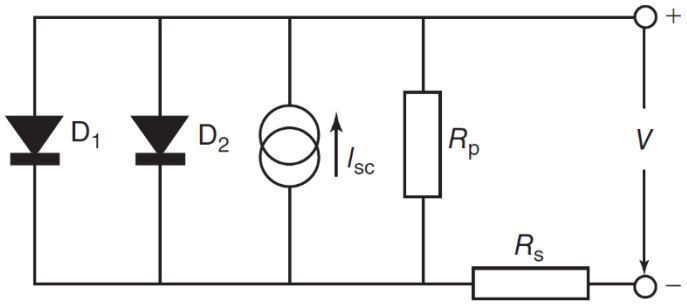

Figure I. 15. Equivalent circuit for a solar cell, based on a 2-diode model (D_1: n_1 = 1 and D_2: n_2 = 2). I_{SC} is the photogenerated current, R_P and R_S are the parallel and series resistance, respectively. Inspired from [102].

The equivalent circuit for a solar cell with recombination and resistive losses is shown in Figure I. 15. A 2-diode model is used to account for recombination with ideality factors of n_1 = 1 (D_1) and n_2 = 2 (D_2). Under illumination, the photogenerated current is represented by the current source I_{SC}. Owing to the different loss mechanisms, the diode equation in the dark can be rewritten as:

$$J_d = J_{01}\left(\exp\left(\frac{q[V - J_d R_S]}{n_1 kT}\right) - 1\right) + J_{02}\left(\exp\left(\frac{q[V - J_d R_S]}{n_2 kT}\right) - 1\right) + \frac{V - J_d R_S}{R_P} \qquad \text{(I. 7)}$$

Finally, under illumination the total current density can be expressed as a sum of the photogenerated current and diode current. However, another loss source needs to be distinguished as the photogenerated current density J_{ph} of CIGS solar cells can be voltage-dependent. Indeed, under forward bias the SCR width is reduced and the collection of electrons is limited by their diffusion length in the QNR. As a result, the I(V) relationship of illuminated CIGS solar cells is expressed as:

$$J_{light} = J_{diode} + J_{ph}(V) = J_{diode} + J_{SC} \times f_C(V) \qquad \text{(I. 8)}$$

with J_{SC} being the current density at V = 0 and f_C the voltage-dependent collection function of charge carriers.

Now that CIGS solar cells and their main loss processes have been described, the standard characterization methods to assess and compare the efficiency of solar cells will be introduced.

2.5.I(V) characteristics and EQE

The performances of photovoltaic devices are commonly analyzed with their current-voltage I(V) characteristics and external quantum efficiency (EQE). The typical characterization results for a CIGS solar cell are shown in Figure I. 16.

To determine the efficiency of a solar cell, its I(V) curve is measured under one-sun illumination (AM 1.5 G spectrum). Three parameters influencing the efficiency can be distinguished:

- **The Short-Circuit Current density, J_{SC}**. It is the photocurrent density $J_{SC} \times f_C(V)$ measured at $V = 0$. It corresponds to the amount of charges that are collected after generation. Hence, recombination, incomplete charge collection as well as optical losses like light reflection, parasitic light absorption or transmission to the back contact decrease the J_{SC} of solar cells.
- **The Open-Circuit Voltage, V_{OC}**. At open-circuit condition, all charges generated in a solar cell recombine as the photocurrent density is equal to $J_{light} = 0$ (Equation (I. 8)). For an ideal solar cell where only radiative recombination occurs, the maximum V_{OC} predicted by the Shockley-Queisser model is approximately $E_g - 250$ mV for an absorber bandgap of 1.2 eV [101], [104]. In practice, the V_{OC} is also limited by the non-radiative recombination processes described in the previous section. In addition, a voltage dependent photocurrent density and a low shunt resistance can contribute to a lower V_{OC}.
- **The Fill Factor, *FF***. It is calculated from the following ratio: $J_{mpp} \times V_{mpp}$ / $J_{SC} \times V_{OC}$, where J_{mpp} and V_{mpp} are the current density and voltage at the maximum power point, respectively. According to the Shockley-Queisser model, the maximum *FF* that can be obtained for a solar cell with an absorber bandgap of 1.2 eV is ~83%. In the non-ideal case, the *FF* can be decreased because of a high series resistance, a low shunt resistance, but also due to recombination and collection losses.

The efficiency of a solar cell can be calculated based on these three light I(V) parameters:

$$\eta = \frac{P_{MAX}}{P_{INC}} = \frac{J_{mpp} \times V_{mpp}}{P_{INC}} = \frac{J_{SC} \times V_{OC} \times FF}{P_{INC}} \qquad \text{(I. 9)}$$

with P_{MAX} the maximum generated power density and P_{INC} the incident power density of the AM 1.5 G spectrum.

The dark I(V) curve of a solar cell measured in the dark also provides some information on the solar cell performances, in particular regarding its departures from ideality. Without illumination, the contribution of the possibly voltage-dependent photocurrent is avoided. This effect can be seen in Figure I. 16.(A), where the slope of the I(V) curve is steeper under illumination than in the dark over the voltage range from -0.5 V to 0.5 V. As a result, the dark I(V) characteristics can be fitted to determine the saturation current density as well as the series and shunt resistance values, for example using a 2-diode model with ideality factors of 1 and 2 as in Equation (I. 7).

The contribution of the different recombination mechanisms can be compared based on the values of J_{01} and J_{02}. It is also possible to use a one-diode model where the ideality factor of the single diode is fitted, with a value generally comprised between 1 and 2. In this case, the ideality factor indicates which recombination type is dominant, and the J_0 accounts for the total amount of recombination.

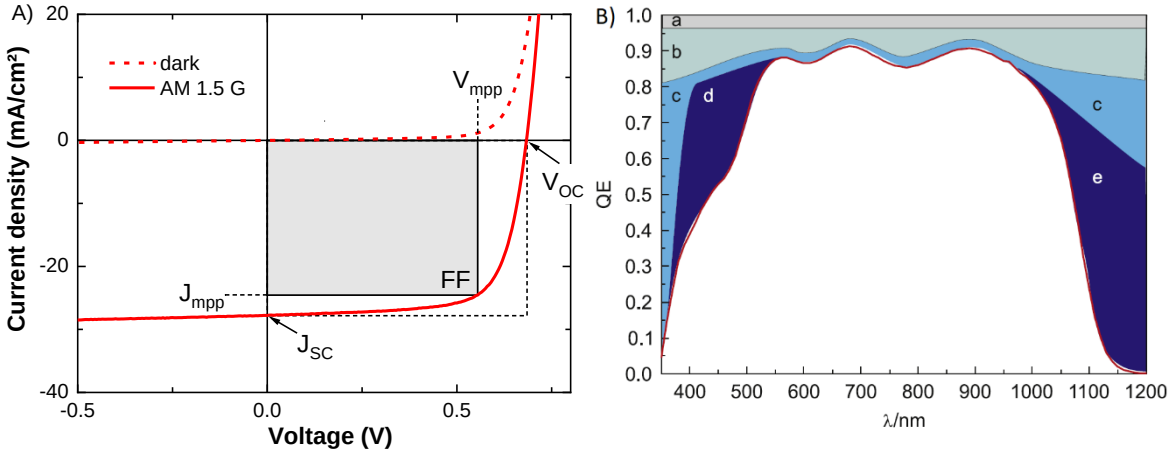

Figure I. 16. Schematic representations of (A) typical light and dark I(V) characteristics, and (B) External Quantum Efficiency (EQE, red line) of a CIGS solar cell. In (B), filled areas indicate EQE losses due to (a) grid shading, (b) total light reflection, parasitic absorption in (c) ZnO-based as well as (d) CdS layers, and (e) incomplete absorption and collection. Panel (B) is from [112].

The External Quantum Efficiency of a solar cell is defined as the ratio of charge carriers that are collected for a given number of incident photons with a fixed wavelength. The EQE is usually measured over the wavelength range where charge carriers are generated and collected, as seen in Figure I. 16.(B). When the EQE is determined without applied bias (V = 0), it is possible to calculate the J_{SC} of the solar cell by integration of the EQE with respect to the wavelength (λ):

$$J_{SC} = \frac{q}{hc}\int_0^{\infty} EQE(\lambda)\, P(\lambda)\, \lambda\, d\lambda \qquad \text{(I. 10)}$$

where q is the electron charge, h the Planck's constant, c the speed of light, $P(\lambda)$ the incident spectral power density per unit area of the AM 1.5 G spectrum. The theoretical maximum J_{SC} of a solar cell with an absorber bandgap E_g can be derived from Equation (I. 10), using the following step-like function for the EQE: EQE = 1 for photon energy ≥ E_g and EQE = 0 for photon energy < E_g.

The analysis of the EQE spectrum provides several information on the origin of current losses. The EQE losses due to the main parasitic effects occurring in a CIGS solar cell are indicated by filled areas in Figure I. 16.(B). In addition, it is possible to measure the EQE of a solar cell with an applied bias to investigate the effect of a varied thickness of the SCR on the charge collection. The Internal Quantum Efficiency of a (monofacial) photovoltaic device can also be determined by measuring its total light reflection R and calculating the ratio $IQE = EQE/(1 - R)$ at each wavelength.

The bandgap of the absorber can also be estimated from the EQE curve of the complete solar cell [110]. Assuming that the hypotheses of the Gärtner model are verified, it is found that for photons with an energy close to the bandgap of the absorber, $IQE \propto \alpha$ with α the absorption coefficient. Besides, for direct bandgap transitions $\alpha \propto \sqrt{E_{ph} - E_g}$, where E_{ph} is the photon energy and E_g is the bandgap of the absorber. Hence, assuming that IQE ≈ EQE leads to $EQE^2 \propto E_{ph} - E_g$ for E_{ph} close to E_g. The bandgap of the absorber can thus be determined from a linear fit of $EQE^2 = f(E)$ where $f(E_g) = 0$.

2.6.Conclusion of the chapter

Standard CIGS solar cells are fabricated with the following stack of materials: SLG / Mo (300 – 1000 nm) / CIGS (1.5 – 3 µm) / CdS (40 – 60 nm) / i-ZnO (40 – 60 nm) / ZnO:Al (150 – 400 nm). Recently, the efficiency of CIGS photovoltaic devices was improved thanks to the incorporation of heavy alkali elements to the CIGS layer as well as the optimization of the buffer and front contact layers.

The CIGS solar cell, as well as other photovoltaic technologies, relies on the absorption of photons emitted by the sun to generate power. Electron-hole pairs are first created in the CIGS semiconductor by absorption of photons. These charge carriers are then collected selectively at the contacts of the solar cell. Solar cells can exhibit several departures from ideality, such as non-radiative recombination, parasitic resistances, or non-absorption of light in the CIGS layer. In this regard, the I(V) and EQE curves of photovoltaic devices allow to compare and analyze their performances.

This work investigates the development of ultrathin CIGS solar cells, *i.e.* solar cells with a CIGS absorber thinner than 500 nm. The advantages and drawbacks of this cell architecture will now be presented, together with a short state of the art.

Chapter 3. Development of ultrathin CIGS solar cells

3.1. Benefits and challenges of ultrathin CIGS solar cells

3.1.1. Industrial cost reduction

From an industrial point of view, reducing the thickness of the CIGS layer can be beneficial as it would reduce materials usage and increase the throughput of module manufacturing.

In particular, the European Commission as well as the U.S. Department of the Interior have listed both Indium and Gallium as critical raw materials, because of their high economic importance and supply risk [8], [113]. The main characteristics of the Indium and Gallium markets are given below:

- The main source of Indium is the refining of zinc minerals, and it is mainly used as indium-tin oxide in flat panel devices [8]. The world total resource of In is estimated to 125 000 tonnes, but accessible reserves of In are limited to 18 800 tonnes [8], and the world total refinery production in 2018 was as high as 750 tonnes [113]. Since 2015, the price of Indium has been stable, at around 300 $/kg [114].
- Gallium is mostly extracted as a by-product of aluminum production [8]. Ga is primarily used to produce GaAs and GaN compounds for applications in integrated circuits and light emitting diodes. The world total resource of Ga is estimated to exceed 1 million tonnes [8], and the easily available reserves are estimated to be higher than 75 000 tonnes [114]. As of 2018, the world primary production of Ga was estimated at 410 tonnes [113]. Since 2013, its price varied between 100 and 300 $/kg [114].

Hence, it is clear that In and Ga are both costly materials, and that the reserves of In are limited with regards to the world total production of In in 2018. In addition, the In demand is expected to grow during the next 10 years, which makes the improvement of In recovery rate during refining and recycling processes a critical parameter [8], [114]. However, it is worth mentioning that as flat panel displays account for more than 50% of the world total consumption of In, the development of alternative technologies that do not require indium-tin oxide could reduce the In demand and consumption [8], [114].

Reducing the thickness of the CIGS absorber would not only limit the risks related to the supply of Indium, but it would also decrease the price of modules. Studies on the cost of industrial CIGS modules have showed that regardless of the CIGS deposition method, the cost of materials account to ~50% of the total CIGS module price [7], [115].

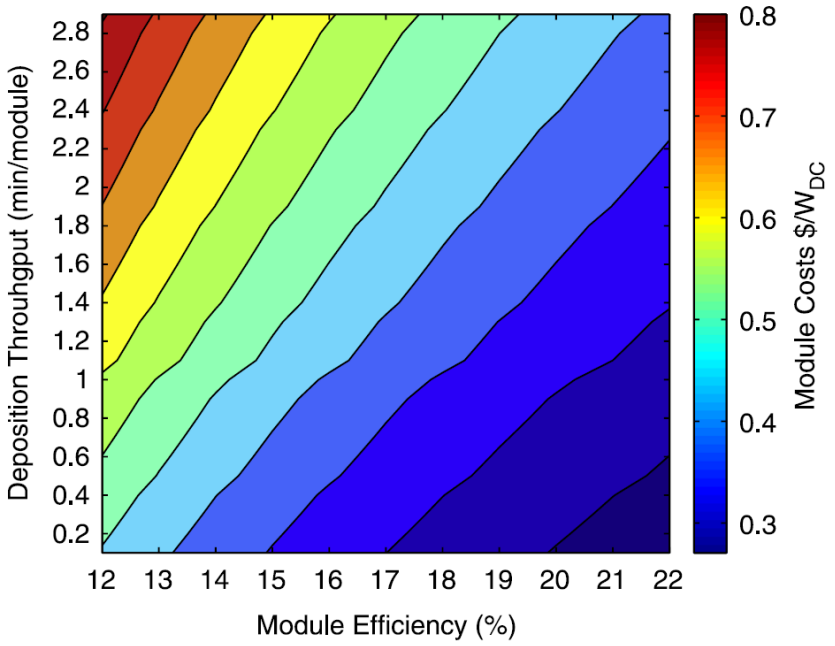

Figure I. 17. Module cost for a CIGS layer co-evaporated in a 3-stage process, depending on the module efficiency and deposition throughput. From [7].

Looking at the expenses due to the CIGS layer only, a manufacturing cost of ~18 $\$_{2015}/m^2$ was calculated by Horowitz *et al.*, assuming a 1.5 µm-thick CIGS layer deposited with a sequential process, a 1 GWp/year manufacturing volume and U.S. manufacturing [7]. In this case, the total module cost amounts to 69 $\$_{2015}/m^2$, or 0.49 \$/Wp for a 14% module efficiency. This means that the CIGS layer accounts for approximately 26% of the total module cost.

In comparison, the cost of a CIGS layer deposited by 3-stage co-evaporation is even higher, at ~27 $\$_{2015}/m^2$. However, it is worth mentioning that using a 3-stage process can improve the efficiency of modules by 2% absolute, resulting in significant savings when comparing the price of modules in terms of \$/Wp [7]. The development of efficient modules with ultrathin absorbers can lead to lower module prices, as decreasing the thickness of the CIGS layer from 1.5 µm to 0.5 µm is estimated to reduce the module price by 3.1 $\$/m^2$ [7]. Besides, co-evaporating ultrathin CIGS layers would contribute to a higher deposition throughput, which can strongly decrease the module cost as long as a similar efficiency is achieved (see Figure I. 17).

To conclude, ultrathin CIGS absorbers show a promising potential for cost reduction. However, high efficiencies are required to achieve lower module prices in terms of \$/Wp. The next section will detail the main bottlenecks that limit the efficiency of ultrathin CIGS solar cells.

3.1.2. Challenges facing ultrathin CIGS

Solar cells with ultrathin CIGS absorbers were first fabricated and studied by Shafarman *et al.* [116] as well as Negami *et al.* [117], by deposition of CIGS in a shortened 3-stage process. The efficiency of these photovoltaic devices was lower for ultrathin absorbers than for standard thicknesses, in correlation to a decrease of each light I(V) parameter.

Following these studies, several works have investigated the origin of the lower solar cell efficiency due to the thinning of the CIGS film. In particular, the photovoltaic performances of ultrathin CIGS solar cells suffer from two main detrimental effects:

- **Increased recombination at the CIGS back contact**. In the case of ungraded CIGS absorbers, the high recombination velocity at the back contact was shown to limit the V_{OC} of solar cells even in the case of a standard CIGS thickness of ~2 µm [118]. This effect is more pronounced for thinner CIGS films, as charge carriers are generated closer to the CIGS back interface [13]. Simulation results revealed that the carrier recombination at the back contact of ultrathin CIGS films leads to substantial V_{OC} and J_{SC} losses [9], [10], [119].
- **Insufficient light absorption**. Solar cells with sub-micron CIGS layers lead to an increased light intensity at the interface between CIGS and the back contact, because of the incomplete light absorption in CIGS. This effect was demonstrated experimentally by Orgassa *et al.* [33] and Jehl Li-Kao *et al.* [120], as well as numerically by Edoff *et al.* [121] and Dahan *et al.* [122]. In fact, the standard $MoSe_2$/Mo back contact of CIGS was shown to be poorly reflective. As a result, the fraction of light that is transmitted through the thin CIGS layer is absorbed in the Mo film, leading to a photocurrent loss as light absorption in Mo does not contribute to the generation of charge carriers.

It is worth mentioning that thinner absorber layers are also expected to have a beneficial effect on cell performances. Indeed, a reduced CIGS thickness should result in a lower total amount of recombination centers in the CIGS bulk, as well as a shorter path for minority carriers before separation at the *p-n* junction if the absorber is thinner than the diffusion length of minority carriers. This in turn could improve the V_{OC} of ultrathin devices [9], [111].

It can be seen that the main losses occurring in ultrathin CIGS layers are related to the back contact of the solar cell. For this reason, strategies to improve the efficiency of ultrathin devices are focused on the rear passivation of the CIGS layer and the development of reflective back contacts. The next section will briefly review the different approaches toward the fabrication of ultrathin CIGS solar cells with high efficiencies.

3.2.State of the art of ultrathin CIGS solar cells

The rear passivation of ultrathin CIGS layers can be improved thanks to the composition grading of the CIGS film and/or the insertion of a passivation layer with nanoscale point contacts at the CIGS/Mo interface. As these two strategies are generally studied separately, they will be detailed independently here. The various architectures of flat and nanostructured reflective back contacts that are reported in the literature will then be presented.

3.2.1. Optimization of the CIGS composition

CIGS solar cells fabricated by co-evaporation of an absorber with a standard thickness are usually prepared with a GGI composition grading. This composition grading modifies the CIGS bandgap mainly via a change of the conduction band minimum: a high GGI leads to an increase of the conduction band minimum.

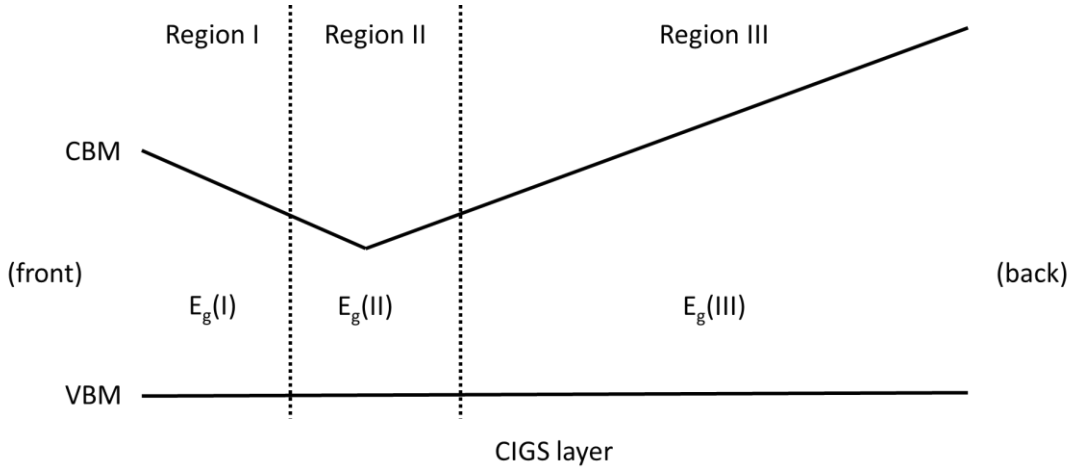

Figure I. 18. Schematic band diagram of a CIGS layer co-evaporated in a 3-stage process. The bandgap (E_g) grading results from the evolution of the conduction band minimum and valence band maximum along the depth of the CIGS layer. Three regions can be distinguished in the CIGS layer: the front interface (I), the notch (II) and the back interface (III). Inspired from [52].

For thick CIGS layers, the optimal GGI composition consists in a V-shape profile with increased GGI composition at the front and back contact of CIGS, and in-between a region with a lower GGI. The resulting grading of the CIGS band diagram is represented schematically in Figure I. 18. It can be divided in three zones:

- **The front interface, region I**. The bandgap at the interface with the CdS buffer layer strongly influences the V_{OC} of complete solar cells [54], [123]. A negative conduction band offset ΔE_C (spike-like offset) is required to mitigate the front interface recombination. However, for low GGI composition leading to $\Delta E_C > 0.3$ eV, an electron barrier is formed at the CIGS front interface and the efficiency of complete cells decreases due to a *FF* loss. A ΔE_C in the range of 0.1 eV to 0.3 eV is predicted to lead to the highest V_{OC} values [94].

- **The notch, region II**. At a depth of a few hundreds of nm, a zone with lower GGI and E_g values is found. The reduced E_g results in an enhanced absorption of infrared photons, thus increasing the J_{SC} of solar cells [52], [54], [118]. A too deep GGI notch can decrease the collection efficiency of complete devices by creating an electron barrier [29], [124].

- **The back interface, region III**. An increasing GGI back grading is also formed toward the CIGS back interface. The resulting conduction band grading creates a back surface field at the rear CIGS interface that drifts minority carriers toward the *p*-*n* junction. Consequently, fewer electrons diffuse up to the Mo film, thereby hindering back contact recombination. The V_{OC} of complete cells is thereby improved [52], [54], [125], [126].

As ultrathin CIGS solar cells exhibit an increased sensitivity to back contact recombination, efforts have been made to introduce a GGI back grading in ultrathin CIGS films. Even if the composition and bandgap engineering of ultrathin layers is challenging due to the reduced deposition time and thickness of CIGS, significant progress have been achieved (see also Table I. 2):

Lundberg *et al.* [13], [125] reported an efficiency improvement for ultrathin solar cells with the co-evaporation of a pure $CuGaSe_2$ layer prior to the deposition of CIGS. The resulting GGI grading led to higher *FF* and V_{OC} values thanks to a reduced back contact recombination and better collection efficiency. An efficiency of 12.1% was obtained with a 0.6 µm-thick absorber, which was approximately 2% absolute more than in the case of an ungraded CIGS layer.

Yin *et al.* [127] achieved a V-shaped composition grading in ultrathin CIGS by reducing the substrate temperature during CIGS co-evaporation from 610°C to 440°C. The GGI grading was shown to be beneficial to cell performances due to the reduced back contact recombination but also to the absorption of infrared photons closer to the *p*-*n* junction. For 460 nm-thick CIGS layers, the composition grading improved the average efficiency of photovoltaic devices from 9.0% to 10.6%.

Mansfield *et al.* [11] hold the current record efficiency of 15.2% for an ultrathin CIGS film of 490 nm, with remarkable V_{OC} and *FF* values of 733 mV and 78.2%, respectively. It was calculated that a difference in the GGI composition between the back and front CIGS interface of ΔGGI = 0.3 would efficiently prevent back contact recombination. Besides, this high GGI region near the Mo back contact should be less than 0.15 µm-thick to ensure a strong light absorption in the CIGS layer. However, the record cell exhibits a linear GGI grading with ΔGGI = 0.2, which was achieved with a 2-stage co-evaporation process.

3.2.2. Nanopatterned passivation layers

An alternative way to reduce the back contact recombination in ultrathin CIGS solar cells with flat composition profiles is to insert a passivation layer between the CIGS and the back contact films. Such passivation layers are generally insulating, and thus need to be nanopatterned in order to allow a current flow through point contact openings.

This strategy for CIGS rear passivation stems from the Si technology, as crystalline Si solar cells with a Passivated Emitter and Rear Cell (PERC) or an Interdigitated Back Contact (IBC) architecture have reached efficiencies over 25.0% [6]. The passivation of *p*-type Si can be achieved for example with alumina (Al_2O_3), SiC, SiO_2 or hydrogenated silicon nitride (SiN_X:H), with micro-openings [128] separated with a distance of a few hundreds of micrometers.

Recombination at the CIGS/Mo back contact generally occurs with a high surface recombination velocity of minority carriers $S_{n,BC} > 10^6$ cm/s [129]–[131]. Based on time-resolved photoluminescence results, a study reported a significant decrease of the recombination velocity down to $S_{n,BC} < 10^2$ cm/s depending on the quantity of NaF that was incorporated to the CIGS in a PDT [131].

In order to achieve the rear passivation of CIGS, layers like Al_2O_3, HfO_2, MgF_2, SiO_2 or TiO_2 can be added on the Mo back contact. To ensure a sufficient carrier collection at the CIGS back contact, the period between point contacts should be in the 1–10 µm range, owing to the lower diffusion length of carriers in CIGS as compared to the case of Si [132]–[134]. Adding a passivation layer can reduce the back contact

recombination velocity $S_{n,BC}$ in two ways, according to two distinct parameters of the passivation layer [10], [135], [136] (see also Figure I. 19):

- **The fixed charge density, Q_f.** A deviation from the stoichiometric composition of the passivation layer, for instance due to vacancies or interstitial atoms, results in a fixed charge density Q_f in the bulk of the passivation layer. The Q_f value generally lies between -10^{13} and $+10^{13}$ cm^{-2} [136]. In order to passivate a *p*-type semiconductor, a negative Q_f is required to create a built-in electric field that can assist the electrons toward the *p-n* junction [10], [135]. This phenomenon is usually called a "field-effect passivation".

- **Density of interface traps, D_{it}.** The interface of a given passivation layer with CIGS will exhibit a specific trap density D_{it} where carriers can recombine. Typical D_{it} values of passivation layer in contact with crystalline Si are found between 10^{10} and 10^{12} eV^{-1}.cm^{-2} [136]. A decrease of the D_{it} can reduce the surface recombination velocity thanks to a lower amount of electrically active defects at the interface [10], [135]. This is often referred to as a "chemical passivation" of the interface.

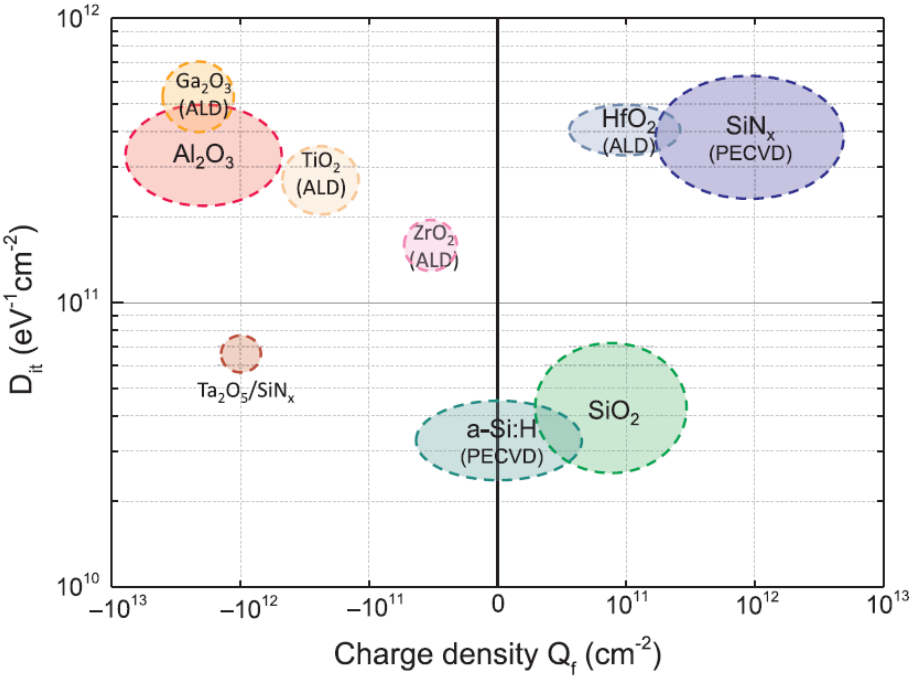

Figure I. 19. Summary of the approximate densities of interface defects and fixed charge, measured experimentally for various materials deposited on crystalline Si. From [136].

Figure I. 19 shows a summary of the Q_f and D_{it} that were experimentally determined for various passivation layers in contact with crystalline Si. It provides some insights to determine which materials are eligible as rear passivation layers in ultrathin CIGS solar cells, though replacing Si by CIGS is expected to modify the D_{it}. In addition, the CIGS deposition process can affect the Q_f of the passivation layer [137]. As a comparison, average $-Q_f$ of 8×10^{12} cm^{-2} and D_{it} of 1×10^{12} eV^{-1}.cm^{-2} were measured for an alumina layer deposited by atomic layer deposition (ALD) on CIGS and annealed at 510°C in Se atmosphere [135], [137].

A numerical study of a 2 nm-thick passivation layer by Kotipalli *et. al* [135] revealed that for a CIGS interface with a high D_{it} of 1×10^{12} $eV^{-1}.cm^{-2}$, increasing the density of negative fixed charges from $-Q_f = 1 \times 10^{10}$ cm^{-2} to 5×10^{13} cm^{-2} significantly improves the V_{OC}, J_{SC} and efficiency of solar cells with sub-micron CIGS thicknesses. On the other hand, if a high $-Q_f$ of 8×10^{12} cm^{-2} is assumed, a $D_{it} < 5 \times 10^{12}$ $eV^{-1}.cm^{-2}$ has negligible impact on the V_{OC} of ultrathin solar cells. Besides, in the absence of negative fixed charges ($-Q_f = 1 \times 10^{8}$ cm^{-2}) the V_{OC} of CIGS cells strongly decreases as the CIGS thickness is reduced from 1 µm to 0.25 µm. This V_{OC} drop is similar for a wide range of D_{it} values from 1×10^{10} to 5×10^{12} $eV^{-1}.cm^{-2}$ but stronger for $D_{it} > 5 \times 10^{12}$ $eV^{-1}.cm^{-2}$. As a result, for $D_{it} < 5 \times 10^{12}$ $eV^{-1}.cm^{-2}$ a field-effect passivation is necessary to further improve the rear passivation of ultrathin CIGS layers. In summary, an efficient rear passivation of ultrathin CIGS films with $S_{n,BC} < 10^2$ cm/s is predicted for $-Q_f > 5 \times 10^{12}$ cm^{-2} and $D_{it} < 1 \times 10^{13}$ $eV^{-1}.cm^{-2}$.

The rear passivation of ultrathin CIGS solar cells results in lower J_0 and thus higher V_{OC} values due to the reduction of back contact recombination. A slightly higher J_{SC} is also expected as the collection efficiency of carriers is improved, but also because the low-index passivation layer at the CIGS back contact leads to a slightly improved reflectivity as compared to the standard CIGS/$MoSe_2$/Mo interface [10].

It is worth mentioning that an external supply of Na is usually provided to CIGS cells with a rear passivation layer, as most oxides block the diffusion of Na [138]. Below are the results of some recent investigations on the rear passivation of ultrathin CIGS, sorted by type of oxide (see also Table I. 2):

Al_2O_3 **Vermang *et al.*** [139] have studied the passivation of a 400 nm-thick CIGS layer with 25 and 50 nm-thick Al_2O_3 layers deposited by DC sputtering. CdS nanoparticles were deposited on Mo before alumina deposition to create point contact openings with a diameter of ~250 nm, with a random sub-micron spacing. Cells with a 50 nm-thick alumina passivation layer exhibited an average efficiency of 13.2 ± 0.4 %, thanks to a V_{OC} of 644 ± 6 mV and a J_{SC} of 30.2 ± 0.8 mA/cm^2. Passivation with a bilayer stack of MgF_2 (60nm, evaporation) / Al_2O_3 (5 nm, ALD) further improved the J_{SC} of ultrathin devices to 31.1 ± 0.1 mA/cm^2 thanks to the improved reflectivity at the CIGS back interface with the low-index MgF_2. The resulting efficiency was 13.5 ± 0.4 % with a V_{OC} of 633 ± 2 mV. In comparison, the performances of the unpassivated Mo baseline were η = 9.1 ± 0.1 %, V_{OC} = 576 ± 2 mV, J_{SC} = 23.2 ± 0.3 mA/cm^2. Similar average $FF \approx 68\%$ were achieved for all ultrathin cells. These solar cells were all covered with a MgF_2 antireflection coating.

Solar cells with a 240 nm-thick CIGS layer were also passivated by a 10 nm-thick Al_2O_3 layer in another study [140]. Here, the alumina film was patterned by electron-beam (e-beam) lithography to form a well-controlled array of point contacts with a diameter of ~300nm and a spacing of 2 µm. A transmission electron microscopy image of the cross-section of the resulting complete CIGS solar cell is shown in Figure I. 20. Implementing the passivation layer improved all I(V) parameters as compared to the unpassivated reference, and led to an average efficiency of 11.8 ± 0.3 %.

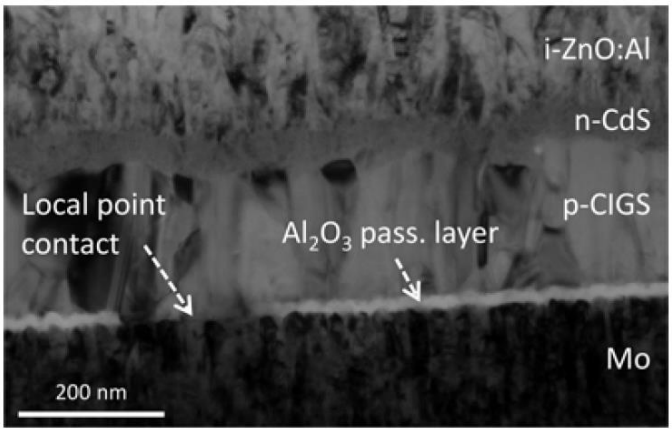

Figure I. 20. Cross-section image of a passivated ultrathin CIGS solar cell in transmission electron microscopy (TEM). Electron-beam lithography was used to form point contact openings in the 10 nm-thick passivation layer made of Al_2O_3. From [140].

Salomé *et al.* [10] also achieved an average efficiency of 9.7 ± 0.7 % and V_{OC} of 627 ± 11 mV with 350 nm of CIGS and an 18 nm-thick alumina layer patterned by e-beam lithography (point contact diameter: ~400 nm, pitch: 2 µm). This was respectively 2.2% absolute and 89 mV more than for a standard Mo back contact.

Ledinek et al. [141], [142] reported that alumina layers with a thickness < 6 nm did not require patterning if the passivation layer is combined with a NaF precursor layer. It is not clear whether NaF modifies the Al_2O_3 composition or creates holes in it, but it allows a sufficient current conduction. Combining a 15 nm-thick NaF precursor layer with a 6 nm-thick Al_2O_3 layer gives an average efficiency close to 8 % for a 215 nm-thick CIGS layer, and a V_{OC} gain of about 120 mV is obtained as compared to the Mo reference. Based on photoluminescence characterization, hafnium oxide (HfO_2) was also identified as a candidate passivation layer for ultrathin CIGS solar cells, but a 6 nm-thick layer without patterning blocked the current collection even if a NaF precursor layer is applied.

Choi *et al.* [143] developed a patterning process for a 5 nm-thick Al_2O_3 layer deposited by ALD, with the deposition of a photolithography mask and the etching of point contacts by a reactive plasma. As this patterning process relies on photolithography rather than e-beam lithography, it should be easier to upscale. An array of point contacts with a 1 µm pitch and diameters of 350 to 500 nm was achieved, and resulted in an average efficiency of 10.3 ± 0.3 % with a V_{OC} of 644 ± 22 mV for a 380 nm-thick CIGS layer. This represented respective gains of 2.7 % absolute and 103 mV as compared to unpassivated cells.

Casper *et al.* [144] also used a photolithography process to pattern the passivation layer, but instead of forming point contacts they fabricated stripes with a width of 3 µm to allow a direct contact between the 500 nm-thick CIGS film and Mo. For a 50 nm-thick alumina layer deposited by ALD, Al_2O_3 stripes with a width of 9 µm led to an average efficiency of 9.6 ± 0.2 % and V_{OC} of 564

± 2 mV. The rather low back contact coverage of the passivation layer (75 %) could explain the more modest efficiency and V_{OC} improvements with respect to the Mo reference, +0.5 % absolute and + 7 mV respectively. It is worth mentioning that in this case, CIGS was co-evaporated in a multistage process and that a GGI composition grading might contribute to the CIGS rear passivation.

Mollica *et al.* [138] fabricated a patterned passivation layer by nanoimprint lithography (NIL) of a sol-gel mask, also an upscalable technique. An array of point contacts with a size of 200 nm and a pitch of 8 µm was etched in the 15 nm-thick alumina layer. The passivated solar cells with a 420 nm-thick CIGS layer exhibited a best efficiency of 9.2 % while the Mo baseline led to a best efficiency of 8.4 %. This efficiency gain was mostly related to an improved J_{SC}, possibly due to enhanced carrier collection and back contact reflectivity, as well as an increased *FF* thanks to a higher shunt resistance.

TiO_2 **Mollica *et al.*** [138] also investigated sol-gel Ti oxide as a passivation layer. However, using the same point contact geometry and CIGS thickness led to a lower best efficiency of 7.4%. In addition, the photoluminescence intensity measured for samples passivated with TiO_2 was much lower than in the case of alumina, indicating the absence of a passivation effect related to Ti oxide.

MgF_2 **Casper *et al.*** [144] studied the rear passivation of CIGS by an evaporated MgF_2 layer of 100 nm. 3 µm-wide stripes of MgF_2 spaced by 3 µm-wide stripe of direct CIGS contact with Mo resulted in an average efficiency of 9.9 ± 0.1 %. The low-index MgF_2 layer improved the J_{SC} of complete cells as compared to the unpassivated reference. Again, a limited V_{OC} gain of 5 mV was achieved, which could be related to the low back contact coverage by the MgF_2 stripes (50%).

SiO_2 **Yin *et al.*** [145] prepared an evaporated Si oxide nanomesh on Mo by simple colloidal NanoSphere Lithography (NSL). A solar cell based on a 370 nm-thick CIGS layer with a GGI grading as well as a SiO_2 nanomesh with a period of 350 nm and a thickness of 150 nm yielded an efficiency of 11.4%. This was 2.6 % abs. more than on flat Mo thanks to increased V_{OC} and J_{SC} values. These improvements were achieved thanks to the back contact passivation and light trapping effects of the SiO_2 nanomesh.

3.2.3. Flat reflective back contacts for ultrathin solar cells

Several research efforts have been made to fabricate ultrathin solar cells on reflective back contact, and to thereby improve their J_{SC} values.

As discussed in the previous section, passivation schemes with low-index materials can slightly increase light absorption in ultrathin CIGS layer thanks to an enhanced back contact reflectivity [139], [144], [145]. However, the CIGS absorption of passivated ultrathin solar cells still have room for improvement as compared to cells with thick CIGS layers [139].

To increase the back reflectance of CIGS solar cells, Orgassa *et al.* [33] have studied the substitution of Mo by other metals. However, highly reflective metals like Cu, Au or Ag diffuse in the CIGS layer [33], [146], and cannot be used as a back contact. Over the investigation of 8 metals, only W, Mo, Ta and Nb were found to be inert during the deposition of CIGS, and only W led to a similar device efficiency as compared to Mo. As W and Mo back contacts result in a similar average light reflection that is below 60 % in the 500 -1000 nm wavelength range, other strategies need to be investigated to achieve a flat reflective back contact for CIGS solar cells.

In this regard, a promising way to avoid parasitic light absorption in the Mo layer consists in using transparent conductive oxides (TCO) as a back contact with CIGS. In an ideal case without Fermi level pinning nor chemical reactions at the interface, a TCO back contact should have a high work function Φ so that $\Phi > \chi + E_g$, where χ and E_g are respectively the electron affinity and bandgap of the CIGS layer. However, in most cases *n*-doped TCO are used as a back contact and $\Phi < \chi + E_g$, which results in a hole barrier that can be approximately calculated as $\Phi_B = \chi + E_g - \Phi$. The schematic band diagram corresponding to this situation is shown in Figure I. 21, in the case of a CIGS back contact with In_2O_3:Sn (ITO, $\Phi_{ITO} \approx 4.7$ eV*)* [147]. The hole barrier Φ_B is predicted to be much higher than 0.3 eV, and is thus expected to be detrimental to hole collection and cell performances [111]. The reversed conduction band grading toward the ITO back contact is also expected to hinder the collection of electrons.

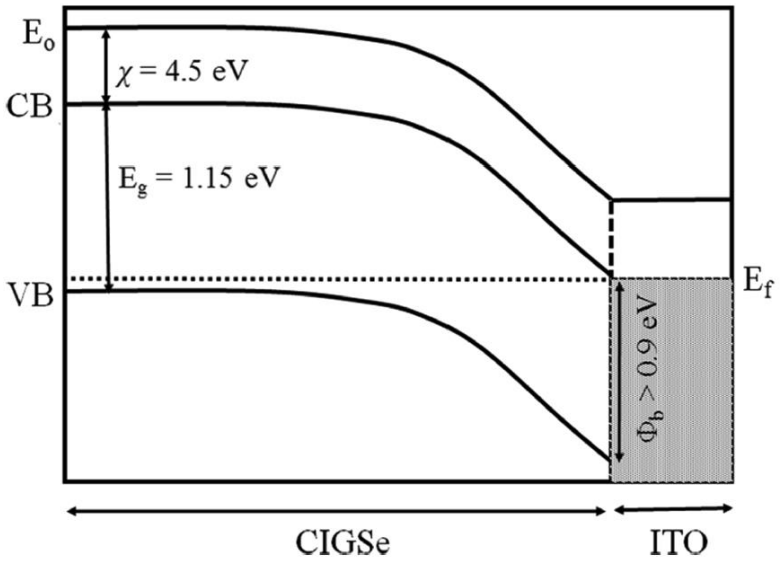

Figure I. 21. Schematic band diagram of the CIGS back contact with ITO (not to scale). E_0 is the vacuum level and E_f the Fermi level. The ITO work function corresponds to $E_0 - E_f$. From [147].

To avoid this detrimental band bending, a hole extraction layer with a high thermal stability and work function could be deposited on the TCO back contact, *e.g.* NiO, MoO_3, WO_3 and V_2O_5 [147], [148]. A better hole collection was demonstrated for CIGS deposited on glass/ITO/WO_X [147]. MoO_X was also shown to be a good candidate as a back contact for CIGS solar cells in superstrate configuration [149].

Nevertheless, efficient CIGS solar cells fabricated directly on top of TCO layers were reported. Nakada *et al.* [36], [150] achieved efficiencies of 15.2 and 13.7 % with ITO and SnO_2:F (FTO) back contacts, respectively. However, the efficiency of solar cells on ITO dropped for CIGS co-evaporation temperatures > 520°C, due to the detrimental formation of a resistive and wide bandgap Ga oxide layer at the CIGS/ITO interface. For a back contact made of FTO, a CIGS deposition temperature > 500 °C led to lower efficiencies as the resistivity of the FTO layer increased due to the outdiffusion of fluorine dopants from the FTO film. On the other hand, a ZnO:Al back contact resulted in low efficiencies even at low CIGS deposition temperatures. This was related to a stronger growth of Ga oxide in the case of ZnO:Al. Terheggen *et al.* also reported the detrimental formation of a thick Ga oxide at the CIGS/ZnO interface of superstrate solar cells [151]. Using a thermodynamical approach, the growth of Ga_2O_3 is found to be highly promoted by its formation enthalpy of –1100 kJ/mol, as compared to –926 kJ/mol for In_2O_3 and –348 kJ/mol for ZnO [38]. Note that the lower formation enthalpy of ZnO as compared to In_2O_3 could also explain why ZnO leads to a stronger growth of Ga oxide.

It is also worth mentioning that Na was shown to promote the formation of Ga oxide at the CIGS/TCO interface [38]. As a result, ultrathin CIGS solar cells with a NaF PDT were successfully fabricated on FTO and ZnO:Al back contacts, without the growth of a thick Ga oxide layer [152]. Keller *et al.* also achieved efficient bifacial solar cells on hydrogenated In_2O_3 back contacts, by combining a thin Al_2O_3 layer with a NaF precursor layer at the back contact which hindered the growth of Ga oxide [37]. Interestingly, Son *et al.* [153] proposed that a very thin Ga oxide layer (<5 nm) at the CIGS/ITO interface resulted in an ohmic contact because defects introduced by the formation of Ga oxide allow the collection of holes thanks to a trap-assisted tunneling mechanism.

A short overview of CIGS solar cells fabricated on reflective back contacts including a metallic mirror is given below (see also Table I. 2):

Lopes *et al.* [146] deposited stacks of metals (20 nm)/Al_2O_3 (18 nm) on the standard Mo back contact, with a goal to provide both rear passivation and reflection to a 500 nm-thick CIGS layer. A square array of point contacts with a diameter of 200 nm and a pitch of 2 µm was then fabricated by e-beam lithography. However, the Al_2O_3 layer did not provide a sufficient encapsulation for almost all metallic layers, and their diffusion into CIGS degraded the photovoltaic performances of complete cells. Only a TiW alloy was found to be inert during CIGS deposition and led to a best cell efficiency of 11.0 % without antireflection coating (ARC). This was 1.6% abs. more than for a Mo back contact with an Al_2O_3 passivation layer, thanks to a V_{OC} increase.

Jehl Li-Kao *et al.* [120] developed a process to lift-off CIGS layers grown on Mo back contacts. The bare CIGS interface can then be covered with a metallic mirror to fabricate solar cells in superstrate configuration with a reflective back contact. As a result of the higher back contact reflectivity, solar cells with a 400 nm-thick CIGS layer and a back contact made of Au exhibited a J_{SC} increase of ~4 mA/cm^2 as compared to a Mo back contact, and an efficiency of 10.2% without ARC.

Mollica *et al.* [152] co-evaporated ultrathin CIGS layer on back contacts made of various TCOs. After cell fabrication, a metallic mirror was added on the backside of the glass substrate to reflect the fraction of light transmitted by the solar cell stack. Solar cells with a SnO_2:F back contact coupled with a Cu mirror achieved a best efficiency of 11.4 % and J_{SC} of 25.9 mA/cm^2 with 450 nm of CIGS and no ARC, respectively 1.2% abs. and 4.8 mA/cm^2 more than on Mo.

Simchi *et al.* [154] fabricated ultrathin CIGS solar cells in superstrate configuration with a backwall Ag reflector deposited on the ZnO contact that ensures the collection of electrons. The back contact consisted of the following TCO stack: glass/In_2O_3:Sn/MoO_3. A 300 nm-thick ACIGS layer led to a best efficiency of 9.7% and a J_{SC} of 23.6 mA/cm^2 without ARC, which was 8.4 mA/cm^2 more than the case of a Mo back contact in substrate configuration. This J_{SC} increase was related to the improved back contact reflectivity but also to the elimination of the CdS parasitic absorption in superstrate configuration.

Bissig *et al.* [155] reported a reflective back contact architecture including a metallic reflector that is compatible with the direct co-evaporation of CIGS. It consists of a glass/Mo/Al (100 nm)/InZnO (260 nm) stack that was also covered with 2.6 nm of Mo to avoid the formation of Ga oxide. This back contact was only tested for solar cells with a standard CIGS thickness of 3 µm, but it still led to an increase of the best cell J_{SC} of 0.7 mA/cm^2 as compared to Mo. Interestingly, this back contact architecture can be textured for further light trapping.

3.2.4. Patterned reflective back contacts for ultrathin solar cells

Flat reflective back contacts can improve the J_{SC} of ultrathin solar cells as they provide a double-pass absorption in the CIGS layer. In particular, they enhance the amplitude of Fabry-Pérot resonances that are generated by light reflection at the planar interfaces of the solar cell stack. These resonances lead to absorption maxima that can be described in 1D, along the vertical direction z (Figure I. 22.a). For a given absorber layer of thickness t and refractive index n_2 that is in contact with semi-infinite mediums of refractive indices n_1 at the front side and n_3 at the back side, the conditions for Fabry-Pérot resonances are:

$$\frac{4\pi n_2}{\lambda_0} t + \varphi_{21} + \varphi_{23} = 2\pi q \qquad \text{(I. 11)}$$

where λ_0 is the wavelength, and q is an integer that defines the Fabry-Pérot order. φ_{21} and φ_{23} are the phase changes induced by reflection at the front and back interfaces. It is possible to calculate these phase changes from the complex Fresnel coefficient of reflection. Hence, for a given layer stack the position of Fabry-Pérot resonances shifts to higher wavelengths as the thickness of the absorber t increases.

Nevertheless, numerical simulations show that light trapping strategies based on nanopatterned back mirrors can further improve the J_{SC} values of complete cells, even in the case of thick CIGS layers (~2 µm) [122], [156]–[158]. For example, using a two dimensional grating of period p as a back reflector results in additional absorption resonances that are due to the coupling of light into waveguide modes, as shown schematically in Figure I. 22.b. The periodic grating provides the additional in-plane

momentum that is necessary to the light coupling, as it scatters light into diffracted waves with the following in-plane wavevectors:

$$\vec{k}_{||\,(m_1,m_2)} = \vec{k}_{||\,(0,0)} + m_1 \frac{2\pi}{p}\overrightarrow{e_x} + m_2 \frac{2\pi}{p}\overrightarrow{e_y} \qquad \text{(I. 12)}$$

with $\vec{k}_{||\,(0,0)}$ the in-plane wavevector of incident waves, (m_1,m_2) integers that define the diffracted wave order, $\overrightarrow{e_x}$ and $\overrightarrow{e_y}$ the unit vectors perpendicular to the z-direction. For a given layer stack, the conditions for the coupling of light into waveguide modes will thus depend on the period p of the grating.

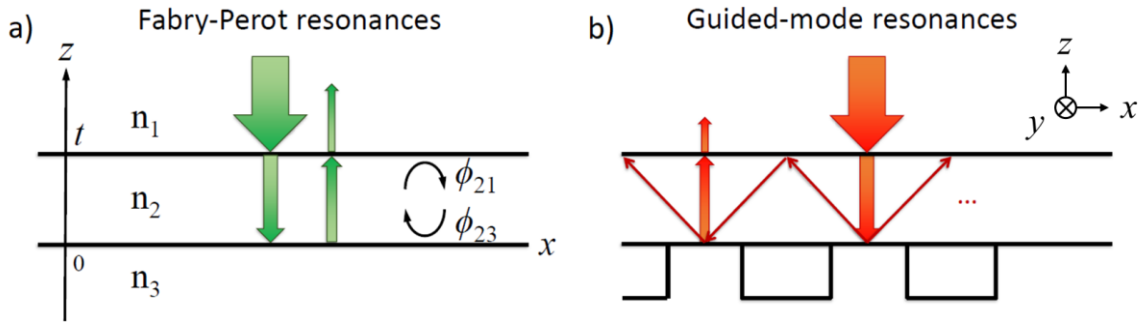

Figure I. 22. Schematics of the (a) vertical Fabry-Pérot resonances and (b) in-plane waveguide resonances induced by a nanostructured back mirror. Inspired from [159].

The concept of nanostructured back mirrors has been investigated in other photovoltaic technologies, like ultrathin GaAs solar cells [160], as well as ultrathin CIGS solar cells:

Van Lare *et al.* [161] fabricated solar cells with 460 nm of CIGS and an array of SiO_2 nanoparticles (NPs) on Mo prepared by substrate conformal imprint lithography. This nanostructured back contact resulted in an enhancement of the best J_{SC} from 28.2 mA/cm² to 30.5 mA/cm² as compared to the flat Mo back contact, without ARC. The EQE of cells with SiO_2 NPs exhibited an improved EQE for wavelength above 700 nm, with a peak at ~1100 nm that was attributed to waveguide-mode coupling. The best efficiency for a cell with SiO_2 nanostructures was 12.3 %.

Jarzembowski *et al.* [162] used laser interference lithography to produce periodic nanostructures in a layer of SiO_2 deposited on the Mo back contact. With only 190 nm of CIGS, a best J_{SC} of 23.7 mA/cm² and efficiency of 9.0% (without ARC) were achieved for a quadratic array of point contacts with a hole diameter of 660 nm, a pitch of 1.1 µm and a SiO_2 thickness of 130 nm. The absorption gains for wavelengths around 800 nm and 1100 nm were respectively attributed to scattering and waveguide effects.

Yin *et al.* [163] added SiO_X NPs on a flat reflective back contact consisting of a glass/ITO stack with a silver mirror on the backside of the glass substrate. A tetragonal array of SiO_X NPs was prepared by substrate conformal imprint lithography, with an average diameter of ~150 nm, a pitch of ~510 nm and a height of 210 nm. CIGS solar cells with a 390 nm-thick absorber exhibit a high average J_{SC} of 32.1 ± 0.2 mA/cm² (without ARC) that is 6.9 mA/cm² more than the flat ITO reference. For wavelengths between 480 and 700 nm, the enhancement of CIGS absorption is attributed to Fabry-

Pérot resonances, while absorption peaks at 850 and 1040 nm are attributed to waveguide modes within the CIGS film. However, the efficiency of solar cells on this nanostructured back contact is limited to 10.0 ± 0.3 % (and 6.8 ± 0.1 % on Mo) due to a low *FF*.

3.2.5. Summary of the state of the art on ultrathin CIGS solar cells

The results presented in this state of the art on ultrathin CIGS solar cells are listed in Table I. 2. Light I(V) parameters are given, together with some important parameters: the CIGS thickness and its GGI grading, the method for alkali incorporation as well as the optional presence of an ARC. A short discussion of the different strategies presented in this state of the art is provided in the next section.

Strategy & ref.			CIGS thickness (µm)	GGI grading	Alkali incorporation	ARC	Eff. (%)	J_{SC} (mA/cm²)	V_{OC} (mV)	*FF* (%)
GGI grading	CGS bottom layer	[13]	0.6 (+0.1 CGS)	graded	SLG	Ø	12.1	22.7	690	77.8
	V-shaped grading	[127]	0.46	graded	SLG	Ø	10.6*	26.6*	591*	67.5*
	linear grading	[11]	0.49	graded	SLG	MgF_2	**15.2**	26.4	**733**	**78.2**
Passivation layer	MgF_2/Al_2O_3 / CdS NP	[139]	0.4	flat	NaF precursor	MgF_2	**13.5** ± 0.4*	**31.1** ± 0.1*	633 ± 2*	68.7 ± 1.9*
	Al_2O_3 / e–beam	[140]	**0.24**	flat	NaF precursor	MgF_2	**11.8** ± 0.3*	23.3 ± 0.5*	**659** ± 5*	77.0 ± 0.6*
	Al_2O_3 / e–beam	[10]	0.35	flat	NaF precursor	Ø	9.7 ± 0.7*	21.6 ± 1.0*	627 ± 11*	71.8 ± 3.3*
	flat Al_2O_3 (6 nm)	[142]	0.22	flat	NaF precursor	Ø	~9	~24	~580	~65
	Al_2O_3 / photolitho.	[143]	0.38	graded	SLG	Patterns	10.3 ± 0.3*	23.8 ± 2.1*	644 ± 22*	66.7 ± 1.5*
	Al_2O_3 / photolitho.	[144]	0.5	graded	SLG	Ø	9.6 ± 0.2*	24.7 ± 0.3*	564 ± 2*	69 ± 1*
	Al_2O_3 / NIL	[138]	0.42	flat	NaF PDT	Ø	9.2	20.9	604	73
	TiO_2 / NIL	[138]	0.42	flat	NaF PDT	Ø	7.4	19.5	606	63
	MgF_2 / photolitho.	[144]	0.5	graded	SLG	Ø	9.9 ± 0.1*	24.8 ± 0.2*	562 ± 3*	71 ± 0*
	SiO_2 nanomesh / NSL	[145]	0.37	V-shaped	SLG	Ø	11.4	27.5	589	70.3
Flat reflective back contact	Mo/TiW/Al_2O_3	[146]	0.5	flat	NaF precursor	Ø	11.0	25.8	635	67.2
	lift-off then Au	[120]	0.4	graded	SLG	Ø	10.2	~25	~650	~63
	Cu/SLG/SnO_2:F	[152]	0.45	flat	NaF PDT	Ø	11.4	25.9	630	72
	superstrate + Ag	[154]	0.3	flat	SLG?	Ø	9.7	23.6	640	63.8
	glass/Mo/Al/InZnO	[155]	thick: *3.0*	V-shaped	RbF PDT	MgF_2	*19.9*	*36.5*	*721*	*75.6*
Patterned reflective back contact	SiO_2 NP on Mo	[161]	0.46	V-shaped	SLG	Ø	**12.3**	**30.5**	592	68.2
	Mo/patterned SiO_2	[162]	0.19	linear	NaF PDT	Ø	9.0	23.7	597	69.6
	Ag/SLG/ITO/SiO_X NP	[163]	0.39	V-shaped	SLG?	Ø	10.0 ± 0.3*	**32.1**	558 ± 2*	55.2 ± 1.7*

Table I. 2. Selection of published results on ultrathin CIGS solar cells, up to 2019. These works are sorted by type of strategy for efficiency improvement: GGI composition grading, rear passivation layer and reflective back contact. The light I(V) parameters of the best cells are indicated, together with the CIGS thickness, the GGI composition grading, the method for alkali incorporation and the optional presence of an ARC. *Average values, with standard deviation if available.

3.3.Conclusion of the chapter

Decreasing the CIGS thickness of complete solar cells while maintaining their efficiency is expected to improve the competitiveness of CIGS solar cells. The reduced material consumption and increased throughput of ultrathin CIGS modules result in a lower manufacturing cost in terms of $/m^2. If the efficiency of such ultrathin CIGS modules is maintained, a reduced $/Wp cost is also predicted.

However, there are two main detrimental effects that limit the photovoltaic performances of ultrathin CIGS solar cells: their increased sensitivity to back contact recombination and their incomplete light absorption. As a result, strategies to improve the efficiency of ultrathin CIGS solar cells have focused on the CIGS rear passivation on the one hand, and the development of reflective back contacts on the other hand. A non-exhaustive state of the art on the approaches for efficient ultrathin CIGS solar cells was presented in this chapter.

In particular, a record efficiency of 15.2% has been reached for ultrathin CIGS (490 nm) solar cells, thanks to a linear GGI grading that contributes to the passivation of the CIGS/Mo back contact [11]. This ultrathin cell also exhibits remarkable values of V_{OC} = 733 mV and FF = 78.2%, which are comparable to those of record devices with standard absorber thicknesses [26], [31], [32]. The linear GGI grading of ΔGGI = 0.2 that led to the record ultrathin efficiency was achieved by co-evaporating CIGS in a 2-stage process with a high GGI ratio during the first stage. However, there should be room for improvement as simulations indicate that a $\Delta GGI \geq 0.3$ is necessary to minimize back contact recombination [11]. In this regard, decreasing the substrate temperature during the 3-stage co-evaporation process of ultrathin CIGS layers was shown to create an adequate GGI grading [127].

An efficient rear passivation of CIGS was achieved by fabricating a MgF_2/Al_2O_3 bilayer with local point contacts [139]. It led to an average efficiency of 13.5 ± 0.4 % and V_{OC} of 633 ± 2 mV for a 400 nm-thick CIGS layer with an ungraded GGI depth profile. This strategy of rear passivation layers can also allow ultrathin cells to maintain a high V_{OC} of 659 ± 5 mV with only 240 nm of CIGS, resulting in an efficiency of 11.8 ± 0.3 % [140]. Nevertheless, higher V_{OC} values were achieved in ultrathin cells including a ≈500 nm-thick CIGS layer with a GGI composition grading, but without any passivation layer [11].

Regarding the investigations of reflective back contacts for ultrathin CIGS solar cells, a J_{SC} of 25.9 mA/cm^2 and an efficiency of 11.4 % were obtained for a solar cell with 450 nm of CIGS on a flat transparent back contact equipped with a Cu back mirror [152]. A higher J_{SC} of 30.5 mA/cm^2 was reported for a solar cell with a 460 nm-thick CIGS layer, thanks to the light trapping effects of a SiO_2 nanoparticle array prepared on Mo [161]. It resulted in an efficiency of 12.3%. A best J_{SC} of 32.1 mA/cm^2 was reported for an ultrathin CIGS solar cell on a reflective back contact composed of an ITO back contact, a silver back mirror, as well as SiO_X nanoparticles for light trapping [163]. However, the J_{SC} of ultrathin solar cells remains well below the J_{SC} of standard solar cells, which highlights the need to develop architectures of highly reflective back contacts that are compatible with the CIGS deposition process and with light trapping strategies.

The work reported here will present some strategies to improve the performances of ultrathin CIGS solar cells via CIGS rear passivation as well as enhanced light reflection at the back contact. Before reporting the results of this contribution, the materials and methods that were used for the fabrication, characterization and simulation of ultrathin CIGS devices will be detailed in the next chapter.

Chapter 4. CIGS solar cells: materials and methods

The following sections provide the details related to the fabrication, characterization and optical simulation of ultrathin CIGS solar cells that were performed in this work. Note that the name of the samples used to produce experimental data are indicated in square brackets, at the end of the caption of the relevant figures.

This study was conducted in three different laboratories: the C2N and IRDEP/IPVF[1] in France as well as the Ångström Solar Center in Sweden. Hence, the experimental details reported here will be distinguished depending on the laboratory where they were carried out.

4.1.CIGS co-evaporation and cell fabrication

4.1.1. CIGS

- At IRDEP:

CIGS layers were co-evaporated in a reactor purchased from *MBE – Komponenten* [164] (see Figure I. 23). The substrates are first transferred from the load-lock chamber to the vacuum chamber, which is then pumped down to a secondary vacuum of $\sim 10^{-7}$ mbar. Pure Cu, In, Ga and Se elements are evaporated from their respective effusion sources. Their evaporation rates are calibrated individually with a quartz crystal microbalance prior to CIGS co-evaporation, by varying the power of the heater for each source. The source shutters can be freely opened and closed to respectively enable or prevent the evaporation of a given element. The substrate is loaded downward and its temperature is controlled by a thermocouple placed behind the substrate holder, which is rotated and heated during the deposition process. The co-evaporation reactor is also equipped with an infrared (IR) camera (*FLIR ThermaCam SC640*) that was used in a previous study to refine the calibration of the substrate temperature [126]. Automatized processes for CIGS co-evaporation are defined, allowing for a precise and reproducible control of the deposition parameters. A mass spectrometer is also used as a qualitative process control to ensure that elements are being evaporated according to the intended CIGS process. Importantly, the co-evaporation reactor also contains a NaF effusion source that is used for the PDT of CIGS layers.

In this work, ultrathin CIGS layers prepared at IRDEP were co-evaporated in a 1-stage process, *i.e.* the co-evaporation rates of Cu, In, Ga and Se were fixed during the whole deposition. This results in an ungraded CIGS composition, and in particular a flat GGI profile. To clarify the fabrication steps reported here, one should keep in mind that all complete solar cells with a CIGS film co-evaporated in a 1-stage process were fabricated at IRDEP, and that their composition and performance were characterized at IRDEP. Other cells were fabricated and analyzed at the Ångström Solar Center.

[1] Institut de Recherche et Développement sur l'Énergie Photovoltaïque (IRDEP). IRDEP merged with IPVF in 2018.

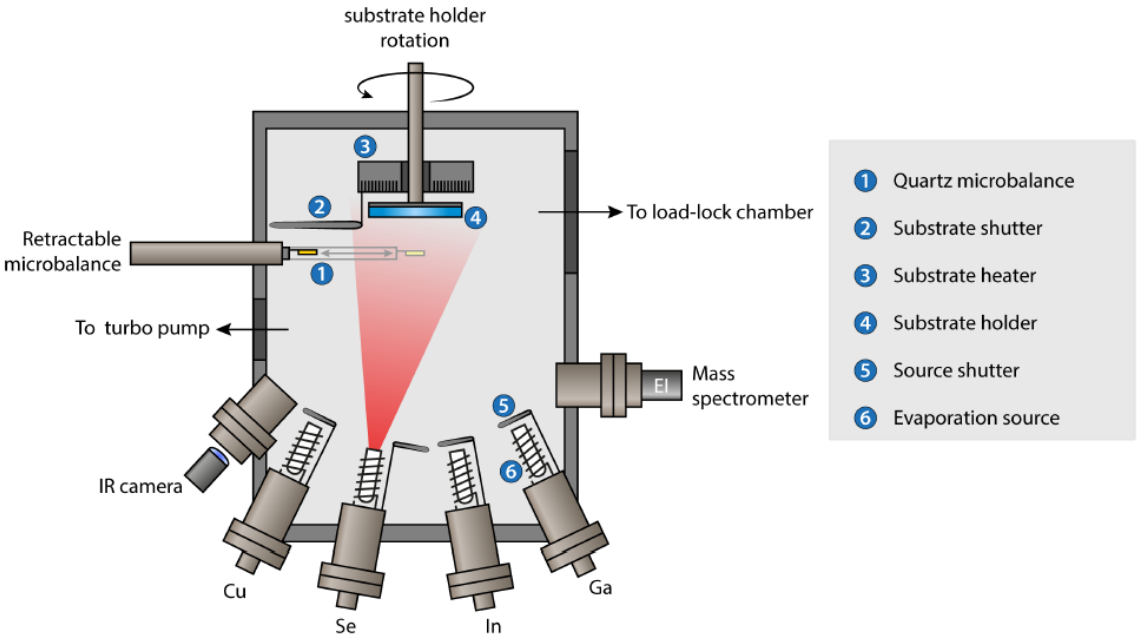

Figure I. 23. Schematics of the vacuum chamber used at IRDEP for co-evaporation of CIGS. From [12].

- At the Ångström Solar Center:

CIGS layers were prepared by co-evaporation of elemental Cu, In, Ga and Se in a *Baltzer BAK 550* vacuum chamber. The substrates are introduced directly inside the co-evaporation reactor, facing downward. During CIGS co-evaporation, the substrate holder is heated and its temperature is controlled via a thermocouple placed on a graphite plate. The holder does not rotate, which is why Cu, In and Ga are evaporated from boat sources to achieve the most homogeneous composition possible. It is worth mentioning though that the composition and thickness of the CIGS films are slightly dependent on their lateral position on the substrate holder. The co-evaporation process of CIGS follows predefined and automatized recipes, where the evaporation rates of Cu, In and Ga are tuned in real time thanks to the feedback loop signal of a quantitatively calibrated mass spectrometer. This method allows the reproducible deposition of ultrathin CIGS layers in a multi-stage process, see Part II for more details. Finally, an evaporation boat of Ag is also available for the deposition of ACIGS absorbers.

As the co-evaporator used at the Ångström Solar Center does not contain a source of NaF, precursor layers of NaF were thermally evaporated on the substrates prior to CIGS co-evaporation. NaF was deposited in a *Baltzer UMS* evaporator equipped with a rotating substrate holder. The thickness of the NaF layer was calibrated with a quartz crystal microbalance and profilometer measurements.

4.1.2. Mo and other back contacts

- At IRDEP:

The SLG substrates with a thickness of 3 mm are first cleaned with a detergent and an argon plasma etching. 800 nm-thick Mo layers are then deposited by DC sputtering with an Ar plasma, a pressure of ~5 mTorr and a DC power of 65 W. The Mo films exhibit a typical sheet resistance of 0.2 Ω/sq.

The effects of alumina passivation layers with local openings on Mo back contact were also investigated. The passivation layers were fabricated by deposition of Al_2O_3 on Mo by ALD. The layers were patterned with a process combining nano-imprint lithography and chemical etching in an aqueous solution. More details regarding the fabrication of these passivation layers are provided in Part II.

- At the Ångström Solar Center:

Substrates consist of 1 mm-thick SLG that are cleaned in ultrasonic baths containing a mix of deionized water and detergent. The Mo back contact is then deposited by DC sputtering in an *MRC 603* system. A plasma of Ar is applied with a DC power of 1500 W and a pressure of 0.8 Pa. The Mo layers are usually 300 nm-thick with a sheet resistance of 0.6 Ω/sq.

- At the C2N:

The investigated reflective back contacts (RBC) consist of a multi-layer stack that is deposited on SLG substrates. The architecture of the RBC is represented below in Figure I. 24.

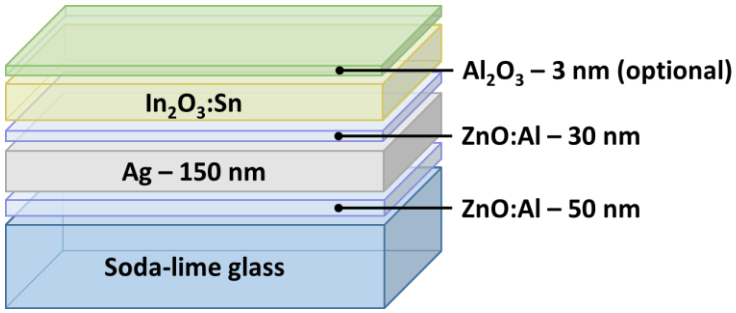

Figure I. 24. Schematic representation of the multi-layer stack that is investigated as a reflective back contact for ultrathin CIGS solar cells.

ZnO:Al layers were deposited in a *Plassys MP800S* sputtering tool. The deposition was achieved with an Ar plasma at a pressure of 3 mTorr and a RF power of 200 W. The Ag layer was deposited by e-beam evaporation (*Plassys MEB550SL*) at a pressure of a few 10^{-7} mbar. An acceleration voltage of 10 kV was applied and the emission current was gradually increased to a few tens of mA/cm², until an evaporation rate of 1 nm/s was reached. To limit the risks of Ag oxidation, the samples were transferred from the e-beam evaporator to the *Plassys MP800S* sputtering system in less than 5 min. ITO was sputtered with an Ar plasma at a pressure of 3 mTorr and a RF power of 200 W. ITO thicknesses of 30 nm, 100 nm and 200 nm were investigated. The impacts of an optional Al_2O_3 layer deposited on top of ITO were also studied. 1.5 or 3 nm of alumina were deposited at the Ångström Solar Center by ALD (*Picosun R200*) at a substrate temperature of 300°C, using H_2O and trimethylaluminium ($Al(CH_3)_3$, TMA) as precursors.

4.1.3. CdS buffer layer

- At IRDEP:

The CIGS surface is immersed in an aqueous solution of KCN prior to CdS deposition, in order to etch the Cu_XSe copper phases that might remain at the CIGS front interface. The CdS layer is then deposited by CBD at 60°C, in a solution of ammonia containing

Cd acetate $Cd(CH_3CO_2)_2$ and thiourea $SC(NH_2)_2$. The usual deposition time ranges from 6 to 8 minutes to deposit the desired thickness of ≈ 50 nm.

- At the Ångström Solar Center:

The CIGS layers are transferred straight from the CIGS co-evaporator to the aqueous solution to grow the CdS buffer layer by CBD. This process relies on the same chemical reagents as the ones used at IRDEP, but the deposition time is fixed to 8 min and 15 s, resulting in a CdS thickness close to 50 nm.

4.1.4. i-ZnO and ZnO:Al front contact

- At IRDEP:

The front contact layers are usually deposited in a *Plassys MP600* sputtering system. The intrinsic ZnO layer is deposited with a thickness of 50 nm, by RF sputtering of a ZnO ceramic target in a plasma of Ar and O_2. A 350 nm-thick ZnO:Al layer is then deposited by RF sputtering of a ZnO ceramic target with 2 wt% of Al_2O_3. An Ar/O_2 plasma is used, with a pressure of 0.9 mTorr and a RF power of 90 W. The ZnO:Al exhibits a typical donor concentration in the range of 10^{20} to 10^{21} cm^{-3}, a mobility of ~10 cm^2/V and a sheet resistance of 25 to 40 Ω/sq.

- At the Ångström Solar Center:

A *von Ardenne CS600S* RF sputtering tool was used for the deposition of a 50 nm-thick *i*-ZnO and 250 nm-thick ZnO:Al. The ZnO:Al target also consists of a ZnO ceramic target with 2 wt% of Al_2O_3. The Ar/O_2 plasma is applied with a pressure of 1 mTorr and a RF power of 200 W and 300 W for the *i*-ZnO and ZnO:Al targets, respectively. The typical sheet resistance of the ZnO:Al layer is 30 ± 10 Ω/sq.

4.1.5. Photolithography

Solar cells with an area of 0.1 cm^2 were separated with a photolithography process.

- At IRDEP:

A negative resist (AZ® 2070, *AZ Electronics Materials*) was spin-coated on complete solar cells at 4000 rpm for 30 s, then pre-baked at 105°C for 1 min 30 s. It was then exposed to ultraviolet (UV) light (365 – 435 nm light, *Karl Süss MJB* mask aligner) and baked again at 105°C for 1 min 30 s. The resist was finally developed with a commercial developer containing $(CH_3)_4N^+HO^-$ (*AZ® 326 MIF*).

- At the Ångström Solar Center:

A positive resist (AZ® 9260, *AZ Electronics Materials*) was spin-coated on complete devices at 6000 rpm for 45s. It was pre-baked at 115°C for 2 min, and exposed to UV light (365 – 405 nm light, *Karl Süss MA6/BA6* mask aligner). It was then baked again at 115°C for 5 min, and eventually developed in a KOH-containing commercial developer (*AZ® 400 K*) that was diluted 5 times in deionized water.

- In both laboratories, after the development of the photoresists the CdS/i-ZnO/ZnO:Al layers were etched by immersing the solar cells for 30 to 60 s in an aqueous solution of HCl with a concentration of 1 M. This process resulted in an efficient cell separation and also avoided the formation of detrimental shunt paths. Lastly, the photoresists were stripped in a pure solution of acetone prior to the characterization of complete cells.

4.2.Characterization methods

4.2.1. Optical characterization

The reflectance and transmittance spectra were acquired over the 300 – 2000 nm wavelength range with a UV-vis-NIR spectrophotometer (*Agilent Cary 5000*). The spectrophotometer includes an integrating sphere that allows to collect the total reflection and transmission of thin films.

Ellipsometric measurements (*HORIBA Jobin-Yvon UVISEL 2*) were performed on a 200 nm-thick ITO deposited in the C2N cleanroom using the *Plassys MP800S* equipment and process described in section 4.1.2. This ITO layer was characterized before and after a 10-minute annealing at 540°C in air. The real and imaginary parts of the ITO optical index, respectively *n* and *k*, were fitted from experimental data for wavelengths between 200 and 2000 nm. The optical indices after annealing were used in the Reticolo optical model to simulate the ITO layers deposited at C2N.

4.2.2. Electrical characterization

The sheet resistivity of TCO layers and RBC stacks deposited on SLG was determined with a four-point probe set-up (*Lucas Labs S-301-4*).

The resistivity values ρ were crosschecked with Hall effect measurements in the Van der Pauw configuration (*Ecopia HMS-5000*, at IPVF), which also allowed to determine the doping concentration of the TCO [165]. The carrier mobility of the *n*-doped TCO was then derived from the following formula:

$$\rho = {}^{1}/_{q\mu_n n} \qquad \text{(I. 13)}$$

where μ_n is the electron mobility and n the electron concentration.

4.2.3. Material characterization

- SEM and TEM:

The morphology of the samples was analyzed in scanning electron microscopy (SEM). At IRDEP, images were acquired with a *Zeiss Merlin VP* microscope, with an acceleration voltage of 15 kV and a working current of 1.6 nA. In this case, a thin and conductive carbon layer was evaporated on the cross-section of the samples to avoid artifacts due to charge accumulation. This microscope was equipped with a calibrated detector for energy dispersive x-ray (EDX) spectroscopy, which allowed a quantitative determination of the CIGS composition on Mo layers. At the Ångström Solar Center, samples were analyzed in SEM using a *Zeiss Merlin* tool. At the C2N, SEM studies were conducted in a *FEI Magellan 400L* microscope, generally at an acceleration voltage of 7 kV and an emission current of 0.2 nA. The EDX detector of this microscope was not calibrated and only allowed a qualitative analysis of the composition.

At the C2N, the transmission electron microscopy (TEM)/EDX (*FEI Titan Themis XFEG*) study was carried out by Dr. Gilles Patriarche, at an acceleration voltage of 200 kV. The other TEM/EDX analyses were performed by Dr. Lars Riekehr at the Ångström Solar Center, in a probe corrected TEM (*FEI Titan Themis*) operated at 200 kV. The EDX results were obtained in scanning TEM mode, with the SuperX EDS system. In both cases, the thin lamellas characterized in TEM were prepared by focused ion beam.

- CIGS thickness:

The thickness of CIGS layers deposited on Mo were measured with a *Veeco* profilometer at IRDEP, and a *Dektak 150* profilometer at the Ångström Solar Center. The CIGS layers were locally scratched with a blade to create a step for the profilometer measurements. In some cases, the CIGS thickness was also determined from cross-sectional SEM images.

- X-ray diffraction (XRD):

XRD studies were performed at IPVF (*PANalytical Empyrean*) in the Bragg-Brentano configuration, using Cu Kα_1 (0.1541 nm) radiation operated at 40 kV (40 mA), and at the Ångström Solar Center (*Siemens/Bruker D5000*) both in the Bragg-Brentano and grazing incidence configurations.

4.2.4. Compositional characterization

The average composition of ultrathin CIGS layers deposited on Mo were determined by x-ray fluorescence (XRF, *Fischerscope X-ray XDV-SDD* at IRDEP and *Spectro X-Lab 2000* at the Ångström Solar Center). CIGS reference samples with known compositions and thicknesses were used to quantitatively calibrate the XRF set-ups.

The composition profiles of CIGS layers co-evaporated on various back contacts were measured by glow-discharge optical emission spectroscopy (GD-OES, *HORIBA Jobin-Yvon* at IRDEP and *Spectruma Analytik GDA 750 HR* at the Ångström Solar Center). The power and pressure of the Ar plasma were optimized in order to etch the samples homogeneously. The GD-OES analyses did not allow a quantitative determination of the CIGS composition, but the elemental profiles of Cu, In, Ga and Se were calibrated based on the average CIGS composition characterized in XRF or EDX.

4.2.5. Opto-electrical analysis of complete solar cells

Solar cells were separated with a relatively small area of 0.1 cm^2. For this size of solar cell, the front contact layer is conductive enough and the cells do not require the deposition of a grid on ZnO:Al. Hence, during opto-electrical characterizations the cells were contacted by applying the probes directly on the ZnO:Al layer. To connect the back contact of the solar cells, the layers on top of it were mechanically scribed and pure In was then soldered on the bare back contact. Probes were then put in contact with the soldered In pad.

- At IRDEP:

The I(V) characteristics of complete solar cells were measured with a four-point probe set-up connected to an *Agilent* voltage source. The samples were placed on a surface that was thermostated at 25°C. A *Newport* class AAA instrument was used as a light source corresponding to the AM 1.5 G irradiance.

The EQE were determined with a *Newport IQE200* tool, using a monochromator filter and Si and Ge detectors as calibration references.

- At the Ångström Solar Center:

The I(V) curves were determined in a home-built system equipped with a white halogen lamp. The average intensity was calibrated to 100 mW/cm^2 with a Si solar cell reference. The temperature of the substrate holder was fixed at 25°C thanks to a refrigeration circuit containing water, and controlled by a temperature sensor (*pt100* element) as well as a Peltier element. However, the emission spectrum of the halogen lamp does not reproduce accurately the standard AM 1.5 G irradiance. As a result, the J_{SC} of complete solar cells were calibrated by integration of their EQE.

The EQE were measured with a home-built set-up. The light emitted by a xenon-arc lamp was filtered by a monochromator wheel to select the transmitted wavelengths. It was calibrated with references consisting of GaAs and Si solar cells.

- In both laboratories, the dark I(V) characteristics were also measured by covering the samples with a black piece of cloth. The experimental curves were then fitted with a 1-diode or a 2-diode model.

4.3.Optical simulation with the Reticolo software

The optical simulation of complete CIGS solar cells was performed with the Reticolo software [166]. It was developed by Philippe Lalanne and Jean-Paul Hugonin from the *Institut d'Optique*, with a contribution from Christophe Sauvan. The software code is written in the Matlab language and run on Matlab®.

Reticolo uses the rigorous coupled wave analysis (RCWA) method to calculate the exact electromagnetic field. It derives the eigenmodes of the different layers constituting a stack in a plane-wave basis (Fourier basis). A scattering matrix method is applied in order to solve the continuity equations at the interfaces of the layer stack.

Contrary to 1D optical models relying for example on the ray transfer matrix method [12], Reticolo allows the simulation of 2D rectangle nanostructures with periods p_x and p_y along the respective horizontal axes x and y. These periods are the same for each layer of the stack, which also makes the computation of 1D architectures possible. The electromagnetic field is calculated over one period of the investigated geometry only, where periodic boundary conditions are applied to simulate the whole 2D architecture. An example of a nanostructured layer stack simulated with Reticolo is shown in Figure I. 25.

A structured layer can consist of 2 distinct materials in the xy horizontal plane. For example, a material with an optical index $n_{j,m}$ forming a nanopillar that is embedded in an array of another material with an optical index of n_j. The linear filling fraction ff of the material forming a nanopillar with a width w is defined as $w = ff \times p$. Note that this filling fraction has to be defined along the x and y directions in the case of a rectangular geometry. However, nanostructures with a square geometry only were investigated in this work. The list of the complex optical indices used in this study can be found in Appendix C.

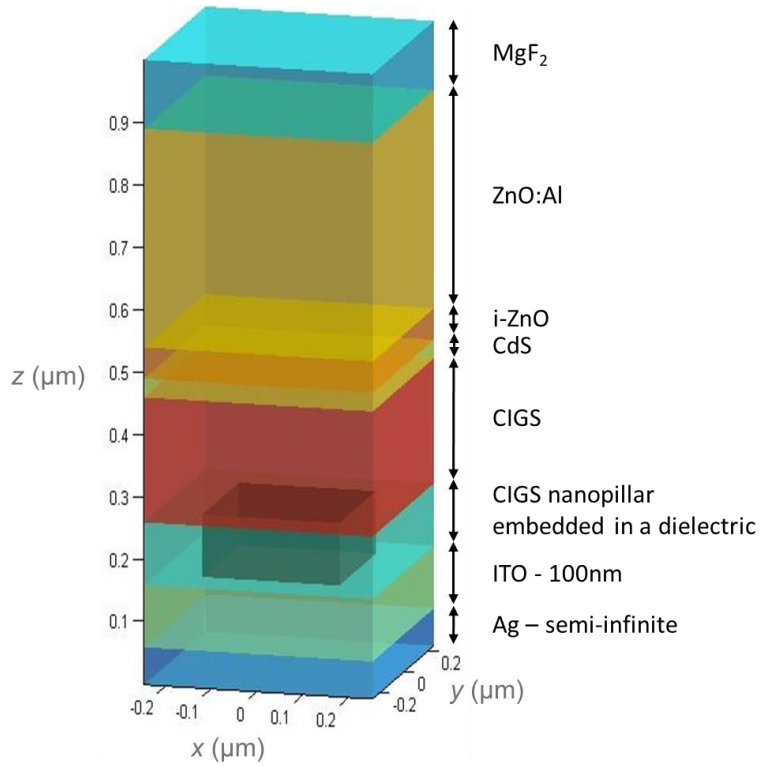

Figure I. 25. Schematic of a unit cell used to simulate a CIGS cell with a nanostructured back contact.

The simulations were performed considering an incident light polarized in TE mode, *i.e.* with the electric field transverse to the incidence plane. However, as the calculations reported here were done at normal incidence, TE and TM (*i.e.* with the magnetic field transverse to the incidence plane) modes give similar absorption results. Light absorption in non-structured layers is determined from the computation of the Poynting vector, while the absorption in nanostructured materials is derived from the integration of the electromagnetic field in each point over a single period.

With the RCWA method, the plane waves of the electromagnetic field are decomposed on a Fourier basis with a given number of Fourier harmonics, respectively M_x and M_y along the x and y axes. As the values of M_x and M_y are increased, the precision of the calculation is improved but its duration is increased. Here, values of $M_x = M_y \geq 20$ were found to result in similar absorption spectra, which is why M_x and M_y were fixed at the value of 20 in this study.

Conclusion of Part I

In the context of a growing global energy demand and climate change related to the emission of greenhouse gases from human activities, it is critical to develop the renewable energy sector. The solar photovoltaic technology is an advantageous energy supply, in particular thanks to an abundant solar resource and a low energy payback time of industrial photovoltaic modules.

This work is focused on the $Cu(In,Ga)Se_2$ thin film technology. CIGS solar cells rely on a *p*-*n* heterojunction formed with a *p*-doped CIGS and an *n*-doped CdS layer. They are usually fabricated on glass substrates, but are also compatible with flexible substrates. Standard cells include a Mo back contact and a front contact made of ZnO-based transparent layers. The current world record efficiency for the CIGS technology is 23.4% [26].

The physics of the CIGS solar cell was briefly described to explain the optical and electrical phenomena that allow the generation of electricity from a light source. The main loss mechanisms that occur in CIGS photovoltaic devices were detailed, and the characterization methods to determine the performance of solar cells were introduced.

This thesis reports on the development of ultrathin CIGS solar cells, *i.e.* with a CIGS thickness ≤ 500 nm. Hence, the expected benefits and challenges of ultrathin devices were also reviewed. In particular, the efficiency of ultrathin CIGS devices is limited by a low reflectivity as well as a high surface recombination velocity at the standard CIGS back contact with Mo. A brief review of the recent works on ultrathin CIGS solar cells was presented, sorted by type of strategy for performance improvement: (1) the optimization of the CIGS composition, (2) the addition of a passivation layer at the CIGS/Mo interface and (3) the use of a flat or nanostructured reflective back contact.

Finally, the materials and methods used in this study were listed. The following of this manuscript is divided into 2 parts; the first one dealing with the CIGS rear passivation via the grading of the CIGS composition and via the fabrication of a rear passivation layer, and the second one describing the development of a novel reflective back contact architecture.

Part II. Ultrathin CIGS-based solar cells with Mo back contacts

Introduction to part II

CIGS solar cells with submicrometer-thick absorbers generally exhibit lower open-circuit voltage (V_{OC}) and fill factor (FF) than devices with standard absorber thicknesses [13], [116], [117]. These losses are related to a degradation of the CIGS material quality and a higher risk of shunt paths [9], [117], as well as an increased recombination of charge carriers at the back contact that can also result in substantial J_{SC} losses [9], [10], [13], [119].

Hence, this second part focuses on three distinct approaches to increase the V_{OC}, FF and efficiency of ultrathin CIGS solar cells on Mo back contacts. In order to improve the quality of ultrathin absorbers and to passivate the rear interface between CIGS and Mo, the three following strategies were investigated:

- The first strategy consisted in optimizing the composition grading of ultrathin CIGS absorbers. In particular, a GGI back grading was formed in order to create a conduction band grading that results in a passivating back surface field [11], [13], [127]. To do so, the standard 3-stage process developed at the Ångström Solar Center was shortened to co-evaporate 500 nm-thick CIGS films with a graded composition. The composition profile of CIGS layers deposited at standard and lower substrate temperatures were also compared.

- The second approach to improve the quality of the ultrathin absorber is to fabricate complete cells with Ag-alloyed CIGS layers (ACIGS). Indeed, introducing a small amount of Ag to CIGS absorbers was reported to reduce the amount of structural disorder [86], [87] and to decrease the voltage deficit, *i.e.* $E_g - V_{OC}$, of complete solar cells [84], [88], [89]. The properties of ACIGS films co-evaporated at 550°C and 500°C were also compared.

- The last strategy was to implement a passivation layer between the CIGS absorber and the Mo back contact [139], [140]. Here, an alumina layer was deposited by ALD on Mo. As Al_2O_3 is insulating, point openings were formed prior to CIGS co-evaporation thanks to a nanoimprint lithography process (NIL) and a step of chemical etching. Ultrathin CIGS layers were co-evaporated in a 1-stage process on Mo back contacts with and without an alumina passivation layer, and the resulting photovoltaic performances of complete solar cells were compared.

Chapter 5. Optimization of CIGS deposition on Mo

5.1.Introduction and co-evaporation process

A modified 3-stage process was used to co-evaporate ultrathin CIGS layers with a composition grading, as shown in Figure II. 1. In contrast to the usual 3-stage process, Cu is evaporated during the whole deposition of CIGS, but with a higher rate during the second stage in order to obtain a Cu-rich composition at the end of this stage. Note that the first stage begins with a higher Ga rate and a lower In rate so that the CIGS layers exhibit a linear GGI profile.

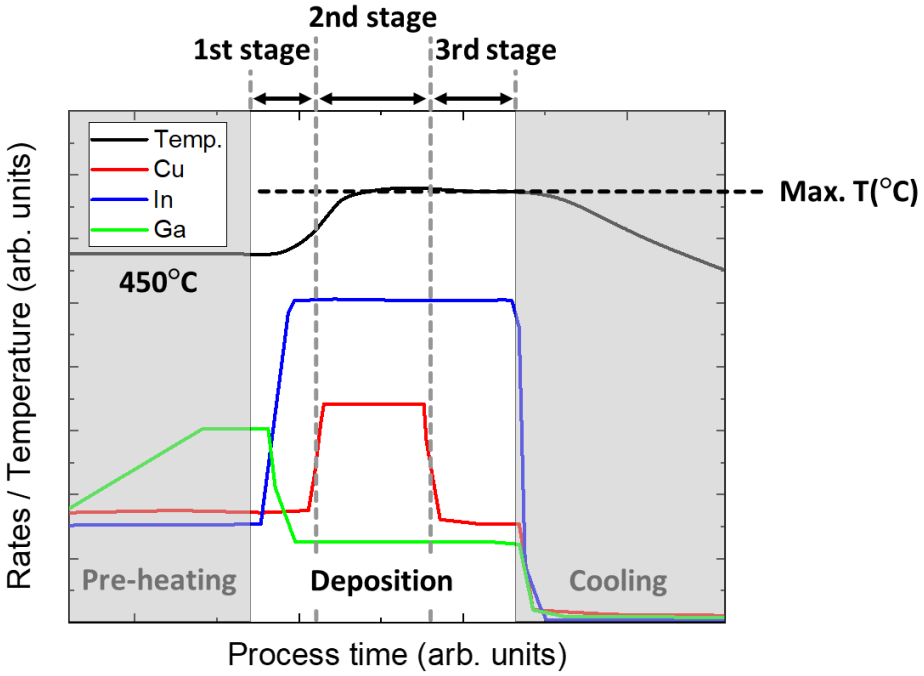

Figure II. 1. Schematic representation of the modified 3-stage process used at the Ångström Solar Center to co-evaporate ultrathin CIGS layers. The relative rates of Cu, In and Ga are shown, contrary to the Se rate as CIGS is deposited with an excess pressure of Se. The first stage of the process starts with a substrate temperature of 450°C, which is then increased to a given maximum value during the second and third stages.

Note that CIGS was co-evaporated on SLG/Mo substrates that did not include a diffusion barrier of Na. An additional supply of Na was provided to the absorber via the thermal evaporation of a NaF precursor layer on the Mo back contact, prior to CIGS co-evaporation.

A temperature of 450°C is applied to the substrate during the first stage. In the case of the standard co-evaporation process used at the Ångström Solar Center, the substrate temperature is increased to a maximum value of 550°C throughout the second and third stages. In this work, this maximum substrate temperature was also varied and decreased to lower values of 500°C and 450°C, in order to determine the impacts of the substrate temperature on the material properties of CIGS layers, in particular its GGI depth profile. Finally, the performances of complete ultrathin solar cells are compared with respect to the CIGS deposition temperature and thickness of the NaF precursor layer.

5.2.Material characterization of CIGS

In this chapter, three batches of CIGS layers are studied. For each batch, two CIGS films were co-evaporated in a modified 3-stage process with a distinct maximum substrate temperature. All CIGS layers were deposited on Mo back contacts, with NaF precursor layers with thicknesses of 8 or 15 nm. It is worth mentioning that NaF layers thicker than 15 nm were not tested, because they are not compatible with back contacts that act as a diffusion barrier for Na. Indeed, it is shown in Appendix B that 12 and 15 nm-thick NaF layers evaporated on a TCO-based reflective back contact lead to CIGS delamination during the CBD process for CdS deposition. The average thicknesses of these CIGS layers were measured with a profilometer, and their average composition was determined by XRF. These values are summarized in Table II. 1.

	NaF thickness (nm)	deposition temperature	CIGS thickness (nm)	CGI	GGI
Batch n°1 [180322]	15	550°C	650 ± 20	0.88 ± 0.02	0.46 ± 0.02
		450°C	640 ± 20	0.88 ± 0.01	0.46 ± 0.02
Batch n°2 [180410]	15	550°C	520 ± 20	0.87 ± 0.03	0.40 ± 0.02
		500°C	530 ± 20	0.91 ± 0.03	0.40 ± 0.02
Batch n°3 [180418]	8	550°C	540 ± 20	0.88 ± 0.03	0.40 ± 0.02
		500°C	510 ± 20	0.86 ± 0.03	0.40 ± 0.02

Table II. 1. Average thickness, CGI and GGI of CIGS layers co-evaporated on Mo for various maximum substrate temperatures and thicknesses of NaF precursor layers.

Figure II. 2 shows the SEM cross-section images of complete solar cells on Mo back contacts. The CIGS layers were co-evaporated within batch n°1 and n°2, at a maximum substrate temperature of (a,c) 550°C, (b) 450°C or (d) 500°C. NaF precursor layers with a thickness of 15 nm were evaporated on the Mo films, and solar cells were completed with a standard stack of CdS/*i*-ZnO/ZnO:Al. As observed, the CIGS thicknesses determined from these SEM images are in good agreement with the thicknesses measured with a profilometer.

CIGS layers co-evaporated at 550°C (Figure II. 2.a and c) exhibits rather large and columnar grains that extend from the back to the front interface. On the other hand, the observed grains are much smaller when CIGS is grown at 450°C (Figure II. 2.b). In the case of an intermediate deposition temperature of 500°C (Figure II. 2.d), large grains are still visible but some smaller grains appear at the CIGS back contact, which were attributed to Ga-rich phases by Kaufmann *et al.* [167]. In addition, the top surface of CIGS looks slightly rougher when it is deposited at lower temperatures. A similar temperature-dependence of the morphology of ultrathin CIGS films was also reported by Yin *et al.* [127].

Figure II. 3 shows the depth profiles of the CGI and GGI atomic ratios of ultrathin CIGS layers determined by GD-OES analysis. The characterized CIGS layers were prepared in batch n°1 and n°3, on Mo control samples without the deposition of NaF precursor layers. CIGS was co-evaporated at maximum substrate temperatures of 550°C, 500°C and 450°C.

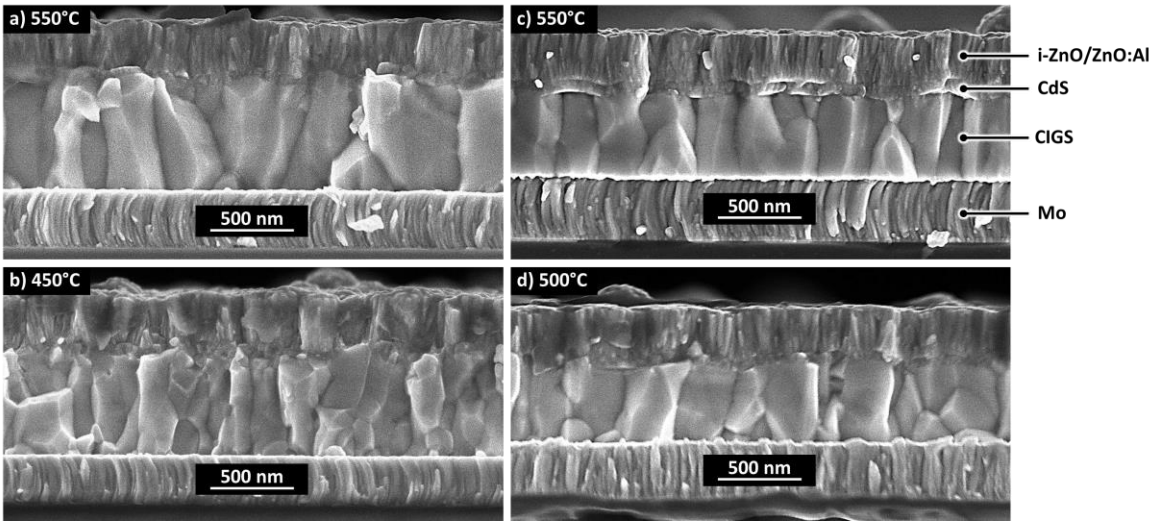

Figure II. 2. SEM cross-section images of complete CIGS solar cells fabricated on Mo back contacts with 15 nm-thick NaF precursor layers. CIGS was co-evaporated at (a) 550°C and (b) 450°C with thicknesses of 640 ± 20 nm (batch n°1), and at (c) 550°C and (d) 500°C with thicknesses of 500 ± 20 nm (batch n°2). (a) [180322-1B2], (b) [180322-2B2], (c) [180410-2A2], (d) [180410-3A2].

Regardless of the CIGS co-evaporation temperature, flat CGI profiles are detected in GD-OES. However, the GGI composition grading is dependent on the maximum substrate temperature: while linear GGI profiles are formed at 550°C, a stronger GGI back grading is created when CIGS is co-evaporated at 450°C (Figure II. 3.a). In contrast, the GGI depth profile formed at 500°C is only slightly steeper than the one obtained at 550°C (Figure II. 3.b). The increasing steepness of the GGI profiles with decreasing temperatures can be attributed to the inhibition of the In and Ga interdiffusion [29], [127], [167]. Similarly, Yin *et al.* [127] achieved a V-shaped GGI grading with a 3-stage process and a maximum substrate temperature of 440°C, instead of a flat GGI profile that was formed at 610°C.

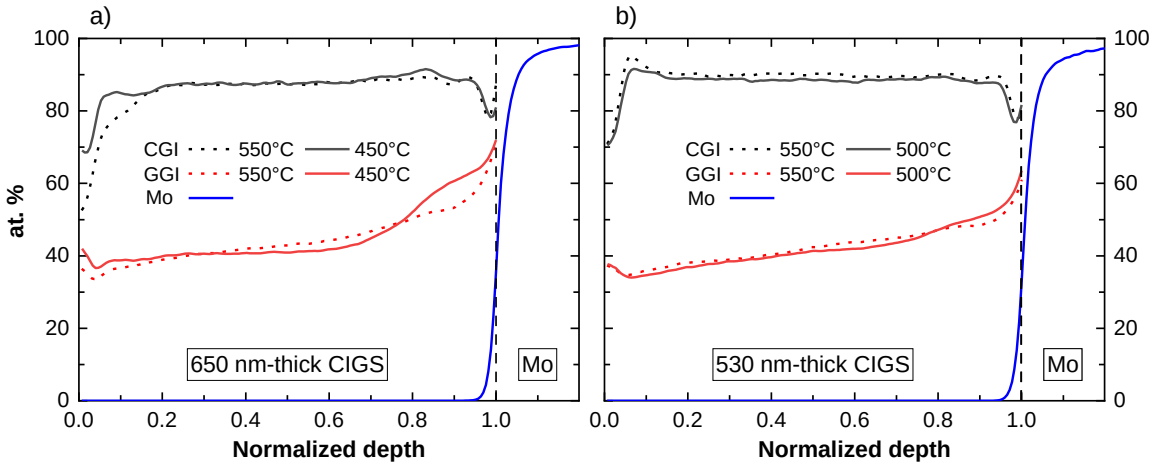

Figure II. 3. GD-OES composition profiles of Mo as well as CGI and GGI atomic ratios of ultrathin CIGS layers. CIGS was co-evaporated at (a,b) 550°C (dashed lines), as well as (a) 450°C and (b) 500°C (solid lines). The thickness of each CIGS layer was measured with a profilometer and the average CGI and GGI compositions were calibrated with XRF data. The CIGS/Mo interface is indicated by vertical dashed lines. (a) 550°C: [180322-1XA], 450°C: [180322-2XA]. (b) 550°C: [180418-2XB], 500°C: [180418-3XA].

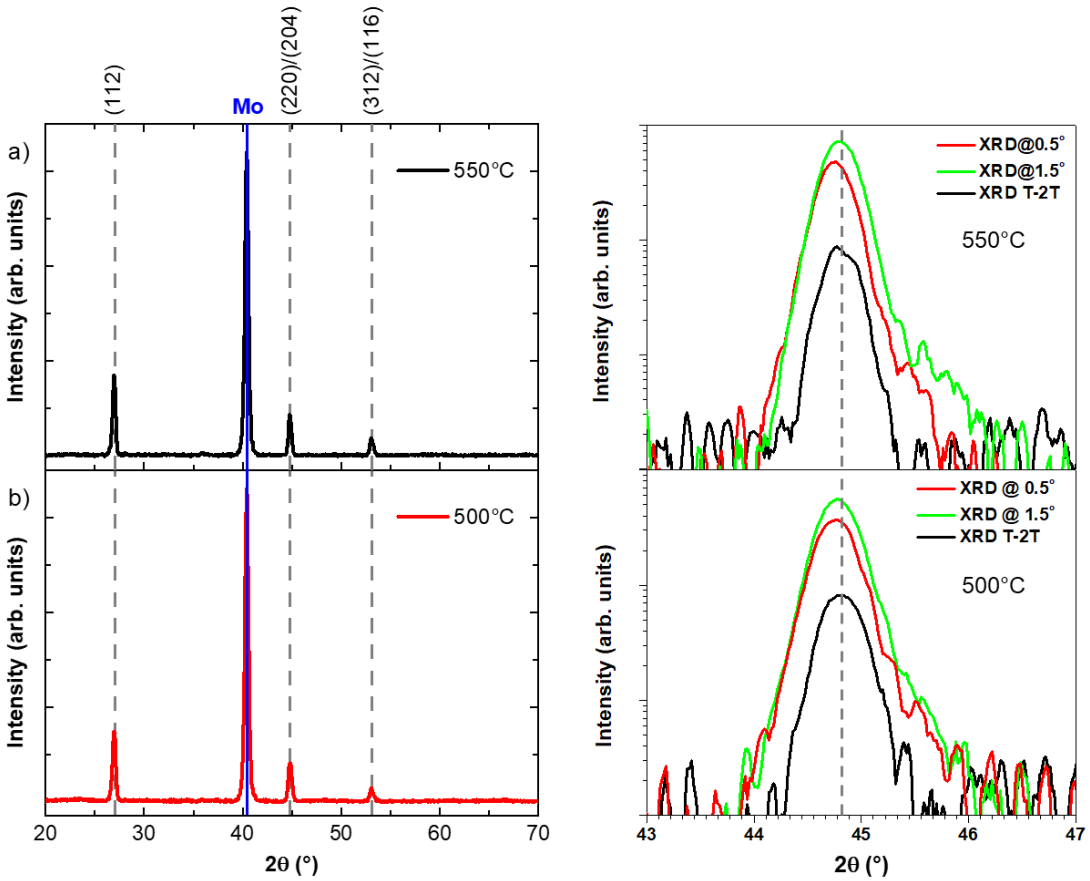

Figure II. 4. XRD measurements of ultrathin CIGS layers co-evaporated on Mo at (a) 550°C and (b) 500°C. Left panel shows the diffractograms in the Bragg-Brentano ($\theta - 2\theta$) configuration, and right panel compares the (220)/(204) reflection peak measured in XRD (black), and in GIXRD with incidence angles of 0.5° (red) and 1.5° (green). Dashed lines are added as a guide to the eye. [Samples from W.-C. Chen].

A steep GGI composition is expected to be beneficial to the performances of solar cells, as it creates a back surface field that repels electrons toward the heterojunction and passivates the rear interface of ultrathin CIGS absorbers [11], [13], [127]. It is worth mentioning that the GGI profile formed at 450°C is promising, as it is close to the optimal grading modeled by Mansfield *et al.* [11], *i.e.* a ΔGGI of at least 0.3 and a Ga-rich region that is located at the CIGS/Mo interface and is less than 150 nm-thick.

To further analyze the effects of the CIGS deposition temperature, XRD measurements were performed on ultrathin layers co-evaporated on Mo at 550°C and 500°C (see Figure II. 4). First, the diffractograms exhibit the reflection peaks of the CIGS chalcopyrite phase, in good agreement with the reflective indices of the $CuIn_{0.7}Ga_{0.3}Se_2$ compound (ICDD: 00-035-1102). The intense peak observed at $2\theta \approx 40.5$ is attributed to the Mo back contact (ICDD: 00-001-1207).

As In has a larger atomic radius than Ga, the positions of the CIGS diffraction peaks are shifted to smaller 2θ values when the In content increases [127]. Here, the peak positions of CIGS are almost identical regardless of the deposition temperature, which confirms that they have the same average GGI ratio. In addition, a strong GGI composition grading within the CIGS layer usually results in a doubling or shouldering

of the diffraction peaks, especially when Ga-rich phases are formed at the CIGS back contact [13], [124], [126], [127]. Despite the linear GGI gradings that were determined by GD-OES analysis (Figure II. 3), the diffractograms shown in Figure II. 4 exhibit single peaks for the (112) and (220)/(204) reflections, for both deposition temperatures of 550°C and 500°C. Besides, the position of the (220)/(204) orientation determined in the Bragg-Brentano configuration and in grazing incidence XRD (GIXRD) is almost unchanged, indicating a similar GGI composition of the CIGS bulk and front interface. A rather smooth GGI grading is thus expected within CIGS layers co-evaporated at 550°C and 500°C.

A full width at half maximum (FWHM) of 0.37° was measured for the (112) reflection peak of the CIGS layer deposited at 550°C. In comparison, a FWHM of 0.39° is found for a deposition temperature of 500°C. This suggests a similar crystallinity for ultrathin CIGS layers co-evaporated at 550°C and 500°C.

Complete solar cells with ultrathin CIGS layers co-evaporated on Mo at 550°C, 500°C and 450°C were then fabricated, and their performances were compared with respect to the material characterization results. To investigate the effects of Na incorporation, solar cells were also prepared at 550°C and 500°C with NaF precursor layer thicknesses of 8 nm and 15 nm.

5.3. Solar cell performances

Figure II. 5 shows the I(V) curves under one-sun illumination and in the dark for each best solar cell. 650 nm-thick CIGS layers were co-evaporated at substrate temperatures of 550°C and 450°C, with a 15 nm-thick NaF precursor layer. CIGS films with a thickness of ~500 nm were deposited at 550°C and 500°C, with a NaF layer thickness of either 15 nm or 8 nm. The SLG/Mo substrates did not include a sodium diffusion barrier. The average and best light I(V) parameters are summarized in Table II. 2. The dark I(V) parameters of best solar cells fitted with a 1-diode model are also shown in Table II. 3, together with the E_g values deduced from the linear fit of EQE^2 curves.

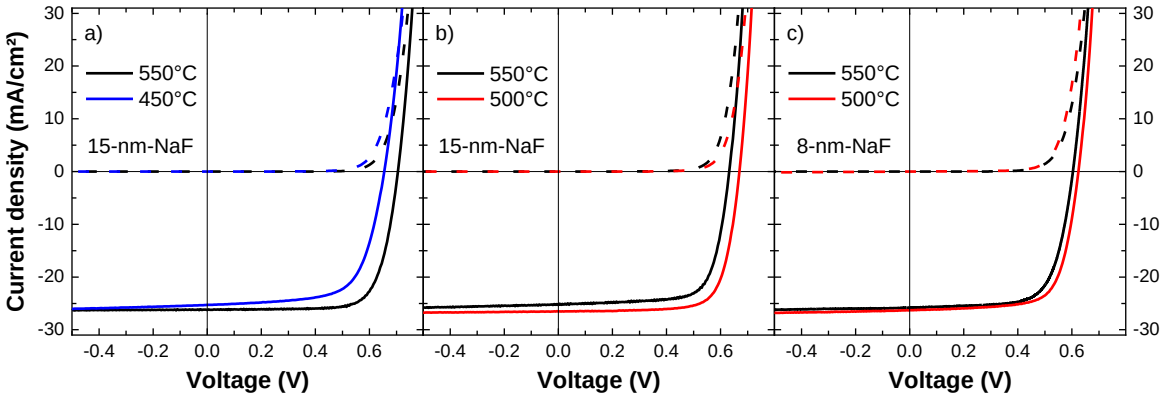

Figure II. 5. I(V) curves of best solar cells from batches (a) n°1, (b) n°2 and (c) n°3, under one-sun illumination (solid lines) and in the dark (dashed lines). CIGS was deposited on Mo at 550°C (black), 500°C (red) and 450°C (blue). A 15 nm-thick NaF precursor layer was evaporated on Mo in the case of batches n°1 and 2, while 8 nm of NaF were used for batch n°3. (a) 550°C: [180322-1B2_c8], 450°C: [180322-2B2_c13]. (b) 550°C: [180410-2A2_c12], 500°C: [180410-3A2_c13]. (c) 550°C: [180418-2A1_c4], 500°C: [180418-3A1_c1].

			Average / best cell light I(V) parameters			
Batch & NaF layer thickness	CIGS deposition temperature		Eff. (%)	J_{SC} (EQE) (mA/cm^2)	V_{OC} (mV)	*FF* (%)
n°1, 15-nm-NaF [180322-]	550°C	[-1B2]	13.8 ± 0.04 / 13.9	26.2	705 ± 1 / 706	74.9 ± 0.2 / 75.2
	450°C	[-2B2]	11.1 ± 0.1 / 11.3	25.3	653 ± 2 / 657	66.9 ± 0.9 / 67.7
n°2,15-nm-NaF [180410-]	550°C	[-2A2]	11.5 ± 0.2 / 11.7	25.2	629 ± 5 / 634	72.3 ± 0.7 / 73.5
	500°C	[-3A2]	12.6 ± 0.4 / 13.4	26.5	645 ±15 / 672	73.9 ± 0.9 / 75.3
n°3, 8-nm-NaF [180418-]	550°C	[-2A1]	10.7 ± 0.2 / 11.0	25.8	601 ± 4 / 608	69.1 ± 0.8 / 70.4
	500°C	[-3A1]	11.5 ± 0.2 / 11.8	26.3	619 ± 5 / 626	70.4 ± 0.9 / 71.7

Table II. 2. Summary of light IV parameters of ultrathin CIGS solar cells. CIGS was deposited on Mo at 550°C, 500°C and 450°C, with a NaF precursor layer thickness of 15 nm or 8 nm. Average values and standard deviation were calculated from the 10 best solar cells.

Reducing the co-evaporation temperature from 550°C to 450°C leads to a decrease of the average efficiency from 13.8 ± 0.04 % to 11.1 ± 0.1 %, which is mostly due to a drop of the V_{OC} and *FF*, respectively from 705 ± 1 mV to 653 ± 2 mV and from 74.9 ± 0.2 % to 66.9 ± 0.9 %. The reduction of the V_{OC} is correlated to an increase of the J_0 and *n* fitted for the best cell deposited at 450°C. This indicates that a higher amount of non-radiative recombination occurs in CIGS layers prepared at 450°C. The decrease of the *FF* at 450°C is not linked to the R_{SH} and R_S of complete solar cells, as they are similar to the ones fitted for a deposition temperature of 550°C. On the other hand, a voltage-dependent photocurrent is observed when comparing the slopes of the light and dark I(V) curves in the voltage range from –0.5 V to +0.5V (Figure II. 5.a). This reveals that the performances of cells fabricated at 450°C suffer from significant collection losses.

The lower collection efficiency of devices prepared at 450°C is also confirmed by their EQE curves, see Figure II. 6.a. First, co-evaporating CIGS at 450°C instead of 550°C leads to a lower EQE, especially for wavelengths between 700 nm and 950 nm. Besides, the ratio of the EQE measured at short-circuit condition and at a bias of –0.5 V, *i.e.* $EQE(0V)/EQE(-0.5V)$, is close to 1 over the whole wavelength range when CIGS is deposited at 550°C. This means that a suitable collection efficiency is achieved, because the photocurrent is independent of the voltage and thus of the SCR width. In contrast, for wavelengths above 600 nm an EQE ratio of ~0.9 is found for CIGS layers prepared at 450°C. This indicates an imperfect collection of charges generated in the CIGS bulk, as the collection efficiency depends on the width of the SCR that drifts charges at the *p*-*n* junction. Finally, an E_g of ~1.23 eV was determined from the linear fit of EQE^2 curves.

Despite the promising GGI back grading that was determined by GD-OES (Figure II. 3.a), solar cells with a 650 nm-thick CIGS layer co-evaporated at 450°C exhibit collection losses as well as a lower V_{OC} and *FF* as compared to cells with a linear GGI grading formed at 550°C. Hence, the beneficial passivation effect related to the GGI composition grading and the subsequent back surface field is not observed. Based on the morphology of CIGS films deposited at 450°C, the lower performance could be a result of a poorer material quality and other possible effects like a modification of the Na depth profile, which can all affect the voltage deficit and performances of CIGS solar cells [168], [169]. As a consequence, an intermediate deposition temperature of 500°C was also investigated.

530 nm-thick CIGS layers deposited at 500°C with a 15 nm-thick NaF precursor layer result in an average efficiency of 12.6 ± 0.4 %, which is 1.1 % absolute more than at 550°C. This increase is related to an improvement of each light I(V) parameter. A remarkable best efficiency of 13.4% is achieved at 500°C, with a J_{SC} of 26.5 mA/cm², a V_{OC} of 672 mV and a *FF* of 75.3%. In comparison, a best efficiency of 11.7% is measured for a deposition temperature of 550°C. A slight improvement of the best cell's fitted J_0 is observed when CIGS is deposited at 500°C rather than 550°C, and both solar cells exhibit satisfactory R_{SH} and R_S values that allow for a high *FF*.

The collection efficiency is improved at 500°C as compared to 550°C, as indicated by a photocurrent that is less dependent on the applied bias under one-sun illumination (Figure II. 5.b) and an EQE that is enhanced for wavelengths between 550 nm and 1000 nm (Figure II. 6.b). The reduced voltage-dependence of the photocurrent accounts for the increase of the best *FF* from 73.5% to 75.3%, while the improved collection efficiency in the infrared region results in an improvement of the J_{SC} from 25.2 mA/cm² to 26.5 mA/cm². In addition, both solar cells exhibit a ratio of $EQE(0V)/EQE(-0.5V)$ that is close to 1 for wavelengths from 500 nm to 1050 nm. This confirms the adequate collection efficiency of ultrathin solar cells with CIGS layers co-evaporated at 550°C and 500°C. For these CIGS layers from batch n°2, E_g values of ~1.20 eV were determined from the linear fitting of EQE². This is ~0.03 eV lower than the E_g of CIGS from batch n°1, due to a lower average GGI.

		Dark I(V) parameters of best cells				EQE² fit
Batch & NaF layer thickness	CIGS deposition temperature	J_0 (mA/cm²)	n	R_{SH} (Ω.cm²)	R_S (Ω.cm²)	E_g (eV)
n°1, 15-nm-NaF [180322-]	550°C [-1B2_c8]	3.10^{-6}	1.8	> 8.10^5	< 0.1	1.23
	450°C [-2B2_c13]	3.10^{-5}	2	4.10^5	< 0.1	1.23
n°2,15-nm-NaF [180410-]	550°C [-2A2_c12]	5.10^{-5}	2	3.10^5	< 0.1	1.20
	500°C [-3A2_c13]	3.10^{-5}	2	7.10^5	< 0.1	1.20
n°3, 8-nm-NaF [180418-]	550°C [-2A1_c4]	8.10^{-5}	2	> 1.10^6	< 0.1	1.19
	500°C [-3A1_c1]	9.10^{-5}	2	3.10^3	< 0.1	1.19

Table II. 3. Dark I(V) parameters of each best solar cell, fitted with a 1-diode model (J_0: saturation currents, n: ideality factor, R_{SH}: shunt resistance, R_S: series resistance), as well as E_g values determined from a linear fit of EQE².

Contrary to solar cells with a CIGS layer deposited at 450°C, using a deposition temperature of 500°C instead of 550°C results in improved cell performances. The J_{SC} and *FF* improvements are related to a better collection efficiency, which can be attributed to the slightly steeper GGI grading that is formed at 500°C. This composition grading also contributes to the CIGS rear passivation and leads to an increase of the best cell V_{OC}, from 634 mV at 550°C to 672 mV at 500°C. In particular, it seems that the material properties of the CIGS layer are not degraded when it is co-evaporated at 500°C. To investigate the effects of Na incorporation in ultrathin CIGS layers with optimized deposition temperatures, solar cells with a thinner NaF precursor layer of 8 nm were also fabricated at 550°C and 500°C.

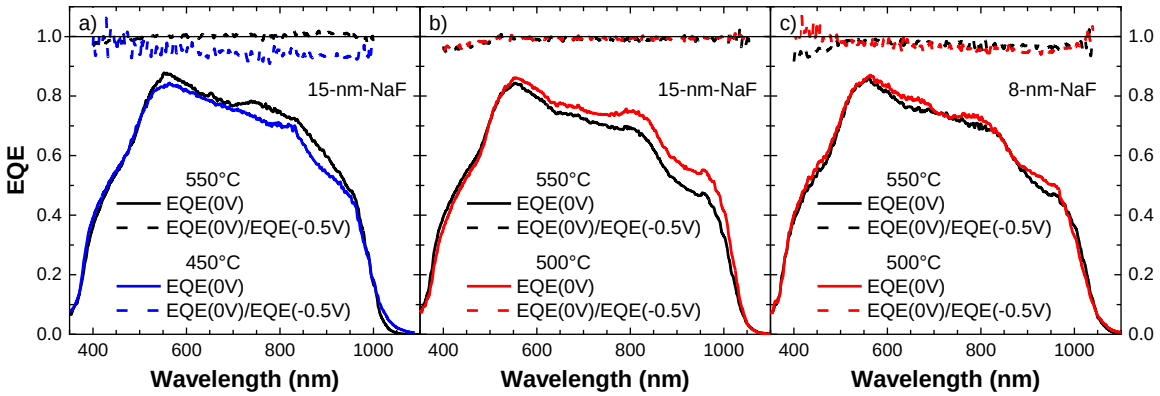

Figure II. 6. EQE (solid lines) of solar cells from batches (a) n°1, (b) n°2 and (c) n°3. CIGS was co-evaporated on Mo at 550°C (black), 500°C (red) and 450°C (blue). For each cell, dashed lines represent the ratios of EQE(0V)/EQE(-0.5V). A 15 nm-thick NaF precursor layer was deposited on Mo in the case of batches n°1 and 2, while 8 nm of NaF were used for batch n°3. (a) 550°C: [180322-1B2_c13], 450°C: [180322-2B2_c16]. (b) 550°C: [180410-2A2_c16], 500°C: [180410-3A2_c13]. (c) 550°C: [180418-2A1_c4], 500°C: [180418-3A1_c1].

For both deposition temperatures of 550°C and 500°C, decreasing the thickness of the NaF precursor layer from 15 nm to 8 nm results in a degradation of photovoltaic performances: at 550°C the efficiency is decreased from 11.5 ± 0.2 % to 10.7 ± 0.2 %, and from 12.6 ± 0.4 % to 11.5 ± 0.2 % at 500°C. The lower efficiencies are related to smaller average V_{OC} and *FF* values. Consistently with the measured V_{OC} decrease, a higher J_0 is fitted for cells with 8 nm of NaF, suggesting an increased amount of non-radiative recombination. This could be due to an insufficient passivation of the In_{Cu}^{2+} donor defect by Na, also resulting in a lower doping concentration.

Regardless of the CIGS deposition temperature, the lower *FF* values of cells with 8 nm of NaF are related to a voltage-dependent photocurrent collection rather than a degradation of the R_{SH} and R_S (Figure II. 5.c). Besides, the ratio of EQE is slightly below unity in the case of a thinner NaF layer (Figure II. 6.c). These two phenomena indicate a deterioration of the collection efficiency when the NaF layer is thinned from 15 nm to 8 nm. The fitted EQE^2 indicate E_g values of ~1.19 eV for CIGS layers from batch n°3, close to the E_g for batch n°2 which has a similar GGI ratio of ~0.40.

Decreasing the CIGS deposition temperature from 550°C to 500°C also improves the performances of cells prepared with 8 nm of NaF. However, it is worth mentioning that the beneficial effect of the GGI grading formed at 500°C is less pronounced than when using a 15 nm-thick NaF layer: the increase of the V_{OC} and *FF* (Table II. 2) as well as the enhancement of the EQE are reduced (Figure II. 6.c). Hence, the impacts of the somewhat steeper GGI grading might be compensated by the lower collection efficiency of cells with an 8 nm-thick precursor layer of NaF. Note that the thickness of the NaF film might have additional effects on the morphology and crystallinity of the CIGS layer [57], but they were not investigated here.

To conclude, this study of ultrathin CIGS layers co-evaporated on Mo indicates that optimal photovoltaic performances are achieved for a deposition temperature of 500°C and a 15 nm-thick NaF precursor layer. This is thanks to the slightly steeper GGI back grading and possibly to the preservation of the CIGS material properties at 500°C.

5.4.Conclusion of the chapter

The co-evaporation of ultrathin CIGS layers with graded GGI compositions was investigated on standard Mo back contacts. A modified 3-stage process was used, with a higher Ga rate and lower In rate to intentionally create a GGI grading. Three different maximum substrate temperatures were applied during the CIGS co-evaporation process: 550°C, 500°C and 450°C. Their impacts on the morphology, composition depth profile and crystallinity of CIGS films were analyzed. Complete solar cells were fabricated for each CIGS deposition temperature with 15 nm-thick NaF precursor layers, and their performances were compared. The effects of a thinner NaF layer of 8 nm were also investigated for cells with CIGS films co-evaporated at 550°C and 500°C. The main findings of this study are summarized below:

- At 550°C, the morphology of CIGS layers observed in SEM shows large grains and a smooth front interface. In contrast, small grains appear at the CIGS back interface when it is deposited at 500°C. The grain size is further reduced at 450°C, and a rougher CIGS/CdS interface is also formed.
- GD-OES measurements reveal that a linear GGI grading is created at 550°C. The GGI back grading is slightly steeper at 500°C, and much stronger at 450°C. On the other hand, XRD diffractograms indicate that CIGS layers deposited at 550°C and 500°C have a quite homogeneous composition, as Ga-rich and In-rich phases were not distinguished in XRD.
- Co-evaporating CIGS at 450°C rather than 550°C leads to lower cell performances due to a deteriorated collection of carriers. This could be due to the degradation of the material quality of CIGS films deposited at 450°C and/or other detrimental effects like the distribution of Na.
- The average and best light I(V) parameters of solar cells are improved when decreasing the CIGS deposition temperature from 550°C to 500°C. It was attributed to the slightly steeper GGI grading that contributes to the passivation of the rear CIGS interface. An efficiency of 13.4% was achieved for the best ultrathin cell fabricated at 500°C with 15 nm of NaF.
- For cells prepared at 550°C and 500°C, using 8 nm-thick NaF precursor layers instead of 15 nm led to lower cell performances. The thinner NaF film resulted in collection losses that could be due to an insufficient incorporation of Na in the CIGS layer.

All in all, it was shown that a steeper GGI back grading can improve the V_{OC} of ultrathin CIGS solar cells, but the experimental V_{OC} values remain quite low. As ACIGS solar cells with a standard absorber thickness were reported to exhibit promising efficiencies and lower voltage deficits, [84], [89], ultrathin ACIGS solar cells were also fabricated in this study. The corresponding results are reported in the next chapter.

Chapter 6. Optimization of ACIGS deposition on Mo back contacts

6.1. Introduction and experimental details

In order to improve the material properties of the ultrathin absorber as well as the V_{OC} of complete cells, Ag was added to the CIGS layer as it was shown to reduce the amount of structural disorder [86], [87] and to lower the voltage deficit of complete cells [84], [88], [89].

The elemental rates used to co-evaporate ultrathin ACIGS layers are presented in Figure II. 7. The co-evaporation process of ACIGS is similar to the one of CIGS, except that Ag is evaporated proportionally to Cu. As a consequence, the Cu rate is adjusted to achieve the targeted [I]/[III] elemental ratio. At the beginning of the first stage, a higher Ga rate and a lower In rate are applied in order to form a linear GGI depth profile in the ACIGS layer.

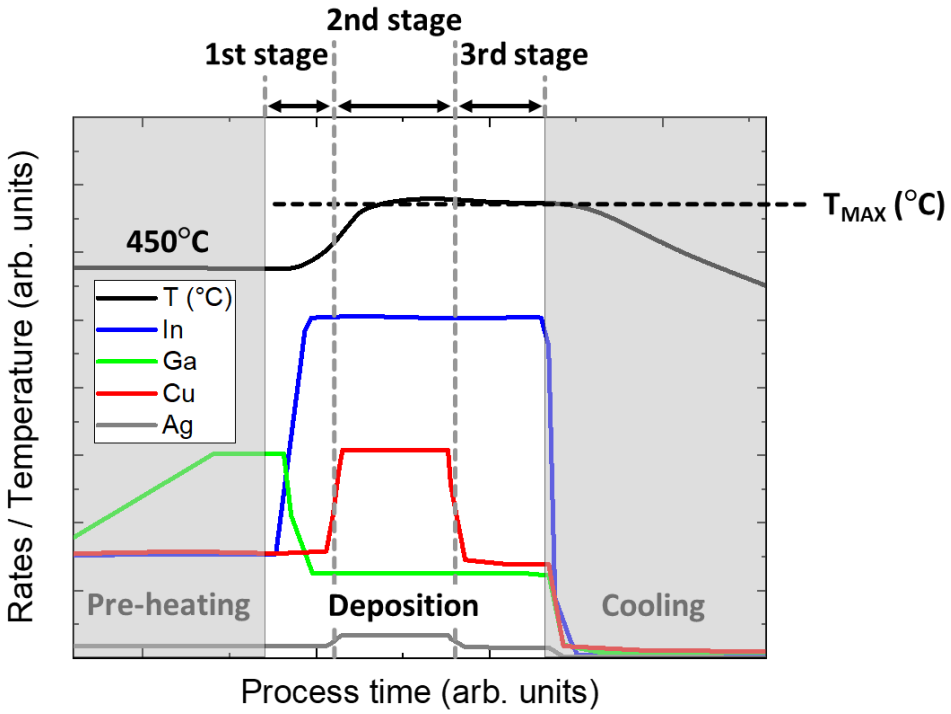

Figure II. 7. Schematic representation of the modified 3-stage processes used for the co-evaporation of ultrathin ACIGS absorbers.

The substrate temperature is set to 450°C during the first stage of the co-evaporation process. In the case of the standard co-evaporation process used at the Ångström Solar Center, the substrate temperature is increased to a maximum value of 550°C throughout the second and third stages. In the following, ACIGS layers deposited with a maximum substrate temperature of 500°C were also studied, in order to investigate the effects of the substrate temperature on the ACIGS layer properties and composition grading. ACIGS films were co-evaporated on SLG/Mo substrates without any diffusion barrier of Na. Finally, complete cells were fabricated and their performances were compared.

6.2.Material characterization

The ACIGS layers analyzed in this section are gathered in two distinct batches of solar cells. The first batch of ACIGS was prepared with a 15 nm-thick NaF precursor layer, while the second one includes an 8 nm-thick NaF film. For each batch, ACIGS layers were co-evaporated on Mo at maximum substrate temperatures of 550°C and 500°C.

Table II. 4 gives an overview of the thickness and average atomic ratios of the studied ACIGS layers, which were measured with a profilometer and by XRF, respectively. All ACIGS layers exhibit a thickness that is close to 500 nm.

A small proportion of Ag is incorporated in these ACIGS layers, as the ratio of [Ag]/([Ag]+[Cu]) or [Ag]/[I] is of ~10%. This means that the ACIGS layers have a silver composition of only ~2 at.%. For each ACIGS film, a quite low ratio of ([Ag]+[Cu])/([Ga]+[In]) or [I]/[III] was determined in XRF, but these values might be underestimated because the XRF calibration was performed on a thick ACIGS reference.

	NaF thickness (nm)	deposition temperature	ACIGS thickness (nm)	[Ag]/[I]	[I]/[III]	GGI
Batch n°1	15	550°C	500 ± 20	0.09 ± 0.01	0.73 ± 0.00	0.39 ± 0.02
		500°C	500 ± 20	0.10 ± 0.01	0.74 ± 0.01	0.42 ± 0.03
Batch n°2	8	550°C	540 ± 20	0.10 ± 0.01	0.78 ± 0.01	0.39 ± 0.02
		500°C	510 ± 20	0.10 ± 0.01	0.79 ± 0.00	0.38 ± 0.02

Table II. 4. Average thickness, [Ag]/[I], [I]/[III] and GGI atomic ratios of ACIGS layers co-evaporated on Mo for various maximum substrate temperatures and thicknesses of NaF precursor layers. Batch n°1, 550°C: [181105-2], 500°C: [181031-2]. Batch n°2, 550°C: [181120-2], 500°C: [181120-3].

Figure II. 8 shows the SEM cross-section and top-view images of ultrathin ACIGS layers deposited in batch n°2, with maximum substrate temperatures of 550°C and 500°C. The back contact consists of Mo layers from control samples that were not covered with a NaF precursor layer. Average ACIGS thicknesses of 530 ± 10 nm were determined in cross-section SEM, in good agreement with the values measured with a profilometer (Table II. 4).

The ACIGS layer co-evaporated at 550°C (Figure II. 8.a) exhibits large and columnar grains that extend from the back to the front interface. In contrast, the ACIGS film deposited at 500°C (Figure II. 8.b) shows smaller grains and a much rougher front interface, as can be seen also on the top-view SEM images (Figure II. 8.c and d).

The composition depth profiles of ultrathin ACIGS layers co-evaporated in batch n°2 are shown in Figure II. 9. Note that the Mo back contacts of the samples analyzed in GD-OES do not include NaF precursor layers, which might affect the interdiffusion of In and Ga and the resulting GGI grading.

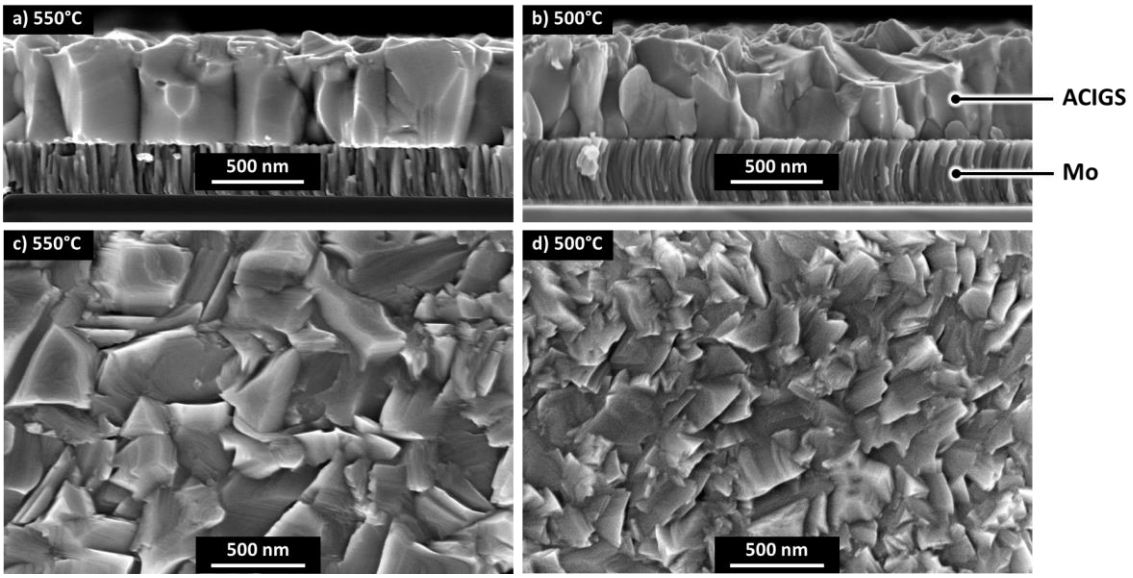

Figure II. 8. SEM cross-section and top-view images of ultrathin ACIGS layers co-evaporated in batch n°2. ACIGS was deposited on Mo back contacts at maximum substrate temperatures of (a,c) 550°C and (b,d) 500°C. Average ACIGS thicknesses of 530 ± 10 nm were determined from cross-section images. (a,c) [181120-2XB], (b,d) [181120-3XB].

For both deposition temperatures of 550°C and 500°C, the atomic ratios of [Ag]/[I] and [I]/[III] detected in GD-OES are rather flat, indicating a homogeneous composition of Cu and Ag. The GGI ratio of ACIGS layer is also found to be quite flat, and only slightly increases from the front to the back interfaces. In addition, reducing the ACIGS deposition temperature to 500°C has almost no effects on the GGI depth profile, which is consistent with previous studies that reported an enhanced diffusion of Ga in thick ACIGS layers co-evaporated at a maximum substrate temperature of 450°C [85].

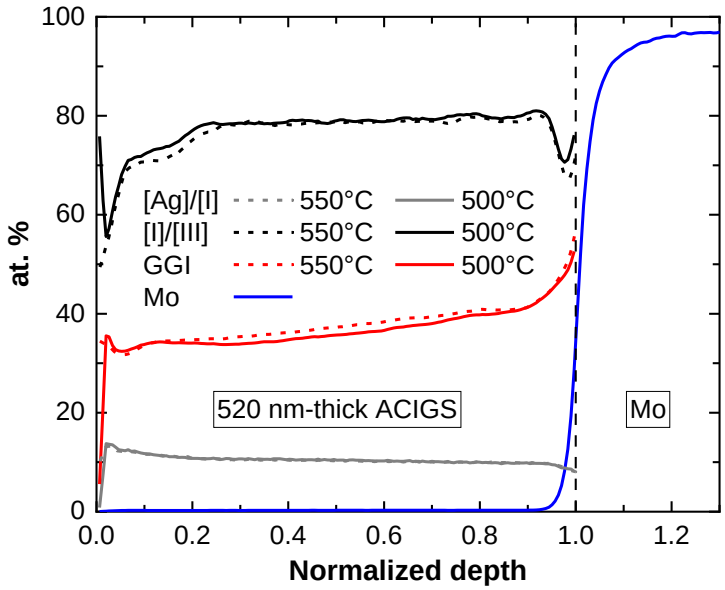

Figure II. 9. GD-OES composition profiles of Mo as well as [Ag]/[I], [I]/[III] and GGI atomic ratios of ultrathin ACIGS layers. ACIGS was co-evaporated at 550°C (dashed lines) and 500°C (solid lines) in batch n°2. The thickness of ACIGS layers was measured with a profilometer, and their average atomic ratios were calibrated with XRF data. The ACIGS/Mo interface is indicated by a vertical dashed line. 550°C: [181120-2XA], 500°C: [181120-3XA].

ACIGS layers co-evaporated on Mo back contacts at 550°C and 500°C were also analyzed in XRD (Figure II. 10). As expected, the diffraction peaks related to the ACIGS chalcopyrite phase (CIGS, ICDD: 00-035-1102) and to the back contact (Mo, ICDD: 00-001-1207) are observed.

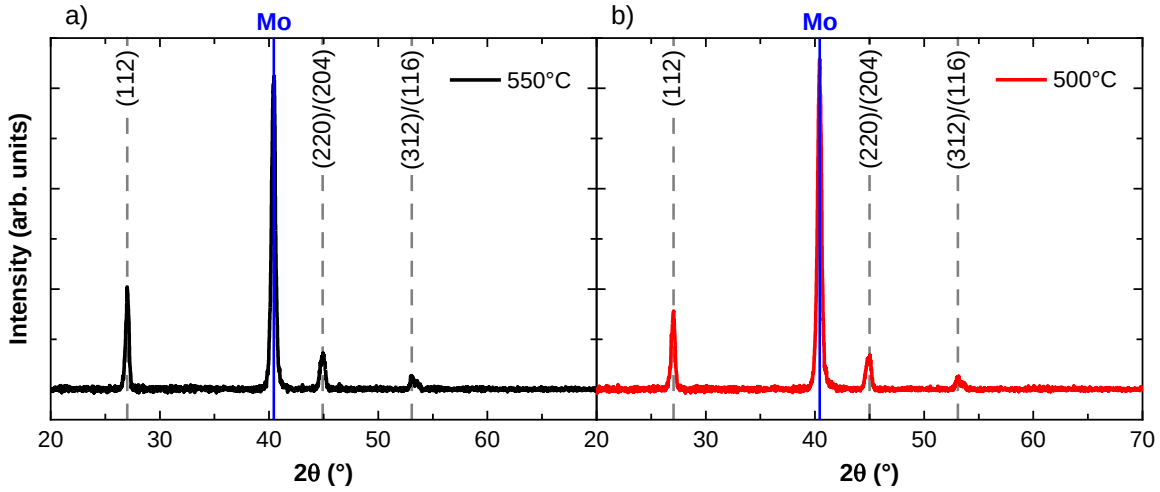

Figure II. 10. XRD measurements of ultrathin ACIGS layers co-evaporated on Mo at (a) 550°C and (b) 500°C. [Samples from W.-C. Chen].

For ACIGS layers deposited at 550°C and 500°C, FWHM of 0.37° and 0.42° were respectively determined for the preferred (112) orientation. These similar FWHM values suggest that reducing the deposition temperature from 550°C to 500°C does not strongly degrades the crystallinity of ACIGS. Regardless of the co-evaporation temperature, the ACIGS diffraction peaks have almost identical 2θ positions in XRD and GIXRD (not shown), indicating rather flat GGI depth profiles.

In comparison to ultrathin CIGS it is found that ACIGS layers deposited at 500°C exhibit rougher grains in cross-section SEM, despite the fact that Ag was reported to facilitate the growth of large grains at 450°C [85]. Contrary to the case of CIGS, the GGI grading obtained when reducing the deposition temperature from 550°C to 500°C is not steeper, because of the enhanced diffusion of Ga [85]. Hence, ACIGS layers co-evaporated at 500°C are not expected to benefit from a stronger back surface field and its subsequent effect of rear passivation. Finally, a similar crystallinity of CIGS and ACIGS layers is deduced from XRD data, as the (112) diffraction peaks exhibit comparable values of FHWM.

Complete solar cells with ultrathin ACIGS layers co-evaporated at 550°C and 500°C were fabricated. In the following section, the photovoltaic performances of these cells are discussed, based on the material characterizations of ACIGS films.

6.3.Solar cell performances: 550/500°C (8 and 15 nm NaF)

Figure II. 11 shows the light and dark I(V) curves of best ACIGS solar cells fabricated on a Mo back contact with 8 or 15 nm of a NaF precursor layer. In each case, ACIGS was co-evaporated at maximum substrate temperatures of 550°C and 500°C. The average and best I(V) parameters are also summarized in Table II. 5.

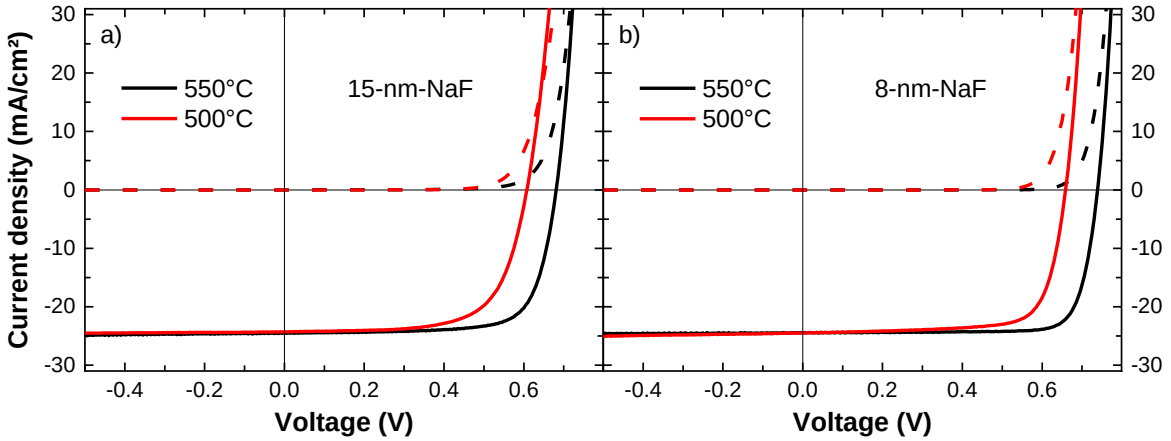

Figure II. 11. I(V) curves of best ACIGS solar cells under one-sun illumination (solid lines) and in the dark (dashed lines). ACIGS layers were co-evaporated at 550°C (black) and 500°C (red), on Mo back contacts with (a) a 15 nm-thick NaF precursor layer (batch n°1) or (b) an 8 nm-thick NaF film (batch n°2). (a) 550°C: [181105-2B1_c5], 500°C: [181031-2B1_c1]. (b) 550°C: [181120-2A2_c10], 500°C: [181120-3A2_c4].

For a deposition temperature of 550°C ACIGS solar cells prepared with a 15 nm-thick NaF layer exhibit an average efficiency of 11.3 ± 0.6 %, while cells including an 8 nm-thick NaF precursor layer show a remarkable average efficiency of 14.6 ± 0.2 %. Decreasing the co-evaporation temperature to 500°C results in lower average efficiencies of 9.7 ± 0.2 % and 11.3 ± 0.4 %, for NaF thicknesses of 15 and 8 nm, respectively. The observed variations of the average efficiencies are related to changes in the average V_{OC} and *FF* of complete cells, as the J_{SC} is not affected by the ACIGS deposition temperature nor by the NaF thickness.

Regardless of the NaF thickness, co-evaporating ACIGS at 500°C instead of 550°C leads to lower V_{OC} and *FF* values. In the case of a 15 nm-thick NaF layer, the average V_{OC} and *FF* are respectively decreased from 669 ± 12 mV to 603 ± 8 mV and from 69.2 ± 2.9 % to 66.0 ± 1.8 %. With 8 nm of NaF, the average V_{OC} and *FF* drop from 736 ± 7 mV to 639 ± 10 mV and from 80.8 ± 0.8 % to 71 ± 1.8 %, respectively.

		Average / best cell light I(V) parameters			
Batch & NaF layer thickness	ACIGS deposition temperature	Eff. (%)	J_{SC} (EQE) (mA/cm^2)	V_{OC} (mV)	*FF* (%)
n°1, 15-nm-NaF	550°C [181105-2B1]	11.3 ± 0.6 / 12.6	24.5	669 ± 12 / 684	69.2 ± 2.9 / 75.0
	500°C [181031-2B1]	9.7 ± 0.2 / 10.1	24.3	603 ± 8 / 610	66.0 ± 1.8 / 67.8
n°2, 8-nm-NaF	550°C [181120-2A2]	14.6 ± 0.2 / 14.9	24.5	736 ± 7 / 741	80.8 ± 0.8 / 81.8
	500°C [181120-3A2]	11.3 ± 0.4 / 12.2	24.5	639 ± 10 / 660	71.9 ± 1.8 / 75.5

Table II. 5. Summary of light IV parameters of ultrathin ACIGS solar cells. ACIGS was deposited on Mo at 550°C and 500°C, with a NaF precursor layer thickness of 15 nm or 8 nm. Average values and standard deviation were calculated from the 10 best solar cells.

To analyze the evolution of the V_{OC} and *FF* with respect to the NaF thickness and co-evaporation temperature, the dark I(V) curves of best solar cells were fitted with a 1-diode model (Table II. 6). As outstanding values are obtained in the case of an ultrathin ACIGS layer deposited at 550°C with an 8 nm-thick NaF film, Figure II. 12 also provides

the experimental and fitted dark I(V) curves in a lin-log scale, together with the contribution of the fitted diode and R_{SH}. Some measurement artefacts/noise are observed for current densities < 2.10^{-4} mA/cm², which prevents an accurate determination of the R_{SH}. Still, the experimental and fitted curves show a satisfactory agreement. However, it is worth mentioning that the measured and fitted dark curves of the best ACIGS cell prepared at 550°C with 15 nm of NaF (Figure II. 12.a) exhibit a discrepancy at low forward bias. Hence, the fitted values of J_0 and n fitted in this case should not be over-interpreted.

		Best cell dark I(V) parameters				EQE² fit
Batch & NaF layer thickness	CIGS deposition temperature	J_0 (mA/cm²)	n	R_{SH} (Ω.cm²)	R_S (Ω.cm²)	E_g (eV)
n°1, 15-nm-NaF	550°C *	5.10^{-7}	1.5	5.10^{4}	< 0.1	1.25
	500°C	4.10^{-5}	2	> 6.10^{5}	0.3	1.26
n°2, 8-nm-NaF	550°C	2.10^{-10}	1.1	> 1.10^{6}	< 0.1	1.25
	500°C	1.10^{-8}	1.2	6.10^{5}	< 0.1	1.25

Table II. 6. Dark I(V) parameters of each best solar cell, fitted with a 1-diode model (J_0: saturation currents, n: ideality factor, R_{SH}: shunt resistance, R_S: series resistance). *Experimental dark I(V) curve is not accurately fitted with a 1-diode model. The E_g value of each best cell was also determined from a linear fit of EQE². [see Figure II. 12 below].

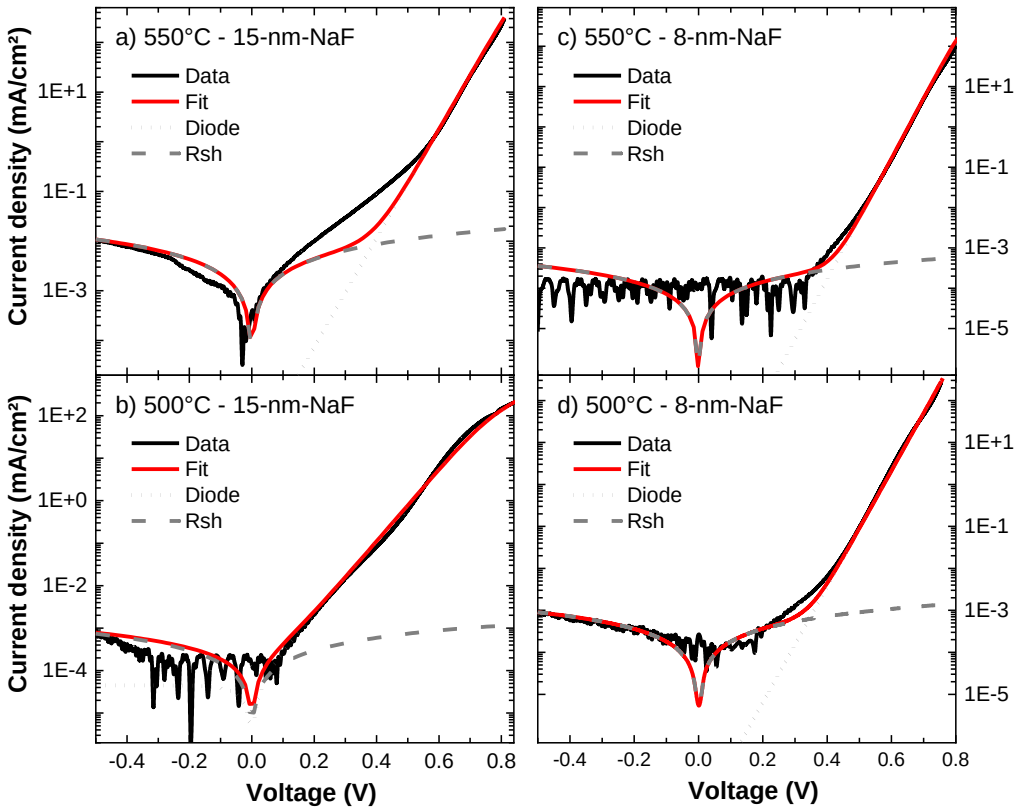

Figure II. 12. Experimental dark I(V) characteristics of best ACIGS solar cells (black lines) and associated curves fitted with a 1-diode model (red lines), from (a,b) batch n°1 and (c,d) batch n°2. The contribution of the dark saturation current density (J_0, dotted lines) and of the shunt resistance (R_{SH}, dashed lines) are also shown. (a) [181105-2B1_c5], (c) [181031-2B1_c1], (c) [181120-2A2_c10], (d) [181120-3A2_c4].

For both thicknesses of NaF, this V_{OC} decrease is correlated to an increase of both the J_0 and ideality factor n, as indicated by the values fitted from the dark I(V) curves of the best solar cells (Table II. 6). This indicates a higher amount of recombination in ACIGS layers deposited at 500°C, which could be related to a degraded material quality of the absorber in addition to the absence of a stronger back surface field, due to a linear GGI composition grading that is similar for co-evaporation temperatures of 550°C and 500°C.

Independently of the NaF thickness, best solar cells with ACIGS absorbers deposited at 550°C and 500°C exhibit similar and satisfactory values of R_{SH} and R_S fitted with a 1-diode model. However, lower FF are measured at 500°C because of a voltage-dependent photocurrent (Figure II. 11). This means that a better collection efficiency is achieved when ACIGS is co-evaporated at 550°C. Again, this is correlated to the smaller grains and rougher front interface observed in SEM when ACIGS is deposited at 500°C, but other effects might be responsible for the observed efficiency trends.

For both deposition temperatures, using 8 nm of NaF instead of 15 nm improves the average V_{OC} and FF of complete cells. Consistently, lower J_0 values are fitted from the dark I(V) curves of the best solar cells. The ideality factor n is also much lower and close to 1 in the case of an 8 nm-thick NaF layer, indicating reduced carrier recombination in the space charge region. The quality of the heterojunction is thus improved.

Finally, the EQE curves of each best solar cell were measured (Figure II. 13). Regardless of both the ACIGS deposition temperature and NaF thickness, best cells exhibit very similar EQE curves and J_{SC} values of ~24.5 mA/cm². The ratios of $EQE(0V)/EQE(-0.5V)$ are also almost identical and close to 1. Hence, the EQE curves do not evidence significant collection losses in those cells, despite the voltage-dependent photocurrent shown by the I(V) curves of the best cells prepared at 500°C (Figure II. 11). E_g values of ~1.25 eV were determined from a linear fit of the EQE² of the best cells (see also Table II. 6).

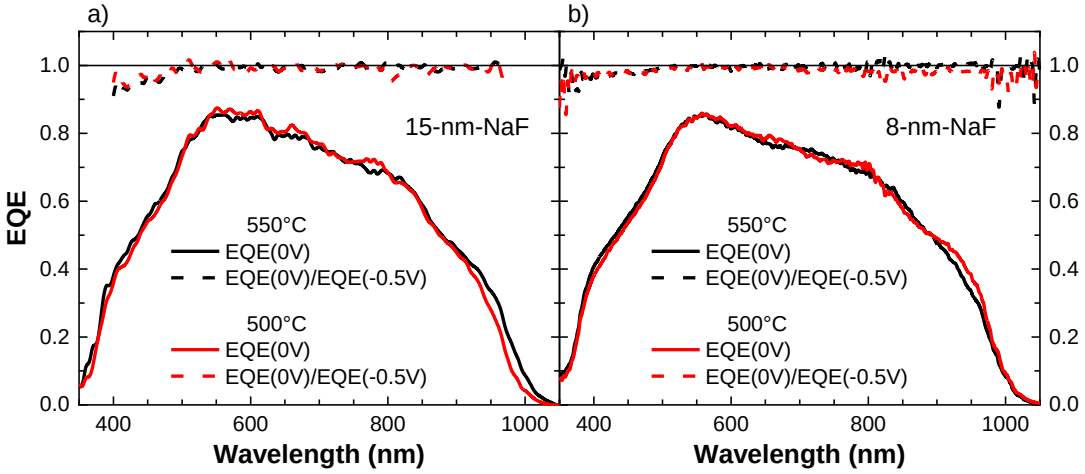

Figure II. 13. EQE (solid lines) of best solar cells with (a) a 15 nm-thick NaF precursor layer (batch n°1) and (b) an 8 nm-thick NaF film (batch n°2). ACIGS was co-evaporated on Mo at 550°C (black) and 500°C (red). For each cell, the ratios of EQE(0V)/EQE(-0.5V) are also shown (dashed lines). (a) 550°C: [181105-2B1_c5], 500°C: [181031-2B1_c1]. (b) 550°C: [181120-2A2-c10], 500°C: [181120-3A2_c4].

Contrary to the case of ultrathin CIGS layers, the co-evaporation of ultrathin ACIGS at 550°C leads to better photovoltaic performances than at 500°C. This difference can be explained by the fact that decreasing the deposition temperature absorber leads to a steeper GGI grading only in the case of CIGS. Hence, ACIGS solar cells fabricated at 500°C do not benefit from a passivating back surface field. Interestingly, the NaF layer was thinner for the best ACIGS solar cell than for the best CIGS device, which could indicate a better quality of the ACIGS bulk with less In_{Cu}^{2+} substitution defects.

Nevertheless, a best efficiency of 14.9% was achieved with an ultrathin ACIGS absorber deposited at 550°C with an 8 nm-thick NaF precursor layer, with a V_{OC} of 741 mV, a *FF* of 81.8% and a J_{SC} of 24.5 mA/cm². In comparison, the best ultrathin CIGS solar cells prepared at 500°C reached an efficiency of 13.4%, a V_{OC} of 672 mV, a *FF* of 75.3% and a J_{SC} of 26.5 mA/cm². A smaller J_{SC} value is obtained in the case of the best ACIGS cell, which is related to the incorporation of Ag that leads to a slightly higher bandgap value of ~1.25 eV. In comparison, the E_g of the best CIGS device is of ~1.20 eV, using a similar GGI ratio of ~0.40. This results in a stronger absorption of infrared photons in CIGS devices.

Despite this J_{SC} loss, a better efficiency is obtained for the ACIGS absorber thanks to the improvement of the V_{OC} and *FF*. This can be attributed to a better materials quality and a lower amount of recombination, as indicated by lower values of the J_0 and n fitted from the dark I(V) curve for the best ACIGS cell. In particular, the voltage deficit W_{OC}, as defined by $W_{oc} = E_g/q - V_{OC}$, is decreased from ~529 mV for the best CIGS cell to ~505 mV for the best ACIGS device.

All in all, the efficiency of ultrathin CIGS-based solar cells on Mo back contacts was successfully improved by incorporating Ag in the absorber. An ACIGS co-evaporation temperature of 550°C and an 8 nm-thick NaF precursor layer were found to be the best deposition conditions.

6.4.Conclusion of the chapter

To sum up, ultrathin ACIGS solar cells were co-evaporated at 550°C and 500°C on Mo back contacts. Structural and compositional characterizations were performed, and complete solar cells were then fabricated with a NaF precursor layer that was either 15 nm or 8 nm-thick. The main findings are summarized below:

- SEM images show that decreasing the deposition temperature of ACIGS leads to smaller ACIGS grains and a rough interface.
- A GD-OES analysis shows that similar GGI gradings are formed in ACIGS layers co-evaporated at 550°C and 500°C.
- As a result, the performances of complete cells are degraded when ACIGS is deposited at 500°C rather than 550°C. This could be due to a poorer material quality of ACIGS layers co-evaporated at 500°C.
- A remarkable best efficiency of 14.9% is reached for an ultrathin ACIGS cell fabricated at 550°C on a SLG/Mo substrate, and with a NaF precursor layer of 8 nm.
- The photovoltaic performance of ultrathin ACIGS devices is improved as compared to CIGS solar cells, thanks to a reduced voltage deficit and an increased *FF*.

Despite a strong enhancement of the best cell efficiency from 13.4% in the case of CIGS to 14.9% with an ACIGS absorber, it was not possible to create a steep GGI grading in ACIGS layers. Hence, the efficiency improvement achieved with ACIGS devices is rather attributed to a better bulk quality than to a rear passivation effect due to the presence of a back surface field. In addition, a strong degradation of the morphology of CIGS and ACIGS absorbers was observed to be correlated with lower cell performances. In order to further investigate the effects of the deposition temperature on the absorber properties and quality, a cathodoluminescence study was performed on samples with stacks of SLG/Mo/CIGS/CdS and SLG/Mo/ACIGS/CdS prepared at 550°C and 500°C.

Chapter 7. Cathodoluminescence study of ultrathin CIGS & ACIGS layers on Mo

7.1.Introduction

A cathodoluminescence (CL) tool was used to characterize the luminescence of CIGS and ACIGS layers upon excitation by an electron beam. It can notably provide luminescence data at the nanometer scale, with the possibility to distinguish grain boundaries for example [78], [170], [171]. Besides, fitting the luminescence spectra with the generalized Planck law can give further information like the E_g value, and the Urbach energy can be determined from the sub-bandgap luminescence. The CL setup was operated by Thomas Bidaud, PhD student and Joya Zeitouny, postdoctoral researcher. It was performed on the absorbers of complete solar cells with Mo back contacts. These cells were chosen from the samples that exhibited the best average efficiencies: the CIGS cells were fabricated at a co-evaporation temperature of 550°C and 500°C with a NaF precursor layer thickness of 15 nm (CIGS batch n°2), and the ACIGS cells were prepared at 550°C and 500°C with 8 nm of NaF (ACIGS batch n°2). Each of these samples were split to analyze a single solar cell that is representative of the sample performances: the I(V) parameters of the solar cells selected for CL characterization are given in Table II. 7, where they can be compared to the average I(V) values of each respective sample.

		Light I(V) parameters of cells investigated in CL / average values			
	deposition temperature	Eff. (%)	J_{SC} (EQE) (mA/cm^2)	V_{OC} (mV)	FF (%)
CIGS	550°C (a)	11.5 /11.5 ± 0.2	25.2	628 / 629 ± 5	72.5 / 72.3 ± 0.7
	500°C (b)	12.7 / 12.6 ± 0.4	26.5	646 / 645 ± 15	74.1 / 73.9 ± 0.9
ACIGS	550°C (c)	14.4 / 14.6 ± 0.2	24.5	727 / 736 ± 7	81.0 / 80.8 ± 0.8
	500°C (d)	11.2 / 11.3 ± 0.4	24.5	631 / 639 ± 10	72.6 / 71.9 ± 1.8

Table II. 7. Summary of the light I(V) parameters of the CIGS and ACIGS solar cells characterized in CL, together with the average and standard deviation values calculated from the 10 best solar cells of each respective sample. (a) [180410-2A2_c7], (b) [180410-3A2_c6], (c) [181120-2A2_c1], (d) [181120-3A2_c15].

Before the top-view characterization in CL, the i-ZnO/ZnO:Al front contact stack was removed to avoid its parasitic absorption of electrons. To do so, the complete solar cells were dipped for 2 minutes in an aqueous solution containing HCl at a concentration of 0.05 mol/L. This wet etching step completely dissolved the ZnO-based layer in a selective way, because the etching rate of CdS is much slower at this concentration in HCl. As a result, the sample stacks studied in CL consist of: SLG/Mo/(A)CIGS/CdS.

These choice and preparation of samples allow to study the effects of the co-evaporation temperature and Ag incorporation on the luminescence behavior of the absorbers. Interestingly, it also enables a comparison of the CL results with the photovoltaic performances of complete devices.

The CL setup is first briefly described to provide an overview of this characterization tool. To provide a better understanding of the CL results, the interactions of the electron beam with the characterized stacks were simulated with the CASINO software. The experimental CL data of each sample are then discussed and compared with regards to the performances of complete solar cells.

7.2.Cathodoluminescence setup

This CL study was conducted with the *Attolight Allalin 4027 Chronos* quantitative cathodoluminescence microscope [172]. A schematic representation of this tool is provided in Figure II. 14. The CL setup consists of an electronic and an optical part, with a sample stage that is compatible with a helium cryostat to perform CL measurements at low temperature.

A Schottky thermal field emission gun is used as an electron source, with a ZrO-coated tungsten tip. The direct heating of the electron gun provides a continuous emission of electrons. The electron beam is directed and focused thanks to electromagnetic lenses, namely the gun and objective lenses. Eventually, the spot size of the electron beam on the sample is about 10 nm, and SEM images of the sample can be obtained.

An achromatic reflective objective with a numerical aperture of 0.72 is used to collect the light emitted by the sample. It allows a field of view up to 200 µm with a constant and high collection efficiency, as 40% of the photons emitted by a Lambertian source exit the microscope. The collected light is focused on the entrance slit of a *Horiba iHR320* spectrometer (with an optical magnification factor M = 13) and dispersed by a reflective diffraction grating. The correct CL spectra are obtained by dividing the raw data with the spectral responses of the grating and of the detector. In this study, CL spectra measured at room temperature (300K) were acquired with an Andor Newton silicon CCD camera, while an InGaAs array was used to record CL spectra at a low substrate holder temperature of 20K.

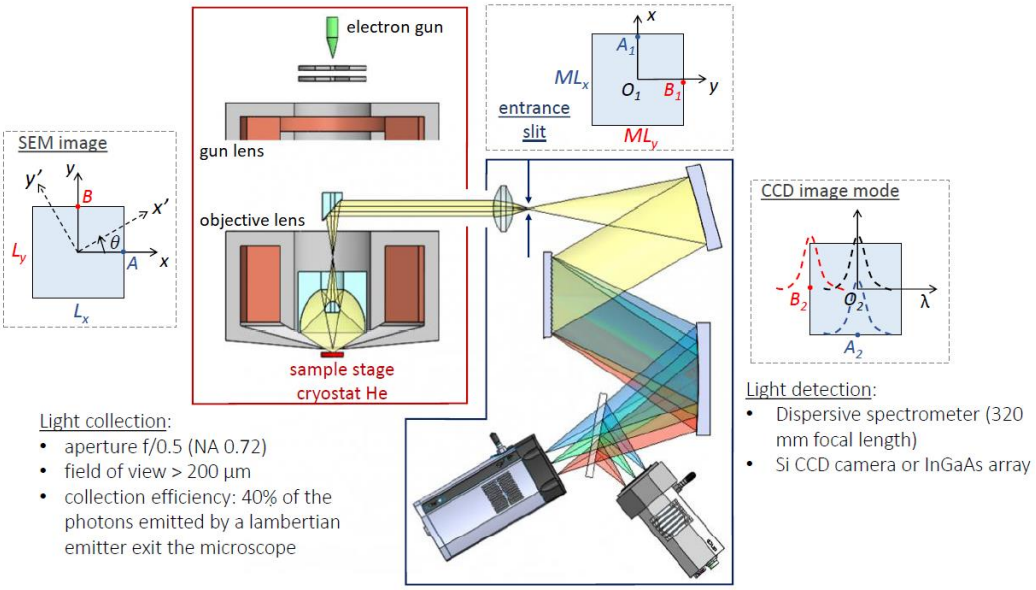

Figure II. 14. Schematics of the cathodoluminescence tool designed by Attolight. The CL system consists of an electron microscope (red frame) and of a spectrometer (blue frame). Dashed frames indicate the respective orientation of the sample image, of the secondary image at the entrance slit and of the final image at the detector. Inspired from [159], [172].

This CL setup allows the electron beam to scan the selected region of the sample surface, and then to record a luminescence spectrum in each position of the electron beam, which corresponds to one pixel in the final CL map. Hence, the resulting luminescence data depend on the interaction volume of electrons with the sample, which is why electron trajectories inside the investigated samples were first simulated.

7.3.Monte-Carlo simulation of electron trajectories in solids (CASINO)

The electron-matter interactions were simulated with the CASINO v2.42 software, see [173] for more information. The program performs a simulation of the complete electron trajectories under normal incidence, considering flat layers and interfaces. The program assesses the distance between successive collisions depending on the material density, as well as the atomic fraction and cross-section of each element. The energy losses between collisions are evaluated based on the atomic number and mean ionization potential of elements. These calculation steps are repeated until the electron energy is below 50 eV, or until the electron is back-scattered.

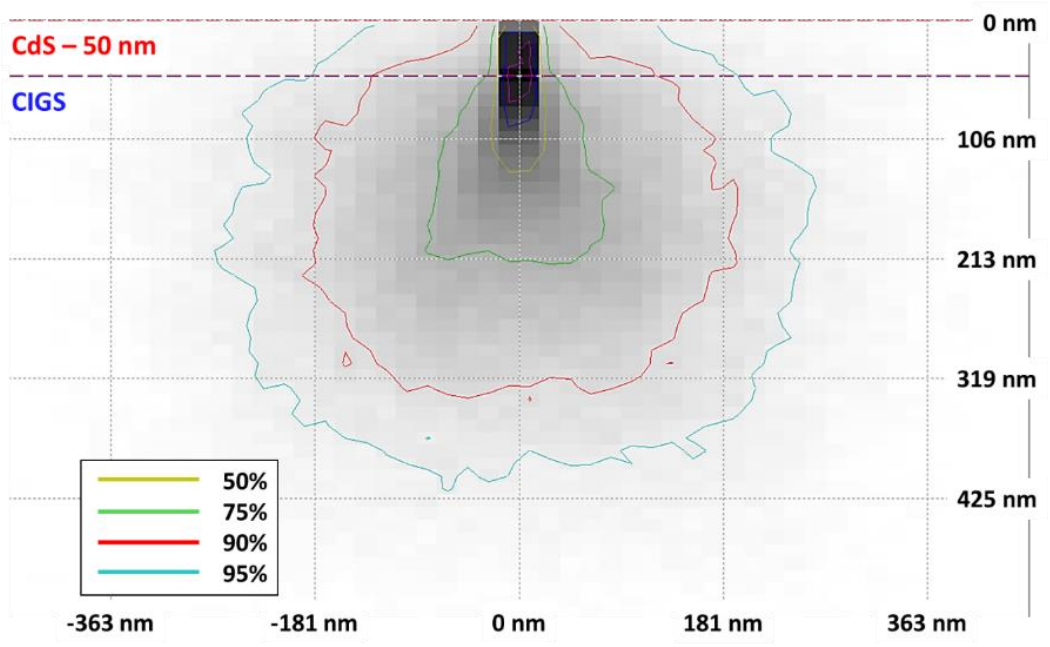

Figure II. 15. Distribution of the dissipated energy, projected on a plane that is perpendicular to the surface of the sample. Each contour plot indicates a region corresponding to a given percentage of the total dissipated energy.

The electron trajectories in the CdS/CIGS layers were simulated using an electron-beam energy of 10 keV and diameter of 10 nm. Considering a top-view CL analysis, Figure II. 15 shows a 2D projection of the corresponding absorbed or dissipated energy along the depth of the sample. The color contour plots indicate the regions where a given percentage of the total energy is dissipated. The CdS layer is shown to be thin enough to allow electrons to penetrate in the CIGS absorber, but these electrons do not reach the CIGS/Mo back contact. Hence, the CL study performed here only probes the front interface and the bulk of the absorbers, and it is not possible to assess the rear passivation effect due to the graded GGI depth profiles. An acceleration

voltage higher than 10 kV could allow to probe the absorber back interface, but 10 kV is the maximum setpoint value for the CL tool used in this work.

The experimental CL results are described in the following section.

7.4.Experimental results

The four samples were mounted on the same substrate holder, then analyzed in CL with an acceleration voltage of 10 kV. The light collection efficiency and the excitation source were kept constant during the experiments, allowing a fair comparison of the luminescence data from each sample. However, note that the investigated samples were not fabricated together. For example, variations of the CdS layer thickness can affect the intensity of the CL signal. The CL data recorded at room temperature are first reported, then the CL results at a nominal substrate holder temperature of 20K are discussed.

7.4.1. Room temperature CL experiment

Figure II. 16 shows the spatially averaged CL spectra of each sample, measured at room temperature. The corresponding peak intensity and peak energy are listed in Table II. 8 together with the fitted values of the Urbach energy E_U. These E_U values describe the sub-bandgap luminescence of our polycrystalline absorbers that arises from structural disorder and defects state [174]–[176]. In the so-called Urbach tail region, the sub-bandgap luminescence is empirically proportional to $exp([E - E_g]/E_U)$, where E_U characterizes the distribution of the bandtail states. A high E_U value indicate a high density of shallow defect states, while a low E_U suggests a reduced structural disorder, and was shown to correlate with improved V_{OC} values in the case of perovskite solar cells [177]. Here, the E_U values were determined from a fit over the linear region below the peak energy of each semi-log CL spectrum.

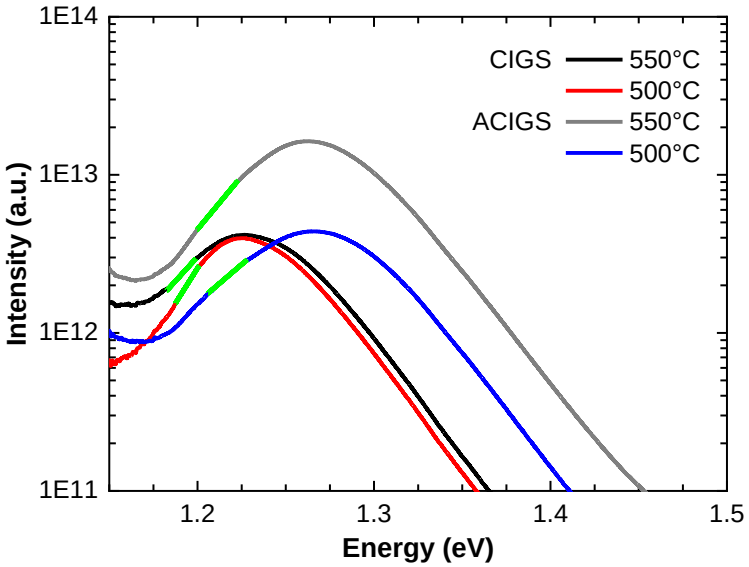

Figure II. 16. Semi-log CL spectra of each sample, measured at room temperature and averaged over the whole 14 × 14 µm² area scanned by the electron beam. For each spectrum, green lines show the linear fit of the Urbach energy E_U. [see Table II. 7].

First, the CL spectra exhibit a higher peak energy (E_{peak}) for the ultrathin ACIGS absorbers (Figure II. 16), which was expected as the E_g of ACIGS is higher than the one of CIGS. In addition, the ACIGS sample co-evaporated at 550°C shows the highest CL intensity. Assuming similar CdS layers for each samples, this indicates that ACIGS absorbers deposited at 550°C have less non-radiative recombination centers. Consistently, for this ACIGS solar cell a lowest W_{OC} of 536 mV was calculated using $E_{peak} - V_{OC}$, considering in a first approximation that $E_g \approx E_{peak}$, instead of W_{OC} = 635 mV for the ACIGS sample co-evaporated at 500°C. In comparison, W_{OC} = 597 mV and 579 mV were calculated for the CIGS samples prepared at 550°C and 500°C, respectively. Note that back contact recombination cannot be assessed in this study, but might also affect the W_{OC} of samples.

	deposition temperature	Peak intensity (normalized)	Peak energy (eV)	E_U (meV)	$E_{peak} - V_{OC}$ (mV)
CIGS	550°C	0.26	1.225	35	597
	500°C	0.24	1.225	24	579
ACIGS	550°C	1	1.263	32	536
	500°C	0.27	1.266	45	635

Table II. 8. Summary of the CL parameters extracted from the spatially averaged CL spectra at room temperature. [see Table II. 7].

In addition, the E_U values fitted from the CIGS and ACIGS spectra show opposite trends: the lower CIGS deposition temperature led to a lower E_U while the higher ACIGS co-evaporation temperature resulted in a lower E_U. This means that the density of bandtail states is decreased in CIGS layers deposited at 500°C, but increased in ACIGS films co-evaporated at 500°C. This correlates well with the observed trends in the V_{OC}, W_{OC} and efficiency of complete cells, as well as the degradation of the absorber's morphology. Note that many other parameters can influence the properties of the absorbers, like the distribution of Na at the grain boundaries in particular.

It was previously suggested that incorporating Ag in CIGS could reduce the structural disorder and the intra-grain defects density of thin films thanks to a lower melting temperature [86], [87]. However, in this study it was found that decreasing the substrate temperature is detrimental to the ACIGS material quality, contrary to the case of CIGS. Nevertheless, it is likely that the ACIGS co-evaporation process at 500°C could be improved, for example by varying the deposition time, the 2nd stage duration and/or the rates of In and Ga to create an adequate GGI grading. For example, flexible CIGS solar cells with high efficiencies were achieved at low substrate temperatures (≤ 450°C) by optimizing the CIGS co-evaporation recipe [29], [62].

To provide more insights on the absorber properties, the CL spectra and mappings recorded at low temperature were also analyzed for each sample and are described in the next section.

7.4.2. Low temperature CL experiment

First, the spatially averaged CL spectra measured at a nominal holder temperature of 20K are given in Figure II. 17, for each of the investigated samples. Similarly to the spectra recorded at room temperature, the peak energy of the ACIGS samples is higher than those of the CIGS due to the higher E_g of ACIGS absorbers. The ACIGS layer co-evaporated at 550°C also yielded the highest CL intensity, and the peak intensity and E_U of these spectra exhibited similar trends at low and room temperatures.

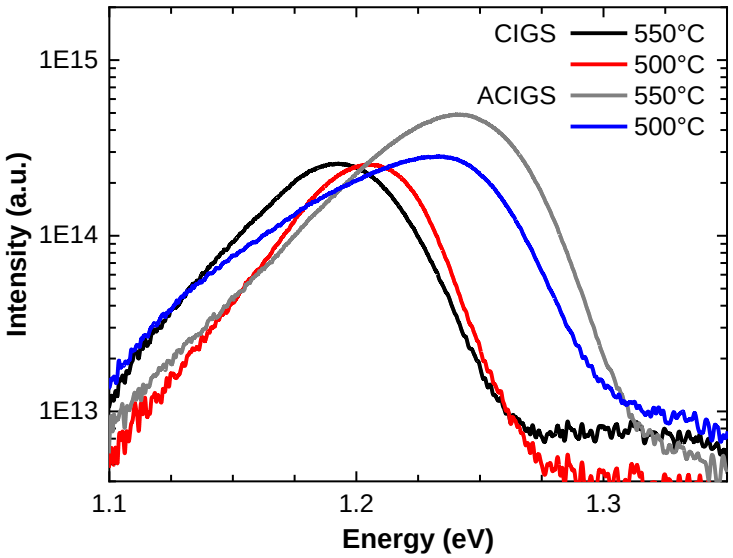

Figure II. 17. CL spectra of each sample, measured at a nominal holder temperature of 20K and averaged over the whole 9 × 9 µm² area scanned by the electron beam. [see Table II. 7].

To provide some information on the homogeneity of the samples at the micrometric scale, the maps of the integrated intensity, peak energy and FWHM over the 9 × 9 µm² area scanned in CL are shown in Figure II. 18 and Figure II. 19 for CIGS and ACIGS samples, respectively. In addition, the normalized integrated intensity, as well as the average and standard deviation values of the peak energy and FWHM are reported in Table II. 9.

The homogeneity of the integrated CL intensity is found to be similar for both CIGS deposition temperatures (Figure II. 18), but the CIGS layer co-evaporated at 550°C exhibits slightly higher intensity values than the one deposited at 500°C (Table II. 9). Contrary to other studies on CIGS and CdTe absorbers [78], [170], it is not possible to distinguish the grain boundaries of our CIGS layers. This is most likely due to the roughness of the investigated samples, which were not polished prior to this CL analysis. Hence, the spatial resolution of this CL study is likely to be limited by topographic artefacts that prevent the observation of grain boundaries.

Regardless of the CIGS deposition temperature, it is found that the regions with a high peak energy tend to correspond to regions with a low FWHM (Figure II. 18). Still, similar peak energy and FHWM values are observed, with an average peak energy of 1 202 ± 4 meV and FWHM of 53 ± 4 meV for the CIGS sample prepared at 500°C, as compared to 1 190 ± 4 meV and 58 ± 4 meV for the CIGS layer co-evaporated at 550°C.

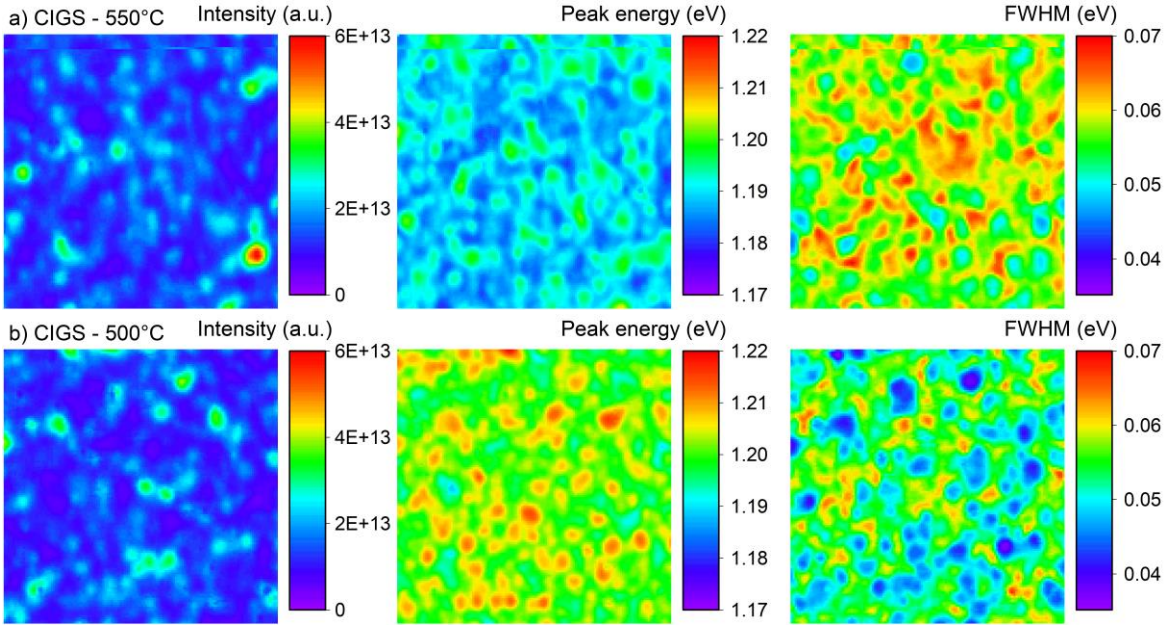

Figure II. 18. Maps of the integrated intensity, peak energy and FWHM of the CL signal measured on CIGS samples co-evaporated at (a) 550°C and (b) 500°C. The nominal temperature of the sample holder was set to 20K. [see Table II. 7].

All in all, the CIGS layers studied in CL led to comparable values of integrated intensity, peak energy and FWHM. This suggests that reducing the CIGS co-evaporation temperature from 550°C to 500°C does not strongly degrade the CIGS materials quality, as indicated by its luminescence behavior. The voltage deficit W_{OC} of CIGS solar cells is improved as the CIGS deposition temperature is decreased from 550°C to 500°C (Table II. 9). This can be attributed to the preserved quality of the CIGS absorber, while the steeper GGI back grading formed at 500°C contributes to the CIGS rear passivation. Note that in the case of the co-evaporation temperature of 500°C, the V_{OC} of complete CIGS cells exhibited a high dispersion, which is why the W_{OC} deduced from the CL data of a representative cell is ~30mV higher than the W_{OC} calculated with the E_g fitted from the best cell EQE.

	deposition temperature	Integrated intensity (normalized)	Peak energy (meV)	FWHM (meV)	W_{OC}, CL (mV)	W_{OC}, EQE (mV)
CIGS	550°C	0.49	1 190 ± 4	58 ± 4	562	566
	500°C	0.43	1 202 ± 4	53 ± 4	556	529
ACIGS	550°C	1	1 236 ± 6	67 ± 4	509	505
	500°C	0.72	1 220 ± 7	79 ± 7	589	587

Table II. 9. Summary of the CL data for each sample, extracted from the spectra of each pixel in the CL map. The voltage deficits W_{OC} were also determined by subtracting either the CL peak energy (W_{OC}, CL) or the E_g fitted from the best cell EQE (W_{OC}, EQE) with the V_{OC} of the corresponding cell. [see Table II. 7].

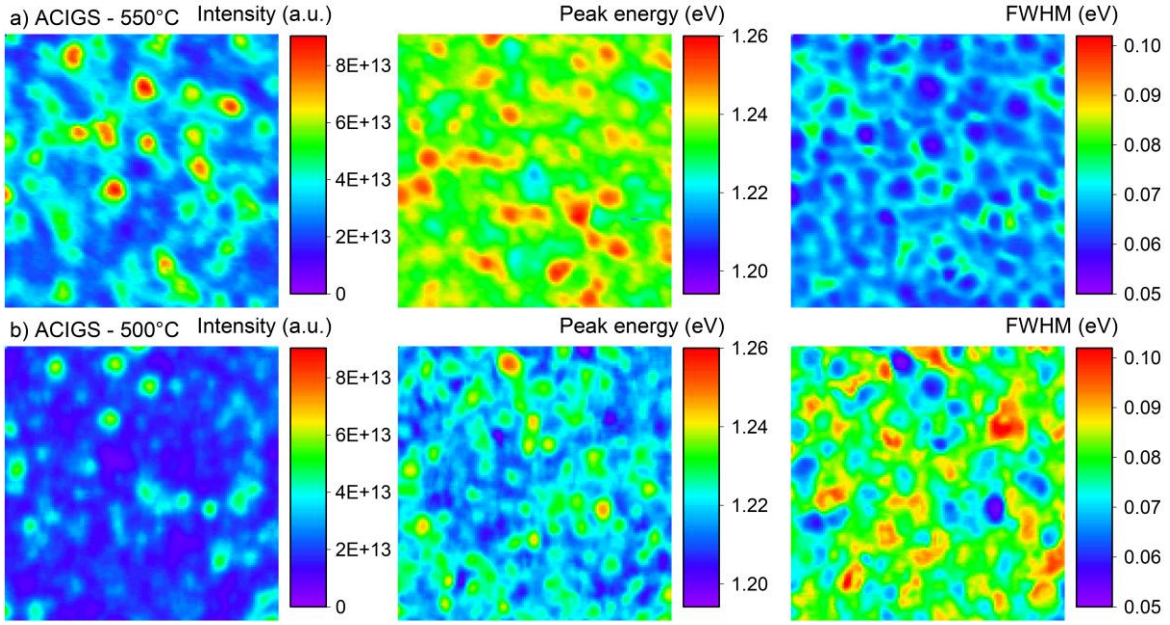

Figure II. 19. Maps of the integrated intensity, peak energy and FWHM of the CL signal measured on ACIGS samples co-evaporated at (a) 550°C and (b) 500°C. The nominal temperature of the sample holder was set to 20K. [see Table II. 7].

For ACIGS absorbers, significantly higher values of integrated intensity and peak energy were measured for a deposition temperature of 550°C. Similarly to the case of CIGS, the regions with a high peak energy generally exhibit a low FWHM, regardless of the ACIGS deposition temperature. However, in the ACIGS case the FWHM of the spectra measured for a co-evaporation temperature of 500°C shows higher average and standard deviation values than for a temperature of 550°C. This suggests an increased structural disorder with more fluctuations when ACIGS is deposited at 500°C. Hence, CL results indicate that a poorer materials quality is achieved when the ACIGS co-evaporation temperature is lowered from 550°C to 500°C.

As the GGI grading in ACIGS layer is not steeper when co-evaporated at 500°C, the degradation of the ACIGS bulk quality leads to a significant W_{OC} increase of ~80 mV (Table II. 9), as calculated both from the CL peak energy and the E_g fitted from the best cell EQE.

All in all, it is concluded that the opposite trends in the performances of ultrathin CIGS and ACIGS solar cells fabricated at 550°C and 500°C are related to the quality of the front interface and bulk of the absorber observed in CL, as well as the steepness of the GGI depth profile. In addition, the fluctuations of the peak energy extend over a quite narrow energy range, as it exhibits standard deviation values below 10 meV for all samples. This is much smaller than the values of FWHM, which lie in the 50 – 80 meV range. Hence, the differences in the material quality of the absorbers are rather attributed to the variation of the FWHM and Urbach energy between samples, than to the spatial fluctuations of the peak energy values.

7.5.Conclusion of the chapter

A cathodoluminescence (CL) study has been performed on the ultrathin CIGS and ACIGS layers co-evaporated on Mo that led to the best cell performances. The i-ZnO/ZnO:Al front contact has been chemically etched prior to the CL analysis, which allowed to characterize the front surface and bulk of the absorbers. However, numerical simulations performed with the CASINO software indicate that the back contact of the absorber is not probed by the electron beam. The main information obtained in CL are summarized below:

- A substantially higher CL intensity was observed for the ACIGS layer deposited at 550°C, indicating a lower density of non-radiative recombination defects than other absorbers.
- For CIGS films, the Urbach energy E_U fitted from the room temperature CL spectra was lower for a co-evaporation temperature of 500°C, indicating a reduced structural disorder. In contrast, the E_U of ACIGS was smaller when co-evaporated at 550°C, which correlates well with the performances of complete cells.
- In the CIGS case, the CL maps of the integrated intensity, peak energy and FWHM measured at a nominal holder temperature of 20K are similar for both deposition temperatures. This, combined with a steeper GGI back grading at 500°C, explains why ultrathin cells perform better and have a lower voltage deficit when fabricated at 500°C rather than 550°C.
- On the other hand, the CL maps of ACIGS layer fabricated at 550°C showed a higher integrated intensity, peak energy and lower FWHM that are also more homogeneous. As a result, considering that reducing the ACIGS co-evaporation temperature from 550°C to 500°C does not improve the GGI grading of the absorber, ultrathin ACIGS cells fabricated at 500°C exhibit lower performances and an increased voltage deficit.
- The fluctuations of the peak energy are smaller than the FWHM values. The material quality of the absorbers is thus related to width of the Urbach tail and the resulting FWHM.

To sum up, improving the composition of ultrathin CIGS-based absorbers was shown to be an effective way to improve the performances of complete solar cells. In particular, an average efficiency of 14.6 ± 0.2 % was achieved by alloying CIGS with Ag, and optimizing the GGI composition grading of CIGS led to higher efficiencies by contributing to the rear passivation of the absorber. Hence, the fabrication of a passivation layer on Mo to reduce the back contact recombination was also investigated.

Chapter 8. Nanostructured back contact for CIGS rear passivation

8.1. Introduction

This chapter is focused on the study of an alumina passivation layer for ultrathin CIGS solar cells. Indeed, Al_2O_3 was shown to efficiently mitigate the recombination of charge carriers at the CIGS back contact via a field-effect passivation due to the fixed negative charges in alumina and/or a chemical passivation thanks to the low density of interface traps at the CIGS/Al_2O_3 interface [135], [137]. Complete ultrathin solar cells with Al_2O_3 passivation layers were reported to achieve a substantial V_{OC} increase as compared to unpassivated reference [139], [140]. As alumina is insulating, passivation layers are generally perforated to create point contact openings with the Mo layer. The local contacts are typically spaced by a few microns, since the minority carrier diffusion length of CIGS is estimated to lie between 0.75 and 1.50 µm [133], [134]. The chosen geometry of the passivation layer, *i.e.* the point contact diameter and pitch, is a compromise between a high surface coverage and a sufficient carrier collection.

Here, the local point contacts in the Al_2O_3 layer were patterned by NanoImprint Lithography (NIL) [178], which should be easier to upscale than the electron beam lithography process used in previous works [10], [140]. In order to avoid a complementary rear passivation effect due to the GGI grading, CIGS was deposited in a 1-stage co-evaporation process with flat elemental rates as well as a fixed substrate temperature of 450°C that was calibrated in a previous work [126]. Note that Se is evaporated in excess during the whole process. This co-evaporation recipe is expected to result in a flat GGI depth profile, which allows to study the passivation effects of the alumina layer alone. It was shown that alumina passivation layers prevent a sufficient diffusion of Na from the SLG substrate [138]. Hence, a post-deposition treatment (PDT) of NaF was performed after CIGS co-evaporation, at a fixed substrate temperature of 350°C. NaF was evaporated at a rate of ~1 nm/min for 8 minutes.

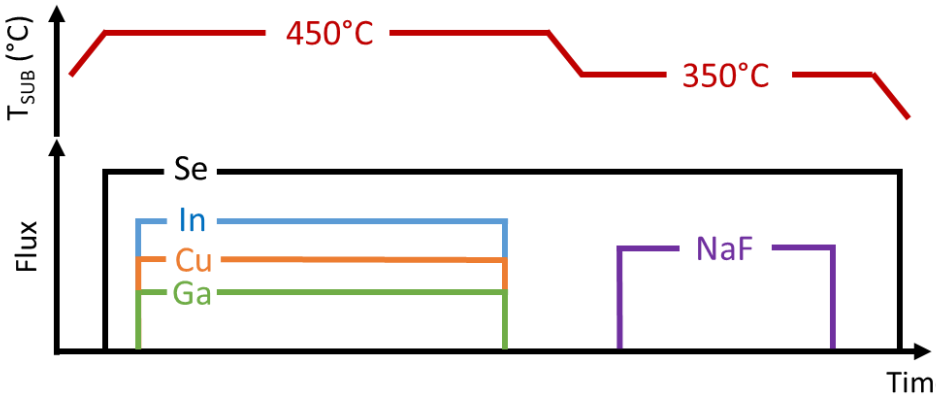

Figure II. 20. Schematic representation of the 1-stage process for the co-evaporation of ultrathin CIGS layers with ungraded composition. A PDT of NaF was performed.

In this process performed at IRDEP, the substrate temperature is set to 450°C during the co-evaporation of CIGS. Ultrathin CIGS layers were deposited on standard Mo back contacts with and without a patterned Al_2O_3 passivation layer in order to investigate the rear passivation of CIGS. The fabrication process as well as the investigated point

contact geometry are first reported. The co-evaporated CIGS films are then characterized. Finally, the photovoltaic performances of complete cells are analyzed.

8.2. Fabrication of the nanostructured back contact

In this work, alumina was chosen as a passivation layer because it was already demonstrated to provide an efficient rear passivation to ultrathin CIGS layers [139], [140]. Besides, a study by Kotipalli *et al.* [137] revealed that alumina layers deposited by thermal ALD should exhibit an adequate density of fixed negative charges after CIGS co-evaporation, making Al_2O_3 a good candidate for passivation layers.

Here, the passivation layer consists of a 50 nm-thick Al_2O_3 layer deposited by ALD. Local point contacts were patterned in the Al_2O_3 layer in order to allow for the collection of holes at the CIGS back contact. The investigated patterning geometry is shown in Figure II. 21. A nominal point contact diameter of 300 nm was chosen, with pitch values of 1 µm, 2 µm, 3 µm and 4 µm, which should allow both the collection of holes and the CIGS rear passivation [133], [134]. With this geometry, the nominal coverage of the Mo layer by alumina ranges from 71.7% for a pitch of 1µm to 99.6% for a period of 4 µm.

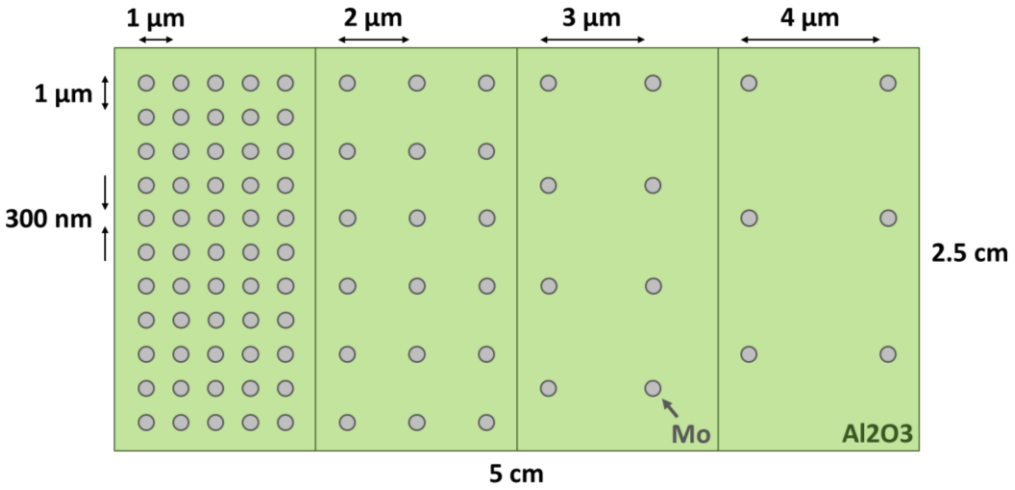

Figure II. 21. Schematic geometry of the local point contacts patterned by nanoimprint lithography (NIL). Mo is used as a back contact, and Al_2O_3 as a passivation layer.

A NIL process was used to create the nano-scale point contact openings. As shown in Figure II. 22, the desired geometry is first patterned by electron beam (e-beam) lithography on a silicon wafer, called the Si master. In this study, this process step was performed by Dr. Andrea Cattoni. The geometry is then transferred to a flexible polymeric stamp made of poly(dimethylsiloxane) (PDMS) that is spin-coated on the Si master. A "hard-PDMS" layer is first deposited to ensure an adequate replication of the patterns, then a more flexible PDMS layer is spin-coated. Finally, the bi-layer PDMS stamp is annealed and removed from the Si master. Contrary to the time-consuming process of e-beam lithography, these fabrication steps can be performed in a shorter amount of time, which is about half an hour at the laboratory scale. The PDMS stamp also has many advantages:

- It can be used multiple times, and can also be replicated several times from the same Si master [179]–[181].
- The patterning process can be performed under atmospheric pressure and at low temperatures.
- The flexibility of the stamp makes it easy to handle. It also allows to imprint flexible or curved substrates.
- The permeability of the stamps prevents air bubbles from being trapped during the imprinting process.
- The low surface energy of PDMS facilitates the demolding of the stamp after imprinting.

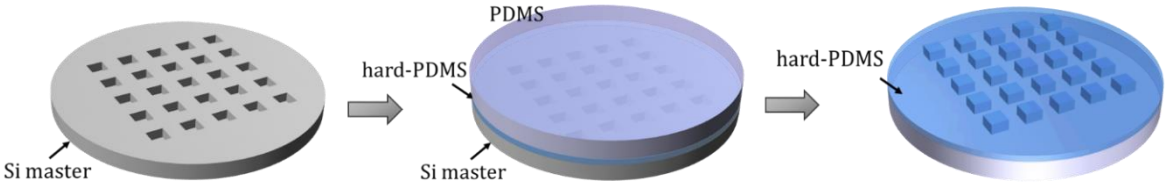

Figure II. 22. Fabrication steps of the PDMS mold used in NIL.

The fabrication process of the patterned passivation layer is detailed in Figure II. 23. It can be described by 4 successive steps:

1. The Al_2O_3 layer is deposited on a standard SLG/Mo back contact by ALD in a BENEQ TFS-200 device. The layer was grown at a rate of ~4.3 nm/min with successive pulses of trimethylaluminium and H_2O precursors, at a substrate temperature of 200°C and a working pressure of 2 mbar. A sol-gel mask of Ti oxide was prepared from a solution of $TiCl_4$/EtOH/H_2O with molar ratios of 1:40:15, and a small amount of a copolymer as a structuring agent (see [182]–[184] for additional details). The sol-gel solution was spin-coated on top of the Al_2O_3 layer at 2000 rpm for 7 s, under a relative humidity of 40%, resulting in a ~100 nm-thick TiO_2 layer.
2. The PDMS stamp was applied on the TiO_2 mask. After 30 s at room temperature, the sample was heated to 100°C for 5 min.
3. The stamp was then demolded, and the residual layer in the holes of the patterned TiO_2 was etched using an O_2 plasma in a reactive ion etching (RIE) device for 20 s. The TiO_2 was calcinated at 300°C for 5 min to stabilize the layer and to fully evaporate the remaining solvents.
4. The sample was dipped for 15 min in a commercial solution of *AZ® 400 K* that contains KOH. This resulted in a selective etching of the Al_2O_3 layer and created the local point contact openings. Finally, the TiO_2 mask was stripped by RIE, with an O_2 plasma that was applied for 3 min.

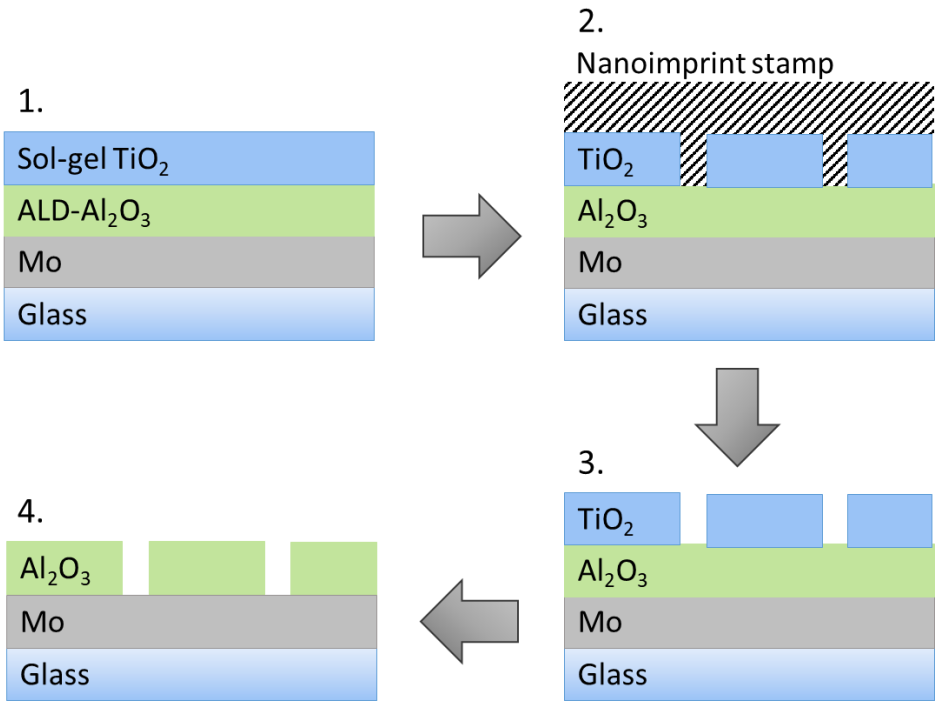

Figure II. 23. Schematized fabrication steps of an Al_2O_3 passivation layer for ultrathin CIGS solar cells based on a NIL patterning process.

Figure II. 24 shows the Al_2O_3 passivation layer patterned by NIL. The point contacts are completely etched, regardless of their spacing. The top alumina layer looks smooth, indicating that the TiO_2 mask efficiently protected it during the wet etching step. An EDX analysis (not shown) confirmed that TiO_2 was fully removed after the patterning process.

The insets in Figure II. 24 show single point contacts at high magnification for each geometry. The usual morphology of Mo can be observed, suggesting that the alumina layer was etched up to the Mo back contact regardless of the hole pitch. The diameter of the point contacts was estimated from these SEM images at high magnification, and was found to vary depending on the geometry of the square patterns: ~300 nm for a pitch of 1 µm, ~370 nm for a period of 2 µm, ~340 nm for a spacing of 3 µm and ~250 nm for a pitch of 4 µm.

Ultrathin CIGS layers were co-evaporated on this patterned alumina passivation layer with Mo point contacts and on a flat Mo back contact. The material characterization of these samples is reported in the next section.

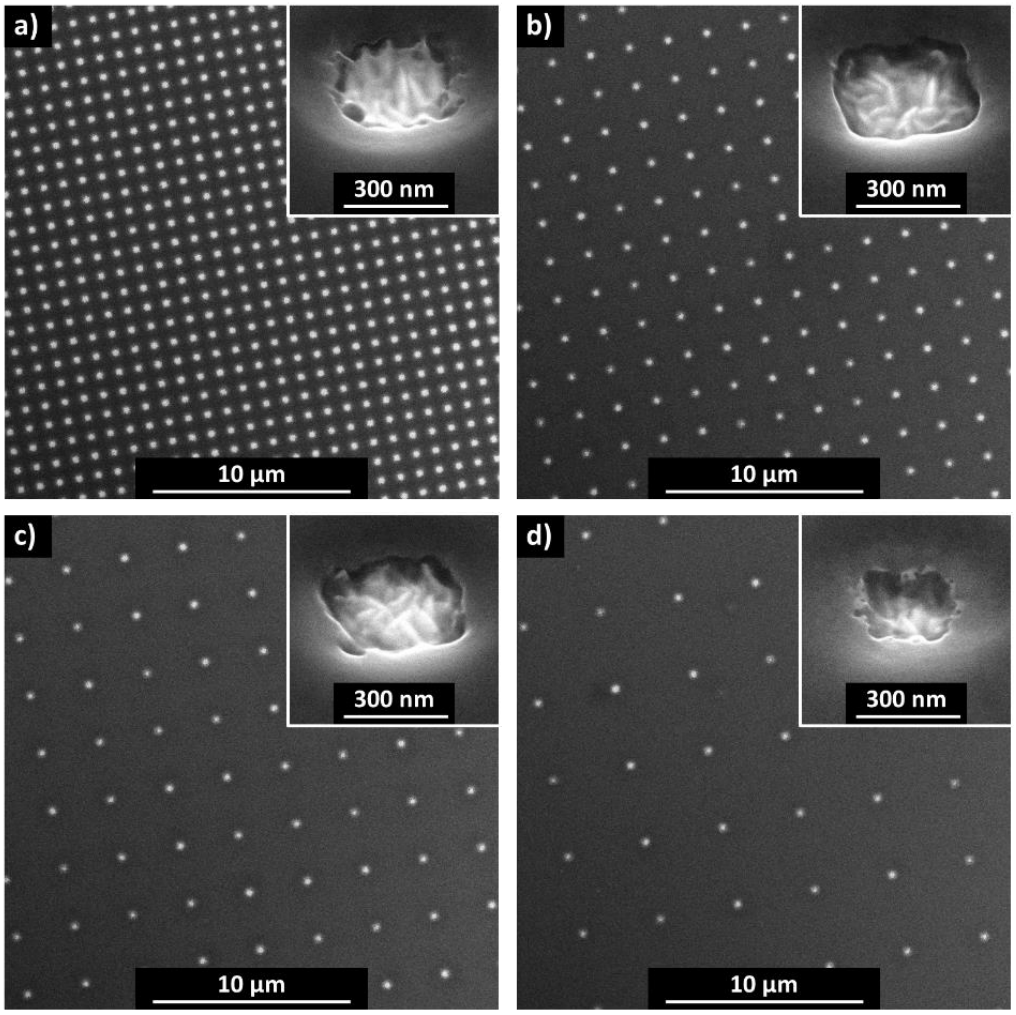

Figure II. 24. SEM top-view image of a 50 nm-thick Al_2O_3 layer deposited on a Mo back contact. Local point contacts with a nominal diameter of 300 nm were patterned in the alumina layer with a NIL process. Pitches of (a) 1 µm, (b) 2 µm, (c) 3 µm and (d) 4 µm were used. The inset in (a) shows a point contact with a 30 times higher magnification and a tilt of 45°. [WP1_4].

8.3.Material characterization of CIGS

The ultrathin CIGS layers studied in this section were co-evaporated in a single batch, using a 1-stage co-evaporation process. Table II. 10 summarizes the main deposition parameters, the CIGS thickness as well as its average CGI and GGI ratios. The CIGS thickness and average composition were obtained from a CIGS layer deposited on a Mo reference back contact, using a profilometer and an XRF device, respectively.

CIGS deposition temperature	NaF PDT	CIGS thickness (nm)	CGI	GGI
450°C	8 min, 1 nm/min, 350°C	470 ± 20	0.85 ± 0.02	0.35 ± 0.01

Table II. 10. Main deposition parameters of the ultrathin CIGS layer co-evaporated on Mo back contacts with and without an alumina passivation layer. The average thickness, CGI and GGI of this CIGS film were measured on a Mo reference. [U202]

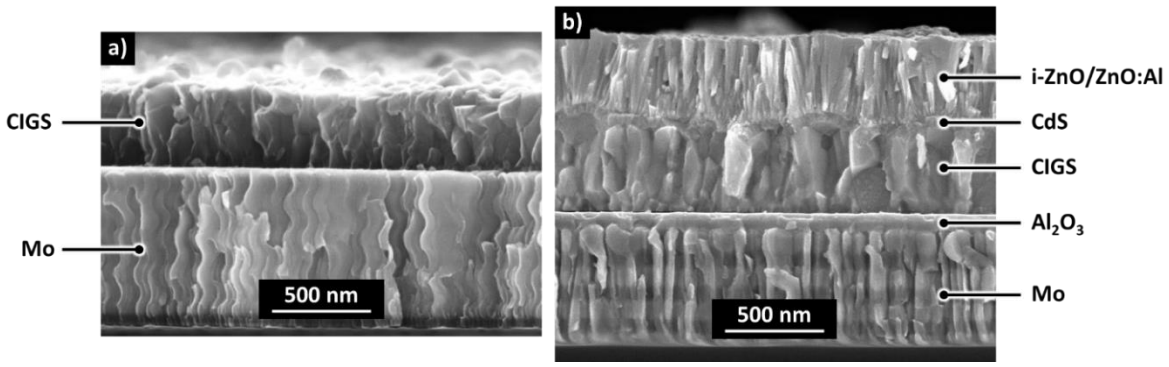

Figure II. 25. SEM cross-section images of (a) the ultrathin CIGS layer co-evaporated on a standard Mo back contact, and (b) the complete solar cell stack including a 50 nm-thick Al_2O_3 passivation layer. An average CIGS thickness of 440 ± 10 nm was determined from these images. (a) [U202_A], (b) [U202_C] (back contact is [WP1_4]).

Figure II. 25 shows the SEM cross-section image of this ultrathin CIGS layer, deposited on Mo back contacts with and without an alumina passivation layer. An average CIGS thickness of 440 ± 10 nm was determined from these images, in good agreement with the profilometer measurement.

The morphology of the CIGS layer exhibits small grains, which is expected in the case of a 1-stage co-evaporation process. The CIGS morphology is similar for both types of back contacts, suggesting that the Al_2O_3 passivation layer does not strongly affect the growth of the ultrathin CIGS film.

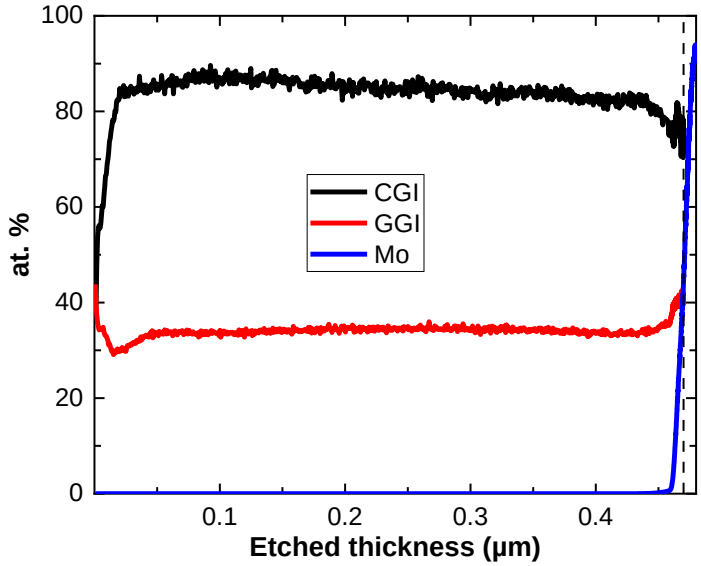

Figure II. 26. GD-OES composition profile of Mo as well as CGI and GGI atomic ratios of the ultrathin CIGS layers co-evaporated in a 1-stage process. The CIGS thickness was measured with a profilometer and the average CGI and GGI compositions were calibrated with XRF data. The CIGS/Mo interface is indicated by a vertical dashed line. [U202_A].

The composition depth profile of the ultrathin CIGS layer was determined in GD-OES (Figure II. 26). This analysis confirms that a flat GGI was obtained. Hence, the CIGS conduction band is ungraded, which allows to study the passivation effects related to the alumina layer without the contribution of a back surface field. As the Mo back

contact covered with an Al_2O_3 passivation layer was fully used to fabricated complete cells, it was not possible to compare the composition depth profiles of Na in the CIGS layers grown on the passivation layer and on the Mo reference. However, one should keep in mind that the incorporation of Na, in particular the Na quantity and supply method, is known to affect the doping concentration in CIGS and thus the V_{OC} of complete devices [27], [55].

Complete solar cells were fabricated on Mo back contacts with and without a 50 nm-thick Al_2O_3 passivation layer. The photovoltaic performances of these devices is reported in the next section. The passivation effects of the alumina layer are discussed with respect to the geometry of the point contact openings.

8.4.Solar cell performances

A summary of the average and best cell light I(V) parameters can be found in Table II. 11. Figure II. 27 also shows the light and dark I(V) characteristics of the best solar cells, as well as their EQE curves. Finally, the dark I(V) parameters were fitted with a 1-diode model for each type of back contact (Table II. 12).

	Average / best cell light I(V) parameters			
Back contact	Eff. (%)	J_{SC} (EQE) (mA/cm²)	V_{OC} (mV)	*FF* (%)
Mo – unpass. ref. [U202_A]	7.7 ± 0.1 / 7.9	20.3	565 ± 2 / 562	68.2 ± 0.9 / 69.4
Mo/Al_2O_3 – 1 µm [U202_C]	8.7 ± 0.4 / 9.1	21.2	592 ± 22 / 621	69.5 ± 3.9 / 69.3
Mo/Al_2O_3 – 2 µm [U202_C]	9.4 ± 0.1 / 9.5	21.8	615 ± 1 / 617	70.3 ± 0.5 / 70.6
Mo/Al_2O_3 – 3 µm [U202_C]	6.9 ± 0.1 / 7.0	21.5	606 ± 10 / 613	52.8 ± 2.1 / 52.9
Mo/Al_2O_3 – 4 µm *[U202_C]	4.9	21.3	599	38.5

Table II. 11. Summary of light I(V) parameters for an ultrathin CIGS layer co-evaporated on Mo back contacts with and without an Al_2O_3 passivation layer. Point contact openings were patterned in the alumina layer with a pitch of 1 µm, 2 µm, 3 µm or 4 µm. Average values were calculated from the 5 best solar cells. *Light I(V) parameters for the best cell only.

First, the unpassivated Mo reference exhibits a rather low efficiency of 7.7 ± 0.1 %, associated with a V_{OC} of 565 ± 2 mV, a *FF* of 68.2 ± 0.9 and a J_{SC} of 20.3 mA/cm². These low values obtained with a 1-stage co-evaporation process can be attributed to the insufficient light absorption in ultrathin CIGS but also to strong back contact recombination in the absence of a passivating back surface field.

CIGS solar cells including an Al_2O_3 passivation layer all show a significant improvement of the V_{OC} as compared to the bare Mo. In particular, the passivation layers with point contact pitches of 1 µm and 2 µm result in best V_{OC} values of 621 mV and 617 mV, respectively. This represents a respective increase of 59 mV and 55 mV as compared to Mo. This was attributed to the passivation effects of the Al_2O_3 layer, *i.e.* the reduced back contact recombination. However, the J_0 and *n* values fitted for these samples and for the unpassivated reference are unexpectedly very similar (Table II. 12). In the case of the solar cell on a passivation layer with 3 µm-spaced point contacts even shows increased J_0 and *n* values, despite a V_{OC} of 613 mV.

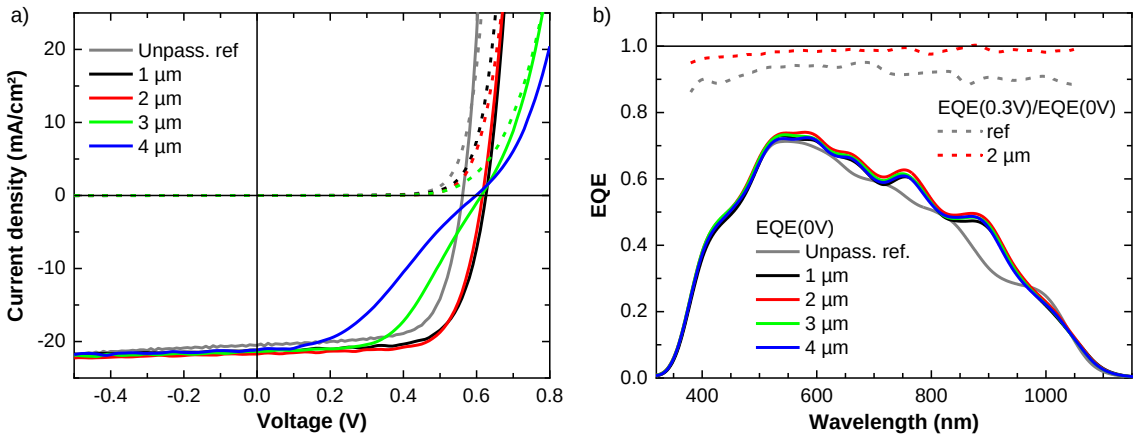

Figure II. 27. (a) Light and dark I(V) characteristics of best ultrathin CIGS solar cells (respectively solid and dashed lines), together with (b) the corresponding EQE curves. Back contacts consist of Mo with and without a patterned Al_2O_3 passivation layer. Point contact openings in the passivation layer have a pitch of 1 µm, 2 µm, 3 µm or 4 µm. In (b), the ratios of EQE(0.3V)/EQE(0V) (dashed lines) are also shown in the case of the unpassivated reference and of the passivation layer with point contacts spaced by 2 µm. (gray) [U202A_11], (black) [U202C_1_300_ 0], (red) [U202C_2_300_7], (green) [U202C_3_300_2], (blue) [U202C_4_300_1]. Cases of EQE from different cells to avoid measurement artifacts: (black) [U202C_1_300_1], (blue) [U202C_4_300_2].

Solar cells on passivation layers with openings periods of 1 µm and 2 µm respectively show average *FF* values of 69.5 ± 3.9 % and 70.3 ± 0.5 %, which are similar to the unpassivated reference. In contrast, spacings of 3 µm and 4 µm lead to low *FF* values below 55% that are correlated to a rollover effect (Figure II. 27.a) and a high series resistance (Table II. 12).

This rollover effect indicates the presence of a barrier for hole collection [141], [185], [186]. As the point contacts observed in SEM appear to be fully opened, this suggests that periods of 3 µm and 4 µm between each opening are too large as compared to the hole diffusion length, which in turn also leads to an increased R_S.

		Dark I(V) parameters			
Back contact		J_0 (mA/cm²)	n	R_{SH} (Ω.cm²)	R_S (Ω.cm²)
Mo – unpass. ref.	[U202A_11]	5.10^{-6}	1.6	1.10^4	< 0.1
Mo/Al_2O_3 – 1 µm *	[U202C_1_300_4]	4.10^{-6}	1.6	3.10^4	0.8
Mo/Al_2O_3 – 2 µm	[U202C_2_300_6]	3.10^{-6}	1.6	2.10^6	0.7
Mo/Al_2O_3 – 3 µm	[U202C_3_300_2]	2.10^{-5}	2	2.10^6	3.3
Mo/Al_2O_3 – 4 µm °		/	/	/	/

Table II. 12. Dark I(V) parameters for each type of back contact, fitted with a 1-diode model (J_0: saturation currents, n: ideality factor, R_{SH}: shunt resistance, R_S: series resistance). *Experimental dark I(V) curve shows a discrepancy with the 1-diode model fit under forward bias. °Due to measurement artefacts the experimental dark I(V) curve could not be fitted. Best cells were not selected due to measurement artefacts.

Using passivation layers with opening pitches of 1 µm and 2 µm reduces the voltage-dependence of the photocurrent as compared to the standard Mo back contact (Figure II. 27.a). This indicates a better carrier collection, possibly thanks to the CIGS rear passivation. This is also confirmed by the higher ratio of $EQE(0.3)/EQE(0V)$ in the case of a passivated cell (Figure II. 27.b). However, as the R_S values of passivated solar cells is slightly increased, even for opening periods of 1 µm and 2 µm, the *FF* of passivated solar cells is not improved as compared to the Mo reference.

All passivated best cells show improved J_{SC} that are above 21.2 mA/cm^2, instead of 20.3 mA/cm^2 for the bare Mo back contact. The EQE curves show a slight enhancement in the 550 – 950 nm wavelength range in the case of the passivated solar cells. (Figure II. 27). In addition, an E_g of 1.17 eV was fitted from the EQE^2 of the best unpassivated cell, which is similar to the E_g of 1.16 eV for passivated cells. This confirms the effective rear passivation of cells with an Al_2O_3 layer as they exhibit a reduced voltage deficit $E_g - V_{OC}$.

Vermang *et al.* [139] showed that the low-index Al_2O_3 layer can improve the reflectance of the CIGS/Mo interface, leading to a higher CIGS absorption and J_{SC}. Hence, to determine whether our EQE improvement results from an electrical or optical effect of the passivation layer, optical simulations of complete devices were performed to calculate their CIGS absorption. As a first approximation, a flat passivation layer was simulated with the Reticolo software, using the Al_2O_3 optical indices from [187]. The complete solar cell consists of the following stack: SLG/Mo (800 nm)/Al_2O_3 (50 nm)/CIGS/CdS (50 nm)/*i*-ZnO (50 nm)/ZnO:Al (250 nm). The CIGS layer was simulated with a thickness of 440 nm and an E_g of 1.16 eV, according to the characterization results obtained from the experimental layer.

Figure II. 28 shows the experimental EQE of the passivated solar cell with a point contact pitch of 2 µm, as well as its simulated CIGS absorption. As electrical losses are neglected in the optical model, the simulated absorption is significantly higher than the measured EQE. Still, the wavelength positions of the resonances are in good agreement. This simulated absorption can be compared with the one calculated for an unpassivated cell architecture, where the Al_2O_3 film is removed. It shows a similar absorption, with a small decrease for wavelengths between 600 nm and 1000 nm. Theoretical J_{SC} values were derived from the simulated CIGS absorption integrated with the AM1.5G spectrum. J_{SC} of 28.6 mA/cm^2 and 28.1 mA/cm^2 were calculated for the passivated and unpassivated cells, respectively. This indicates that the experimental J_{SC} gain of 1.5 mA/cm^2 is mainly due to the passivation effects of the Al_2O_3 layer leading to a better collection efficiency. These results are in good agreement with the study from Salomé *et al.* [10], where two-dimensional optical simulations of cells with an Al_2O_3 passivation layer indicated that the J_{SC} gain of passivated devices can be mostly attributed to the electrical passivation effects of the Al_2O_3 film.

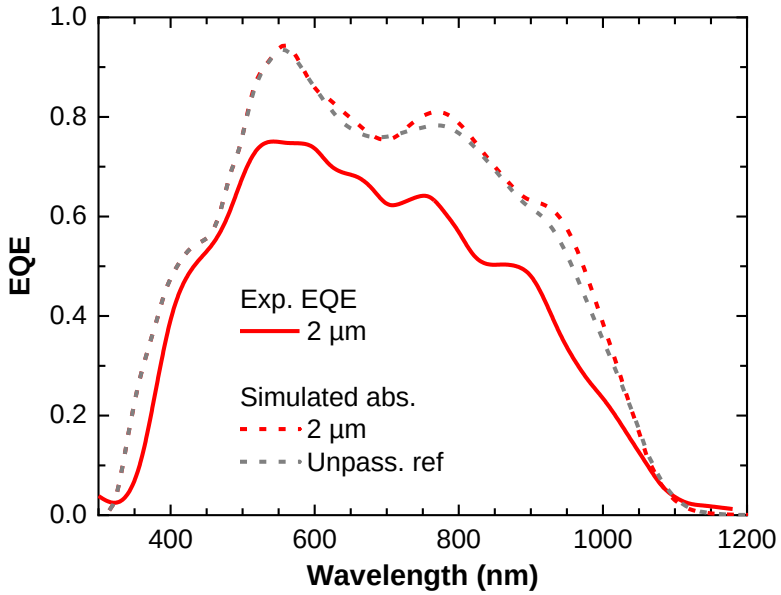

Figure II. 28. Simulated CIGS absorption for solar cells with and without an Al_2O_3 passivation layer, *i.e.* a device stack of: SLG / Mo (800 nm) / (Al_2O_3 (50 nm) / CIGS (440 nm) / CdS (50 nm) / *i*-ZnO (50 nm) / ZnO:Al (250 nm). The experimental EQE of the passivated solar cell is shown for comparison.

All in all, the Al_2O_3 passivation layer led to improved efficiencies as compared to the Mo reference when the point contact openings are spaced by 1 µm or 2 µm. In particular, a pitch of 2 µm between point contacts was found to be optimal, as the Al_2O_3 layer provides both a high surface coverage of 92.9% and a sufficient hole collection with R_S values below 1.0 Ω.cm². A best efficiency of 9.5% was achieved with this optimized geometry of point contacts, which is 1.6% absolute more than the best unpassivated CIGS cell. This efficiency improvement is attributed to the passivation effects of the Al_2O_3 layer that result in V_{OC} and J_{SC} improvements, respectively from 562 mV to 613 mV and from 20.3 mA/cm² to 21.5 mA/cm².

8.5.Conclusion of the chapter

In conclusion, an Al_2O_3 passivation for ultrathin CIGS layers including a Mo back contact was fabricated with a NIL patterning process, which allowed to create local openings in the Al_2O_3 film using a wet etching step. This reliable and fast method should be easier to upscale than the time-consuming e-beam lithography technique used in previous works [10], [140]. The investigated geometry of point contacts consists in a nominal hole diameter of 300 nm and different pitch values of 1 µm, 2 µm, 3 µm and 4 µm. CIGS was co-evaporated on Mo back contacts with and without a passivation layer, using a 1-stage process that resulted in an ungraded GGI composition. Complete solar cells were then fabricated and characterized, leading to the following findings:

- In SEM, the morphology of CIGS layers deposited on Mo back contacts with and without a passivation layer is identical, suggesting similar material quality.
- Solar cells with a passivation layer exhibit a substantially higher V_{OC} and J_{SC} than the unpassivated reference. This is attributed to the reduction of the back contact recombination thanks to the passivation layer.
- Passivated cells with a point contact period of 3 µm and 4 µm suffer from a rollover effect and high R_S values.
- In the case of a hole pitch of 1 µm and 2 µm, reasonable R_S < 1.0 Ω.cm² are obtained. For these cells, the voltage-dependence of the photocurrent is also reduced as compared to the bare Mo case, thanks to a better carrier collection. This results in similar average *FF* for these cells and the unpassivated reference.
- A pitch of 2 µm was found to be optimal, leading to a best efficiency of 9.5% with a J_{SC} of 21.5 mA/cm² and a V_{OC} of 613 mV. In comparison the best unpassivated cell exhibits an efficiency of 7.9%, a J_{SC} of 20.3 mA/cm² and a V_{OC} of 562 mV.

The addition of a passivation layer was shown to be beneficial to the photovoltaic performances of solar cells including an ultrathin CIGS layer co-evaporated with a 1-stage process on Mo. However, the efficiency of the best passivated cell is limited to 9.5% with this suboptimal co-evaporation process, and to only 7.9% for the unpassivated best cell. In comparison, the best ultrathin CIGS and ACIGS solar cells grown with a 3-stage process on bare Mo exhibit efficiencies of 13.4% and 14.9%, respectively. Besides, a respective best V_{OC} and *FF* of 741 mV and 81.8% were achieved with an ACIGS absorber, which is comparable to record CIGS cells with a standard absorber thickness [26], [31]. Hence, a sufficient rear passivation might be achieved without using a passivation layer. Combining passivation layers with composition-graded (A)CIGS films should provide more insights on the passivation effects of these two approaches, and on the necessity of a passivation layer to achieve highly-efficient ultrathin solar cells.

Conclusion of Part II

Two different approaches for the rear passivation of ultrathin CIGS layers deposited on Mo were investigated. The first one relies on the formation of a GGI grading to create a back surface field that repels electrons toward the *p-n* heterojunction. The second one consists in fabricating an Al_2O_3 passivation layer with local openings on the Mo back contact, which can passivate the CIGS rear interface thanks to a fixed density of negative charges and a lower density of interface traps.

First, ultrathin CIGS layers were co-evaporated with a 3-stage process, using maximum substrate temperatures of 550°C, 500 °C and 450 °C. It was found that decreasing the deposition temperature forms a steeper GGI back grading, but also leads to a CIGS morphology with smaller grains and a rougher front interface. Absorbers deposited at 550°C and 500°C exhibited a similar behavior in cathodoluminescence (CL). As a result, the deposition temperature of 500°C was found to be optimal, with an efficiency of 13.4% and a V_{OC} of 672 mV, thanks to the improved GGI grading.

In contrast, ultrathin ACIGS layers co-evaporated in a 3-stage process at 550°C and 500°C show similar GGI gradings. However, ACIGS films prepared at 500°C show a very rough front interface in SEM, as well as a degradation of the integrated intensity, peak energy and FWHM in CL. ACIGS solar cells fabricated at 550°C exhibited the best efficiency of 14.9%, with a V_{OC} of 741 mV, a J_{SC} of 24.5 mA/cm^2 and a *FF* of 81.8%. This remarkable photovoltaic performance is attributed to the improved materials quality of the ACIGS film.

Ultrathin solar cells were also co-evaporated on Mo back contacts with and without an Al_2O_3 passivation layer. In this case, CIGS was co-evaporated in a one-stage process to avoid the presence of a back surface field that contributes to the CIGS rear passivation. A best efficiency of 9.5% with a V_{OC} of 617 mV was measured for an Al_2O_3 passivation layer with 300 nm-wide point contacts spaced by 2 µm. Despite the beneficial passivation effects of the Al_2O_3 layer, the efficiency of the complete device remained quite low due to the use of a suboptimal 1-stage process. Combining a passivation layer with a graded ultrathin CIGS layer should provide insights on the most effective passivation scheme: the use of a GGI grading or of a passivation layer.

Finally, it is worth mentioning that the efficiencies of the ultrathin solar cells presented in this section might be further increased by implementing a heavy alkali PDT, but also by using Zn-based buffer layers and an antireflection coating. However, the J_{SC} of such ultrathin devices is still expected to be significantly lower than the best J_{SC} value above 41 mA/cm^2 that was achieved with the record thick CIGS solar cell [26]. Hence, to further improve the J_{SC} of ultrathin solar cells, the following part will investigate the development of a highly reflective back contact that is compatible with the direct deposition of CIGS.

Part III. Flat Reflective Back Contacts (RBCs) for ultrathin CIGS solar cells

Introduction to part III

The lack of light absorption in ultrathin CIGS layers has been demonstrated to limit the efficiency of ultrathin CIGS solar cells [13], [188], and novel architectures of reflective back contacts are needed to increase light absorption in ultrathin CIGS layers. Hence, the following chapters report on the successful development of a reflective back contact (RBC) that is compatible with the high deposition temperature of CIGS and improves the absorption of ultrathin CIGS solar cells. The investigated RBC architecture consists of a multi-layer stack that is shown in Figure III. 1, with each layer having a specific and well-defined role.

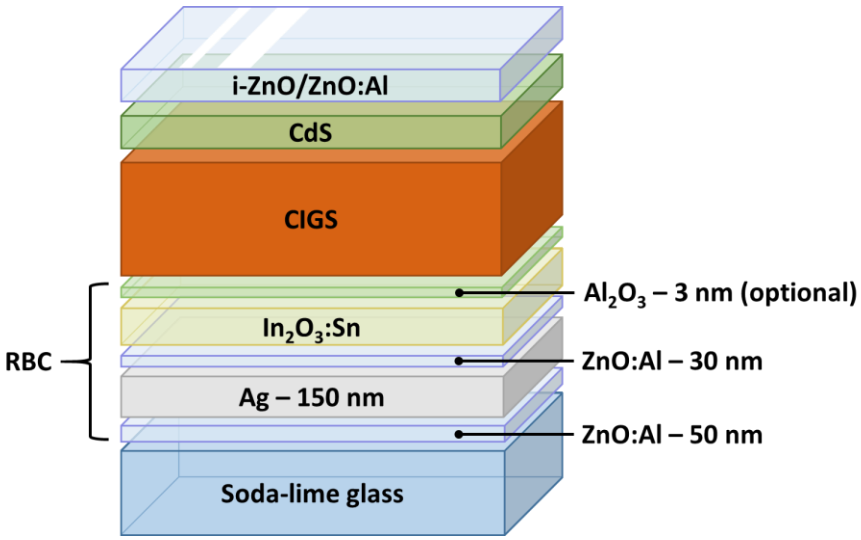

Figure III. 1. Schematic of a complete solar cell stack including a reflective back contact (RBC).

- First, a silver layer is used as a highly reflective mirror. In this study, the RBCs include a 150 nm-thick Ag film as a proof of concept, but using a 100 nm-thick Ag layer should provide a similar reflectivity, thereby allowing a reduced material consumption.

- The Ag mirror is encapsulated between two ZnO:Al layers with thicknesses of 50 nm under the Ag film, and 30 nm on top of it. The role of the ZnO:Al layers is to hinder the diffusion of Ag during the co-evaporation of CIGS at temperatures ≥ 450°C. In particular, it has been reported that Ag nanowires embedded in 30 to 40 nm-thick ZnO layers are stable under annealing temperatures up to 375°C [189], [190],

- ZnO:Al was shown to strongly react during CIGS co-evaporation, forming a detrimental and insulating layer of Ga oxide at its interface with CIGS [38], [150], [191]. The ZnO:Al/CIGS interface was also reported to lead to a strong series resistance, even when the formation of Ga oxide is avoided [152]. Hence, ITO was used as a back contact with CIGS as it was reported to form an ohmic

contact with CIGS by reducing the growth of Ga oxide for co-evaporation temperatures ≤ 520°C [36], [150]. ITO layers of 200 nm, 100 nm and 30 nm were used to study the impacts of the ITO thickness on the properties of the RBC and on the CIGS/ITO interface.

- Finally, the optional deposition of a 3 nm-thick layer of Al_2O_3 on top of ITO was investigated. Indeed, it has been shown that a thin alumina layer can prevent the excessive growth of interfacial Ga oxide at the interface between CIGS and a TCO back contact made of hydrogen-doped In_2O_3 [37], [192].

In order to assess the optical benefits of the RBC, the photocurrent of complete solar cells with a RBC is first simulated. The RBCs and the ITO layers are then characterized before the deposition of CIGS absorber layers. A simpler RBC architecture that is more straightforward to fabricate is also studied: it includes a single ITO layer deposited on Ag, thus consisting of a stack of SLG/ZnO:Al (50 nm)/Ag (150 nm)/ITO (100 nm). The properties and stability of the RBC stacks with a bilayer and a monolayer of TCO on Ag are then compared. After the co-evaporation of CIGS, the CIGS/ITO interface is extensively analyzed by STEM/EDX and its impacts on the photovoltaic performances of complete cells are discussed. Different architectures of CIGS-based solar cells on RBCs are examined and optimized in order to improve cell efficiencies. Finally, optical simulations of solar cells on top of nanostructured RBCs are performed to investigate the potential for further enhancement of light absorption in ultrathin CIGS layers.

Chapter 9. Optical modeling of ultrathin CIGS solar cells with RBCs

9.1. Introduction

In order to determine the absorption losses resulting from the thinning of the CIGS absorber, light absorption of complete solar cells was first simulated under one-sun illumination with the Reticolo software. Absorption of solar cells is compared for a standard Mo back contact and a hypothetical Ag back contact in direct contact with CIGS. Though Ag is not compatible with the direct co-evaporation of CIGS, this back contact was simulated because it can be considered as an almost perfectly reflective back contact that provides a double-pass absorption in the CIGS film [33], [120], [193]. Note that it is possible to lift-off the CIGS layer from the Mo back contact and then to cover it with a metal like Au, but this technique is hardly upscalable [120].

The light absorption enhancement of ultrathin CIGS solar cells with a RBC is then calculated and compared to the case of the Mo and Ag back contacts. Three different thicknesses of the ITO top layer (200 nm, 100 nm and 30 nm) are investigated.

9.2. Thickness dependence of CIGS absorption

Figure III. 2 shows the calculated CIGS absorption for complete solar cells with a 350 nm-thick back contact made of Mo or Ag. The simulated CIGS layer has a bandgap of 1.2 eV, and its thickness is varied between 2 µm and 0.1 µm. The front layers consist of a stack of CdS (50 nm)/i-ZnO (50 nm)/ZnO:Al (250 nm). The optical indices of each of these layers are available in Appendix C.

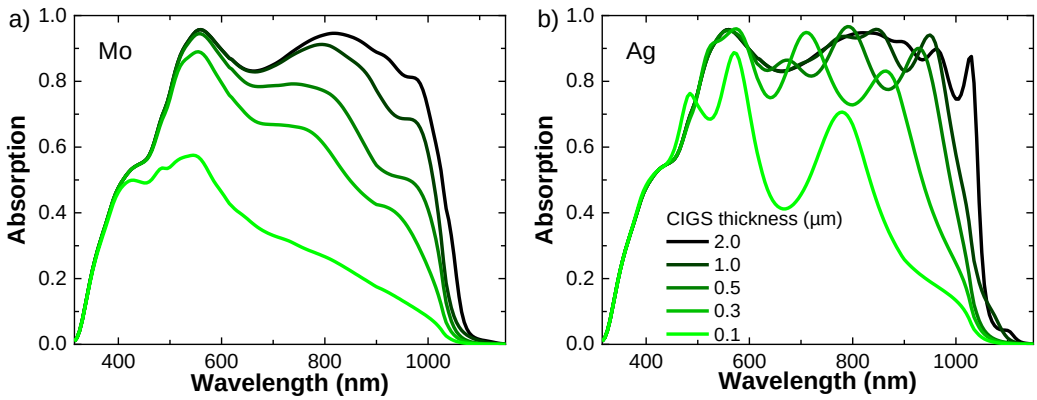

Figure III. 2. Simulation of the CIGS light absorption under one-sun illumination, for a complete solar cell stack with (a) a Mo or (b) a silver back contact. The thickness of the simulated CIGS film is varied between 2 µm and 0.1 µm.

In the case of a Mo back contact (Figure III. 2.a), for wavelengths above 600 nm less than 40% of incident photons are absorbed when the CIGS thickness is thinned from 2 µm down to 100 nm [194]. Because the CIGS/Mo interface exhibits a poor reflectance [33], [120], [122], [152], [194], the absorption of CIGS on a Mo back contact is dramatically reduced when its thickness is decreased to 500 nm and below. In contrast, CIGS layers simulated on a silver back contact (Figure III. 2.b) show higher absorption for wavelengths above 600 nm thanks to the superior reflectance of the Ag back contact in this spectral range [33], [120]. As a result, the CIGS absorption spectrum exhibits resonances due to Fabry-Perot interferences, which are generated

by light reflection occurring at the CIGS interfaces. Nevertheless, it is found that a very thin CIGS layer of 100 nm on Ag still exhibits significant absorption losses as compared to a standard 2 µm-thick CIGS film.

To get a clearer picture of light absorption in complete devices, absorption of each layer was plotted for CIGS thicknesses of 2 µm and 500 nm, both for Mo and Ag back contacts (Figure III. 3). The J_{SC} of complete cells were also derived from the simulated CIGS absorption integrated with the AM1.5G spectrum, assuming no collection losses. They are reported in Figure III. 4, together with the equivalent J_{SC} losses due to the parasitic absorption in other layers for photon energies below the CIGS bandgap of 1.2 eV.

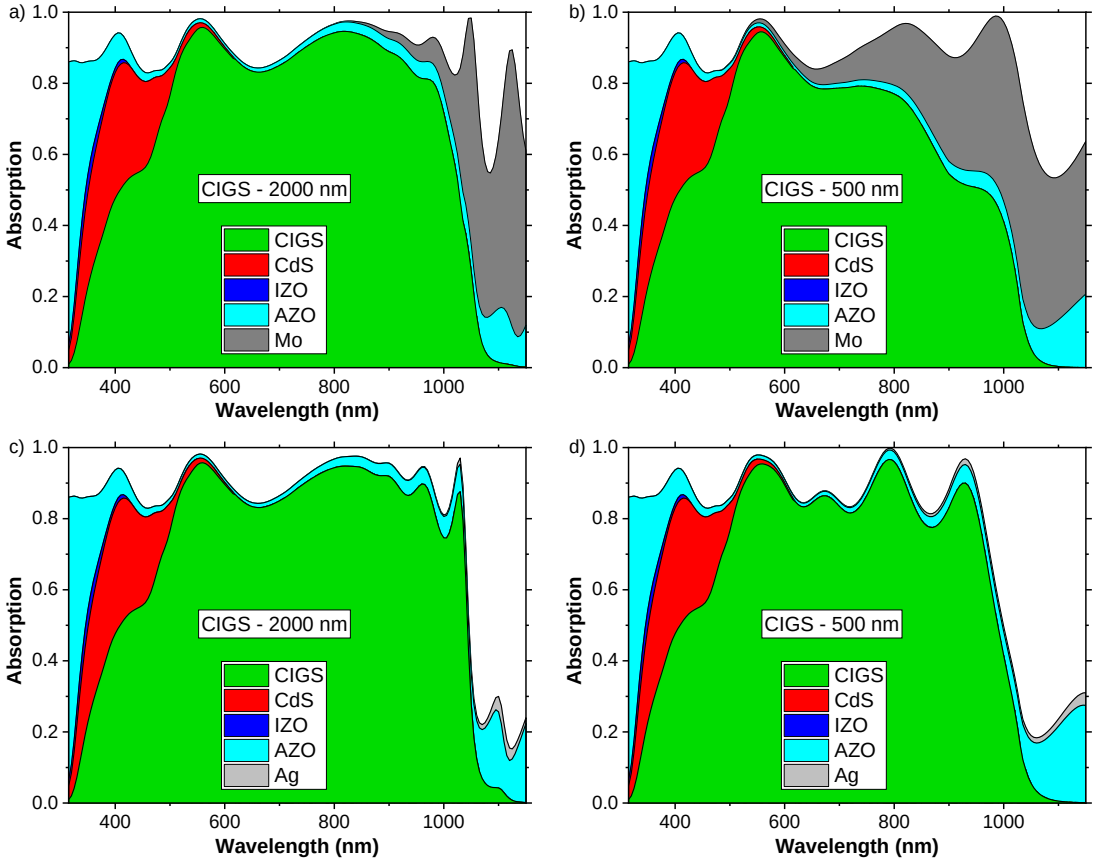

Figure III. 3. Simulated absorption in each layer of complete solar cells. The back contact consists of (a,b) Mo or (c,d) Ag. The thickness of the simulated CIGS layer is either (a,c) 2000 nm or (b,d) 500 nm.

First, the CdS layer shows a strong light absorption in the 300 – 550 nm wavelength range. Regardless of the CIGS thickness, it accounts for a 1.7 mA/cm² loss. Note that recent record efficiencies of CIGS solar cells were achieved with thinner CdS films or Cd-free buffer layers, combined with highly transparent conductive oxide layer [26], [31], [32]. However, this work is focused on the absorption losses due to the fraction of light that is transmitted through the CIGS layer.

In the case of a standard absorber thickness of 2 µm, replacing Mo by Ag leads to a slight improvement of the CIGS absorption in the infrared region thanks to the enhanced reflectance of the CIGS back interface. As a result, the calculated J_{SC} of

complete solar cells is increased from 33.1 mA/cm² to 34.0 mA/cm² (see Table III. 1), and the J_{SC} loss of 0.7 mA/cm² due to the Mo absorption is avoided. This suggests that even solar cells with a standard CIGS thickness can benefit from a more reflective back contact. This was also demonstrated by Bissig *et al.*, who reported J_{SC} gains up to 0.8 mA/cm² in the case of solar cells with 2 µm-thick CIGS layers co-evaporated on a back contact including an Al metallic mirror encapsulated in InZnO [155].

As expected, when the CIGS thickness is reduced to 500 nm the J_{SC} of complete cells on Mo is dramatically decreased to 27.9 mA/cm² with a 5.3 mA/cm² J_{SC} loss in the Mo back contact. In contrast, a decent J_{SC} of 31.0 mA/cm² is maintained in the case of a reflective Ag back contact, with a J_{SC} loss of only 0.2 mA/cm² in the Ag layer. Further reducing the CIGS thickness to 100 nm leads to a low J_{SC} of only 20.4 mA/cm² with a silver back contact, as compared to 13.6 mA/cm² on Mo. This indicates that solar cells with very thin CIGS layers require more sophisticated light trapping strategies to fully absorb the incoming infrared light, such as nanostructured back mirrors [156], [160], [163].

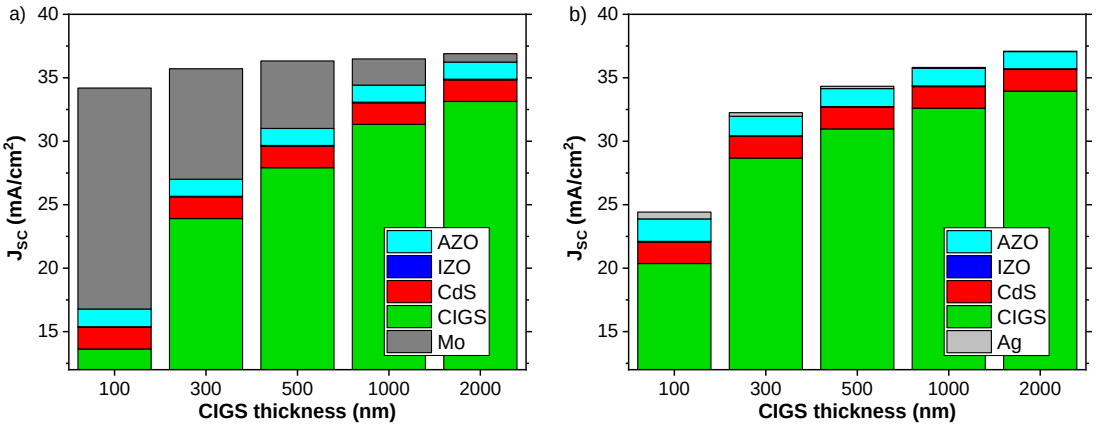

Figure III. 4. J_{SC} of complete solar cells derived from the simulated CIGS absorption. The equivalent J_{SC} losses due to the parasitic absorption in other layers are also calculated. The back contact consists of (a) Mo or (b) Ag, and the thickness of the simulated CIGS film is varied between 100 nm to 2000 nm.

It is also worth mentioning that the fraction of light that is not absorbed in ultrathin CIGS layers on Ag is eventually reflected out of the device, while Mo absorbs most of the light transmitted by CIGS. This enhanced reflection of infrared photons at energies below the CIGS bandgap is beneficial to photovoltaic performance as it lowers the operating temperature of solar cells [195]–[197].

The replacement of the standard Mo back contact by Ag has been simulated for complete solar cells. For ultrathin CIGS layers (<500 nm), the increased reflectance at the CIGS back interface with Ag leads to significant J_{SC} improvements. In the next section, the simulated light absorption of complete solar cells with RBCs will be discussed and compared to the Mo and Ag back contacts.

CIGS thickness (nm)	J_{SC} on Mo (mA/cm²)	J_{SC} loss in Mo (mA/cm²)	J_{SC} on Ag (mA/cm²)	J_{SC} loss in Ag (mA/cm²)
2000	33.1	0.7	34.0	0.0
1000	31.3	2.1	32.6	0.1
500	27.9	5.3	31.0	0.2
300	23.9	8.7	28.7	0.3
100	13.6	17.4	20.4	0.5

Table III. 1. J_{SC} values of complete solar cells with a Mo or Ag back contact, derived from the simulated CIGS absorption. The equivalent J_{SC} loss due to the Mo or Ag back contact is also given. The thickness of the simulated CIGS layers is varied between 100 nm and 2000 nm.

9.3.Simulation of the investigated RBC architectures

In this section, light absorption in CIGS solar cells with a RBC (ZnO:Al (30 nm)/Ag (150 nm)/ZnO:Al (50 nm)/ITO) is simulated. Three thicknesses of ITO are considered: 30 nm, 100 nm and 200 nm.

Figure III. 5 shows an overview of the simulated CIGS absorptions with thicknesses between 2 µm and 100 nm and for the 3 different thicknesses of ITO. Similarly to the case of a silver back contact and regardless of the ITO thickness, absorption in the CIGS layers shows resonances thanks to the enhanced reflectance at the CIGS back contact. Still, the wavelength position of these Fabry-Perot resonances is found to depend on the ITO thickness. To determine whether the ITO thickness can have an impact on the performances of complete cells, the J_{SC} and J_{SC} losses due to each layer of the complete solar cell stack are shown in Figure III. 6.

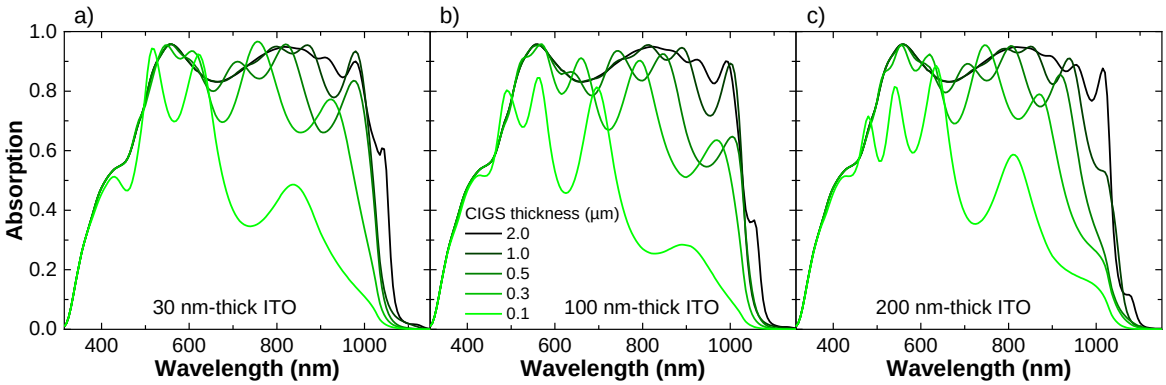

Figure III. 5. Simulation of the CIGS absorption under one-sun illumination, for complete solar cells on a RBC with (a) 30 nm, (b) 100 nm or (c) 200 nm of ITO on top of the RBC. The thickness of the simulated CIGS film is varied from 2 µm to 0.1 µm.

In the case of 2 µm-thick CIGS absorbers, the impact of the ITO thickness on the J_{SC} of complete solar cells is negligible (see also Table III. 2). However, as the CIGS thickness is decreased to 500 nm and below, parasitic absorption in the ITO and Ag layers is increased while absorption in the ZnO:Al film on Ag remains negligible. For example, a solar cell with a 300 nm-thick CIGS absorber exhibits a J_{SC} of 29.0 mA/cm², 28.4 mA/cm² and 28.2 mA/cm² for respective ITO thicknesses of 30 nm, 100 nm and 200 nm. The J_{SC} losses due to the RBC absorption respectively increase from 0.3 mA/cm² to 0.9 mA/cm² and 1.3 mA/cm², as compared to 0.3 mA/cm² when Ag is in direct

contact with CIGS. Still, the J_{SC} losses of the RBC remain much lower than those of a standard Mo back contact, with 8.7 mA/cm² lost for a 300 nm-thick CIGS layer on Mo. Similarly to the case of the Ag back contact, most of the incoming light that is not absorbed in the CIGS layers is reflected out of the solar cell stack. This underlines once again the need for light trapping strategies to achieve full absorption in ultrathin CIGS layers.

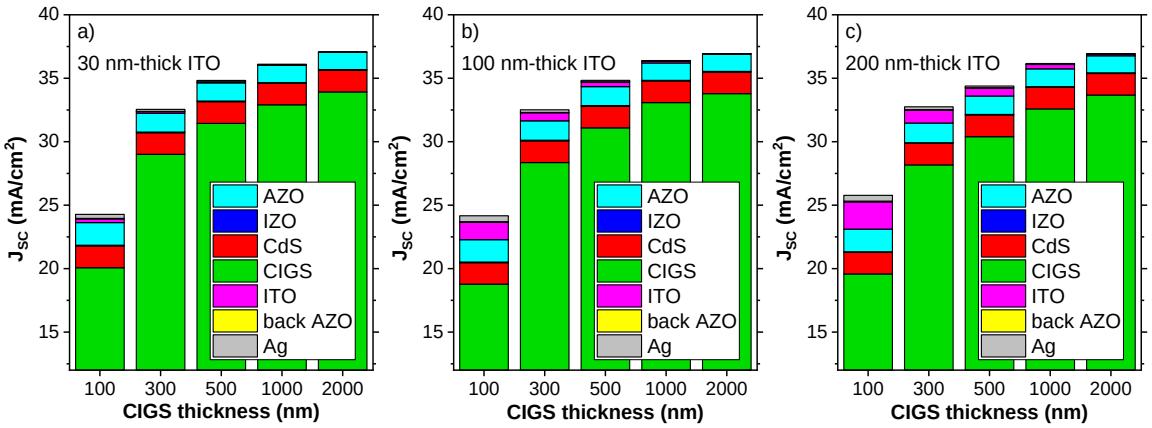

Figure III. 6. J_{SC} values derived from the simulated CIGS absorption of complete solar cells on RBCs with (a) 30 nm, (b) 100 nm or (c) 200 nm of ITO. The equivalent J_{SC} losses due to the parasitic absorption in other layers are also calculated. The thickness of the simulated CIGS film is varied between 100 nm to 2000 nm.

Detailed light absorption in each layer of complete solar cells is shown in Figure III. 7, for a 100 nm-thick ITO layer and two CIGS thicknesses of 2 µm or 500 nm. The RBC is found to improve the simulated CIGS absorptions mainly in the infrared region, as in the case of a silver back contact. As the CIGS thickness is reduced to 500 nm, more light is transmitted to the RBC for wavelengths above 800 nm, leading to parasitic losses in the ITO layer. Still, as long as the CIGS layer is at least 500 nm-thick, losses due to the parasitic absorption of ITO are close to the J_{SC} loss of 0.2 mA/cm² for a bare silver back contact. As a result, for a 500 nm-thick CIGS layer on a RBC with 100 nm of ITO, a promising J_{SC} of 31.1 mA/cm² is expected, which represents a gain of 3.2 mA/cm² as compared to the standard Mo back contact.

	RBC – 30 nm-ITO		RBC – 100 nm-ITO		RBC – 200 nm-ITO	
CIGS thickness (nm)	J_{SC} (mA/cm²)	J_{SC} loss in RBC (mA/cm²)	J_{SC} (mA/cm²)	J_{SC} loss in RBC (mA/cm²)	J_{SC} (mA/cm²)	J_{SC} loss in RBC (mA/cm²)
2000	33.9	0.0	33.8	0.1	33.7	0.2
1000	32.9	0.1	33.1	0.2	32.6	0.4
500	31.4	0.2	31.1	0.5	30.4	0.8
300	29.0	0.3	28.4	0.9	28.2	1.3
100	20.1	0.7	18.8	1.9	19.6	2.7

Table III. 2. J_{SC} values of complete solar cells on RBCs, derived from simulated CIGS absorption. The RBCs include a top layer of ITO with a thickness of 30 nm, 100 nm or 200 nm. The total equivalent J_{SC} losses due to the RBCs are also given. The thickness of the simulated CIGS layers is varied between 100 nm and 2000 nm.

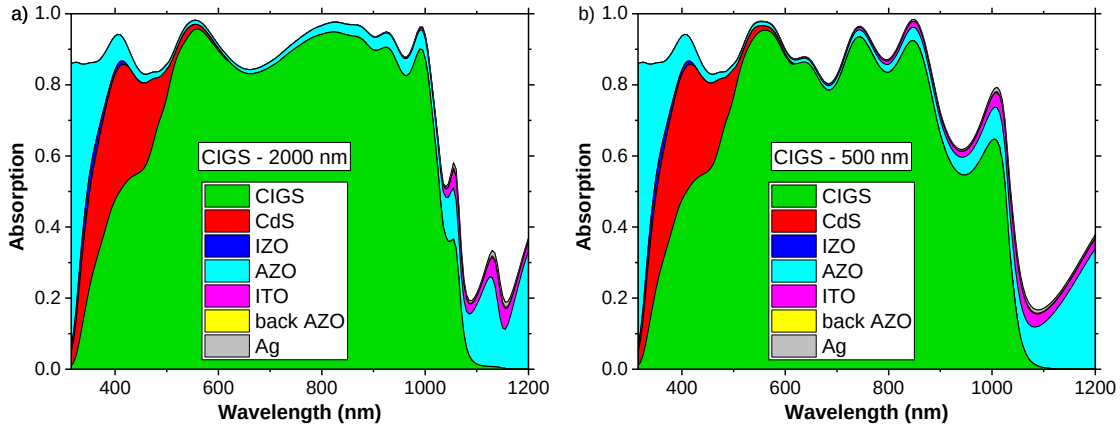

Figure III. 7. Simulated absorption in each layer of complete solar cells. The back contact consists of a RBC with 100 nm-thick top layer of ITO. The thickness of the simulated CIGS layer is either (a) 2000 nm or (b) 500 nm.

9.4.Conclusion of the chapter

To sum up, light absorption in complete CIGS solar cells was simulated in the case of a standard Mo back contact, a bare Ag back contact, and a RBC composed of SLG/ZnO:Al (30 nm)/Ag (150 nm)/ZnO:Al (50 nm)/ITO stacks with ITO thicknesses of 30 nm, 100 nm or 200 nm. Absorption in the CIGS layer was investigated for thicknesses between 2 µm and 100 nm. It was shown that:

- Absorption in CIGS absorbers with a standard thickness of 2 µm can be improved in the infrared region by replacing Mo with a reflective metallic mirror like Ag. The theoretical J_{SC} of complete devices is expected to increase from 33.1 mA/cm² to 34.0 mA/cm².
- Reducing the thickness of the CIGS layer on Mo to 500 nm leads to absorption losses in the Mo film, and to a low J_{SC} of 27.9 mA/cm². In contrast, the higher reflectance at the CIGS back interface with Ag results in an improvement of the J_{SC} up to 31.0 mA/cm².
- Solar cells with a 500 nm-thick CIGS layer on a RBC exhibit a J_{SC} between 30.4 mA/cm² and 31.4 mA/cm², depending on the thickness of the ITO layer on top of the RBC. Hence, the RBC enhances CIGS absorption as efficiently as a bare Ag back contact.
- Light absorption that is simulated in the 30 nm-thick ZnO:Al layer sandwiched between Ag and ITO is negligible.
- The increased total reflectance of ultrathin solar cells with a RBC indicates that light trapping strategies are necessary to fully absorb the incoming light.

Based on the optical simulation described in this chapter, it appears that the optical properties of ultrathin CIGS solar cells are affected by the thickness of the ITO layer on top of the RBC. In addition, the thickness of the ITO layer can be expected to affect its morphology and chemical stability during CIGS co-evaporation [153], and/or the lateral conductivity of the RBC. Hence, the RBCs and complete solar cells studied in the following chapters were fabricated with various ITO thicknesses of 200 nm, 100 nm and 30 nm.

Chapter 10.Characterization of the fabricated RBCs

10.1. Introduction

All of the RBC architectures investigated in this work are made of a multi-layer stack with a top layer consisting of ITO. This ITO layer will be in direct contact with CIGS during its co-evaporation process, which is why we first studied its structural, optical and electrical properties, before and after a 10-minute annealing in air at a nominal temperature of 540°C. This annealing does not exactly reproduce the conditions of CIGS co-evaporation, but can already give some information about the effects of high temperatures (> 450°C) on the properties of ITO. The morphological, electrical and optical properties of the RBC stacks are then characterized before and after annealing in air. Two types of RBC stacks are studied: the first one is SLG/ZnO:Al (50 nm)/Ag (150 nm)/ZnO:Al (30 nm)/ITO (100 or 200 nm), and the second one is a simpler stack without ZnO:Al on Ag: SLG/ZnO:Al (50 nm)/Ag (150 nm)/ITO (100 nm).

10.2. Characterization of ITO on SLG substrates

10.2.1. Structural properties

The morphology of 200 nm-thick ITO layers deposited on SLG was first analyzed, before and after annealing, with SEM top-view images as shown in Figure III. 8.

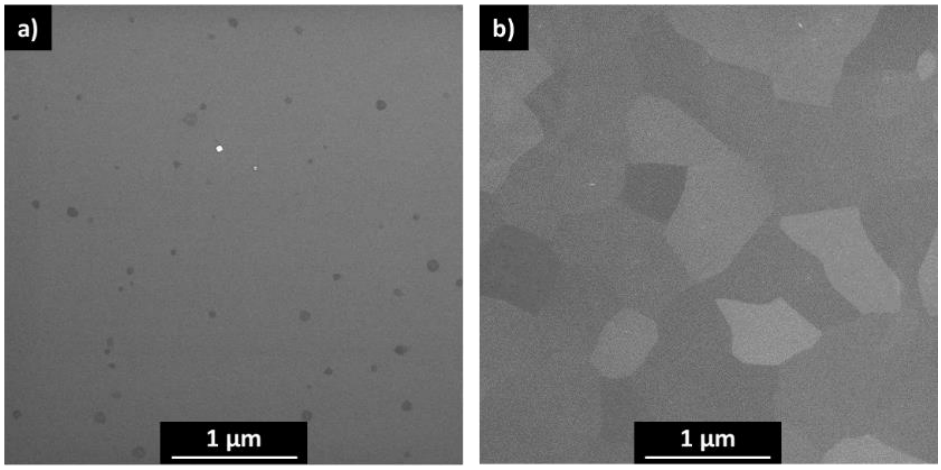

Figure III. 8. SEM top-view images of a 200 nm-thick ITO layer deposited on SLG (a) before and (b) after annealing in air at 540°C for 10 minutes. [ITO_200_1]

While the morphology of ITO does not exhibit grains before annealing, micrometric ITO grains with varying contrast are visible after annealing in air at 540°C. This could be due to the crystallization of ITO during the annealing process. To confirm this, ITO layers before and after annealing were also analyzed by XRD in the Bragg-Brentano configuration, as shown in Figure III. 9.

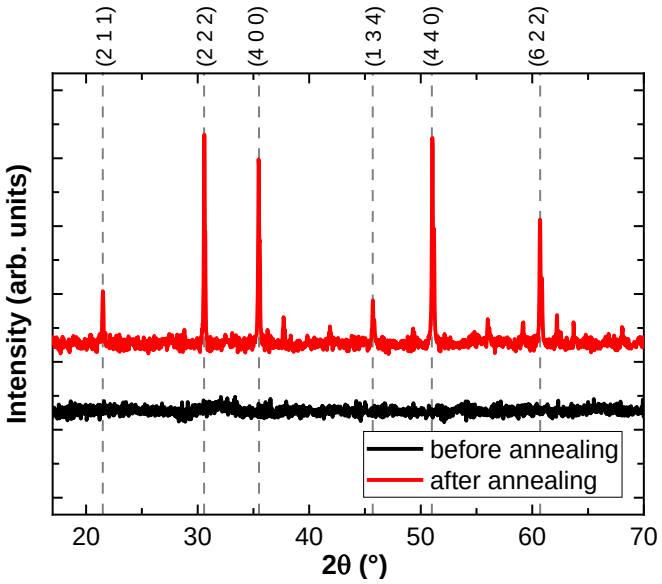

Figure III. 9. XRD measurements of 200 nm-thick ITO layers deposited on SLG, before (black) and after (red) annealing in air at 540°C for 10 minutes. Dashed lines indicate the (*hkl*) values of the main diffraction peaks for an ITO cubic structure (ICDD: 01-088-2160). The background X-Ray signal of the glass substrate was subtracted. (black) [ITO_200_3], (red) [ITO_200_1].

The XRD diffractogram of ITO before annealing shows that as-deposited ITO layers are amorphous while after annealing the ITO layer presents a cubic structure (ICDD: 01-088-2160). This confirms that ITO layers deposited on SLG get crystallized when annealed in air at temperatures > 500°C. The crystallization of amorphous ITO after annealing in air was also reported in previous XRD studies, with annealing temperatures ranging from 122°C to 400°C [198]–[200].

The impacts of the ITO crystallization on its optical and electrical properties are analyzed in the following section.

10.2.2. Optical properties

We first measured the transmittance of a 200 nm-thick ITO layer sputtered on SLG, before and after annealing at 540°C, as seen in Figure III. 10. For comparison, the transmittance of the bare 3 mm-thick SLG substrate is also shown.

The transmittance of the 200 nm-thick ITO layer before annealing exhibits a maximum at a wavelength of λ = 710 nm. For shorter wavelengths, the transmittance of the ITO film is limited by interferences while in the infrared region, free-carrier absorption is responsible for the decreased transmittance of ITO: as ITO is a highly doped semiconductor, free electrons present in the conduction band can absorb infrared light and undergo intraband transitions. However, the transmittance of ITO is strongly increased after annealing, and is less than 10% lower than the transmittance of SLG in the 600 nm – 1200 nm wavelength range. Thus, ITO is expected to have a suitable high transmittance after CIGS deposition, which is necessary to avoid parasitic absorption in the final RBC architecture.

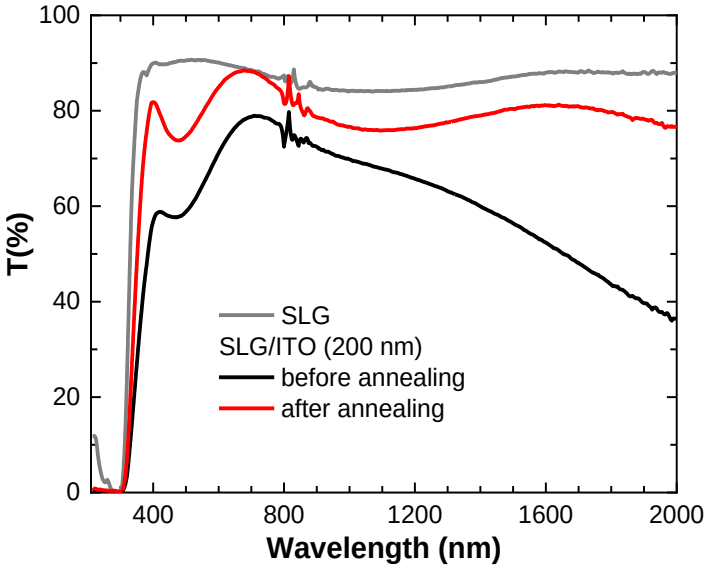

Figure III. 10. Transmittance of 200 nm-thick ITO layers deposited on a 3 mm-thick SLG substrate, (black) before and (red) after annealing. For comparison, the transmittance of a bare 3 mm-thick SLG substrate is also plotted (grey). (black) [ITO_200_3], (red) [ITO_200_1].

The optical properties of the 200 nm-thick ITO layers were further analyzed with ellipsometry measurements, in order to extract the optical indices of ITO, before and after annealing (Figure III. 11). In the visible and infrared areas, the refractive index *n* is increased after annealing while the extinction coefficient *k* is decreased.

This higher *n* can be a result of a denser ITO layer after annealing. Indeed, a maximum film thickness shrinkage of ~10% was previously reported for an amorphous ITO layer [199]. This was attributed to the structural relaxation and crystallization of the ITO layer during annealing, resulting in denser ITO films due to a lower amount of inhomogeneities such as voids.

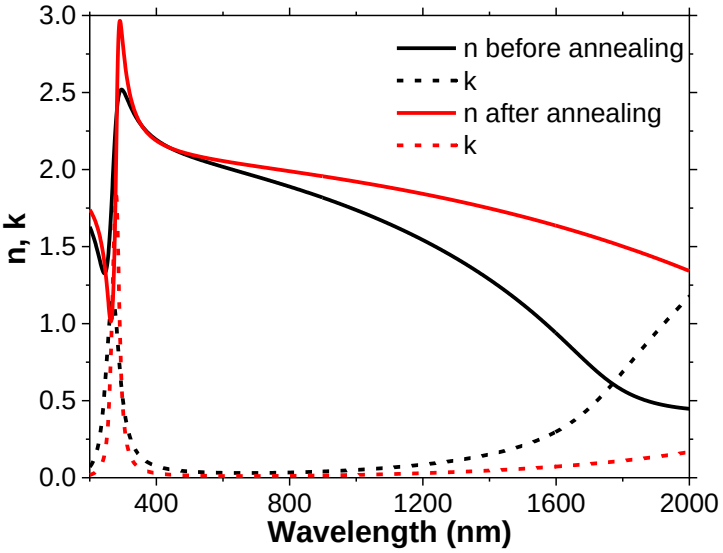

Figure III. 11. Real (*n*) and imaginary (*k*) parts of the refractive indices extracted from the ellipsometric data of 200 nm-thick ITO layers deposited on SLG, (black) before and (red) after annealing in at 540°C for 10 minutes. (*n*,*k*) values of annealed ITO are also given in Appendix C. (black) [ITO_200_2], (red) [ITO_200_1].

The decrease in *k* indicates that the ITO layer is less absorbent upon annealing, which is consistent with the increased transmittance that was also measured. The k index diminishes mostly in the infrared region, which means that free-carrier absorption of ITO is reduced after annealing. This effect was reported to be a result of the crystallization of ITO during annealing, which reduces the amount of structural and chemical defects, thereby decreasing the free carrier concentration of ITO [199]. Besides, it was reported that the incorporation of oxygen in the ITO film can enhance its transmittance [199], [200]. As our annealing process was carried out in air, the addition of oxygen inside the ITO layer cannot be excluded. Given that the co-evaporation of CIGS is performed under high vacuum, ITO films used as a back contact for ultrathin CIGS solar cells might be slightly more absorbent than ITO layers annealed in air.

10.2.3. Electrical properties

The sheet resistance of a 200 nm-thick ITO layer sputtered on SLG was measured with a four-point probe instrument, before and after annealing. The results are summarized in Table III. 3.

	SLG/ITO (200nm)	
	Without annealing [ITO_200_3]	With annealing [ITO_200_1]
R_{SHEET} (Ohm.sq)	45.3 ± 0.4	36.7 ± 0.3

Table III. 3. Sheet resistances of a 200 nm-thick ITO layer deposited on SLG. Average values and standard deviation were calculated from 5 different measurements.

The sheet resistance of the 200 nm-thick ITO film decreases after annealing, as reported in other published works [198]–[200]. In order to determine more precisely the effects of the annealing process on ITO electrical properties, Hall effect measurements were carried out using the Van der Pauw method on SLG/ITO (200nm) samples with and without annealing. The deduced bulk concentration of free carriers, sheet resistance, resistivity and carrier mobility are summarized in Table III. 4.

SLG/ITO (200nm)	Sheet resistance (Ohm.sq)	Resistivity (Ohm.cm)	Bulk carrier concentration (/cm^3)	Carrier mobility (cm^2/V.s)
Before annealing [ITO_200_3]	50.5	9.1 E-4	4.7 E+20	14.5
After annealing [ITO_200_1]	38.1	6.9 E-4	2.0 E+20	46.7

Table III. 4. Hall effect parameters of 200 nm-thick ITO layers deposited on SLG, before and after annealing in air at 540°C for 10 minutes.

The sheet resistance values determined by Hall effect measurements are consistent with the ones assessed with the four-point probe setup. A lower sheet resistance is observed after annealing, which originates from an improved carrier mobility in spite of a decrease of the bulk carrier concentration. Indeed, the free carrier concentration in ITO is commonly attributed to two donor defects: four valent Sn substituting In and oxygen vacancies (respectively noted as Sn_{In}^{+} and V_O^{2+}) [198]–[200]. As discussed in the previous section, the annealing of ITO and its subsequent crystallization is

expected to reduce the amount of donor defects in the ITO structure, leading to a lower free carrier concentration. The possible incorporation of oxygen during the annealing process in air can decrease the concentration of oxygen vacancies, and can also introduce interstitial oxygen sites in the ITO lattice that act as trapping sites that further reduce the density of free carriers [199], [200]. Despite a reduced bulk concentration of free carriers, the crystallization of ITO upon annealing improves the free carrier mobility, which is dependent on the grain size of the ITO layer as the disordered grain boundaries cause electron scattering [199].

10.3. Characterization of the RBCs

10.3.1. Morphology of ITO on top of the RBCs

ITO layers on top of the complete RBC stack were also analyzed in top-view SEM, before and after annealing. Two RBCs are investigated: the first one was made with a ZnO:Al/ITO bilayer on Ag and the following architecture SLG/ZnO:Al (50 nm)/Ag (150 nm)/ZnO:Al (30 nm)/ITO (Figure III. 12), while the second one was prepared with a single ITO layer sputtered on top of Ag, *i.e.* with a stack of SLG/ZnO:Al (50 nm)/Ag (150 nm)/ITO (Figure III. 13).

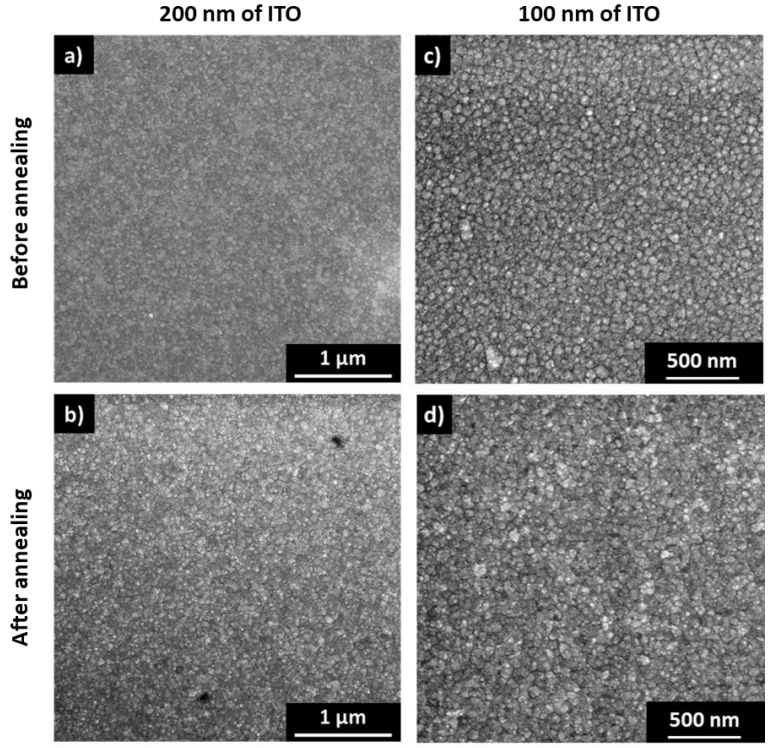

Figure III. 12. SEM top-view images of a RBC (a,c) before and (b,d) after annealing in air at 540°C for 10 minutes. The RBC is made with a stack of SLG/ZnO:Al (50 nm)/Ag (150 nm)/ZnO:Al (30 nm)/ITO, and the top ITO layer has a thickness of either (a,b) 200 nm or (c,d) 100 nm. (a,b) [WP2_26], (c) [WP2_48], (d) [WP2_47].

In the case of a RBC with a ZnO:Al/ITO bilayer on Ag (Figure III. 12), the layer stack appears to be stable under annealing at 540°C as we did not observe any diffusion of Ag or delamination. Prior to annealing, the ITO layer sputtered on top of the RBC shows a rough morphology, which is attributed to the roughness of the underlying Ag layer deposited by e-beam evaporation. Contrary to ITO layers deposited directly on

SLG substrates, micrometric grains of ITO are not observed after annealing. This indicates that the structural properties of ITO after annealing depend on the underlying layer. It is not possible to confirm whether these ITO layers are crystallized upon annealing based on the SEM top-view images only. A grazing incidence XRD analysis could give more information on the crystallinity of the ITO layer, but it was not carried out in this study.

The simplified RBC stack, *i.e.* with a single ITO layer deposited on Ag (Figure III. 13), shows a similar ITO morphology as compared to the case of the RBC including a ZnO:Al layer on Ag. However, micrometric grains of ITO are observed after annealing (Figure III. 13.b), as in the case of an annealed ITO layer deposited on SLG. Note that it is not possible to confirm whether the observed ITO grains are crystallized as this sample was not studied in XRD. Importantly, those micrometric ITO grains were also observed after CIGS co-evaporation in SEM (not shown), in the case of a CIGS batch that for some unknown reason delaminated during the CBD process.

The size of such ITO grains is expected to be a critical parameter for the stability of the RBC during the growth of CIGS layers. Indeed, small ITO grains will lead to a high density of grain boundaries, which could provide nucleation sites for the formation of Ga oxide and/or could promote the diffusion of elements at the CIGS/ITO interface.

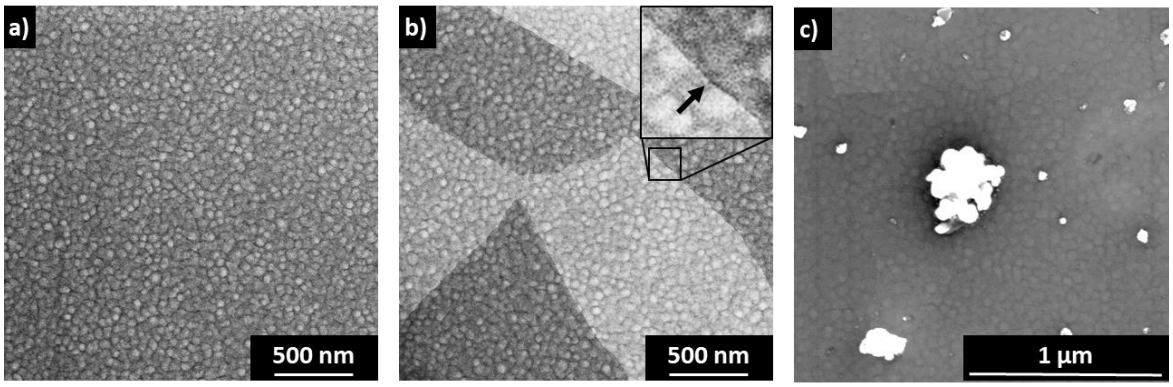

Figure III. 13. SEM top-view images of a RBC (a) before and (b,c) after a 10-minute annealing in air at 540°C. The RBC was prepared with a simplified stack of SLG/ZnO:Al (50 nm)/Ag (150 nm)/ITO (100 nm). Inset in (b): 100 nm × 100 nm region showing a gap at a grain boundary (arrow). After annealing, Ag clusters as seen in (c) were identified on top of the ITO layer by EDX. [WP2_23].

The inset in Figure III. 13.b shows a higher magnification SEM image of a grain boundary in the ITO layer on top of the simplified RBC stack. This feature of the ITO film is emphasized, as some Ag clusters on top of the ITO layer were observed in SEM/EDX (EDX spectra not shown), preferentially at the grain boundaries of the ITO layer (Figure III. 13.c). This indicates that the ITO layer alone does not encapsulate the Ag mirror as efficiently as the ZnO:Al/ITO bilayer. This in turn could lead to Ag diffusion in the CIGS layer, possibly modifying its composition and/or creating local shunt paths due to high ([Ag]+[Cu])/([Ga]+[In]) ratios.

10.3.2. Optical properties of the RBCs

The reflectance in air of RBCs with and without a 30 nm-thick ZnO:Al layer on Ag were determined before and after annealing, as shown in Figure III. 14.

When a ZnO:Al/ITO bilayer is deposited on top of Ag, the RBC is slightly more absorbent in the case of a 200 nm-thick ITO layer as compared to 100 nm (Figure III. 14.a). This is due to the stronger parasitic absorption of the thicker ITO layer. As expected, the wavelength position of the Fabry-Perot resonances depends on the ITO thickness. For both ITO thicknesses the reflectance of the RBCs is improved after annealing, as a result of the improved transparency of ITO. These RBCs exhibit a reflectance over 90% in the wavelength range between 600 nm and 1150 nm. Thus, the RBCs are expected to provide an almost perfect double-pass absorption in ultrathin CIGS solar cells.

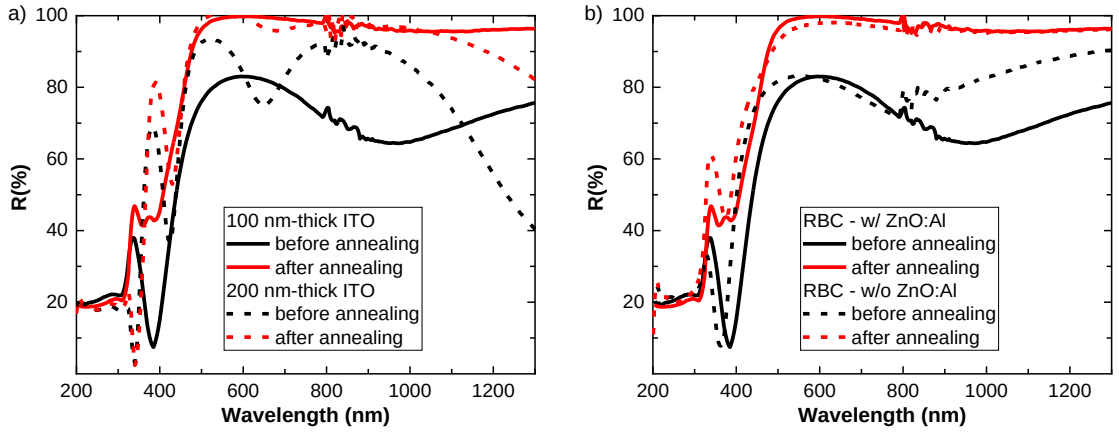

Figure III. 14. Reflectance in air of RBCs before (black) and after (red) a 10-minute annealing at 540°C in air. In (a), the RBCs were prepared with a stack of SLG/ZnO:Al (50 nm)/Ag (150 nm)/ZnO:Al (30 nm)/ITO, with ITO thicknesses of either 100 nm (solid lines) or 200 nm (dashed lines). In (b), RBCs with a ZnO:Al (30 nm)/ITO (100 nm) bilayer (solid lines) and a single ITO (100 nm) layer on Ag (dashed lines) are compared. (a) 100 nm-thick ITO: [WP2_63], 200 nm-thick ITO [WP2_71]. (b) with ZnO:Al: [WP2_63], without ZnO:Al: [WP2_23].

The reflectance of the RBC with a single 100 nm-thick layer of ITO on Ag was also measured in air, before and after a 10-minute annealing in air at 540°C, and compared to the reflectance of the RBC with a ZnO:Al (30 nm)/ITO (100 nm) bilayer sputtered on Ag (Figure III. 14.b).

Before annealing, the RBC without ZnO:Al on top of Ag is more reflective at wavelengths between 800 nm and 1300 nm, as compared to the RBC with ZnO:Al on Ag. However, after annealing both RBCs exhibit a high reflectance above 90% in the 500 – 1300 nm wavelength range thanks again to the improved transmittance of ITO after annealing. RBCs with and without a ZnO:Al layer on Ag are thus expected to provide a similar enhancement of the reflectance at the back interface of CIGS, leading to an almost perfect double-pass absorption in ultrathin CIGS layers.

10.3.3. Electrical properties of the RBCs

The sheet resistance of the various RBC architectures was also determined with a four point probe setup (Table III. 5.).

TCO layers on Ag		R_{SHEET} (Ohm.sq) before annealing	R_{SHEET} (Ohm.sq) after annealing
ZnO:Al (30 nm)/ITO (200 nm)	[WP2_71]	0.12 ± 3.E-4	0.11 ± 3.E-3
ZnO:Al (30 nm)/ITO (100 nm)	[WP2_63]	0.12 ± 1.E-3	0.10 ± 4.E-4
ITO (100 nm)	[WP2_60]	0.15 ± 0.01	0.13 ± 0.01

Table III. 5. Sheet resistances for RBCs with a stack of SLG/ZnO:Al (50 nm)/Ag (150 nm)/ZnO:Al (30 nm)/ITO (100 or 200 nm), and with a simplified architecture consisting of SLG/ZnO:Al (50 nm)/Ag (150 nm)/ITO (100 nm). Average values and standard deviation were calculated from 5 different measurements.

All of the investigated RBCs exhibit a much lower sheet resistance than the ones measured on 200 nm-thick ITO films, with values that are typically observed for metallic layers with thicknesses of ~100 nm. This means that the Ag layer ensures a high lateral conduction in the RBCs. Besides, the sheet resistance of the RBCs is not degraded after annealing, indicating that the lateral transport properties of the RBCs are stable upon annealing and should be compatible with CIGS co-evaporation.

10.4. Conclusion of the chapter

Structural, optical and electrical characterizations were performed on a 200 nm-thick ITO layer sputtered on SLG, and on RBCs with a stack of SLG/ZnO:Al (50 nm)/Ag (150 nm)/ZnO:Al (30 nm)/ITO (100 or 200 nm) or with a simplified architecture of SLG/ZnO:Al (50 nm)/Ag (150 nm)/ITO (100 nm). As a first approximation to reproduce the annealing induced by the co-evaporation of CIGS at temperatures > 450°C, these samples were also analyzed after a 10-minute annealing in air at 540°C. The main findings are summarized below:

- ITO deposited on SLG is amorphous, but is crystallized in the cubic structure upon annealing.
- The crystallization of ITO leads to a denser film and a lower bulk concentration of free carriers. As a result, the ITO layer is more transparent after annealing.
- The formation of ITO crystal grains improves the mobility of free carriers, which in turn reduces the sheet resistance of annealed ITO films.
- The SEM analysis of RBCs with a ZnO:Al (30 nm)/ITO bilayer on Ag does not show any sign of Ag diffusion or delamination after annealing.
- In the case of the RBC with a single 100 nm-thick ITO layer on Ag, large ITO grains as well as local Ag diffusion were detected in SEM/EDX after annealing. The ZnO:Al/ITO stack on Ag is necessary to properly encapsulate Ag at temperatures > 500°C.
- After annealing, both types of RBCs show sheet resistances of ~0.1 Ω.sq and a reflectance above 90% in the wavelength range between 600 and 1150 nm.

To sum up, the RBCs show adequate optical and electrical properties, and the TCO stack deposited on Ag is found to be critical to achieve the encapsulation of Ag. To investigate the compatibility of these RBC architectures with the CIGS co-evaporation process, ultrathin CIGS layers deposited on ITO and RBCs will be characterized in the next chapter.

Chapter 11.Fabrication of ultrathin CIGS solar cells with RBCs

11.1. Introduction and experimental details

The characterization results of ultrathin CIGS layers co-evaporated on Mo, transparent and reflective back contacts are analyzed in the following sections. In particular, the back interface of CIGS with ITO is thoroughly studied by STEM/EDX in order to investigate the presence of an interfacial Ga oxide compound that can be detrimental to solar cell efficiency. Standard CIGS deposition temperatures of 550°C were used, as well as lower temperatures of 500°C and 450°C in order to mitigate the growth of Ga oxide [36], [150], [153]. Importantly, some of the RBCs were also coated with thin Al_2O_3 layers (≤ 3 nm) as such alumina films were shown to reduce the formation of Ga oxide [37], [192]. In addition, these thin alumina layers could also contribute to the CIGS rear passivation, though the fixed negative charges of such thin layers are not expected to create a strong back surface field [141], [142]. The performances of complete solar cells are then discussed with regards to the material characterizations and the growth of Ga oxide.

Three different designs of experiments are reported in separate sections of this chapter. In order to provide a clear overview of the described samples, the specific features of each design of experiment are listed below:

1. A first batch of ultrathin solar cells was made to compare Mo back contacts with RBCs including a 200 nm-thick ITO layer, *i.e.* with a stack of SLG/ZnO:Al (50 nm)/Ag (150 nm)/ZnO:Al (30 nm)/ITO (200 nm). The back contacts were covered with 8 nm-thick NaF precursor layers before the co-evaporation of CIGS at 550°C or 500°C in a 3-stage process. A 1.5 nm-thick layer of alumina was also deposited on half of the RBCs.

2. A second batch of ultrathin solar cells was fabricated with Mo references as well as RBCs including a thinner ITO layer of 100 nm, with and without a ZnO:Al layer on top of Ag, *i.e.* a stack of SLG/ZnO:Al (50 nm)/Ag (150 nm) with ZnO:Al (30 nm)/ITO (100 nm) or ITO (100 nm) on top. Na was incorporated to CIGS by thermal evaporation of 8 nm-thick NaF precursor layers on each back contact prior to CIGS deposition. CIGS was co-evaporated in a 3-stage process, with maximum substrate temperatures of 550°C and 500°C. In addition, RBCs covered with 1.5 nm and 3 nm-thick alumina layers were also investigated. Finally, the EQE of solar cells with a RBC and an additional MgF_2 antireflection coating were analyzed.

3. In a different co-evaporation tool, a third batch of ultrathin solar cells was prepared with a Mo back contact, as well as a transparent back contact and a RBC. CIGS was co-evaporated in a 1-stage process at a low substrate temperature of 450°C. Na was then incorporated via a NaF post deposition treatment (PDT) at a substrate temperature of 350°C under Se flux, with a thickness of 8 nm and a rate of 1 nm/min. The composition of each back contact is given here:

    - The Mo reference consists of: SLG/Al_2O_3 (300 nm)/Mo (800 nm). Here, the 300 nm-thick alumina layer prevents the diffusion of Na from the SLG substrate.

- The transparent back contact is made of: SLG/ZnO:Al (30 nm)/ITO (300 nm). The ZnO:Al layer is used as a diffusion barrier for Na from the SLG.
- The RBC stack consists of: SLG/ZnO:Al (50 nm)/Ag (150 nm)/ZnO:Al (30 nm)/ITO (30 nm). In this case, the RBC was not covered with thin Al_2O_3 layers.

11.2. RBCs with a 200 nm-thick ITO layer

11.2.1. CIGS morphology and composition

Ultrathin CIGS solar cells fabricated on top of RBCs with a 200 nm-thick top layer of ITO are reported in this section. Two batches of CIGS layers were prepared at a maximum substrate temperature of either 550°C or 500°C, and a 1.5 nm-thick alumina layer was deposited on half of the RBCs prior to CIGS co-evaporation. The impacts of these deposition conditions on the formation of Ga oxide at the CIGS/ITO interface were studied.

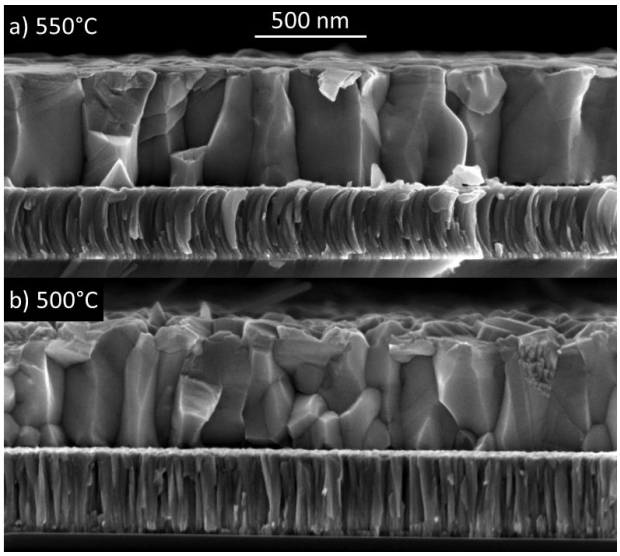

Figure III. 15. SEM cross-section images of ultrathin CIGS layers co-evaporated on Mo at (a) 550°C and (b) 500°C. (a) [180418-2XB], (b) [180418-3XB].

Here, Na was incorporated to the CIGS films by thermal evaporation of an 8 nm-thick NaF precursor layer on each back contact. CIGS was deposited in a three stage co-evaporation process, with average composition ratios of CGI = 0.87 ± 0.01 and GGI = 0.40 ± 0.01 determined by XRF analyses of CIGS layers on Mo control samples, and with an average thickness of 530 ± 20 nm measured with a profilometer.

The morphology and composition profiles of CIGS layers on Mo back contacts were first investigated. SEM cross-section images of CIGS layers deposited at 550°C and 500°C on Mo are shown in Figure III. 15. Similarly to our previous observations, the co-evaporation of CIGS on Mo at 500°C leads to smaller CIGS grains and a rougher top surface.

Regardless of the CIGS deposition temperature, flat CGI profiles are observed in GD-OES (Figure III. 16). In contrast, the GGI composition profile is steeper when CIGS is deposited at 500°C, consistently with previous GD-OES characterizations reported in this thesis. This grading is due to the temperature-dependent diffusion rates of In and

Ga, as they decrease with lower deposition temperatures [29], [60], [124], [126], [201].This steeper GGI depth profile results in a conduction band grading and a subsequent back surface field that drifts electrons toward the *p-n* heterojunction, thereby contributing to the rear passivation of CIGS [11], [13], [54].

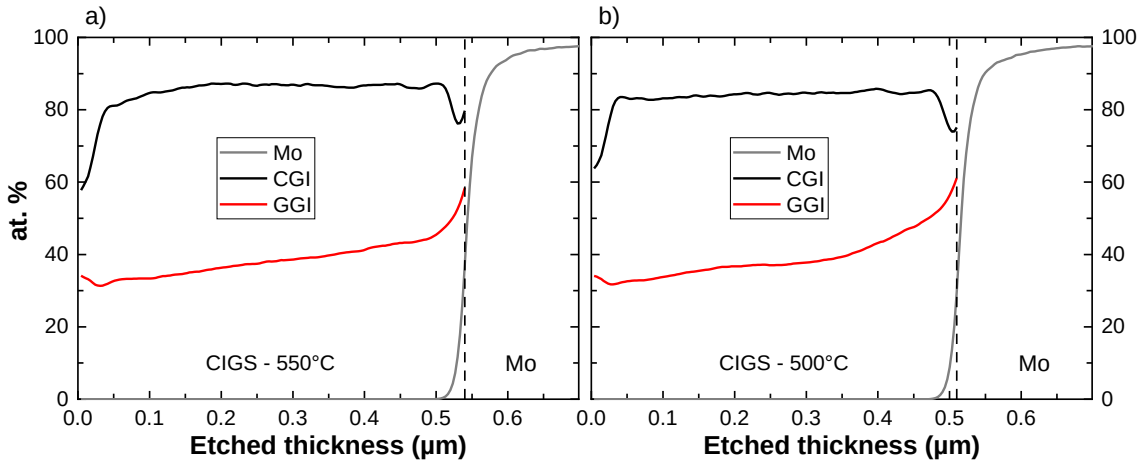

Figure III. 16. GD-OES composition profiles of ultrathin CIGS layers deposited on Mo back contacts. CIGS was co-evaporated in a 3-stage process with a maximum substrate temperature of (a) 550°C or (b) 500°C. Dashed lines indicate the position of the interface between CIGS and Mo. The average CGI and GGI values were calibrated with XRF measurements and the CIGS thickness was determined with a profilometer. (a) [180418-2XA], (b) [180418-3XA].

In order to closely investigate the formation of Ga oxide at the interface between CIGS and ITO, ultrathin CIGS layers co-evaporated on RBCs with a 200 nm-thick top layer of ITO were analyzed in STEM/EDX.

11.2.2. STEM/EDX study of the CIGS back interface with 200 nm-thick ITO

The STEM dark field image of a complete CIGS/RBC stack is shown in Figure III. 17, together with its corresponding EDX elemental maps. In this case, CIGS was co-evaporated at a maximum substrate temperature of 550°C on a RBC with 200 nm of ITO.

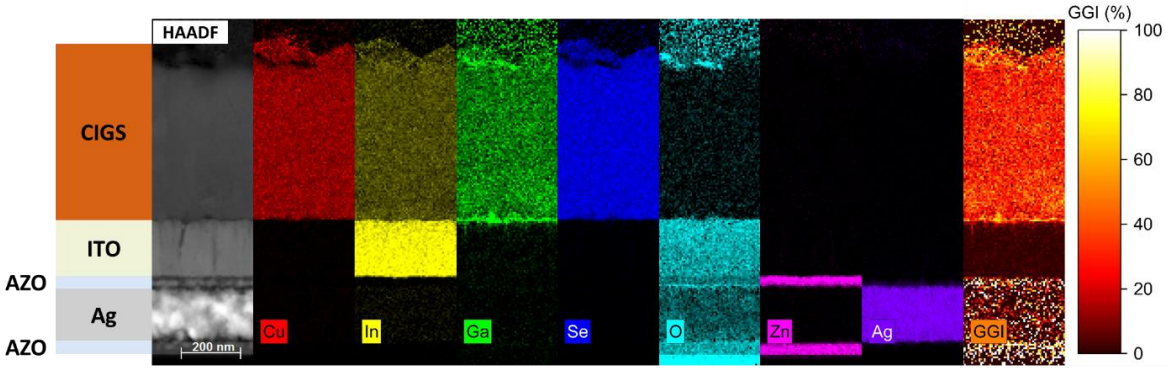

Figure III. 17. Schematic of an ultrathin CIGS solar cell on a RBC, with its high angle annular dark field (HAADF) image and EDX maps. CIGS was deposited at 550°C on a RBC with a 200 nm-thick ITO layer. [180418-2B1].

The layer stack of the RBC appears to be stable during CIGS co-evaporation. Ag is not detected within the ZnO:Al layer, which means that the RBC stack successfully prevents the diffusion of Ag up to the CIGS layer and avoids a change of its [I]/[III] elemental ratio.

Ga is found to segregate at the interface between CIGS and ITO, indicating the possible presence of Ga oxide. This Ga accumulation leads to a high GGI ratio at the back interface of CIGS. Therefore, the GGI maps of CIGS layers deposited on RBCs were compared in order to analyze the effects of the CIGS deposition temperature and of the addition of a 1.5 nm-thick alumina layer on the RBC.

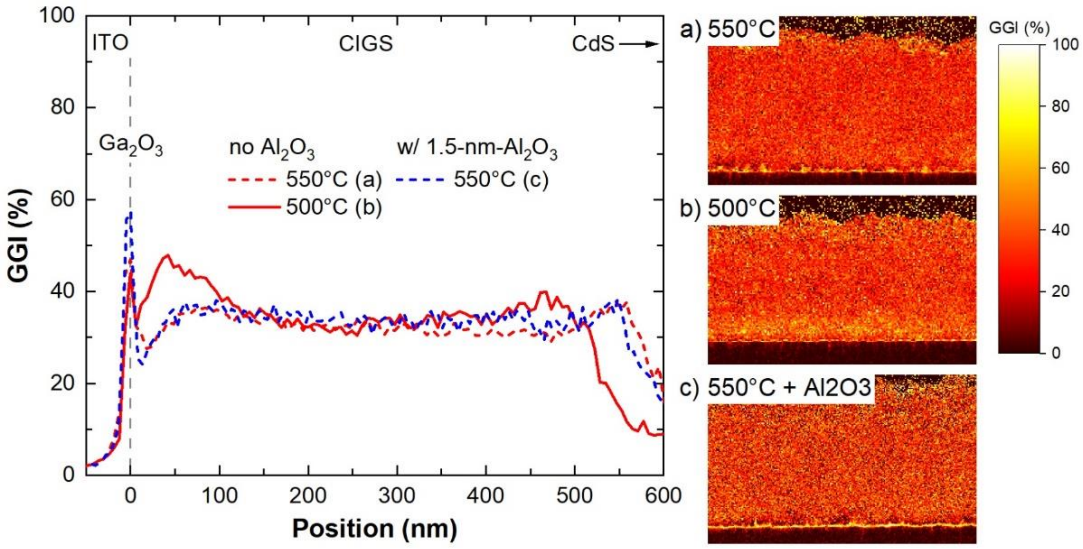

Figure III. 18. Average GGI depth profiles determined from each corresponding STEM/EDX mapping. Ultrathin CIGS layers were co-evaporated on (a,b) bare RBCs and (c) a RBC covered with a 1.5 nm-thick Al_2O_3 layer, at deposition temperatures of (a,c) 550°C and (b) 500°C. (a) [180418-2B1], (b) [180418-3B1], (c) [180418-2B2].

Figure III. 18 shows the GGI maps of CIGS films on RBCs, with their corresponding depth profiles averaged on the total width of the CIGS slabs. CIGS layers were co-evaporated at 550°C on a RBC with and without a 1.5 nm-thick Al_2O_3 layer, and at 500°C on a RBC without alumina. As in the case of Mo back contacts, depositing CIGS on a RBC at a lower temperature of 500°C leads to a steeper GGI back grading. At this scale, the co-evaporation temperature and the addition of alumina do not clearly modify the growth of Ga oxide: all samples exhibit similar GGI peaks and a thin region at the CIGS back contact that is depleted in Ga.

The formation of Ga oxide was also investigated closer to the CIGS/ITO interface (Figure III. 19). The co-evaporation of CIGS at 550°C on a bare RBC leads to a rough Ga oxide layer that also grows inside CIGS and ITO grain boundaries. The GaO_X layer formed at 550°C is smoother when a 1.5 nm-thick alumina film is deposited onto the RBC (Figure III. 19.c). However, it is also thicker, which means that the thin Al_2O_3 layer on ITO does not avoid the formation of a Ga oxide layer but reduces its roughness. Finally, depositing CIGS on a bare RBC at 500°C instead of 550°C leads to a Ga oxide layer with a similar thickness (Figure III. 19.b), but with a lower roughness. There is also less depletion of Cu, In and Se in the CIGS layer, which means that the Ga oxide film might be porous, forming grains or islands at the CIGS back interface.

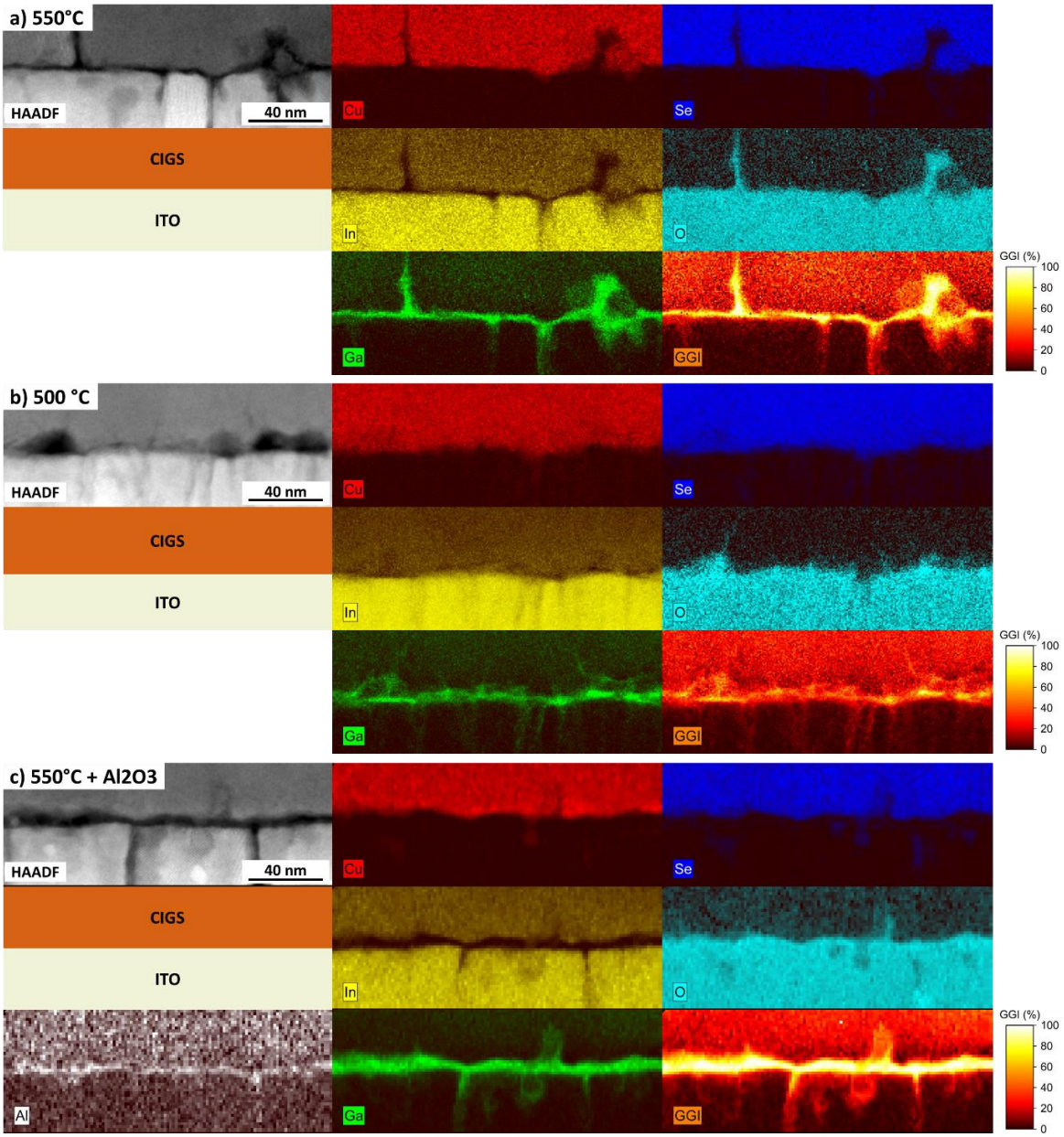

Figure III. 19. STEM/EDX maps zoomed at the CIGS interface with the ITO layer on top of the RBC. Schematics of the observed layers are also shown. CIGS was co-evaporated at (a,c) 550°C and (b) 500°C. In (c), the RBC was covered with a 1.5 nm-thick alumina layer prepared by ALD. (a) [180418-2B1], (b) [180418-3B1], (c) [180418-2B2].

It is also worth mentioning that in the case of a RBC covered with 1.5 nm of Al_2O_3, the EDX signals of Al and Ga are overlapped, possibly due to the formation of a mixed $(Al_xGa_{1-x})_2O_3$ compound [202], [203]. This potential chemical reaction might affect the passivation properties of the alumina film, in particular its density of interface traps.

To determine the impacts of this Ga oxide growth, the performances of ultrathin solar cells on Mo and RBCs with 200 nm-thick ITO layers are described and compared in the following section.

11.2.3. Solar cell performances

The light and dark I(V) characteristics of each best solar cell are shown in Figure III. 20. CIGS was co-evaporated at 550°C or 500°C, on RBCs with and without a 1.5 nm-thick alumina layer and Mo references with a 30 nm-thick Al_2O_3 diffusion barrier. A summary of best and average light I(V) parameters is provided in Table III. 6, and the dark I(V) parameters fitted for each best solar cell are given in Table III. 7.

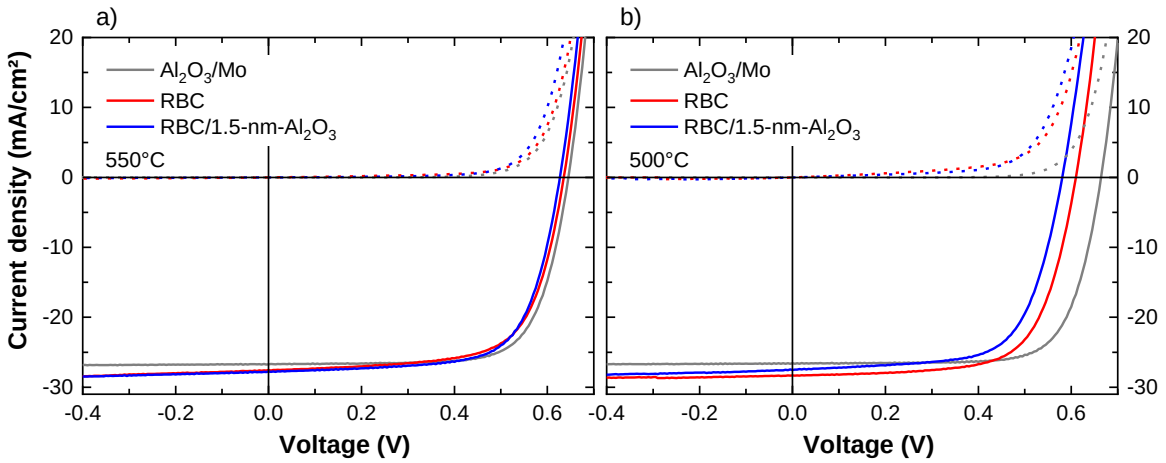

Figure III. 20. I(V) characteristics under one-sun illumination (solid lines) and in the dark (dashed lines), for each best ultrathin solar cell. Back contacts are made of Mo with a 30 nm-thick alumina diffusion barrier, as well as RBCs with and without a 1.5 nm-thick Al_2O_3 layer on top. CIGS was co-evaporated at temperatures of (a) 550°C and (b) 500°C. (a) Mo: [180418-2A2_c8], RBC: [180418-2B1_c9], RBC/Al_2O_3: [180418-2B2_c2]. (b) Mo: [180418-3A2_c9], RBC: [180418-3B1_c1], RBC/Al_2O_3: [1804183-3B2_c13].

		Average / best cell light I(V) parameters			
CIGS deposition temperature	Back contact	Eff. (%)	J_{SC} (EQE) (mA/cm²)	V_{OC} (mV)	*FF* (%)
550°C	Al_2O_3/Mo	11.7 ± 0.5 / 12.6	26.7	624 ± 14 / 647	70.4 ± 1.7 / 72.7
[180418-2]	RBC*	11.3 ± 0.4 / 11.9	27.6	619 ± 10 / 634	66.5 ± 1.4 / 67.8
	RBC/1.5-nm-Al_2O_3	11.4 ± 0.3 / 12.0	27.8	623 ± 9 / 626	66.1 ± 1.9 / 69.0
500°C	Al_2O_3/Mo	12.6 ± 0.5 / 13.1	26.6	657 ± 16 / 666	72.3 ± 1.5 / 74.1
[180418-3]	RBC	10.9 ± 0.4 / 11.7	28.3	601 ± 6 / 609	64.1 ± 2.5 / 67.9
	RBC/1.5-nm-Al_2O_3*	10.6 ± 0.1 / 10.7	27.6	571 ± 6 / 566	67.2 ± 0.8 / 68.5

Table III. 6. Summary of light parameters for each type of back contact, with CIGS co-evaporation temperatures of 550°C and 500°C. The average light I(V) parameters and standard deviation were calculated from the 10 best solar cells, except for J_{SC} values which were calculated from the integrated EQE of each respective best cell. *Average values given for the 5 best solar cells only, because of a strong shunting behavior of unknown origin in most cells.

First, the co-evaporation of CIGS at 550°C on a bare RBC with a 200 nm-thick top layer of ITO leads to a best cell J_{SC} of 27.6 mA/cm², instead of 26.7 mA/cm² for a Mo back contact. This J_{SC} improvement almost compensates for the decrease of the average *FF* from 70.4 ± 1.7 % to 66.5 ± 1.4 % as compared to Mo, and results in an average

efficiency of 11.3 ± 0.4 % with the bare RBC that is close to the average efficiency of 11.7 ± 0.5 % obtained with the Mo reference. The *FF* loss observed in the case of the RBC seems to be related to a voltage-dependent current collection (Figure III. 20.a), rather than a decrease of the fitted R_{SH} values (Table III. 7). Adding a 1.5 nm-thick alumina layer on the RBC leads to the formation of a smoother Ga oxide layer, but it does not clearly improve the solar cell performances as it results in an average efficiency of 11.4 ± 0.3 %, as well as similar light and dark I(V) parameters. For the best solar cells prepared at 550°C, replacing Mo with a RBC enhances the EQE at wavelengths between 800 and 1000 nm (Figure III. 21). However, best solar cells with a RBC show some collection losses in the 500 – 600 nm wavelength range, which could be related to the growth of Ga oxide at the back interface of CIGS and the subsequent depletion of Ga resulting in a reverse back surface field. This effect could also be the origin of the voltage-dependent photocurrent observed in Figure III. 20.a.

			Best cell dark I(V) parameters		
CIGS deposition temperature	Back contact		J_0 (mA/cm^2)	R_{SH} (Ω.cm^2)	R_S (Ω.cm^2)
550°C [180418-]	Al_2O_3/Mo	[-2A2_c8]	5.10^{-5}	> 1.10^6	0.2
	RBC	[-2B1_c9]	6.10^{-5}	2.10^3	< 0.1
	RBC/1.5-nm-Al_2O_3	[-2B2_c2]	8.10^{-5}	4.10^3	0.2
500°C [180418-]	Al_2O_3/Mo	[-2A2_c9]	3.10^{-5}	> 1.10^6	< 0.1
	RBC	[-2B1_c2] *	1.10^{-4}	8.10^2	0.1
	RBC/1.5-nm-Al_2O_3	[-2B2_c13]	2.10^{-4}	3.10^2	1.1

Table III. 7. Dark I(V) parameters of each best solar cell, fitted with a 1-diode model and an ideality factor of 2 (J_0: saturation current, R_{SH}: shunt resistance, R_S: series resistance). *Second best cell was fitted due to measurement artefacts in the case of the best cell.

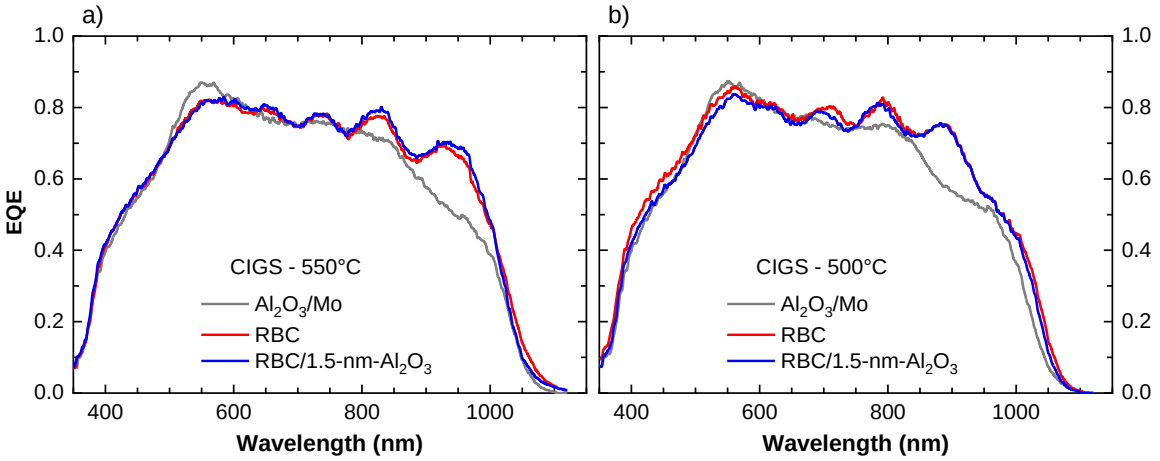

Figure III. 21. EQE of best solar cells prepared on back contacts made of Mo with a 30 nm-thick alumina diffusion barrier, as well as RBCs with and without a 1.5 nm-thick Al_2O_3 layer on top. CIGS was co-evaporated at temperatures of (a) 550°C and (b) 500°C. (a) Mo: [180418-2A2_c8], RBC: [180418-2B1_c9], RBC/Al_2O_3: [180418-2B2_c2]. (b) Mo: [180418-3A2_c9], RBC: [180418-3B1_c1], RBC/Al_2O_3: [1804183-3B2_c13].

Reducing the deposition temperature of CIGS from 550°C to 500°C improves the average efficiency of solar cells on Mo references from 11.7 ± 0.5 % to 12.6 ± 0.5 %, mainly thanks to a V_{OC} increase from 624 ± 14 mV to 657 ± 16 mV. This higher average V_{OC} is attributed to the steeper GGI grading formed at 500°C that contributes to the rear passivation of CIGS. On the other hand, the co-evaporation of CIGS at 500°C on a bare RBC and a RBC covered with a 1.5 nm-thick Al_2O_3 layer results in lower efficiencies of 10.9 ± 0.4 % and 10.6 ± 0.1 %, respectively. These decreased efficiencies are correlated to a lower average V_{OC} and a higher fitted J_0, in spite of the steeper GGI grading that was observed in STEM/EDX when CIGS is deposited on RBCs at 500°C. For a RBC with a 200 nm-thick ITO film, it does not seem critical to control and reduce the growth of Ga oxide by reducing the CIGS deposition temperature. In addition, the *FF* of cells with CIGS deposited at 500°C on RBCs are lower than in the case of the Mo reference. These *FF* losses are not correlated to voltage-dependent photocurrents but to lower values of fitted R_{SH} (Table III. 7), whose detrimental impact on the slope of the dark I(V) curves is visible (Figure III. 20.b). Note that here, the origin of these rather low R_{SH} is unknown. The EQE of the best cell fabricated at 500°C on a bare RBC also results in a slightly higher J_{SC} of 28.3 mA/cm² thanks to reduced collection losses for wavelengths between 500 nm and 600 nm. These effects indicate a better collection efficiency for cells fabricated at 500°C, which has been attributed to a reduced segregation of Ga oxide at the CIGS/ITO interface.

Finally, the EQE of best cells prepared at 550°C on a Mo and a bare RBC were compared to the simulated absorption in each layer of the complete stack (Figure III. 22). The CIGS layers were simulated with a thickness of 510 nm and a bandgap of 1.2 eV in the case of the Mo back contact, and with a thickness of 530 nm and a bandgap of 1.17 eV in the case of the RBCs. The lower bandgap of 1.17 eV that was used to fit the EQE of the cell on the RBCs is a consequence of the Ga oxide formation that consumes Ga from the CIGS layers and thus reduces its bandgap. The simulated CIGS thicknesses are in good agreement with the experimental average thickness of 530 ± 20 nm. Note that for each type of back contact, the simulated CIGS absorption is higher than the EQE because the optical model does not take into account carrier recombination.

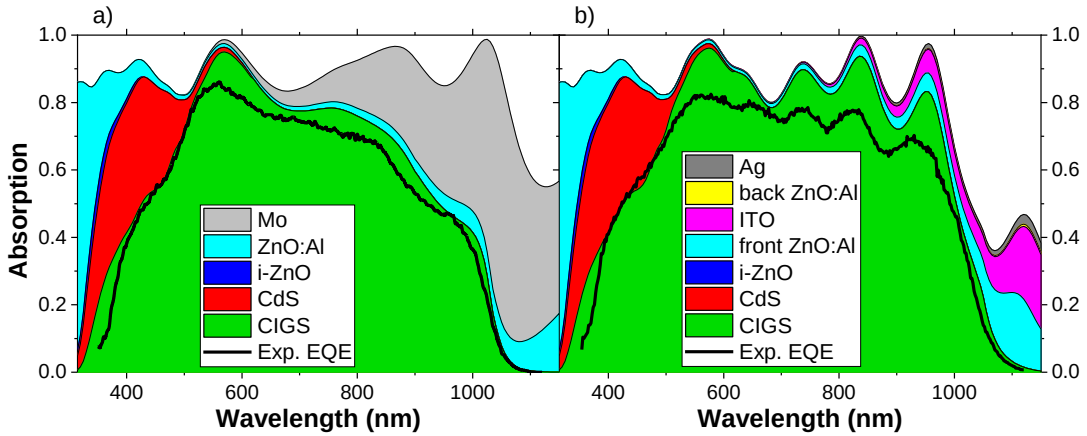

Figure III. 22. Simulated absorption in each layer of complete CIGS solar cells fabricated at 550°C. The back contacts consist of (a) Mo and (b) a RBC with a 200 nm-thick ITO layer on top. The experimental EQE curves are shown for comparison with the simulated absorption of CIGS. (a) [180418-2A2_c8], (b) [180418-2B1_c9].

From these simulation results, the EQE enhancement measured with a RBC can be attributed to the improved back contact reflectivity and CIGS absorption. As a result, the theoretical J_{SC} derived from the simulated CIGS absorption is increased from 28.0 mA/cm^2 on Mo to 31.2 mA/cm^2 on a bare RBC. However, the 200 nm-thick ITO layer is responsible for a J_{SC} loss of 0.7 mA/cm^2 due to its parasitic absorption of photons whose energy is above the CIGS bandgap. This could partly explain the promising but modest maximal J_{SC} gain of 1.7 mA/cm^2 that was achieved by replacing Mo with a RBC including 200 nm of ITO.

To sum up, the average efficiencies of ultrathin CIGS cells fabricated at 550°C on Mo and RBCs with 200 nm of ITO are similar. With this RBC, the J_{SC} is increased from 26.7 mA/cm^2 to 27.6 mA/cm^2 as compared to Mo but a slight decrease of the average *FF* is observed due to a voltage-dependent photocurrent. This has been attributed to the formation of Ga oxide at 550°C. Nevertheless, this Ga oxide compound is not strongly detrimental to the cell performances and V_{OC} in the case of a RBC with a 200 nm-thick ITO layer. Indeed, reducing the co-evaporation temperature of CIGS to 500°C mitigates the growth of Ga oxide but was not found to improve the average V_{OC}, *FF* and efficiency of complete cells.

All in all, CIGS solar cells fabricated on RBCs with 200 nm of ITO do not exhibit higher efficiencies than cells on Mo. In particular, optical simulations reveal that the ITO layer is responsible for most of the parasitic absorption of light in the RBC. Furthermore, adding a 1.5 nm-thick Al_2O_3 layer did not enhance the performances of CIGS devices. This is why RBCs with 100 nm-thick top layers of ITO were investigated, and Al_2O_3 layers with thicknesses of 1.5 nm and 3 nm were tested.

11.3. RBCs with a 100 nm-thick ITO layer

11.3.1. CIGS morphology and composition profile

The RBCs investigated in this section were made with a 100 nm-thick top layer of ITO. Two types of RBCs were used, one with a ZnO:Al layer on top of Ag: SLG/ZnO:Al (50 nm)/Ag (150 nm)/ZnO:Al (30 nm)/ITO (100), and a simpler one without ZnO:Al on Ag, *i.e.* SLG/ZnO:Al (50 nm)/Ag (150 nm)/ITO (100 nm). This simplified RBC stack was studied in an attempt to simplify the architecture of the back contact.

The RBCs with a ZnO:Al/ITO bilayer on top of Ag were tested with four batches of ultrathin CIGS layers prepared in a 3-stage co-evaporation process, with a maximum substrate temperature of 550°C or 500°C. An external supply of Na was provided by thermal evaporation of an 8 nm-thick NaF precursor layer on each back contact. Average atomic ratios of CGI = 0.88 ± 0.02 and GGI = 0.40 ± 0.01 were determined from the XRF signal of CIGS on Mo references, and an average CIGS thickness of 500 ± 20 nm was measured with a profilometer.

To examine the simpler RBC architecture, a single batch of ultrathin CIGS layers was co-evaporated at 500°C on back contacts made of Mo, as well as RBCs with and without a 30 nm-thick ZnO:Al layer on top of Ag. The RBCs were covered with a 3 nm-thick alumina film deposited by ALD. 8 nm-thick precursor layers were deposited on each of the back contact. Average CIGS composition ratios of CGI = 0.85 ± 0.03 and GGI = 0.39 ± 0.03 were determined by XRF analysis of CIGS/Mo samples, and an average CIGS thickness of 550 ± 20 nm was measured with a profilometer.

SEM cross-section images of ultrathin CIGS layers deposited on Mo and RBCs are presented in Figure III. 23. The CIGS layers exhibit an average thickness of 480 ± 30 nm, in good agreement with the profilometer measurements.

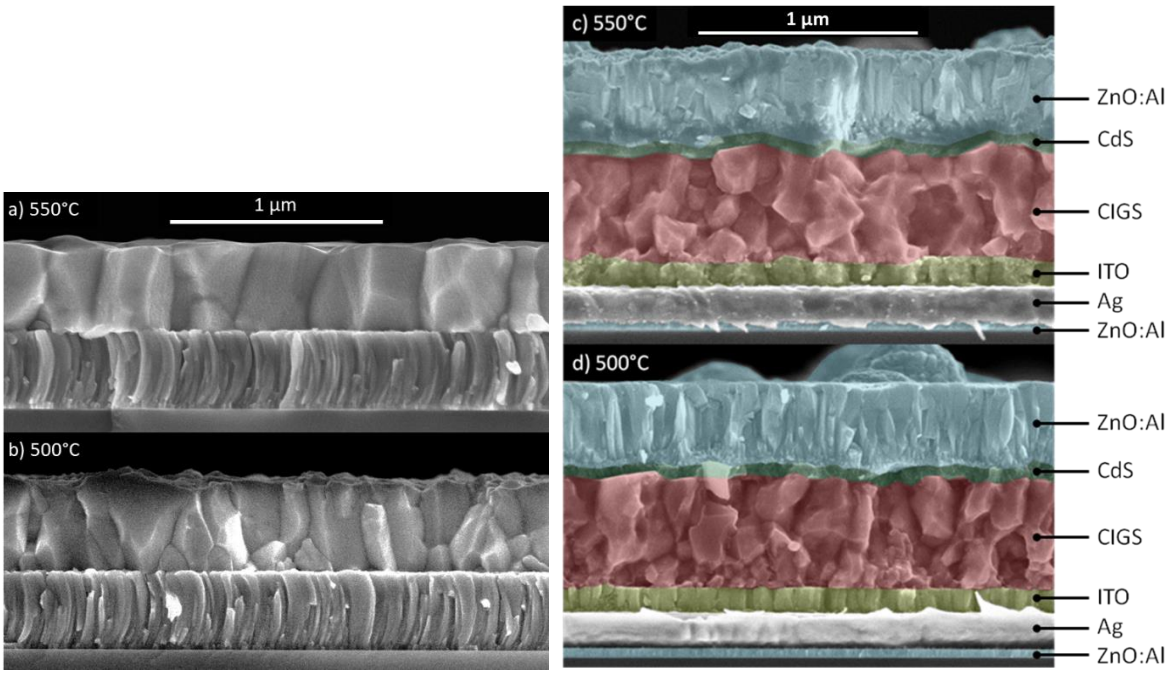

Figure III. 23. SEM cross-section images of ultrathin CIGS layers and complete solar cells co-evaporated in a 3-stage process on (a,b) Mo and (c,d) RBCs with a 100 nm-thick ITO layer. The maximum substrate temperature during CIGS deposition was either (a,c) 550°C or (b,d) 500°C. (a) [180503-2XB], (b) [180503-3XB], (c) [180720-3B1], (d) [180725-3B1].

These SEM images reveal that large and columnar CIGS grains are formed when co-evaporating CIGS in a 3-stage process at 550°C on Mo. However, the size of CIGS grains is reduced when the deposition temperature of CIGS is decreased from 550°C to 500°C, regardless of the type of back contact. The resulting increased density of grain boundaries can possibly be detrimental for the collection efficiency of photogenerated carriers [82]. The back contact also seems to affect the morphology of CIGS, as ultrathin CIGS layers grown on a RBC show smaller grains than their counterparts on Mo.

It is worth mentioning that the morphology of the ITO layer on top of the RBC depends on the deposition temperature of CIGS. Indeed, a smooth ITO film with columnar grains is visible when CIGS is deposited at 500°C. However, ITO grains are not clearly observed after CIGS deposition at 550°C and the back interface of CIGS also looks rougher. To track the interfacial composition between the RBC and the CIGS layer, the composition profiles of those CIGS samples were also analyzed.

The GD-OES analysis of ultrathin CIGS layers co-evaporated in a 3-stage process with a maximum substrate temperature of either 550°C or 500°C is shown in Figure III. 24. Back contacts consist of 300 nm-thick Mo layers and RBC stacks with a 100 nm-thick ITO layer on top.

For CIGS layers grown on Mo, the CGI ratio in the bulk of the CIGS is constant for both deposition temperatures of 550°C and 500°C. Thanks to the intentionally higher Ga

rate during the first stage of CIGS co-evaporation, a GGI grading is achieved. Once again, this GGI grading is also found to be steeper when CIGS is co-evaporated at a lower substrate temperature of 500°C.

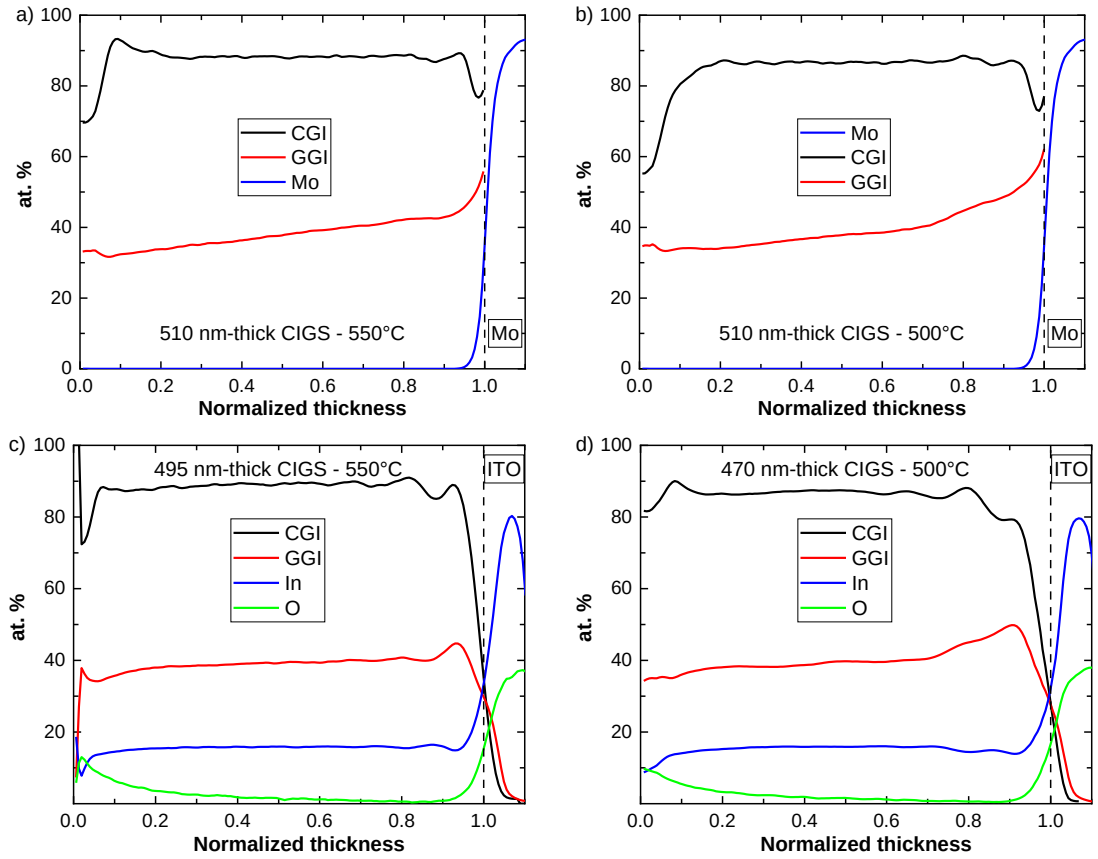

Figure III. 24. Composition profiles of ultrathin CIGS layers measured by GD-OES, on (a,b) Mo back contacts and (c,d) RBCs with a 100 nm-thick top layer of ITO. CIGS was co-evaporated at a substrate temperature of (a,c) 550°C or (b,d) 500°C. The atomic percentage of absorber elements were calibrated from XRF measurements of CIGS on a SLG/Mo control sample, and the CIGS thickness was determined with a profilometer. Dashed lines indicate the position of interfaces. (a) [180720-3A1], (b) [180725-3A1], (c) [180503-2B1], (d) [180503-3B1].

The CGI ratios of ultrathin CIGS layers deposited on RBCs are similar to the ones observed on Mo back contacts. However, the GGI profiles in the bulk of CIGS look flatter in the case of RBCs, but still exhibit a GGI back grading close to the interface with ITO that is steeper for a CIGS co-evaporation temperature of 500°C. Thus, an improved rear passivation of CIGS can also be expected when it is deposited at 500°C on RBCs.

The GD-OES composition profiles of a CIGS layer co-evaporated at 500°C on a RBC without ZnO:Al on top of Ag were also investigated, and compared to the case of back contacts made of Mo and RBCs with a ZnO:Al/ITO stack on Ag (Figure III. 25). Note that GD-OES depth profiles presented in Figure III. 25.a and b are also shown in Figure III. 24.b and d. Each back contact was covered with 8 nm of NaF prior to CIGS co-evaporation, enabling the comparison of the Na composition.

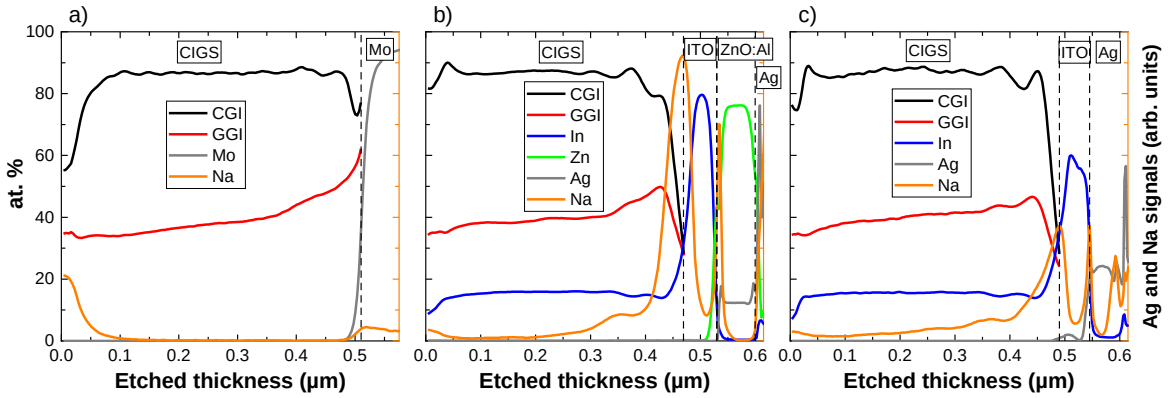

Figure III. 25. GD-OES composition profiles of CIGS layers co-evaporated at 500°C on (a) Mo, as well as RBCs (b) with and (c) without a 30 nm-thick ZnO:Al layer on top of Ag. The raw Na an Ag composition profiles are also shown. Vertical dashed lines indicate the position of interfaces. Average CGI, GGI and In compositions were calibrated based on the XRF signal of CIGS on Mo control samples. The CIGS thickness was calibrated by a profilometer measurement. (a) [180725-3A1], (b) [180503-3B1], (c) [181109-3B2].

The ultrathin CIGS layers co-evaporated at 500°C exhibit the expected flat CGI and graded GGI profiles. To investigate the impacts of the RBC architecture on the diffusion of elements, the Na and Ag composition profiles are also shown. It can be seen that both types of RBCs lead to a higher content of Na in the bulk of CIGS as compared to the Mo case. However, when the RBC includes a ZnO:Al layer on top of Ag the diffusion of Na is blocked and a strong segregation of Na is observed at the CIGS/ITO interface. This accumulation of Na is reduced when the RBC is fabricated with a single layer of ITO on top of Ag, as Na is found to diffuse through ITO and Ag. Besides, some Ag is also detected at the interface between CIGS and ITO, while the RBC with a ZnO:Al/ITO stack avoids the diffusion of Ag beyond the ZnO:Al layer. Hence, it is clear that a single layer of ITO is more permeable to Ag and Na diffusion as compared to the ZnO:Al/ITO bilayer.

Based on this GD-OES study and the top-view SEM images presented in Figure III. 13, it was concluded that after CIGS co-evaporation the simplified RBC stack results in a localized diffusion of Ag through the ITO layer. Indeed, Ag was not detected inside the CIGS layer deposited on this RBC architecture, indicating a limited diffusion of Ag, but stronger than in the case of a RBC with a ZnO:Al/ITO bilayer on Ag.

For both types of RBCs, the In and Zn composition profiles show steep interfaces, indicating that the RBC stack does not lead to an excessive diffusion of elements during CIGS co-evaporation. A small GGI peak and a slight depletion of In can be seen at the back interface of CIGS with ITO, however the limited resolution of GD-OES at the interface between different materials does not allow to conclude on the formation of Ga oxide. To obtain a clearer picture of the interface between CIGS and ITO, a STEM/EDX study was performed on CIGS layers grown on RBCs including a stack of ZnO:Al (30 nm)/ITO (100 nm) on Ag.

11.3.2. STEM/EDX study of the CIGS back interface with 100 nm-thick ITO

The STEM dark field image of a complete ultrathin solar cell with a RBC is shown in Figure III. 26, together with the corresponding EDX maps of absorber elements as well as Cd, O, Zn, Ag and the calculated GGI. CIGS was co-evaporated in a 3-stage process with a maximum substrate temperature of 550°C, and the ITO layer on top of the RBCs has a thickness of 100 nm.

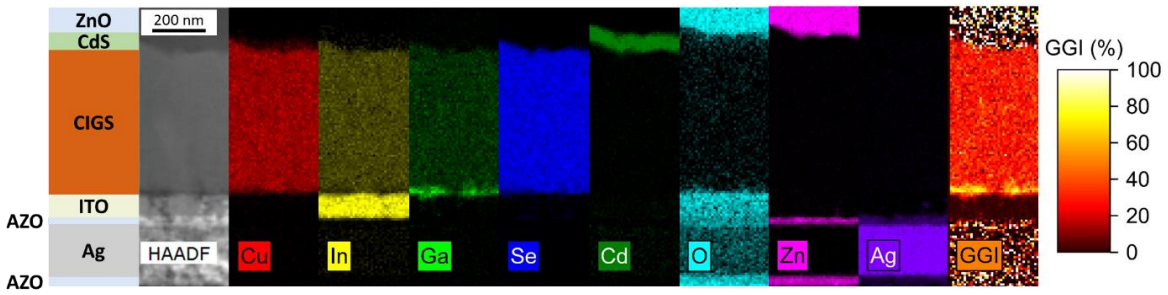

Figure III. 26. Schematic of a complete ultrathin CIGS solar cell on a RBC, along with its HAADF STEM image and EDX maps. CIGS was co-evaporated at 550°C on a bare RBC with a 100 nm-thick top layer of ITO. [180720-3B1].

First, the ITO and ZnO:Al do not show any diffusion, indicating that the RBC stack is stable during the co-evaporation of CIGS at 550°C. However, Ag is slightly detected in the front ZnO:Al layer. This is not due to the diffusion of Ag, but to its oxidation and subsequent expansion, as indicated by the significant detection of O in the Ag layer (Figure III. 26 and Figure III. 28). Indeed, the lamellas were exposed to air for a significant amount of time during their transfer from the FIB to the TEM vacuum chamber. Finally, a strong accumulation of Ga associated with a high GGI ratio is observed at the CIGS/ITO interface, and is attributed to the formation of an interfacial layer of Ga oxide. A comparison of this segregation of Ga at the back contact is shown in Figure III. 27, for CIGS deposition temperatures of 550°C and 500°C on RBCs with and without an additional 3 nm-thick Al_2O_3 layer.

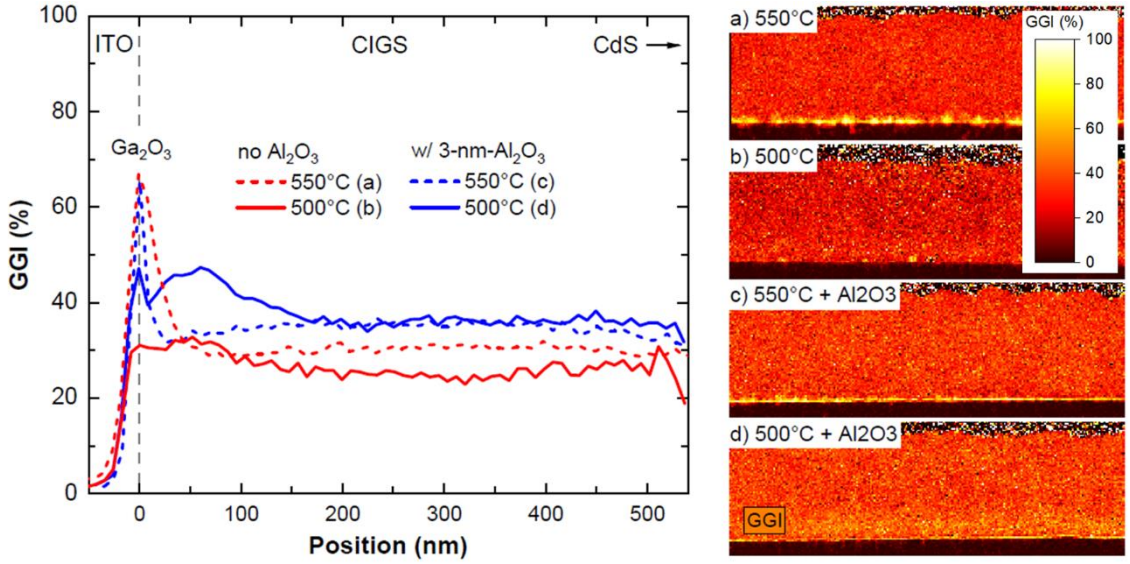

Figure III. 27. Average GGI depth profiles determined from each corresponding STEM/EDX mapping. Ultrathin CIGS layers were co-evaporated at either 550°C (dashed lines) or 500°C (solid lines), on a bare RBC (red) and a RBC covered with a 3 nm-thick Al_2O_3 layer (blue). (a) [180720-3B1], (b) [180725-3B1], (c) [180720-3B2], (d) [180725-3B2].

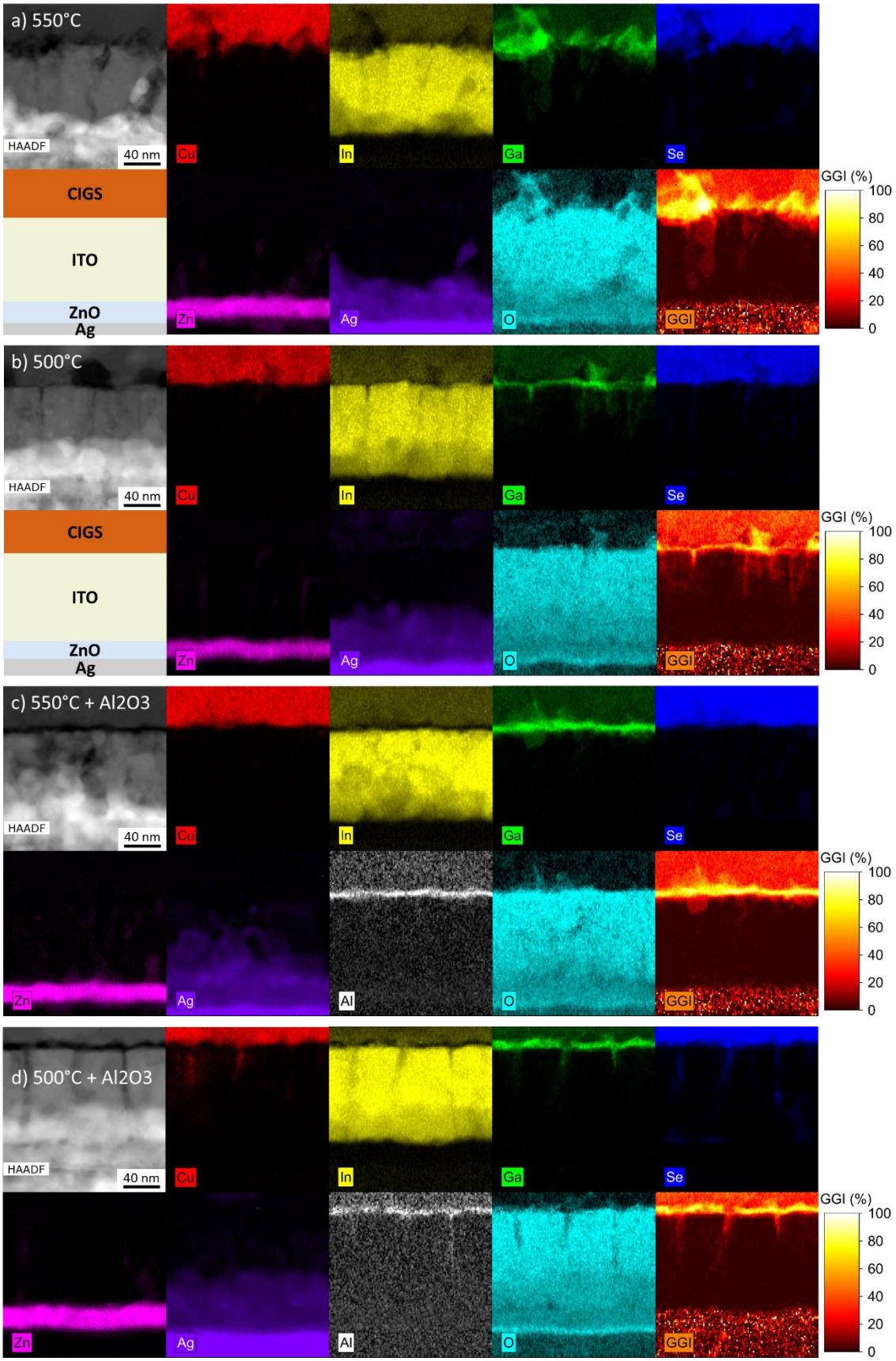

Figure III. 28. STEM/EDX maps zoomed at the CIGS interface with the RBCs. Schematics of the observed layers are also shown in (a) and (b). The three top layers of the RBCs are visible: ITO, ZnO:Al and Ag. CIGS was co-evaporated at (a,c) 550°C and (b,d) 500°C. In (c) and (d), the RBC was covered with a 3 nm-thick alumina layer deposited by ALD. [see Figure III. 27].

The GGI maps in Figure III. 27 reveal a stronger formation of Ga oxide when CIGS is co-evaporated at 550°C. Indeed, the GGI depth profiles averaged on the total width of the EDX maps show the highest GGI peak at the back interface of CIGS co-evaporated at 550°C. In this case, the addition of a 3 nm-thick alumina layer on top of the RBC efficiently limits the growth of the Ga oxide layer, as it approximately reduces its thickness by a factor of 2. The GGI profiles in the bulk of CIGS layers deposited at 550°C on RBC is flat, similarly to the composition profiles determined by GD-OES (Figure III. 24). The linear GGI grading that is observed in CIGS layers deposited at 550°C on Mo completely disappears, which means that these flat GGI profiles cannot be attributed exclusively to the stronger interdiffusion of In and Ga at 550°C than at 500°C [201], but also to the formation of Ga oxide which consumes the Ga from the back interface of the CIGS layer [37], [192].

Interestingly, the co-evaporation of CIGS at 500°C preserves the GGI back grading. This effect of the CIGS deposition temperature on the GGI grading is also present in CIGS layers deposited on Mo, which form a steeper GGI back grading at 500°C thanks to a reduced interdiffusion of In and Ga (Figure III. 24). However, in the case of the RBC the GGI back grading also depends on the formation of Ga oxide. Here, the lower GGI peaks at the interface between CIGS and ITO confirm that the growth of Ga oxide is at least partially hindered for a deposition temperature of 500°C instead of 550°C. As a result, the depletion of Ga at the back contact of CIGS layers co-evaporated at 500°C is limited to a thickness of ≈ 50 nm. While a strong depletion of Ga at the back interface of CIGS can create a detrimental back surface field, such a thin and low Ga deficit should not impede the collection efficiency of complete solar cells [37].

A STEM/EDX study with a higher magnification was also performed close to the back interface of CIGS, in order to investigate the local effects of the CIGS deposition temperature and of the thin interfacial Al_2O_3 layer on the growth of Ga oxide (Figure III. 28). First, Ag is also detected in the ZnO:Al layer and the rear of the ITO film for each type of sample, due to the oxidation and expansion of Ag at the surface of the lamellas. Note that even if some Ag diffusion would occur during CIGS deposition, it probably would not be detrimental to cell performance as long as it does not reach the CIGS layer and does not modify its composition.

For CIGS layers co-evaporated directly on the ITO layer of the RBC, a depletion of Cu, In and Se elements is visible at the CIGS/ITO interface, together with an accumulation of Ga. As the interfacial Ga signal overlaps the O signal, this segregation of Ga has been attributed to the formation Ga oxide at the back contact of CIGS. For a CIGS deposition temperature of 550°C, rough and thick Ga oxide grains are detected at the CIGS/ITO interface and in the grain boundaries of ITO. A thinner Ga oxide layer is formed when CIGS is co-evaporated at 500°C, but it is also rough and extends in the ITO layer.

When an additional 3 nm-thick layer of alumina is deposited on top of the RBC, a much smoother Ga oxide layer is formed. As a result, the segregation of Ga oxide is localized at the CIGS/ITO interface with only a limited extension to the CIGS and ITO layers. The Al_2O_3 and GaO_X layers cannot be distinguished, which could be the result of the formation of a $(Al_xGa_{1-x})_2O_3$ alloy [202], [203]. Contrary to other samples, CIGS rather than GaO_X is detected within the grain boundaries of ITO for a co-evaporation

temperature of 500°C, as confirmed by a depletion of O and In in the ITO layer that overlaps the EDX signals of Cu, Ga and Se. This indicates that the growth of Ga oxide is efficiently hindered by reducing CIGS co-evaporation temperature to 500°C and by adding a thin alumina layer on the RBC, as this sample configuration led to the clearest direct contact between CIGS and ITO.

When comparing the growth of Ga oxide on ITO layers with a thickness of 200 nm and 100 nm, it seems that the GaO_X film is thinner and slightly smoother when the ITO layer is thicker. This dependence of Ga oxide growth cannot be attributed solely to the variation of the ITO thickness, but rather to the subsequent changes in the morphology, grain size or grain orientation of the ITO layer [153].

In the following, the performances of solar cells fabricated on Mo and RBCs with a bilayer of ZnO:Al (30 nm)/ITO (100 nm) are compared with respect to the CIGS deposition conditions and the formation of Ga oxide. Solar cells on RBCs with a single layer of ITO on top of Ag are also characterized.

11.3.3. Performances of solar cells on RBCs with a ZnO:Al layer on Ag

First, four batches of ultrathin CIGS layers with identical nominal compositions and thicknesses are analyzed. The investigated RBCs exhibit a stack of ZnO:Al (30 nm)/ITO (100 nm) on Ag. Bare RBCs and RBCs covered with a 1.5 nm or a 3 nm-thick alumina layer are compared to Mo references with and without a 30 nm-thick Al_2O_3 diffusion barrier. Na was incorporated to CIGS by thermal evaporation of 8 nm-thick NaF precursor layers on each back contact. Figure III. 29 shows the light and dark I(V) curves of each best solar cell, and the EQE for each type of back contact can be found in Figure III. 30. The average performances as well as the best cell light and dark I(V) parameters are detailed in Table III. 8.

First, half of the Mo references include a diffusion barrier made of a 30 nm-thick alumina layer, in order to compare the performances of solar cells on Mo with and without Na diffusion from the SLG substrate. The addition of this diffusion barrier should also provide a fair comparison with cells on a RBC as the RBC also blocks the diffusion of Na. Both types of Mo references show improved average efficiencies when CIGS is co-evaporated at 500°C, thanks to an increase of the average V_{OC}, and of the *FF* too in the case of a SLG/Mo substrate. However, there is no clear trend when comparing Mo with and without a diffusion barrier: the SLG/Al_2O_3/Mo back contact leads to the best average efficiency of 10.2 ± 0.5 when CIGS is co-evaporated at 550°C, while the SLG/ Mo substrate exhibits a higher average efficiency of 12.4 ± 0.1 for a CIGS deposition at 500°C.

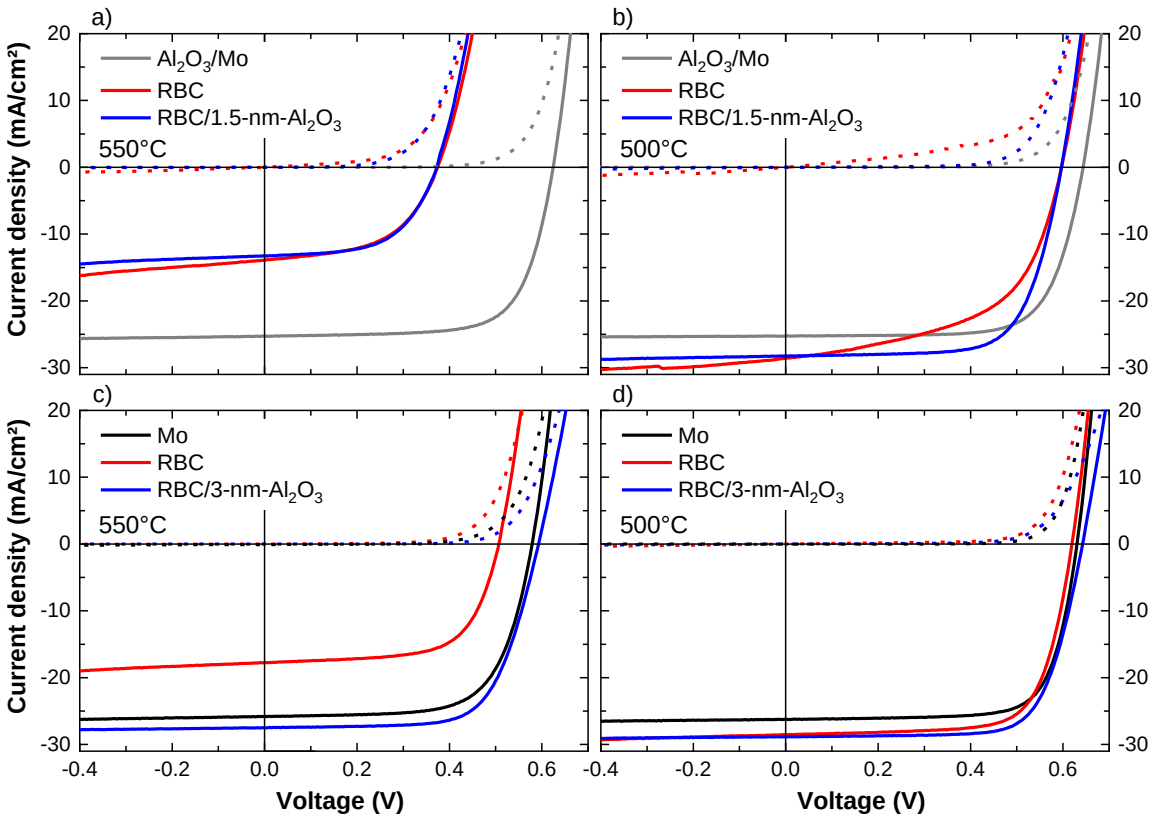

Figure III. 29. I(V) characteristics of ultrathin CIGS solar cells under one-sun illumination (solid lines) and in the dark (dashed lines). CIGS was co-evaporated at (a,c) 550°C and (b,d) 500°C on Mo with and without a 30 nm-thick alumina diffusion barrier, as well as bare RBCs and RBCs covered with a 1.5 nm or 3 nm-thick Al_2O_3 layer on top of ITO. (a) Mo: [180503-2A2_c14], RBC: [180503-2B1_c2], RBC/Al_2O_3: [180503-2B2_c16], (b) Mo: [180503-3A2_c14], RBC: [180503-3B1_c1], RBC/Al_2O_3: [180503-3B2_c5], (c) Mo: [180720-3A1_c3], RBC: [180720-3B1_c5], RBC/Al_2O_3: [180720-3B2_c11], (d) Mo: [180725-3A1_c6], RBC: [180725-3B1_c1], RBC/Al_2O_3: [180725-3B2_c1].

It can be seen that the 2 batches of CIGS layers co-evaporated at 550°C on bare RBCs led to low average efficiencies of 2.6 ± 0.1 % and 4.3 ± 1.2 %. These poor efficiencies are correlated to a degradation of each light and dark I(V) parameter. In particular, the EQE of these solar cells is much lower than the Mo references over the complete wavelength range (Figure III. 30), which means that these devices suffer from poor collection efficiencies. Their optical bandgap is also decreased as compared to cells with Mo back contacts, from 1.20 eV to 1.15 eV in the case of Figure III. 30.c. This could be a result of the strong formation of Ga oxide, consuming Ga from the CIGS layer and thus reducing its GGI ratio and bandgap.

		Average / best cell light I(V) parameters				Best cell dark I(V) parameters		
CIGS deposition temperature	Back contact	Eff. (%)	J_{SC} (EQE) (mA/cm^2)	V_{OC} (mV)	FF (%)	J_0 (mA/cm^2)	R_{SH} (Ω.cm^2)	R_S (Ω.cm^2)
550°C	Al_2O_3/Mo	10.2 ± 0.5 / 11.1	24.9	595 ± 22 / 626	68.9 ± 1.3 / 71.2	7.10^{-5}	$> 3.10^5$	< 0.1
Batch n°1	RBC	2.6 ± 0.1 / 2.8	13.9	366 ± 6 / 376	51.0 ± 1.7 / 53.3	5.10^{-3}	4.10^2	0.7
[180503-2]	RBC/1.5-nm-Al_2O_3	3.0 ± 0.1 / 3.1	13.3	388 ± 11 / 399	57.5 ± 0.5 / 57.7	6.10^{-3}	2.10^4	0.5
500°C	Al_2O_3/Mo	11.0 ± 0.5 / 11.8	25.3	624 ± 17 / 648	69.7 ± 1.6 / 72.0	5.10^{-5}	$> 3.10^5$	< 0.1
Batch n°2	RBC*	9.3	28.6	597	54.8	9.10^{-5}	2.10^2	0.3
[180503-3]	RBC/1.5-nm-Al_2O_3	11.6 ± 0.1 / 11.8	28.3	594 ± 1 / 596	69.1 ± 0.8 / 70.0	2.10^{-4}	1.10^4	0.4
550°C	Mo	9.5 ± 0.6 / 10.2	25.8	568 ± 10 / 582	64.6 ± 2.9 / 68.2	2.10^{-4}	1.10^5	0.4
Batch n°3	RBC	4.3 ± 1.2 / 5.9	17.8	452 ± 60 / 510	53.9 ± 9.1/ 65.7	4.10^{-4}	4.10^3	0.6
[180720-3]	RBC/3-nm-Al_2O_3	9.9 ± 1.1 / 11.2	27.5	581 ± 15 / 595	62.0 ± 6.2 / 68.5	1.10^{-4}	7.10^4	1.1
500°C	Mo	12.4 ± 0.1 / 12.5	26.2	630 ± 4 /635	75.0 ± 0.5 / 75.8	4.10^{-5}	$> 1.10^6$	< 0.1
Batch n°4	RBC	11.4 ± 1.2 / 12.8	28.5	611 ± 16 / 620	65.5 ± 5.5 / 72.3	7.10^{-5}	3.10^3	0.4
[180725-3]	RBC/3-nm-Al_2O_3	12.3 ± 1.0 / 13.5	28.9	618 ± 15 / 644	68.8 ± 3.8 / 72.7	3.10^{-5}	7.10^3	1.5

Table III. 8. Summary of solar cell performances for each type of back contact, with CIGS co-evaporation temperatures of 550°C and 500°C. The average light I(V) parameters and standard deviation were calculated from the 10 best solar cells, except for J_{SC} values which were calculated from the integrated EQE of solar cells for each type of back contact. A 1-diode model with an ideality factor of 2 was used to fit the dark I(V) parameters of the best solar cells (J_0: saturation current, R_{SH}: shunt resistance, R_S: series resistance). *For this sample, light I(V) parameters are specified for the best cell only because of a strong shunting behavior in most solar cells.

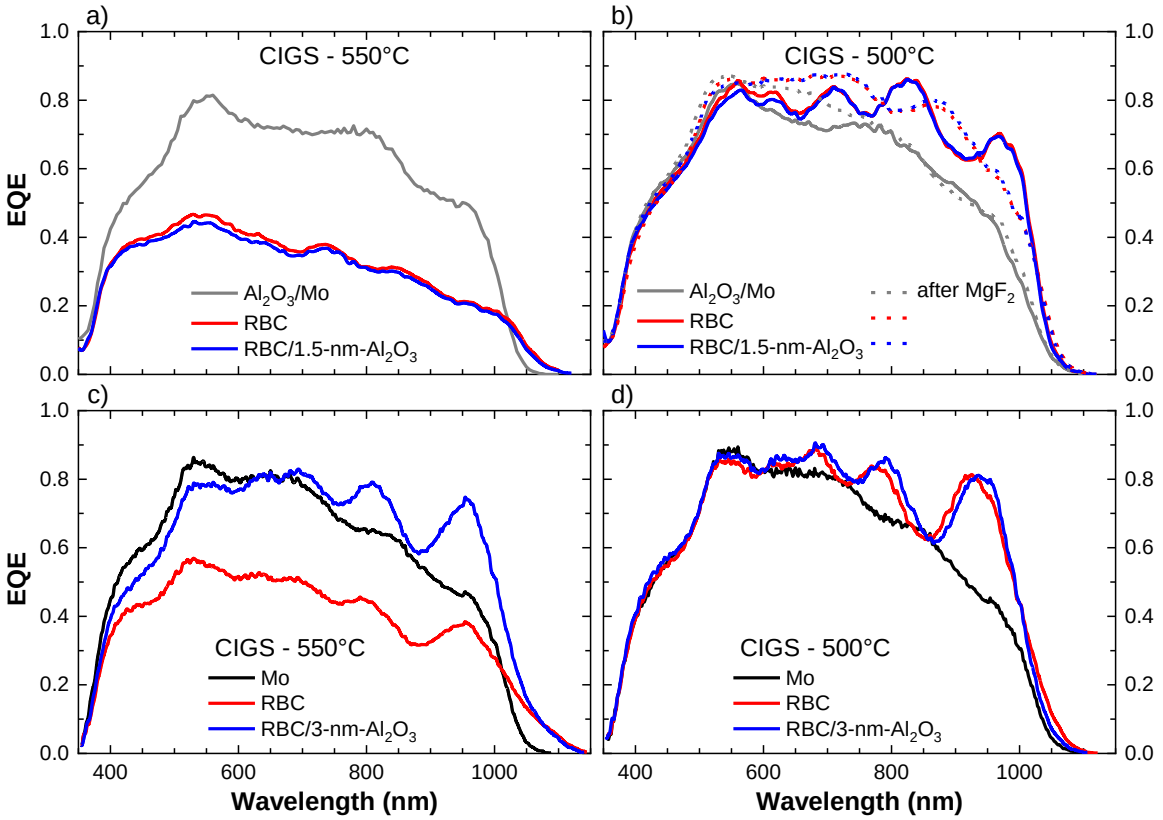

Figure III. 30. EQE curves of ultrathin CIGS solar cells on Mo with and without a 30 nm-thick Al_2O_3 diffusion barrier, bare RBCs and RBCs covered with a 1.5 nm or 3 nm-thick layer of alumina. CIGS was co-evaporated at (a,c) 550°C and (b,d) 500°C. In (b), EQE after the deposition of a MgF_2 antireflection coating are also shown. (a) Mo: [180503-2A2_c14], RBC: [180503-2B1_c2], RBC/Al_2O_3: [180503-2B2_c16], (b) Mo: [180503-3A2_c14], RBC: [180503-3B1_c1], RBC/Al_2O_3: [180503-3B2_c15], (c) Mo: [180720-3A1_c3], RBC: [180720-3B1_c5], RBC/Al_2O_3: [180720-3B2_c14], (d) Mo: [180725-3A1_c10], RBC: [180725-3B1_c10], RBC/Al_2O_3: [180725-3B2_c1].

Interestingly, adding a 3 nm-thick alumina layer on top of the RBC is shown to improve the performances of solar cells prepared at 550°C, contrary to a 1.5 nm-thick Al_2O_3 layer. As a result, cells on a RBC covered with a 1.5 nm and 3 nm-thick Al_2O_3 layer exhibit average efficiencies of 3.0 ± 0.1 % and 9.9 ± 1.1 %, respectively. The best solar cell with a RBC/3-nm-Al_2O_3 substrate shows an efficiency of 11.2%, which is 1.0% absolute more than for Mo, mainly thanks to a J_{SC} improvement from 25.8 mA/cm^2 to 27.5 mA/cm^2. The EQE curves reveal that this RBC architecture results in an enhanced CIGS absorption for wavelengths above 700 nm, as compared to Mo. However, a lower EQE is observed in the 400 nm – 600 nm wavelength range, indicating a lower collection efficiency than cells with a Mo back contact. These findings show that the formation of a rough Ga oxide layer at the CIGS/ITO interface is highly detrimental to solar cell performances. Still, by covering the top ITO layer of the RBC with a 3 nm-thick alumina film, a smoother layer of Ga oxide is grown and complete cells achieve V_{OC} and *FF* values similar to the case of a Mo back contact.

The performances of solar cells with a RBC was further improved by co-evaporating CIGS at a substrate temperature of 500°C. Note that the best cell on a bare RBC prepared in batch n°2 exhibits an efficiency of 9.8% but has a low *FF* of 54.8% due to a

strong shunting behavior of unknown origin. On the other hand, the bare RBC from CIGS batch n°4 leads to a best cell efficiency of 12.8% and a J_{SC} of 28.5 mA/cm², representing respectively a 0.3 % absolute and a 2.3 mA/cm² increase as compared to Mo. Thanks to the increased back reflectance of CIGS, the EQE of solar cells on RBCs are enhanced for wavelengths above 600 nm, and contrary to the case of CIGS deposited at 550°C, the EQE of cells prepared at 500°C on top of bare RBCs do not show strong collection losses for wavelengths below 600 nm. Hence, lowering the co-evaporation temperature of CIGS from 550°C to 500°C reduces the formation of Ga oxide and leads to increased efficiencies for solar cells on bare RBCs. In particular, J_0 decreases for a deposition temperature of 500°C, indicating less non-radiative recombination when thinner Ga oxide layers are formed.

When CIGS is co-evaporated at 500°C, adding a 1.5 nm-thick Al_2O_3 layer on top of the RBC leads to a best efficiency of 11.8% that is identical to the Mo reference. Though the RBC/1.5-nm-Al_2O_3 substrate shows a J_{SC} increase of 3.0 mA/cm² as compared to Mo, its V_{OC} is reduced by 52 mV. In contrast, the best cell on a RBC covered with a 3 nm-thick alumina layer exhibits an efficiency of 13.5% instead of 12.5% for the best cell on Mo. This efficiency improvement is related to a J_{SC} and a V_{OC} increase of 3.0 mA/cm² and 9 mV, respectively, and similar J_0 values were fitted for the RBC/3-nm-Al_2O_3 and Mo back contacts. However, this RBC results in a reduction of the best cell *FF* from 75.8% to 72.7% as compared to Mo, which can be mainly attributed to an increase of the series resistance from < 0.1 Ω.cm² to 1.5 Ω.cm². Hence, the 3 nm-thick alumina layer leads to a significant increase of the best solar cell's series resistance, and using thicker alumina layers is expected to further increase the series resistance of devices and thus to be detrimental to the *FF* [204].

Nevertheless, adding 3 nm of Al_2O_3 on the top layer of ITO was found to be beneficial to the performances of cells prepared at 500°C, as it mitigates *FF* losses due to a voltage-dependent current collection (Figure III. 29). This can be attributed to the formation of a smoother Ga oxide layer at the CIGS/ITO interface and/or the chemical passivation of this interface.

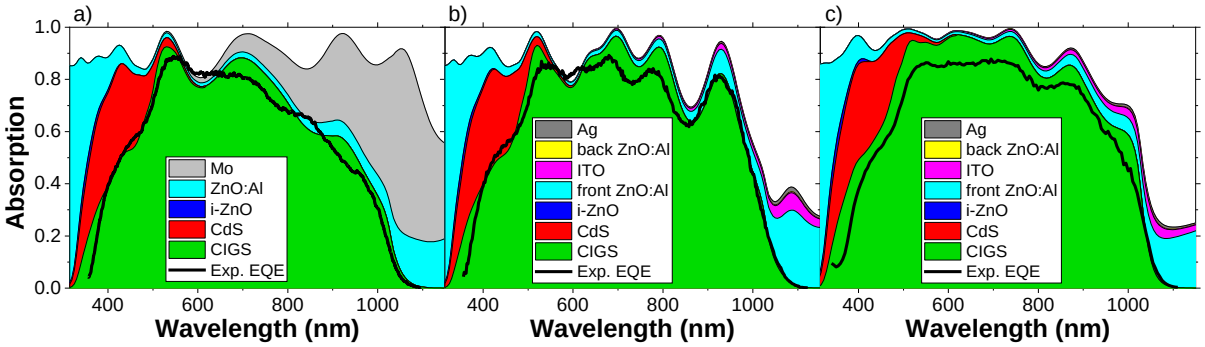

Figure III. 31. Simulated absorption in each stack of complete CIGS solar cells prepared at 500°C. The back contacts consist of (a) Mo and (b,c) a RBC with a 100 nm-thick ITO layer on top. In (c), an additional MgF_2 antireflection coating was applied on top of the solar cell stack. The experimental EQE curves are shown for comparison with the simulated absorption of CIGS. (a) [180725-3A1_c10], (b) [180725-3B1_c10], (c) [180503-3B1_c1].

In order to further improve the J_{SC} of CIGS solar cells with RBCs, an additional MgF_2 antireflection coating (ARC) was deposited by thermal evaporation on one batch of solar cells with Mo and RBCs (Figure III. 30.b). It results in an enhancement of the EQE for wavelengths between 550 nm and 800 nm, and a subsequent increase of the J_{SC} from 25.3 mA/cm^2 to 26.6 mA/cm^2 on a Mo back contact, from 28.6 mA/cm^2 to 29.3 mA/cm^2 on a bare RBC, and from 28.3 mA/cm^2 to 29.5 mA/cm^2 on a RBC covered with 1.5 nm of alumina. Note that light I(V) curves could not be measured due to process issues; the MgF_2 film prevented the probes from contacting the ZnO:Al layers.

To analyze the optical effects of the RBC and ARC, the light absorption in each layer of the complete solar cell stack was simulated in the case of a Mo back contact, as well as a RBC with and without an additional MgF_2 ARC (Figure III. 31). The CIGS layers were simulated using a bandgap of 1.2 eV and the average CIGS thickness of each respective sample batch, *i.e.* 510 nm in Figure III. 31.a and b, and 470 nm in Figure III. 31.c. These calculations confirm once again the beneficial role of the RBC, which avoids absorption losses in the Mo back contact and improves the J_{SC} thanks to an almost perfect double-pass absorption with low parasitic absorption in the TCO and Ag layers of the RBC. Using a 100 nm-thick ITO layer instead of 200 nm reduced the parasitic absorption of light for photon energies above the CIGS bandgap. It resulted in an equivalent J_{SC} loss of 0.3 mA/cm^2 with 100 nm of ITO as compared to 0.7 mA/cm^2 for a RBC with a 200 nm-thick ITO layer

The deposition of an ARC on top of the solar cell is shown to reduce the total reflection of the device, especially in the 550 nm – 800 nm wavelength range, which is in good agreement with the observed variations of the experimental EQE. As a result, the theoretical J_{SC} derived from the calculated CIGS absorption is increased from 30.0 mA/cm^2 to 32.8 mA/cm^2 after deposition of an ARC on solar cells with a RBC, as compared to 27.3 mA/cm^2 for the Mo reference. However, the CIGS absorption in the infrared region below the CIGS bandgap is not significantly enhanced after the ARC treatment. This indicates that advanced light trapping strategies are necessary to improve the CIGS absorption in the 800 – 1100 nm wavelength range and to overcome the double-pass absorption limitation.

In summary, RBCs with a ZnO:Al (30 nm)/ITO (100 nm) bilayer stack on Ag led to poor solar cell performances when CIGS was co-evaporated at 550°C, in correlation with the formation of a thick and rough Ga oxide layer at the CIGS/ITO interface. It is possible to grow a smooth layer of Ga oxide at 550°C by adding a 3 nm-thick alumina film on the ITO layer on top of the RBC, which in turn improves the efficiency of ultrathin solar cells with a RBC. Co-evaporating CIGS at 500°C efficiently reduces the formation of Ga oxide, and creates a steeper GGI grading on both Mo and RBCs. As a result, the Mo references exhibit improved efficiencies for a deposition temperature of 500°C as compared to 550°C, and the best cells on Mo and bare RBCs show similar efficiencies. The best performance is obtained when CIGS is co-evaporated at 500°C on a RBC with a 3 nm-thick alumina layer, which also corresponds to the lowest formation of Ga oxide. Solar cells with a 1.5 nm-thick Al_2O_3 film deposited on the RBCs were also studied, but were shown to be less efficient than cells on RBCs with a 3 nm-thick alumina layer.

11.3.4. Performances of solar cells on RBCs without ZnO:Al on Ag

The I(V) characteristics and EQE curves of the best solar cells prepared at 500°C on Mo, as well as RBCs with and without ZnO:Al on top of Ag are shown in Figure III. 32. Photovoltaic performances are also summarized in Table III. 9.

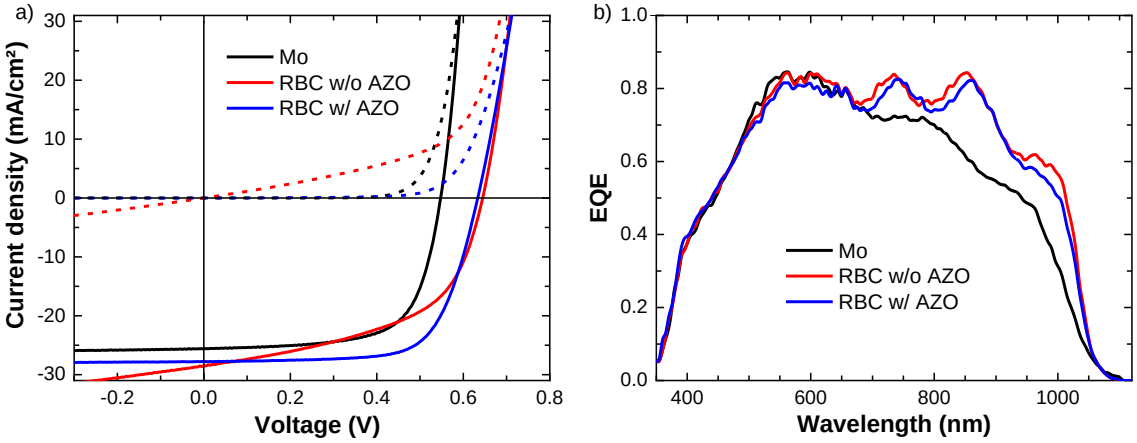

Figure III. 32. (a) I(V) characteristics under one-sun illumination (solid lines) and in the dark (dashed lines) and (b) EQE for best solar cells on top of Mo, as well as RBCs with and without a 30 nm-thick ZnO:Al layer between the Ag and ITO layers. CIGS was co-evaporated at 500°C, and RBCs were covered with a 3 nm-thick Al2O3 layer. Mo: [181026-2A1_c13], RBC w/o ZnO:Al: [181026-2B1_c1], RBC w/ ZnO:Al: [181026-2B2_c11].

For some unknown reason the ultrathin solar cells fabricated on Mo show a low average V_{OC} of 549 ± 3 mV and *FF* of 67.5 ± 0.6 %, despite the low J_0 and *n* values that were fitted from its dark I(V) curve. This leads to a limited average efficiency of 9.5 ± 0.1 %, which is lower than the average efficiencies of about 12% that were usually achieved for a co-evaporation temperature of 500°C.

The best cell with a simplified RBC (no ZnO:Al on Ag) exhibits a shunt resistance of 80 Ω.cm², much lower than 4.10^3 Ω.cm² for a RBC with a ZnO:Al/ITO stack on Ag. Because of this strong shunting behavior, light I(V) parameters are reported only for the best cell on a RBC without ZnO:Al atop of Ag. It has a low *FF* of 52.3%, which results in an efficiency of 9.6% despite a J_{SC} of 28.5 mA/cm² and a V_{OC} of 644 mV. The poor shunt resistance values of these solar cells were attributed to the local diffusion of Ag through the ITO layer that was observed in SEM/EDX. On the other hand, solar cells on a RBC with Ag encapsulated by ZnO:Al layers prevent the diffusion of Ag and show an average *FF* of 65.1 ± 2.9 %, which is close to the Mo reference with an average *FF* of 67.5 ± 0.6 %. This small *FF* loss in the case of a RBC with ZnO:Al on Ag is mainly related to a slight increase of the series resistance, due to the insulating 3 nm-thick layer of Al_2O_3. Thanks to a preserved average *FF* and a high average V_{OC}, these cells achieve an average efficiency of 11.3 ± 0.6 %, which is 1.8% absolute more than for Mo.

The EQE of solar cells confirm once again the beneficial effect of the RBC on the J_{SC} of complete devices. Large resonances are observed for wavelengths above 700 nm when Mo is replaced by a RBC, and the J_{SC} derived from the integrated EQE is increased from 25.6 mA/cm² on Mo to 27.8 mA/cm² and 28.5 mA/cm² for RBCs with and without ZnO:Al on Ag, respectively.

For each type of back contact, the experimental EQE curves were also compared with the simulated absorption in each layer of the complete solar cell stack (Figure III. 33). CIGS layers simulated with a bandgap of 1.2 eV and a thickness of 500 nm were found to be in good agreement with the experimental EQE, which indicates that for this CIGS batch the average thickness of 550 nm measured with a profilometer might be overestimated.

	Average / best cell light I(V) parameters				Best cell dark I(V) parameters			
Back contact	Eff. (%)	J_{SC} (EQE) (mA/cm^2)	V_{OC} (mV)	*FF* (%)	J_0 (mA/cm^2)	*n*	R_{SH} (Ω.cm^2)	R_S (Ω.cm^2)
Mo	9.5 ± 0.1 / 9.7	25.6	549 ± 3 / 553	67.5 ± 0.6 / 68.3	6 E-6	1.5	> 1 E+6	< 0.1
RBC w/o AZO*	9.6	28.5	644	52.3	4 E-5	2	80	0.4
RBC w/ AZO	11.3 ± 0.6 / 12.2	27.8	622 ± 7 / 633	65.1 ± 2.9 / 69.5	5 E-5	2	4 E+3	1.2

Table III. 9. Photovoltaic performances of ultrathin CIGS solar cells fabricated at 500°C on Mo as well as RBCs with and without ZnO:Al on top of Ag. Average values and standard deviation of light I(V) parameters were calculated for the 10 best cells. The dark I(V) parameters of each best cell were fitted with a 1-diode model (J_0: saturation current, *n*: ideality factor, R_{SH}: shunt resistance, R_S: series resistance). *In the case of the RBC without ZnO:Al, light I(V) parameters are specified for the best cell only due to a strong shunting behavior in most cells. Mo: [181026-2A1], RBC w/o ZnO:Al: [181026-2B1], RBC w/ ZnO:Al: [181026-2B2].

Both RBCs avoid the absorption losses occurring in the standard Mo back contact and enhance light absorption of ultrathin CIGS layers. Assuming a perfect collection of photogenerated carriers, theoretical maximum J_{SC} values were derived from the integrated CIGS absorptions. It is increased from 26.9 mA/cm^2 on Mo to respectively 30.6 mA/cm^2 and 30.9 mA/cm^2 on a RBC with and without ZnO:Al. Similar values are obtained for both RBCs, indicating that the ZnO:Al layer on Ag has a negligible impact on the parasitic absorption of the RBC. To confirm this, equivalent J_{SC} losses due to the RBCs were also calculated by integration of the ITO and ZnO:Al absorptions for photons energy above the CIGS bandgap of 1.2 eV. The single ITO layer on top of Ag accounts for a 0.3 mA/cm^2 loss, close to the J_{SC} loss of 0.4 mA/cm^2 due to the ZnO:Al/ITO bilayer stack on Ag. Thus, the 30 nm-thick ZnO:Al layer on top of Ag do not significantly impact CIGS absorption.

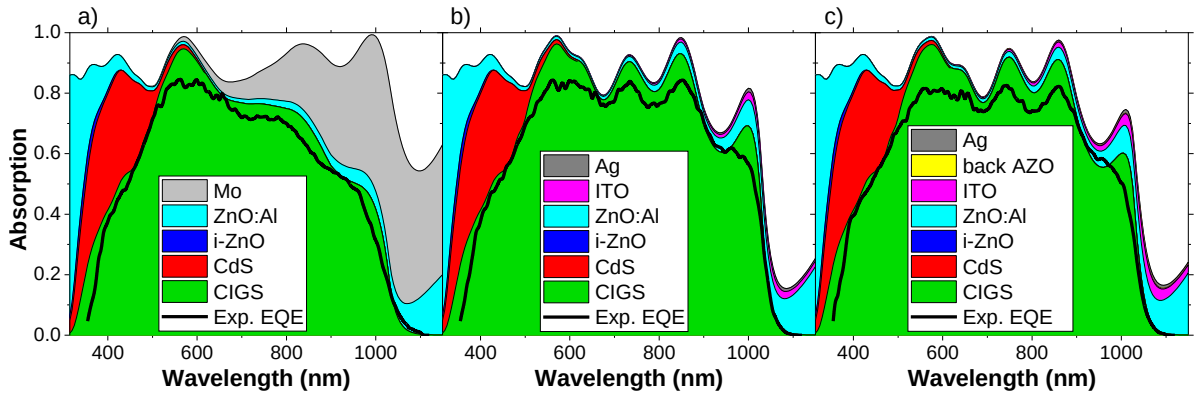

Figure III. 33. Simulated light absorption in each layer of complete ultrathin CIGS solar cells prepared at 500°C. Back contacts consist of (a) Mo, (b) RBC without ZnO:Al on top of Ag and (c) RBC with a 30 nm-thick ZnO:Al layer on Ag. Mo: [181026-2A1_c13], RBC w/o ZnO:Al: [181026-2B1_c1], RBC w/ ZnO:Al: [181026-2B2_c11].

In conclusion, the efficiency of complete devices with a simpler RBC architecture was not improved because of a strong shunting behavior. The poor shunt resistance values were attributed to a localized diffusion of Ag through the ITO layer. However, the efficiency of solar cells including a RBC with a bilayer of ZnO:Al (30 nm)/ITO (100 nm) still have room for improvement. In particular, mitigating the formation of Ga oxide is expected to increase the V_{OC} and *FF* of complete cells, and reducing the ITO thickness should improve their J_{SC}. This is why the next section will investigate RBCs with a 30 nm-thick ITO layer, as well as a low CIGS co-evaporation temperature of 450°C to limit the growth of Ga oxide. In addition, Na was incorporated via a PDT of NaF because Na was shown to promote the formation of Ga oxide [37], [38], [153], [191].

11.4. RBC with a 30 nm-thick ITO layer

11.4.1. CIGS morphology and composition

In this section, an ultrathin CIGS layer was deposited on Mo, as well as transparent and reflective back contacts. The transparent back contact consists of a stack of SLG/ZnO:Al (30 nm)/ITO (300 nm). Thanks to the thicker ITO layer of 300 nm the transparent back contact showed a low sheet resistance of 27.9 ± 0.1 Ω.cm² (four-point probe measurement), which should be sufficient to allow the lateral conduction of charge carriers at the back contact. The RBC was fabricated with the following layer stack: SLG/ZnO:Al (50 nm)/Ag (150 nm)/ZnO:Al (30 nm)/ITO (30 nm). CIGS was deposited at IRDEP, hence with a 1-stage co-evaporation process, at a substrate temperature of 450°C. The average composition of the CIGS film was determined from the XRF signal of CIGS deposited on Mo, leading to atomic ratios of CGI = 0.81 ± 0.01 and GGI = 0.32 ± 0.01. A CIGS thickness of 480 ± 10 nm was measured with a profilometer.

The SEM cross-section images of CIGS films co-evaporated on Mo, transparent and reflective back contacts are shown in Figure III. 34. Before the sputtering of Mo, an Al_2O_3 layer with a nominal thickness of 300 nm was deposited by ALD on the SLG substrate to block the diffusion of Na from the SLG. The RBC include a 30 nm-thick top layer of ITO, while the transparent back contact is made with a 300 nm-thick ITO layer on top of a 30 nm-thick diffusion barrier of ZnO:Al.

The CIGS layers, visible on top of each stack, show a thickness of 470 ± 20 nm and confirm the average CIGS thickness of 480 ± 10 nm that was measured with a profilometer. The CIGS films exhibit small CIGS grains that do not extend from the back contact to the front interface. This can be attributed to the low substrate temperature of 450°C during the deposition of CIGS [126], as well as the single stage process used for the co-evaporation of CIGS which does not include a Cu-rich step for the growth of large CIGS grains [205], [206].

The transparent and reflective back contacts appear to be stable during CIGS co-evaporation. In particular, the SEM cross-section image of CIGS on the RBC does not show any delamination of the layer stack (Figure III. 34.c).

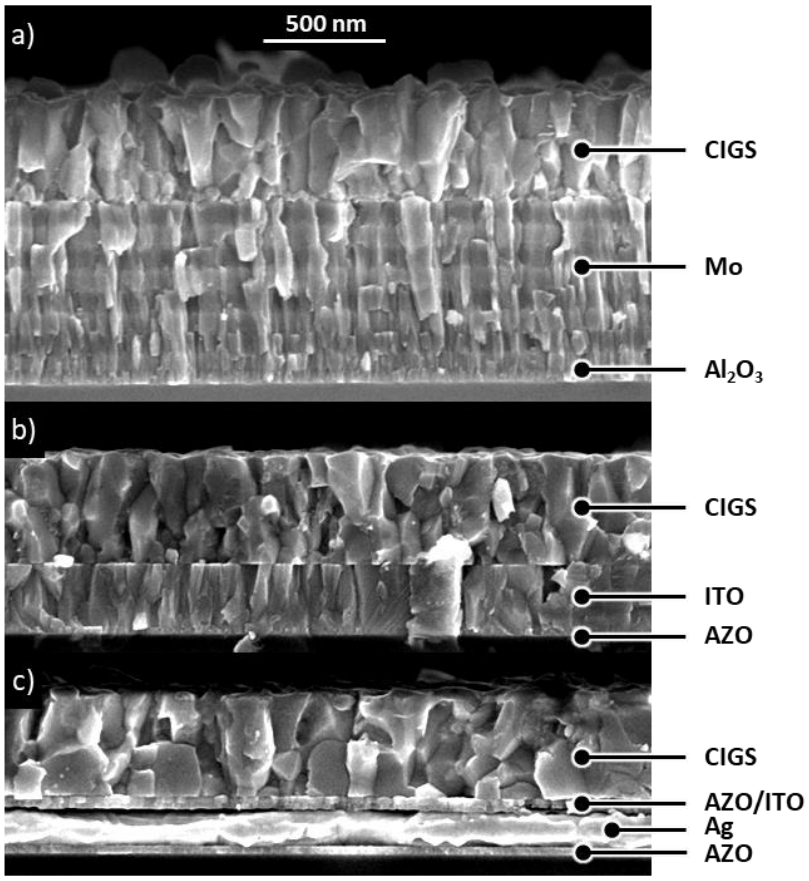

Figure III. 34. SEM cross-section images of ultrathin CIGS layers co-evaporated in a single stage process at 450°C. Back contacts are made of (a) a 800 nm-thick sputtered Mo layer with a 300 nm-thick Al_2O_3 diffusion barrier, (b) a transparent back contact consisting of SLG/AZO (30 nm)/ITO (300 nm) and (c) a RBC with a stack of SLG/ZnO:Al (50 nm)/Ag (150 nm)/ZnO:Al (30 nm)/ITO (30 nm). (a) [U204_A300], (b) [U205_WP2_11], (c) [U205_WP2_8].

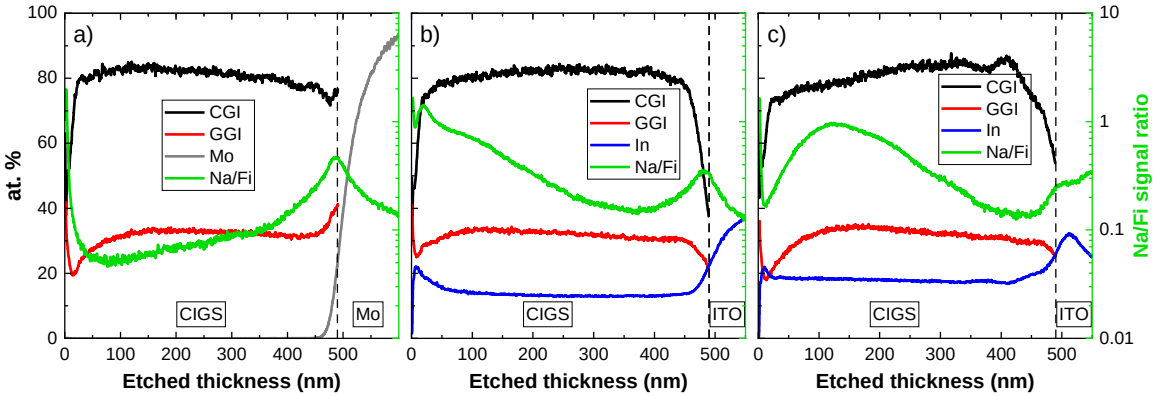

Figure III. 35. Composition profiles of ultrathin CIGS layers measured by GD-OES, on (a) a Mo back contact with an alumina diffusion barrier, (b) a transparent back contact and (c) a RBC with a 30 nm-thick top layer of ITO. CIGS was co-evaporated in a single stage process at a substrate temperature of 450°C. The atomic percentage of absorber elements were calibrated from XRF measurements of CIGS deposited on Mo, and the CIGS thickness was determined with a profilometer. The Na signal was divided by the total light intensity (Fi) to allow a fair comparison. Dashed lines show the position of the CIGS back interface. (a) [U205_A300], (b) [U205_WP2_11], (c) [U205_WP2_8].

The composition profiles of ultrathin CIGS layers co-evaporated on Mo, transparent and reflective back contacts shown in Figure III. 35 were determined from GD-OES measurements. The CGI and GGI atomic ratios observed in the CIGS bulk are rather flat, as expected with a 1-stage co-evaporation process. The 30 nm-thick ZnO:Al layers present in the architecture of the reflective and transparent back contacts act as diffusion barriers and prevent Na diffusion from SLG [152], [191], [207]. Here, Na was introduced intentionally using a NaF PDT at a rate of 1 nm/min for 8 minutes. The resulting composition profiles of Na measured in GD-OES are also compared for each back contact. When CIGS is deposited on Mo, Na seems to accumulate at the front and back interface of CIGS. But with a transparent or reflective back contact, the CIGS layer seems to incorporate more Na as a higher concentration of Na is found in its bulk.

Because GD-OES has a limited resolution, especially at interfaces between different layers, the composition profile of CIGS and its interface with ITO were further analyzed by STEM/EDX in the case of the transparent and reflective back contacts.

11.4.2. STEM/EDX study of CIGS interface with ITO layers

Figure III. 36 presents broad-view STEM images of ultrathin CIGS layers deposited at 450°C, along with their corresponding composition profiles measured by EDX. CIGS was co-evaporated on a transparent back contact consisting of SLG/ZnO:Al (30 nm)/ITO (300 nm) and a RBC with a stack of SLG/ZnO:Al (50 nm)/Ag (150 nm)/ZnO:Al (30 nm)/ITO (30 nm).

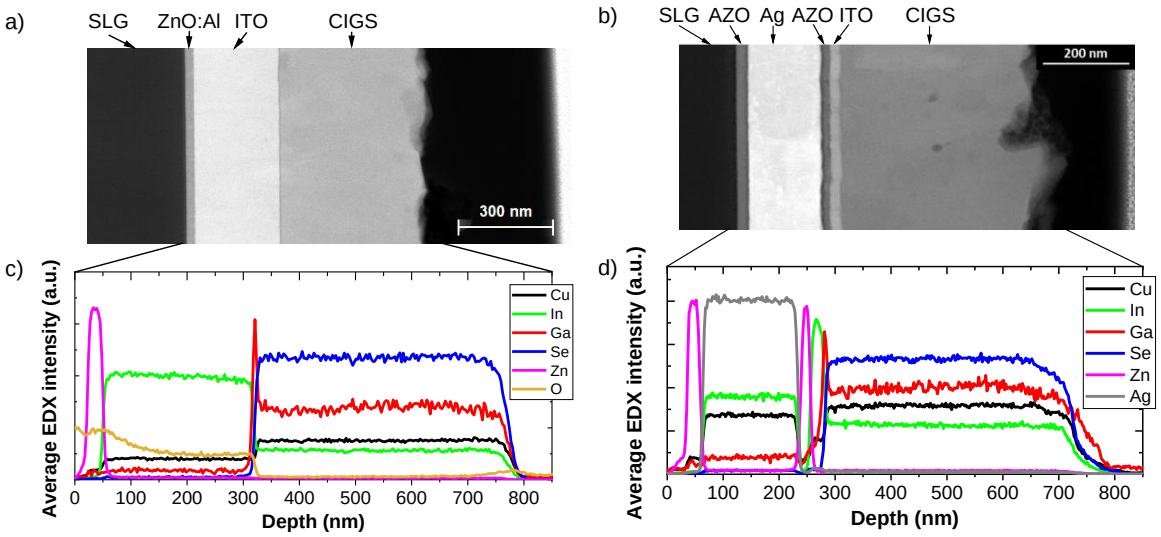

Figure III. 36. High angle annular dark field (HAADF) STEM image of an ultrathin CIGS layer co-evaporated in a single stage process on (a) a transparent back contact: SLG/ZnO:Al (30 nm)/ITO (300 nm) and (b) a reflective back contact: SLG/ZnO:Al (50 nm)/Ag (150 nm)/ZnO:Al (30 nm)/ITO (30 nm). The corresponding composition profiles deduced from the average EDX signal are shown in (c) and (d). (a,c) [U205_WP2_11], (b,d) [U205_WP2_8].

The EDX profiles shown in Figure III. 36.c and d first confirm that the CIGS layers have ungraded compositions, as expected with a 1-stage co-evaporation process. An average GGI of 0.28 was calculated from the average EDX signal in the CIGS layer. However, the accurate CGI ratio could not be determined based on this analysis as the substrate holder contains Cu, resulting in an overestimated Cu signal. From the HAADF

STEM image, a CIGS thickness of about 450 nm is estimated, which is close to the CIGS thicknesses determined in SEM and with a profilometer.

The composition profiles also show that the layer stacks of both back contacts are thermally stable, as the diffusion of ZnO:Al, ITO or Ag is not detected. Besides, the ZnO:Al layers efficiently encapsulate Ag. Here, Ag did not oxidize and was not detected in the TCO layers as the TEM slabs were transferred to the TEM in less than 5 min. The Cu signal present in the Ag layer in Figure III. 36.d is attributed to the substrate holder, and In is detected simultaneously to Ag due to similar energies of X-Ray emission lines.

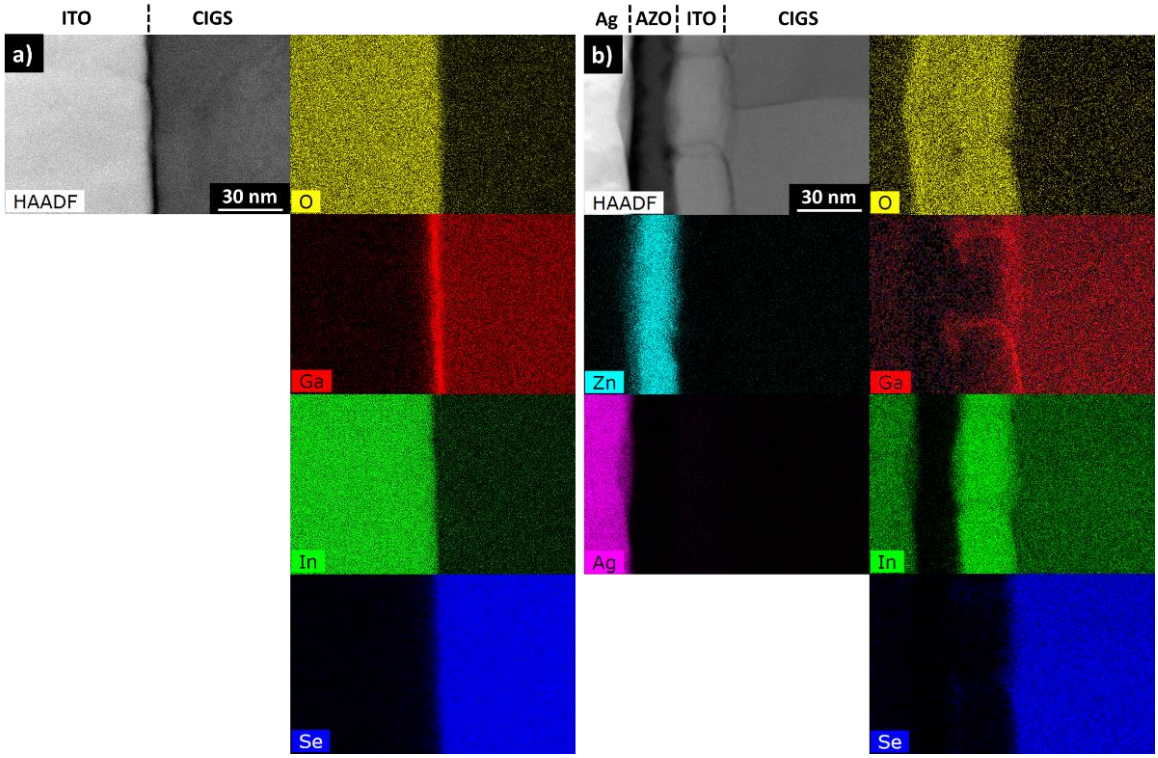

Figure III. 37. HAADF STEM images and corresponding EDX maps of an ultrathin CIGS layer co-evaporated on (a) a transparent back contact: SLG/ZnO:Al (30 nm)/ITO (300 nm), and (b) a reflective back contact: SLG/ZnO:Al (50 nm)/Ag (150 nm)/ZnO:Al (30 nm)/ITO (30 nm). (a) [U205_WP2_11], (b) [U205_WP2_8].

A spike in the EDX signal of Ga is observed at the interface between CIGS and ITO. It is also worth mentioning that in the case of the RBC, the Ga signal extends within the 30 nm-thick ITO layer. To determine whether these features of the Ga composition profiles are due to the formation of Ga oxide, a STEM/EDX analysis was also performed closer to the interface between CIGS and ITO (Figure III. 37). Once again, it confirms that Ag is efficiently encapsulated by ZnO:Al and that it does not diffuse during CIGS deposition.

For both back contacts, a thin Ga oxide layer is observed at the interface between CIGS and ITO. This means that the formation of Ga oxide cannot be suppressed even if CIGS is deposited at a low substrate temperature of 450°C, as reported by Son *et al.* [153]. Interestingly, the Ga oxide layer formed on the transparent back contact is smoother and thinner than the one observed at the interface with the RBC. Besides, Ga oxide is also detected within the grain boundaries of the 30 nm-thick ITO layer and it diffuses up to the ZnO:Al/ITO interface, which is consistent with the detection of Ga in ITO

shown in Figure III. 36.d. Based on these observations, the morphology of the Ga oxide layer appears to be dependent on the morphology and/or the thickness of the ITO layer used as a back contact. In particular, RBCs with thicker ITO layers of 200 nm and 100 nm did not lead to the growth of Ga oxide up to the ZnO:Al/ITO interface, possibly thanks to smoother ITO layers with larger grains.

Based on these material characterizations, the performances of complete ultrathin solar cells with Mo as well as transparent and reflective back contacts were then analyzed.

11.4.3. Solar cell performances

Figure III. 38 shows the light and dark I(V) characteristics, as well as the EQE curves of the best ultrathin CIGS solar cells with Mo, transparent and reflective back contacts. The Mo back contact also includes a 300 nm-thick alumina diffusion barrier, the transparent back contact is made of a SLG/ZnO:Al (30 nm)/ITO (300 nm) stack, and the RBC has a 30 nm-thick ITO layer on top of it. Thin Al_2O_3 layers (< 3 nm) deposited on ITO were not studied, because they need to be combined with a NaF precursor layer to avoid a current blocking behavior [141]. The average I(V) results can be found in Table III. 10, together with the light and dark I(V) parameters of each best solar cell.

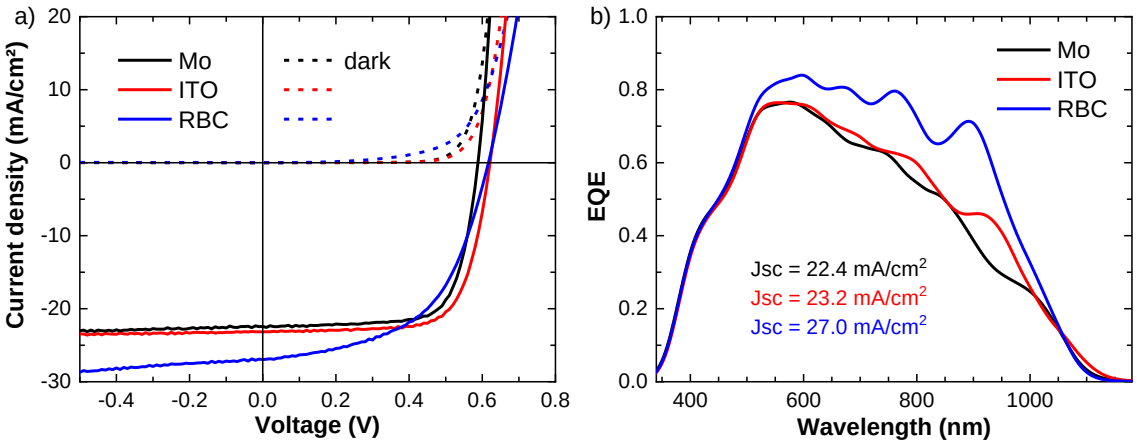

Figure III. 38. (a) Light and dark I(V) characteristics and (b) EQE of the best solar cells fabricated on Mo with an alumina diffusion barrier (black), on a transparent back contact with a 300 nm-thick ITO film (red), and on a RBC with a 30 nm-thick ITO layer (blue). Mo: [U205_A300_c5], ITO: [U205_WP2_11_c1], RBC: [U205_WP2_8_c6].

First, the transparent back contact leads to an improvement of the best cell J_{SC} and V_{OC} values, which respectively increase from 22.4 to 23.3 mA/cm² and from 584 to 613 mV as compared to the Mo reference. This results in an enhancement of the best cell efficiency from 9.5% to 10.3%. Note that the I(V) curves of solar cells with transparent back contacts were measured on top of a black paper to avoid the reflection of transmitted light on the substrate holder. The 300 nm-thick ITO layer is found to achieve an ohmic contact with CIGS, as it does not lead to a strong increase of the best cell's series resistance (R_S = 0.5 Ω.cm²), which also exhibits J_0 and n values that are similar to the ones obtained with a Mo back contact. Solar cells with a transparent back contact preserve a decent average FF value of 70.3 ± 0.7%, as compared to 71.3 ± 1.6% for the Mo reference.

The best cell on a RBC with a 30 nm-thick ITO layer exhibits a strong increase of the J_{SC} as compared to Mo, from 22.4 mA/cm² to 27 mA/cm², which is correlated to an enhancement of the EQE in the 500 – 1000 nm wavelength range. The best cell also shows an improved V_{OC} of 612 mV, but its efficiency is limited to 9.1% instead of 9.5% for the Mo reference, because of a low *FF* of 53.9%. The dark I(V) parameters of the best cell could not be accurately fitted due to an ideality factor > 2, but the light I(V) curve exhibits a high series resistance and a voltage-dependent current collection. The poor average *FF* values observed with a RBC are attributed to the formation of a Ga oxide compound all across the 30 nm-thick ITO layer. In particular, a current blocking behavior was previously reported for thick and rough Ga oxide layers at the CIGS/ITO back contact [36], [150], [153]. In contrast, co-evaporating CIGS on a 300 nm-thick ITO film resulted in the growth of a smooth interfacial layer of Ga oxide, with a higher average *FF* value and a low series resistance for the best cell. This led to the conclusion that it is necessary to prevent the formation of a thick and rough Ga oxide layer at the CIGS/ITO interface in order to achieve an ohmic contact between CIGS and the RBC and to avoid a voltage-dependent current collection.

	Average / best light I(V) parameters				Best cell dark I(V) parameters			
Back contact	Eff. (%)	J_{SC} (EQE) (mA/cm²)	V_{OC} (mV)	*FF* (%)	J_0 (mA/cm²)	*n*	R_{SH} (Ω.cm²)	R_S (Ω.cm²)
Mo	9.3 ± 0.2 / 9.5	22.4	581 ± 3 / 584	71.3 ± 1.6 / 72.6	7.10^{-6}	1.6	1.10^{5}	< 0.1
ITO	10.0 ± 0.1 / 10.3	23.3	618 ± 3 / 613	70.3 ± 0.7 / 69.5	1.10^{-5}	1.7	6.10^{4}	0.5
RBC*	7.3 ± 0.9 / 9.1	27.0	574 ± 22 / 612	47.2 ± 3.8 / 53.9	/	/	/	/

Table III. 10. Summary of solar cell performances for each type of back contact. The average light I(V) parameters and standard deviation were calculated from the 10 best solar cells. A 1-diode model was used to fit the dark I(V) parameters of the best solar cells (J_0: saturation current, *n*: ideality factors, R_{SH}: shunt resistance, R_S: series resistance). *The dark I(V) curve exhibits an experimental ideality factor > 2 and could not be properly fitted. Mo: [U205_A300_c5], ITO: [U205_WP2_11_c1].

To analyze the optical effects of each back contact, the absorption in each layer of the complete solar cells were simulated (Figure III. 39). A good agreement of the different spectral features between the experimental EQE and the calculated CIGS absorption was found for a simulated CIGS thickness of 490 nm, which is consistent with the experimental average thickness of 480 ± 10 nm.

Using a transparent back contact instead of Mo does not lead to an improvement of the CIGS absorption, but it avoids the absorption losses in Mo by allowing the transmission of unabsorbed light through the whole solar cell stack. Hence, this cell architecture has potential for bifacial or semitransparent applications. Figure III. 39.c shows a significant enhancement of the CIGS absorption with the RBC, thanks to strong resonances in the CIGS absorption and negligible parasitic absorption in the RBC. As a result, a theoretical maximum J_{SC} of 32.2 mA/cm² was calculated by integrating the simulated CIGS absorption with the AM1.5G spectrum, which is respectively 3.5 mA/cm² and 3.7 mA/cm² more than for the Mo and transparent back contacts. However, the experimental EQE curves are well below the simulated CIGS absorption, which indicates significant collection losses. This can be attributed to the back contact

recombination, especially as these CIGS layers co-evaporated in a 1-stage process have a flat GGI profile and conduction band.

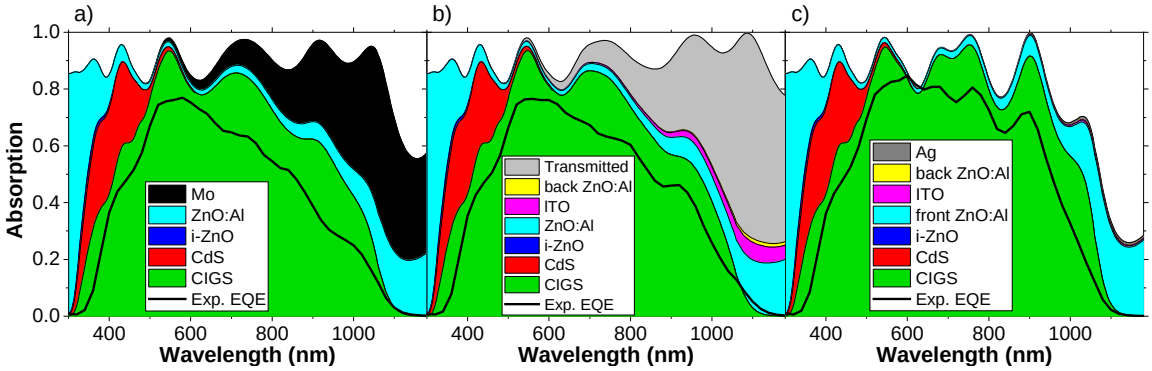

Figure III. 39. Simulated absorption in each stack of the complete CIGS solar cell. The back contacts consist of (a) Mo, (b) a transparent back contact made of SLG/ZnO:Al (30 nm)/ITO (300 nm) and (c) a RBC with a 30 nm-thick ITO layer on top. The experimental EQE curves are shown for comparison with the simulated absorption of CIGS. Mo: [U205_A300_c5], ITO: [U205_WP2_11_c1], RBC: [U205_WP2_8_c6].

To conclude, the limited *FF* and efficiency of solar cells including a RBC with a 30 nm-thick ITO layer were attributed to the formation of Ga oxide across the whole ITO film. Nevertheless, with a low CIGS co-evaporation temperature of 450°C and a NaF PDT, the Ga oxide layers observed in STEM/EDX were thinner than 10 nm. It is expected that with a thicker ITO layer (100 nm or more), a smooth and thin Ga oxide film should form, leading to better photovoltaic performances with a lower R_S and a photocurrent collection that is independent of the applied voltage.

11.5. Conclusion of the chapter

The fabrication of ultrathin CIGS solar cells with RBCs was investigated for different thicknesses of the ITO top layer. In particular, an extensive STEM/EDX study was performed on CIGS layers co-evaporated on RBCs in order to study the segregation of Ga oxide at the CIGS/ITO interface. It is shown that the growth of Ga oxide can be mitigated by reducing the CIGS deposition temperature and by adding 3 nm of Al_2O_3 on top of ITO. We suggest that this Ga oxide compound accounts for the observed trends in solar cell performances as the best efficiencies are achieved when a thin and smooth Ga oxide layer is formed. The main findings that led to this conclusion are listed below:

- For RBC with 200 nm of ITO, the Ga oxide layer observed for a CIGS deposition temperature of 550°C on a bare RBC is thin, and has a limited extent to ITO and CIGS grain boundaries as compared to a 100 nm-thick ITO layer. Thanks to this, the efficiencies of solar cells fabricated at 550°C are similar for Mo and RBCs, and reducing the co-evaporation temperature of CIGS to 500°C does not clearly improve the cell performances. Hence, the Ga oxide layer formed on a 200 nm-thick ITO layer was not found to be strongly detrimental to performances, and it is in turn less critical to mitigate its formation.

- In the case of RBCs with a 100 nm-thick ITO layer, the very rough and thick grains of Ga oxide formed at 550°C on a bare RBC were shown to drastically

degrade the performances of solar cells, in correlation with increased J_0 values. On the other hand, when CIGS is co-evaporated at 500°C on a RBC covered with 3 nm of alumina, a much smoother Ga oxide layer is formed and the best cell J_{SC} is increased from 26.2 mA/cm^2 to 28.9 mA/cm^2 as compared to a Mo back contact, resulting in an increase of the best efficiency from 12.5 % to 13.5%. A simpler RBC architecture with a single ITO layer of 100 nm on top of Ag was also investigated in another CIGS batch. A SEM/EDX study revealed that this RBC architecture allows the local diffusion of Ag clusters through ITO after annealing in air, which means that the ZnO:Al layer is necessary to fully encapsulate Ag. As a result, complete solar cells on this simplified RBC exhibit much lower *FF* and shunt resistances as compared to cells on a RBC with a ZnO:Al/ITO bilayer stack. Best cell efficiencies of 12.2% and 9.6% were obtained for RBCs with and without ZnO:Al on Ag, respectively.

- The co-evaporation of CIGS on a RBC with a 30 nm-thick ITO layer, at a low substrate temperature of 450°C and with a NaF PDT resulted in the formation of a thin Ga oxide film (< 10 nm). However, Ga oxide was found to grow across the whole ITO layer, through its grain boundaries. As a consequence, complete cells exhibit low average *FF* values due to a high series resistance and a voltage-dependent current collection, which in turn limits their efficiency even though a J_{SC} gain of 4.6 mA/cm^2 is achieved as compared to the Mo back contact. In contrast, solar cells with a transparent back contact made of a 300 nm-thick ITO film form a smooth interfacial layer of Ga oxide and show a high average *FF* as well as improved efficiencies as compared to the Mo reference.

As using a NaF PDT led to the formation of a very thin Ga oxide layer, it is expected that the efficiencies of ultrathin solar cells fabricated on RBCs with 100 nm and 200 nm-thick ITO layers could be further improved by incorporating Na through a PDT instead of a NaF precursor layer. However, such a PDT could not be combined with a 3-stage co-evaporation process of CIGS in the present study, because the CIGS co-evaporation reactor was not equipped with a NaF effusion source.

In an attempt to further optimize ultrathin solar cells with RBCs and to increase their V_{OC}, the co-evaporation of ultrathin ACIGS layers on RBCs was also studied, and is reported in the following chapter.

Chapter 12.Ultrathin ACIGS solar cells with RBCs

12.1. Introduction

In this thesis, ultrathin ACIGS solar cells fabricated at 550°C on Mo back contacts were found to lead to higher efficiencies than their CIGS counterparts. Hence, ACIGS was also co-evaporated on RBCs, as the photovoltaic performances of complete solar cells are expected to improve as long as the RBC is compatible with the co-evaporation of ACIGS.

Two batches of ultrathin ACIGS layers were prepared on Mo and on RBCs, at co-evaporation temperatures of 550°C and 500°C. Note that these two batches of ACIGS are the same as the ones in Chapter 6 of Part II. For a discussion of the results obtained on Mo back contacts, refer to this section. Because the lower deposition temperature of 500°C reduced the formation of Ga oxide at the interface between CIGS and ITO, it was also studied in the case of ACIGS even though it led to lower efficiencies on Mo back contacts. The deposited ACIGS layers were characterized, then complete solar cells were fabricated and their performances were analyzed.

12.2. Characterization of ACIGS deposited on RBCs

Ultrathin ACIGS layers were deposited on Mo and RBCs in two different batches with a maximum substrate temperature of either 550°C or 500°C. The investigated back contacts consist of a Mo reference, as well as three different types of RBCs. Two of them include a stack of ZnO:Al (30 nm)/ITO (200 nm) sputtered on Ag, with and without a 3 nm-thick alumina layer on top of it. The last RBC has a single 100 nm-thick layer of ITO on Ag, covered with 3 nm of Al_2O_3. An 8 nm-thick precursor layer of NaF was deposited on each back contact prior to ACIGS co-evaporation. The composition of ACIGS layers was determined by XRF on ACIGS/Mo samples, and the following average atomic ratios were calculated: [Ag]/([Ag]+[Cu]) = 0.10 ± 0.01, ([Ag]+[Cu])/([Ga]+[In]) = 0.78 ± 0.01, [Ga]/ ([Ga]+[In]) = 0.39 ± 0.02. An average ACIGS thickness of 530 ± 20 nm was measured with a profilometer.

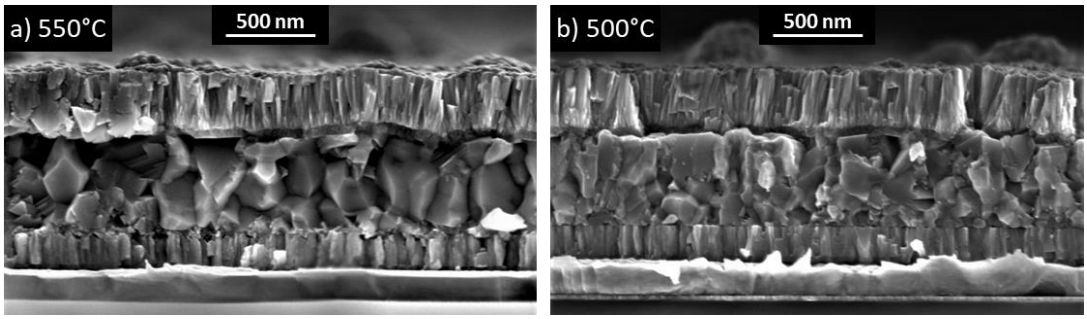

Figure III. 40. SEM cross-section images of complete ultrathin ACIGS solar cells on bare RBCs with a ZnO:Al (30 nm)/ITO (200 nm) bilayer on top of Ag. ACIGS was co-evaporated at (a) 550°C or (b) 500°C. (a) [181120-2B1], (b) [181120-3B1].

The SEM cross-section images of ultrathin ACIGS layers co-evaporated at 550°C and 500°C are shown in Figure III. 40. The back contacts consist of RBCs with a ZnO:Al (30 nm)/ITO (200 nm) stack on top of Ag. An average ACIGS thickness of 520 ± 10 nm was determined from these cross-section images, in good agreement with the thickness of 530 ± 20 nm measured with a profilometer.

As in the case of CIGS layers co-evaporated on RBCs, ACIGS films exhibit smaller grains when deposited at 500°C instead of 550°C. Besides, The ACIGS/ITO interface is also rougher for a co-evaporation temperature of 550°C, but grains are still visible in the ITO layer. Based on this observation, it seems that defects are formed at the ACIGS/ITO interface at 550°C, possibly due to a significant growth of interfacial Ga oxide. To investigate the back interface of ACIGS with ITO, the GD-OES composition profiles of ACIGS layers co-evaporated on those same RBCs were analyzed (Figure III. 41).

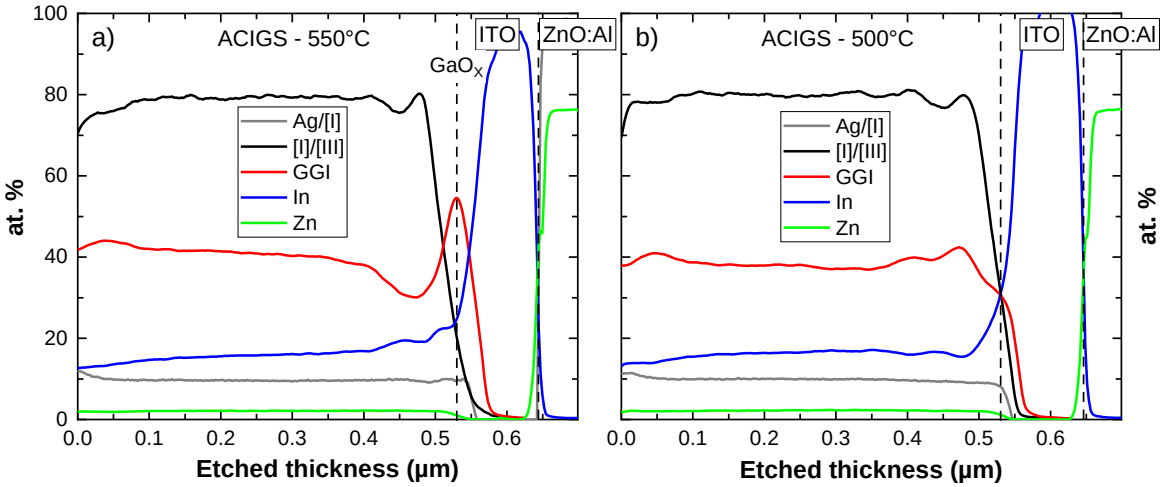

Figure III. 41. GD-OES composition profiles of ACIGS layers co-evaporated at (a) 550°C and (b) 500°C, on a RBC with a ZnO:Al (30 nm)/ITO (200 nm) stack on top of Ag. Vertical dashed lines indicate the position of interfaces. The atomic percentage of absorber elements were calibrated based on the XRF signal of ACIGS on Mo control samples. The ACIGS thickness was calibrated by a profilometer measurement. (a) [181120-2B1], (b) [181120-3B1].

Similar ratios of Ag/[I] and [I]/[III] are observed when ACIGS is co-evaporated on a RBC, regardless of the deposition temperature. However, in the case of the RBCs the GGI profiles are slightly reversed in the top first 350 nm of the ACIGS layers. A strong accumulation of Ga is detected at the ACIGS back interface when co-evaporated at 550°C, which leads to a depletion of Ga over a depth of ≈100 nm in the ACIGS film. This has been attributed to the formation of Ga oxide at the ACIGS/ITO interface. The subsequent depletion of Ga in the ACIGS layer results in a reverse back surface field that was shown to be detrimental to solar cell performances [192]. It is also worth mentioning that this Ga oxide peak detected in GD-OES is much stronger than in the case of CIGS layers co-evaporated at 550°C on a RBC where Ag is covered by a stack of ZnO:Al (30 nm)/ITO (100 nm). This suggests that the kinetics and/or thermodynamics of the Ga oxide formation are favored in the case of ACIGS as compared to CIGS.

When ACIGS is deposited at 500°C, the GGI grading toward the back contact is preserved, which should be beneficial for carrier collection thanks to the subsequent back surface field. However, this does not exclude the formation of Ga oxide, especially as some Ga seems to be detected in the ITO layer. A clearer comparison of the Ga oxide formation could be performed with a STEM/EDX study of the ACIGS/ITO interface.

Complete ultrathin solar cells were then fabricated and their photovoltaic performances were analyzed with respects to the materials characterizations discussed in this section.

12.3. Solar cell performances

Figure III. 42 and Figure III. 43 show respectively the I(V) and EQE curves of the best solar cells for each type of back contact, with ACIGS deposition temperatures of 550°C and 500°C. The back contacts consist of a Mo reference, a RBC with a 100 nm-thick ITO layer atop of Ag, as well as RBCs with a ZnO:Al (30 nm)/ITO (200 nm) stack on Ag with and without an additional 3 nm-thick layer of Al_2O_3. The light and dark I(V) parameters of these samples are also summarized in Table III. 11 and Table III. 12.

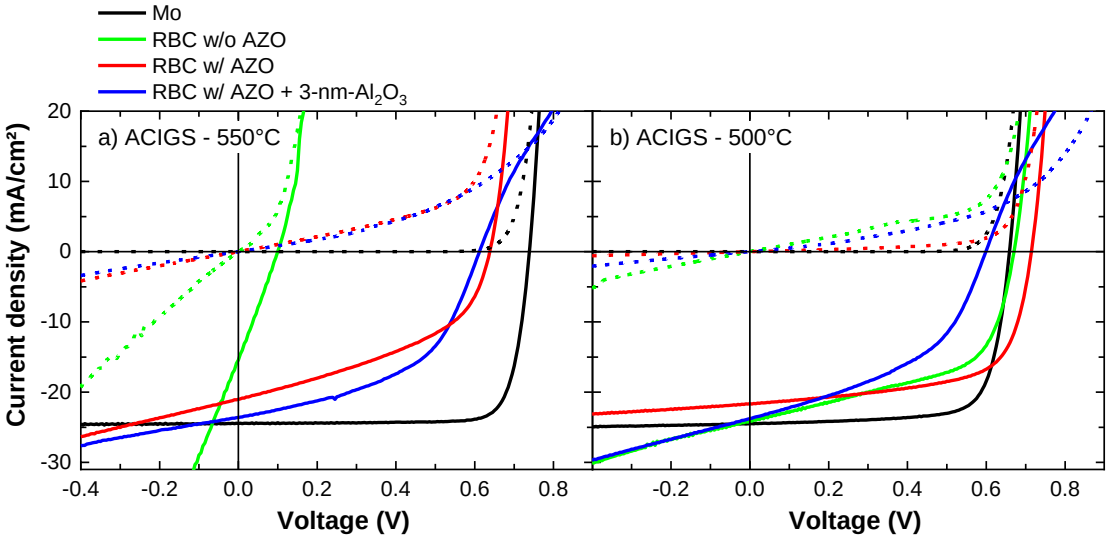

Figure III. 42. I(V) characteristics of each best ACIGS solar cell under one-sun illumination and in the dark. ACIGS was co-evaporated at (a) 550°C and (b) 500°C, on Mo and three different architectures of RBCs. (a) Mo: [181120-2A2_c10], RBC w/o ZnO:Al: [181120-2A1_c11], RBC w/ ZnO:Al [181120-2B1_c14]*, RBC/Al_2O_3: [181120-2B2_c14]. (b) Mo: [181120-3A2_c4], RBC w/o ZnO:Al: [181120-3A1_c7], RBC w/ ZnO:Al [181120-3B1_c4], RBC/Al_2O_3: [181120-3B2_c15]*. *2nd best cells are shown, due to artifacts for the best ones.

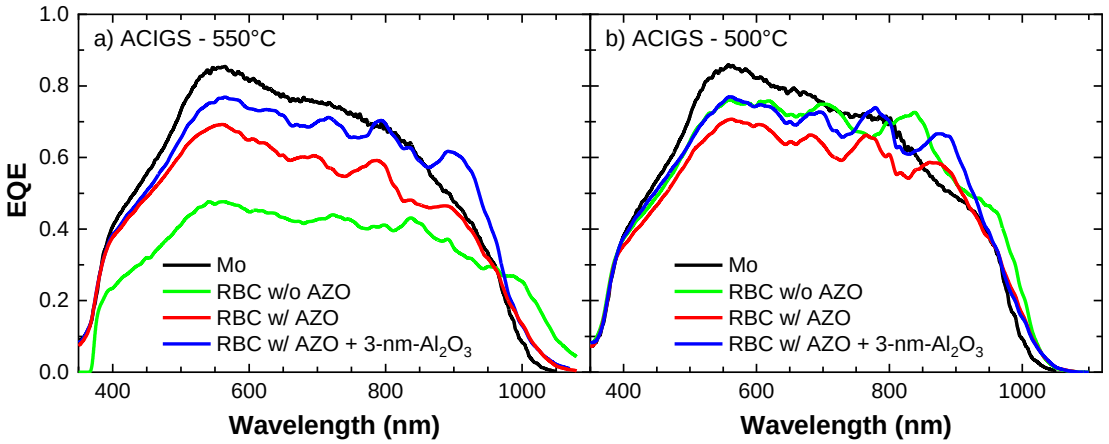

Figure III. 43. EQE of each best ACIGS solar cell prepared at (a) 550°C or (b) 500°C. Back contacts consist of Mo as well as three different stacks of RBCs. (a) Mo: [181120-2A2_c10], RBC w/o ZnO:Al: [181120-2A1_c11], RBC w/ ZnO:Al [181120-2B1_c1], RBC/Al_2O_3: [181120-2B2_c14]. (b) Mo: [181120-3A2_c4], RBC w/o ZnO:Al: [181120-3A1_c7], RBC w/ ZnO:Al [181120-3B1_c4], RBC/Al_2O_3: [181120-3B2_c9].

Contrary to CIGS solar cells, ACIGS devices with RBCs instead of Mo exhibit poor photovoltaic performances, with average efficiencies under 7% regardless of the RBC type and of the ACIGS co-evaporation temperature. This efficiency loss is related to poor average *FF* (< 45%) due to a dramatic reduction of the shunt resistance values, as can be seen from the slopes of the dark I(V) curves at 0 V (Figure III. 42) and the values fitted with a 1-diode model (Table III. 12). The origin of this strong shunting behavior was not identified. Nevertheless, comparing the performances of complete ACIGS devices reveal several trends.

When ACIGS is co-evaporated at 550°C on Mo, a high average efficiency of 14.6 ± 0.2 % is achieved. In the case of a RBC without ZnO:Al on top of Ag, the devices are completely shunted and also suffer from a voltage-dependent current collection. As a result, efficiencies do not exceed 1% and dark I(V) parameters could not be extracted as the dark I(V) curve is dominated by the shunting behavior of those cells. A low J_{SC} of 15.3 mA/cm^2 is achieved, which is 9.2 mA/cm^2 less as compared to the Mo reference. The EQE of the best cell indicates that in these devices, collection losses occur over the whole spectral range of the EQE. The EQE resonances are also attenuated in the wavelength range between 700 and 1000 nm. This could result from a reduction of the reflectance at the ACIGS back interface. Finally, the observed decrease of the optical bandgap suggests a strong formation of Ga oxide that consumes Ga from the ACIGS film. All in all, it is likely that the co-evaporation of ACIGS at 550°C on a RBC with a single layer of ITO on Ag results in a localized diffusion of Ag from the RBC to the ACIGS layer, and in a significant growth of Ga oxide at the ACIGS/ITO interface. These phenomena could in turn be responsible for a deterioration of the reflectivity of the RBC, a voltage-dependent current collection as well as a low shunt resistance.

		Average / best cell light I(V) parameters			
ACIGS deposition temperature	Back contact	Eff. (%)	J_{SC} (EQE) (mA/cm^2)	V_{OC} (mV)	*FF* (%)
550°C	Mo	14.6 ± 0.2 / 14.9	24.5	736 ± 7 / 741	80.8 ± 0.8 / 81.8
	RBC w/o AZO, + Al_2O_3	0.6 ± 0.1 / 0.8	15.3	139 ± 17 / 168	28.1 ± 1.7 / 29.9
	RBC w/ AZO*	5.2 ± 0.6 / 5.7	20.3	612 ± 16 / 638	41.7 ± 3.9 / 44.0
	RBC w/ AZO, + Al_2O_3*	4.6 ± 1.6 / 7.4	23.6	508 ± 72 / 623	37.8 ± 7.9 / 50.2
500°C	Mo	11.3 ± 0.4 / 12.2	24.5	639 ± 10 / 660	71.9 ± 1.8 / 75.5
	RBC w/o AZO, + Al_2O_3*	5.5 ± 2.0 / 8.9	24.1	507 ± 126/672	44.2 ± 8.1 / 55.1
	RBC w/ AZO*	6.6 ± 2.5 / 10.3	21.7	668 ± 46 / 718	44.7 ± 14.0 / 65.8
	RBC w/ AZO, + Al_2O_3*	5.0 ± 1.4 / 6.6	23.8	497 ± 94 / 604	41.5 ± 4.2 / 45.7

Table III. 11. Summary of I(V) parameters under one-sun illumination. Average and standard deviations were calculated from the 10 best solar cells. ACIGS was deposited at 550°C and 500°C, on back contacts consisting of Mo and three different types of RBC architecture. *Due to a strong shunting behavior, light I(V) parameters are specified for the 5 best solar cells only.

ACIGS solar cells prepared at 550°C on a bare RBC with a ZnO:Al/ITO bilayer on top of Ag exhibit an average efficiency of 5.2 ± 0.5 %, with average V_{OC} of 612 ± 16 mV and *FF* of 41.7 ± 3.9 %. The best cell shows a *FF* of 44.0 % and a shunt resistance of 90 Ω.cm², which is why the low *FF* values were attributed to poor shunt resistances. The best cell's V_{OC} is 638 mV and its J_0 is 4.10^{-5} mA/cm², which are lower values than for the Mo reference (741 mV and 2.10^{-10} mA/cm², respectively) but similar to the V_{OC} and J_0 values obtained for the best CIGS solar cells on RBCs. However, the best J_{SC} of this sample is limited to 20.3 mA/cm². In spite of the resonances in the 700 – 1000 nm wavelength range, the EQE of this best cell is lower than in the case of the Mo back contact, indicating that ACIGS cells on a bare RBC suffer from collection losses. Contrary to the cells on a RBC with a single ITO layer on Ag, the RBC with a ZnO:Al/ITO stack maintains its high reflectivity as it leads to significant EQE resonances. The optical bandgap of the best devices is reduced from 1.25 eV on Mo to 1.23 eV on a RBC with ZnO:Al, due to the formation of Ga oxide at the back interface of ACIGS. Indeed, a significant Ga oxide peak was detected in GD-OES, leading to a depletion of Ga in the ACIGS layer close to its back interface. The resulting reverse back surface field could explain the collection losses and V_{OC} drop observed in complete solar cells.

			Best cell dark I(V) parameters			
ACIGS deposition temperature	Back contact		J_0 (mA/cm²)	n	R_{SH} (Ω.cm²)	R_S (Ω.cm²)
550°C	Mo	[-2A2_c10]	2.10^{-10}	1.1	> 1.10^6	< 0.1
[181120-]	RBC w/o AZO, + Al_2O_3 *		/	/	/	/
	RBC w/ AZO °	[-2B1_c14]	4.10^{-5}	2	90	< 0.1
	RBC w/ AZO, + Al_2O_3	[-2B2_c14]	5.10^{-4}	2	110	13.6
500°C	Mo	[-3A2_c4]	1.10^{-8}	1.2	> 4.10^5	< 0.1
[181120-]	RBC w/o AZO, + Al_2O_3	[-3A1_c7]	2.10^{-5}	2	100	< 0.1
	RBC w/ AZO	[-3B1_c4]	2.10^{-6}	1.8	670	< 0.1
	RBC w/ AZO, + Al_2O_3 *	[-3B2_c15]	/	/	180	/

Table III. 12. Dark I(V) parameters of each best solar cell, fitted with a 1-diode model (J_0: saturation currents, n: ideality factor, R_{SH}: shunt resistance, R_S: series resistance). ACIGS was deposited at 550°C and 500°C, on back contacts consisting of Mo and three different types of RBC architecture. *Dark parameters could not be fitted due to strong shunting. °Dark parameters fitted from the second best cell due to measurement artifacts in the case of the best cell.

When a 3 nm-thick alumina layer is added on the RBC with a ZnO:Al/ITO bilayer, complete ACIGS solar cells show an average efficiency of 4.6 ± 1.6 %, with a low average *FF* of 37.8 ± 7.9 %. In this case, the *FF* is limited due to a low shunt resistance of 110 Ω.cm² but also a high series resistance of 13.6 Ω.cm² for the best cell. The light I(V) curve of this best cell also exhibits a distortion under forward bias due to a rollover effect. This can be attributed to the presence of a barrier for hole injection at the ACIGS back contact [141], [185], [186]. Such a rollover effect has been reported for CIGS solar cells deposited on Mo covered with a few nanometers of alumina by ALD and a NaF post-deposition treatment, but not when a NaF precursor layer is used

[141]. This suggests that contrary to CIGS, the deposition of ACIGS on ITO layers with a 3 nm-thick alumina and an 8 nm-thick NaF films creates a barrier for hole injection at the back contact. As a result, the average efficiency of ACIGS devices on a RBC with alumina is lower than for a bare RBC. The average V_{OC} of these devices is also found to fluctuate, as indicated by a standard deviation of 72 mV. This is related to the fluctuating rollover effect for the 5 best solar cells. A J_{SC} of 23.6 mA/cm^2 was obtained for this RBC covered with alumina, which is 3.3 mA/cm^2 more than for a bare RBC thanks to reduced collection losses, as can be seen in the EQE curves. Though the additional alumina layer on the RBC might be beneficial for charge carrier collection, the resulting EQE is still lower than for the Mo back contact in the wavelength range between 400 and 800 nm.

The average efficiency of ultrathin ACIGS solar cells on Mo is decreased from 14.6 ± 0.2 % to 11.3 ± 0.4 % when the co-evaporation of ACIGS is reduced from 550°C to 500°C. This efficiency loss is related to a lower average V_{OC} of 639 ± 10 mV and *FF* of 71.9 ± 1.8 %. In contrast, the average efficiency of cells on a RBC without ZnO:Al on Ag is improved from 0.6 ± 0.1 % at 550°C to 5.5 ± 2.0 % at 500°C. This efficiency gain is mainly due to an enhancement of the shunt resistance (100 Ω.cm^2 for the best cell), possibly thanks to a reduced diffusion of Ag through the ITO layer at 500°C. However, the 5 best cells exhibit highly fluctuating V_{OC}, *FF* and shunt resistance values. The EQE of the best cell prepared at 500°C on this RBC shows less collection losses as compared to Mo, than in the case of cells fabricated at 550°C. The EQE curve also exhibits resonances for wavelengths between 700 and 1000 nm due to the enhanced reflectance of the back contact. Based on the EQE curves, this RBC leads to an optical bandgap of 1.22 eV instead of 1.25 eV for Mo. This bandgap is higher than for cells prepared at 550°C, which indicates that decreasing the co-evaporation temperature of ACIGS from 550°C to 500°C reduces the growth of Ga oxide at the ACIGS/ITO interface in the case of RBC with a single ITO layer on Ag.

The best ACIGS solar cell on a bare RBC with a ZnO:Al/ITO bilayer exhibits an efficiency of 10.3%, with a V_{OC} of 718 mV, a J_{SC} = 21.7 mA/cm^2 and *FF* of 65.8 %. However, the average *FF* of these devices shows a high standard deviation because of a voltage-dependent current collection as well as strong variations in the shunt resistances. This results in an average efficiency of 6.6 ± 2.5 %. The improved reflectance at the ACIGS back contact leads to interferences in the EQE for wavelengths between 650 nm and 950 nm. However, the EQE of the best cell with this RBC is lower than the EQE of the Mo reference in the 400 – 850 nm wavelength range, because of collection losses. Still, GD-OES data showed that the co-evaporation of ACIGS at 500°C instead of 550°C reduces the formation of interfacial Ga oxide, which in turn limits collection losses in complete devices as indicated by a J_{SC} gain of 1.4 mA/cm^2.

Adding a 3 nm-thick alumina layer on the RBC covered with a ZnO:Al/ITO stack improves the collection efficiency of complete cells, as seen from the enhancement of the EQE over the whole spectral range resulting in a J_{SC} of 23.8 mA/cm^2. However, the best cell efficiency is limited to 6.6% and there is a strong fluctuation of the I(V) parameters leading to a decreased average efficiency of 5.0 ± 1.4 %, with average V_{OC} of 497 ± 94 mV and *FF* of 41.5 ± 4.2 %. The experimental dark I(V) curve shows an

ideality factor n > 4 under forward bias, preventing a proper fit of the dark I(V) parameters. Nevertheless, the light and dark I(V) curves of the best cell shows that its poor *FF* is related to a voltage-dependent photocurrent, as well as degraded series and shunt resistances. Similarly to solar cells fabricated at 550°C, the addition of alumina leads to a rollover effect, suggesting that the Al_2O_3 layer also forms a barrier for hole injection at 500°C.

All in all, ACIGS solar cells with RBCs perform better when fabricated at 500°C rather than 550°C, but their efficiency suffers from the same types of losses: low shunt resistances, collection losses and lower J_0 as compared to Mo. Despite the promising efficiency achieved on Mo, the deposition of ACIGS layers on RBCs did not improve the performances of complete solar cells. The behavior of ACIGS solar cells with RBCs was shown to be quite different from CIGS devices. A summary of these results is given in the next section.

12.4. Conclusion of the chapter

Ultrathin ACIGS solar cells were fabricated on three different types of RBCs and compared to Mo. The RBC architectures consist of a single layer of ITO (100 nm) on top of Ag, as well as a ZnO:Al (30 nm)/ITO (200nm) bilayer on Ag with and without an additional 3 nm-thick alumina film. The main findings are described below:

- SEM cross-section images show that the co-evaporation ACIGS layers at 550°C creates a rough back interface with ITO, while a smooth interface is observed when ACIGS is deposited at 500°C.
- A GD-OES analysis reveals that co-evaporating ACIGS at 550°C on a RBC forms a significant amount of Ga oxide, resulting in a reverse GGI back grading. The growth of Ga oxide is mitigated when ACIGS is deposited at 500°C, and the GGI back grading looks preserved.
- ACIGS solar cells including a RBC with a single ITO layer are completely shunted when prepared at 550°C, with an average efficiency of 0.6 ± 0.1 %. This is most likely due to the localized diffusion of Ag from the RBC to the ACIGS layer. Reducing the co-evaporation temperature to 500 °C increased the average efficiency to 5.5 ± 2.0 % thanks to higher shunt resistances.
- The bare RBC with a ZnO:Al/ITO bilayer leads to an average efficiency of 5.2 ± 0.6 % at 550°C and 6.6 ± 2.5 % at 500°C. The cell performances are limited by low shunt resistances as well as collection losses attributed to the formation of Ga oxide.
- Solar cells with a stack of ZnO:Al/ITO/Al_2O_3 (3 nm) on top of the RBC show an average efficiency of 4.6 ± 1.6 % at 550°C, and 5.0 ± 1.4 % at 500°C. Though the alumina layer enhances the EQE thanks to a better carrier collection, the solar cells exhibit a rollover effect as well as degraded series and shunt resistances.
- For each type of RBCs, the performances of ACIGS solar cells are improved when prepared at 500°C instead of 550°C, but their efficiencies remain below the Mo reference.

- In contrast to the case of CIGS, the J_{SC} of ACIGS solar cells was not improved by replacing Mo with a RBC. The EQE show resonances in the infrared region thanks to the enhanced reflectance of the ACIGS back contact, but collection losses reduce the J_{SC} as compared to Mo.

The origin of the poor performances and shunt resistances of ultrathin ACIGS devices with RBCs was not fully elucidated, but could be due to the strong formation of Ga oxide. Investigating the fabrication and characterization of ACIGS solar cells on a transparent ITO back contact could help to determine whether the ACIGS/ITO back interface intrinsically results in photovoltaic performance degradations. If that is the case, other TCO materials could be studied as a top layer of the RBC, as for example hydrogen-doped In_2O_3 which was shown to be a suitable transparent back contact for ACIGS solar cells [192]. If the growth of Ga oxide at the ACIGS back contact is responsible for the low performances, incorporating Na via a NaF PDT rather than a precursor layer should mitigate the formation of Ga oxide [192].

Chapter 13.Nanostructured RBCs for ultrathin CIGS solar cells

13.1. Introduction

The simulation and fabrication of flat RBCs was studied in the previous chapters. These flat RBCs increase light absorption in ultrathin CIGS layers via Fabry-Pérot resonances. The next step to further increase the absorption of CIGS is to use light trapping strategies like nanopatterned RBCs. These architectures notably allow the coupling of light into waveguide modes in the absorber layer, which was numerically [156] and experimentally [161]–[163] demonstrated to result in ultrathin CIGS solar cells with J_{SC} values that exceed those of flat cells including a back reflector.

This chapter consists in a preliminary numerical study of nanopatterned RBCs for ultrathin CIGS solar cells. The optimization of the pattern geometry was performed by Joya Zeitouny, postdoctoral researcher, using the Reticolo software for two-dimensional optical simulations of the solar cell architecture [166]. The studied architectures are based on the flat RBC stack that was developed in this work. Here, an almost ideal case is considered in order to provide an upper limit of the J_{SC} that can be achieved with ultrathin CIGS solar cells on these patterned RBCs. The investigated nanostructured RBCs are first described, then the simulation results of light absorption are discussed.

13.2. Geometry of the nanostructured RBCs

Complete cells including the investigated architectures of nanopatterned RBCs are schematically represented in Figure III. 44, together with top views of the respective nanostructured layers.

Two nanostructured architectures were simulated, with either a dielectric nanogrid or dielectric nanopillars on top of the flat RBC stack (semi-infinite Ag/TCO). In order to determine the best J_{SC} that such patterned RBCs can yield, a case close to ideality was considered:

- The parasitic absorption in the front layers is mitigated by using a thin ZnO:Al film of 100 nm, and a 30-nm-thick CdS layer. In comparison, state-of-the-art solar cells usually include very transparent TCO layers as a front contact, like ZnO:B, as well as thin CdS layers combined with a heavy alkali PDT or a Zn-based buffer layer.
- The TCO spacer between the Ag mirror and the CIGS absorber is modeled by a single layer with fixed optical indices of n = 1.9 and k = 0. While idealized, this TCO layer should provide an accurate description of the flat RBCs studied previously. Indeed, the ZnO:Al/ITO bilayer stack on top of Ag have refractive index values close to 1.9 in the relevant wavelength range [208], [209], and it is also reasonable to neglect the parasitic light absorption in the TCO layers because they don't require a low sheet resistance as the Ag mirror ensures the lateral transport of charge carriers. Finally, the modeled TCO layer exhibits a fixed thickness of 150 nm, which is in line with the ZnO:Al (30 nm)/ITO (100 nm) stack that led to the best cell efficiency with a flat RBC.

- The nanopatterned dielectric is simulated with fixed optical indices of n = 1.4 and k = 0. In this regard, sol-gel layers of porous TiO_2 or SiO_2 have adequate optical indices and are eligible materials to fabricate nanoscale patterns, using for example the NIL technique [183], [184].
- Under the aforementioned assumptions, the geometry of the nanostructures was varied to maximize the J_{SC} of complete cells, with a total volume of CIGS that is below the one of a flat 300 nm-thick layer. The geometrical parameters of the optimized nanopatterned RBCs are described in Figure III. 44. Note that the geometry of the dielectric nanogrid leads to an effective CIGS thickness of 300 nm, as compared to 250 nm with the dielectric nanopillars.

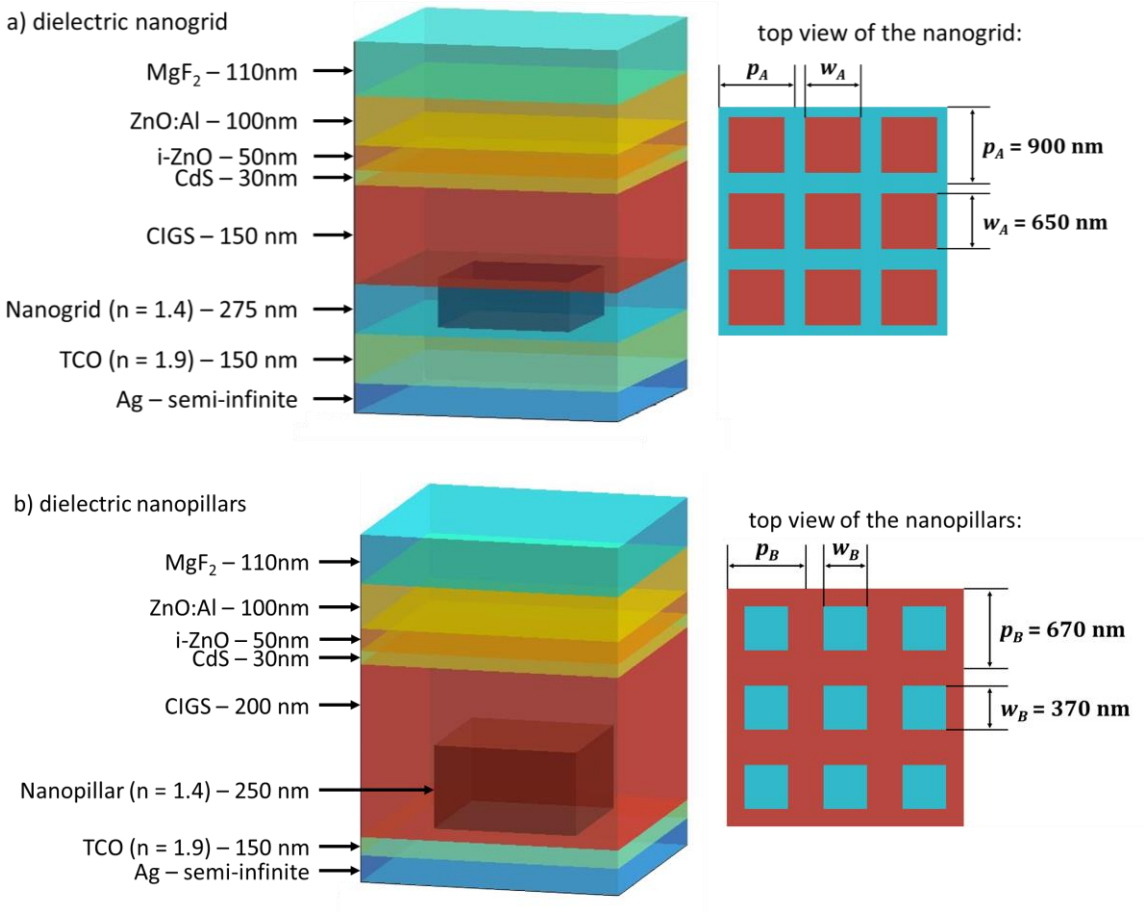

Figure III. 44. Schematics of the unit cells used for the simulation of nanostructured RBCs (not to scale), together with top views of the respective patterned layers. In (a), a square dielectric nanogrid is added on the TCO back contact, with a height of h_A = 275 nm, and a period of p_A = 900 nm. The CIGS pillars embedded in this nanogrid have a width of w_A = 650 nm, resulting in a linear filling fraction of ff_A = 73 % for CIGS. The total volume of CIGS (flat layer + nanopillars) is equivalent to a flat CIGS layer with a thickness of t_A = 300 nm. In (b), a square array of dielectric nanopillars is added on the TCO back contact, with a height of h_B = 250 nm, a width of w_B = 370 nm and a period of p_B = 670 nm. This leads to a linear filling fraction of ff_B = 45% for CIGS, and to a total volume of CIGS (flat layer + nanogrid) that is equivalent to a flat CIGS layer with a thickness of t_B = 250 nm.

The geometry of the dielectric patterns was not constrained during its optimization. As a result, the nanostructures show a height of 275 nm for the dielectric nanogrid, and of 250 nm in the case of the dielectric nanopillars. It is not straightforward to fabricate nanoscale patterns with such aspect ratios with a NIL process [178].

Nevertheless, Yin *et al.* [163] reported the fabrication of SiO_X nanopatterns using substrate conformal imprint lithography. The nanoparticles had the shape of a conical frustum with a height of 210 nm, a base radius of 205 nm, a top radius of 102 nm and a pitch of 513 nm. Hence, it was possible to fabricate nanopatterns with a geometry that is close to the one of the dielectric nanopillars shown in Figure III. 44. In addition, ultrathin solar cells with a 390 nm-thick CIGS absorber, an ITO back contact and SiO_X nanopatterns did not exhibit performance losses as compared to a flat ITO back contact. This demonstrates that ultrathin CIGS solar cells are compatible with rough and nanostructured back contacts.

The simulation results of the optimized nanostructured RBCs are discussed in the next section.

13.3. Absorption of complete solar cells with nanostructured RBCs

Figure III. 45 shows the simulated absorption in each layer of ultrathin solar cells with nanostructured RBCs. Their CIGS absorption can also be compared to the one of planar solar cells on Mo and flat RBCs. The flat RBCs were simulated using the cell architectures presented in Figure III. 44, but without a patterned dielectric material. In planar cells, the CIGS thickness corresponds to the respective equivalent CIGS thicknesses of 300 nm in the case of the dielectric nanogrid (Figure III. 45.a), and 250 nm for the dielectric nanopillars (Figure III. 45.b).

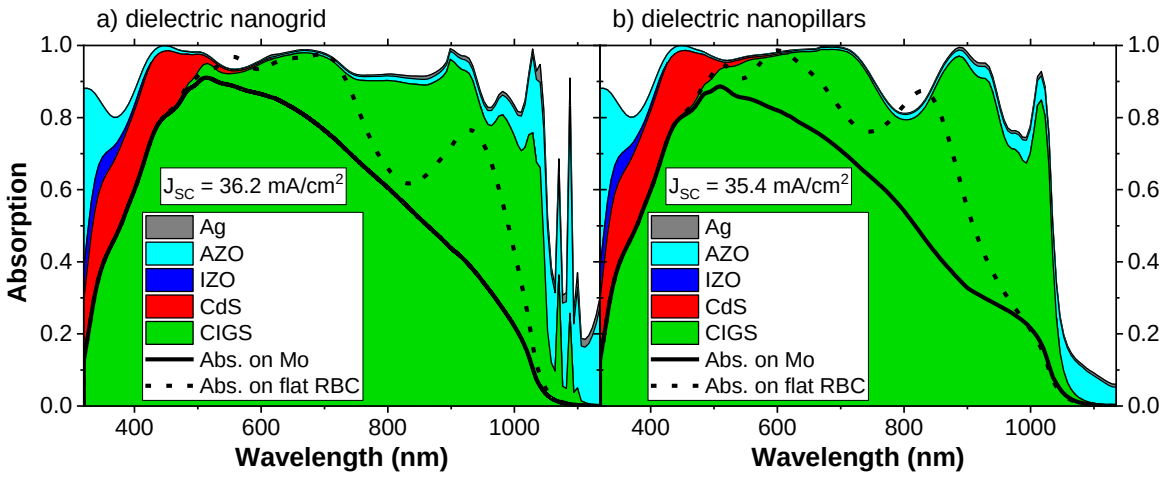

Figure III. 45. Light absorption simulated in each layer of complete solar cells including nanostructured RBCs with an optimized geometry. The patterned RBCs result in an effective CIGS thickness of (a) 300 nm and (b) 250 nm. Using the corresponding effective thicknesses of CIGS, the CIGS absorption of solar cells with planar Mo (solid lines) and flat RBCs (dashed lines) are also shown for comparison.

For both types of patterned RBCs, CIGS absorption is mostly improved in the infrared region as compared to planar Mo and flat RBCs. Theoretical J_{SC} values were calculated from the simulated absorption integrated with the AM 1.5 G solar spectrum, assuming a perfect collection of the photogenerated charge carriers. The dielectric nanogrid architecture leads to a high J_{SC} of 36.2 mA/cm^2, with an equivalent CIGS thickness of only 300 nm. In comparison, the J_{SC} of planar cells on a flat RBC or on Mo are respectively 31.4 mA/cm^2 and 26.5 mA/cm^2. The RBC patterned with dielectric nanopillars result in a J_{SC} of 35.4 mA/cm^2 for an effective CIGS thickness of 250 nm, as compared to 30.1 mA/cm^2 on a flat RBC and 24.6 mA/cm^2 on a planar Mo back contact. The J_{SC} calculated with nanostructured RBCs are close to the J_{SC} of best solar cells with standard absorber thicknesses [31], [32], and not far from the J_{SC} of 39.6 mA/cm^2 for the current record efficiency of 23.4%, which was achieved with a highly transparent Zn-based buffer layer and a bandgap minimum ≤1.14 eV [26].

Replacing the flat RBC with a nanostructured RBC is shown to produce additional resonances in the CIGS absorption spectra, for wavelengths between 750 and 1100 nm in the case of a dielectric nanogrid (Figure III. 45.a), and in the 600 – 1100 nm wavelength range when considering dielectric nanopillars (Figure III. 45.b). Note that the architecture of dielectric nanopillars leads to an incomplete CIGS absorption at wavelengths around 800 nm and 950 nm (Figure III. 45.b), but it does not result in a substantial J_{SC} loss as H_2O present in the atmosphere already absorbs the solar light at these wavelengths.

Those absorption resonances can be attributed to the coupling of light into waveguide modes. To further analyze the optical modes at stake, it would be insightful to plot the dispersion diagrams of total absorption versus the wavelength and period of the nanostructures, as well as the 2D density of the photons absorbed at the resonance wavelengths. However, these analyses were not performed in this preliminary study.

Experimentally, the first fabrication tests of nanostructured RBCs with a NIL process were not successful. Indeed, the sol-gel TiO_2 material that was nanoimprinted on flat RBCs contains traces of HCl, which in turn sufficiently etched the ITO and ZnO:Al layers to result in the oxidation of the underlying Ag mirror. Hence, other materials for the fabrication of nanopatterns need to be investigated. In this regard, Yin *et al.* proposed an architecture of SiO_X nanoparticles fabricated on a back contact made of ITO [163].

13.4. Conclusion of the chapter

To conclude, two different architectures of nanostructured RBCs were simulated. A dielectric material patterned on top of a flat RBC was considered, where the layer stack of the flat RBC was based on the RBC architecture developed in this work. The simulation results of the CIGS absorption on top of nanopatterned RBCs are promising:

- Thanks to an enhanced CIGS absorption in the infrared region, a J_{SC} of 36.2 mA/cm^2 was calculated with a dielectric nanogrid structure and a total volume of CIGS that is equivalent to only 300 nm of a flat layer. This represented a J_{SC} gain of 4.8 mA/cm^2 and 9.7 mA/cm^2 as compared to a flat RBC and a planar Mo back contact, respectively.
- A second architecture of RBC with dielectric nanopillars also improved the CIGS absorption, and yielded a J_{SC} of 35.4 mA/cm^2 for an effective CIGS thickness as low as 250 nm. This was respectively 5.3 mA/cm^2 and 10.8 mA/cm^2 more than in the cases of a flat RBC and of a Mo back contact.

These numerical results pave the way toward the fabrication of ultrathin CIGS solar cells on nanostructured RBCs, with J_{SC} values that are on par with the ones of standard solar cells.

Conclusion of Part III

A RBC architecture has been successfully developed to improve light absorption of ultrathin CIGS solar cells. This RBC consists of a multi-layer stack of SLG/ZnO:Al (50 nm)/Ag (150 nm)/ZnO:Al (30 nm)/ITO. Three different thicknesses of ITO were investigated: 200 nm, 100 nm and 30 nm. For a 500 nm-thick CIGS layer on a RBC, optical simulations predicted a promising J_{SC} gain of about 3.0 mA/cm^2 as compared to Mo. However, the thickness of the top ITO layer was shown to affect the chemical stability of the CIGS/ITO interface and the growth of an interfacial Ga oxide compound was observed in STEM/EDX, with significant impacts on the performances of complete devices. The main findings are summarized below:

- In the case of a RBC with a 200 nm-thick ITO layer, the formation of Ga oxide is not strongly affected by the CIGS co-evaporation temperature and the presence of an interfacial alumina layer. With this RBC, an average efficiency of 11.3 ± 0.4 % was achieved at 550°C, close to the case of Mo with 11.7 ± 0.5 %. Reducing the co-evaporation temperature to 500°C led to a similar average efficiency of 10.9 ± 0.4 % with a RBC.
- For RBC with a 100 nm-thick ITO layer, the formation of Ga oxide was efficiently mitigated by decreasing the co-evaporation temperature of CIGS from 550°C to 500°C. Adding a 3 nm-thick Al_2O_3 layer on top of ITO reduced the roughness of the Ga oxide layer. The RBCs led to significant EQE enhancements thanks to a high reflectivity. At 500°C and with 3 nm of Al_2O_3, a best cell efficiency of 13.5% was achieved with a J_{SC} of 28.9 mA/cm^2, which are respectively 1.0% absolute and 2.7 mA/cm^2 more than the Mo reference.
- Another RBC architecture was investigated, with a 100 nm-thick ITO layer deposited directly on top of Ag. After annealing in air this RBC leads to a local diffusion of Ag trough ITO, and complete cells show low *FF* and shunt resistances. The best cell efficiency is limited to 9.6%, as compared to 12.2% for a RBC with a ZnO:Al/ITO bilayer on Ag, despite a similar J_{SC} increase.
- Co-evaporating CIGS at 450°C with a NaF PDT led to the growth of a very thin Ga oxide film (< 10 nm), but it was found to extend inside the grain boundaries of the 30 nm-thick ITO layer on top of the RBC. It resulted in low average efficiencies and *FF* values due to a voltage-dependent current collection, although a J_{SC} increase of 4.6 mA/cm^2 was achieved as compared to cells on a Mo back contact.
- Ultrathin ACIGS layer co-evaporated on RBCs were shown to form a significant amount of Ga oxide at 550°C, leading to a reverse GGI grading. For both co-evaporation temperatures of 550°C and 500°C, the average efficiencies of ACIGS solar cells with RBCs remain below 7%, mainly due to low shunt resistances and collection losses.
- As a perspective, CIGS solar cells including nanostructured RBCs were simulated. Using optimized architectures, promising J_{SC} values above 35 mA/cm^2 were calculated for cells with an effective CIGS thickness of only 250 – 300 nm. It is thus expected that the experimental J_{SC} of ultrathin solar cells could be further improved thanks to patterned RBCs.

General conclusion and perspectives

Thinning the CIGS-based absorber of complete solar cells can improve the industrial competitiveness of the CIGS technology thanks to a lower material usage and an increased industrial throughput, but to do so it is necessary to maintain an efficiency comparable to standard thickness devices. However, the efficiency of ultrathin CIGS solar cells on standard Mo back contacts is limited by the high surface recombination velocity and the poor light reflectance at the CIGS back interface. Hence, this work investigated strategies to improve the efficiency of ultrathin CIGS solar cells based on the rear passivation of the CIGS absorber and/or the enhancement of the CIGS back reflectance.

First, the composition grading of ultrathin CIGS layers (≈500 nm) co-evaporated on Mo with a modified 3-stage process was improved. Co-evaporating CIGS at a standard maximum substrate temperature of 550°C was found to create a linear GGI depth profile throughout the CIGS layer. It was also shown that reducing the CIGS deposition temperature to 500°C and 450°C led to a steeper GGI back grading at the interface with Mo. It results in a graded conduction band and a subsequent back surface field that contributes to the CIGS rear passivation by drifting electrons toward the *p-n* junction. Lower co-evaporation temperatures also led to a CIGS morphology with rougher interfaces and smaller grains. Still, the crystallinity of CIGS layers deposited at 550°C and 500°C appears to be similar.

Complete solar cells with a standard stack of CdS/i-ZnO/ZnO:Al and a 15 nm-thick NaF precursor layer were then characterized. It was found that reducing the CIGS co-evaporation temperature from 550°C to 450°C decreased the efficiency of complete cells due to lower V_{OC} and *FF* values. They were respectively ascribed to an increased amount of non-radiative recombination and a voltage-dependent current collection. Still, the **CIGS deposition temperature of 500°C** allowed an increase of the average efficiency from 11.5 ± 0.2 % to **12.6 ± 0.4 %** as compared to 550°C. This was achieved thanks to an improvement of the V_{OC} and J_{SC}, which were attributed to the steeper GGI back grading formed at 500°C. Indeed, the lower fitted J_0 value and the improved EQE in the 550 – 1000 nm wavelength range suggest a reduced amount of back contact recombination. These performances were also compared to the case of cells with thinner NaF precursor layers of 8 nm. For both deposition temperatures of 550°C and 500°C, a smaller amount of NaF led to decreased efficiencies, due to a drop of the V_{OC} and *FF* as well as a lower collection efficiency.

Ultrathin ACIGS layers (≈500 nm) were also fabricated by co-evaporating Ag proportionally to Cu during the deposition of CIGS in a modified 3-stage process. The resulting ACIGS films contained about 2 at.% of Ag. Contrary to the case of CIGS, the co-evaporation of ACIGS at 550°C and 500°C yielded very similar GGI profiles. The morphology of ACIGS layers deposited at 500°C instead of 550°C showed smaller grains and a much rougher front interface. Still, the XRD data of these ACIGS films suggest a similar crystallinity.

Complete solar cells were fabricated, with 15 nm or 8 nm of NaF as a precursor layer. Cells were found to perform better with 8 nm of NaF, thanks to better V_{OC}, *FF*, J_0 and *n* values. In contrast to ultrathin CIGS solar cells, ACIGS devices prepared at 500°C rather than 550°C exhibited lower efficiencies due to decreased *FF* and V_{OC}. This was respectively correlated to a voltage-dependent current collection, and higher J_0 and *n* values. As a result, the best ultrathin solar cell was obtained for an **ACIGS co-evaporation temperature of 550°C and an 8 nm-thick NaF precursor layer**. With an ACIGS thickness of 540 ± 20 nm, it achieved an **efficiency of 14.9%, with a V_{OC} of 741 mV, a *FF* of 81.8%** and a J_{SC} of 24.5 mA/cm^2. This best efficiency is close to the current record efficiency of 15.2% for ultrathin CIGS absorbers. It is also remarkably higher than the efficiencies reached with our CIGS solar cells, in particular thanks to a reduced voltage deficit.

To provide a better understanding of the performances of ultrathin CIGS and ACIGS solar cells, a cathodoluminescence study was also performed. It was shown that spatial fluctuations of the composition do not play a significant role. On the contrary, the best performances obtained for ACIGS layers deposited at 550°C are correlated with a higher luminescence intensity and a narrower Urbach tail, indicating a reduced density of shallow defects.

Ultrathin CIGS solar cells were also prepared on Mo back contacts with and without a perforated alumina passivation layer. A process relying on nanoimprint lithography and wet etching steps was used to pattern point contact openings in the 50 nm-thick passivation layer. The patterned holes had a diameter of ~300 nm and pitches of 1 µm, 2 µm, 3 µm and 4 µm. CIGS was deposited in a 1-stage co-evaporation to form an ungraded GGI depth profile and thus to avoid an additional back surface field.

The characterization of complete cells indicates that pitches of 3 µm and 4 µm are too large as compared to the hole diffusion length, because they lead to high series resistances and a rollover effect. *FF* values measured for pitches of 1 µm and 2 µm and for the unpassivated reference are similar, with only a slight increase of the series resistance due to the passivation layer. Higher V_{OC} and J_{SC} values are obtained with the passivation layer. This has been attributed to the CIGS rear passivation by alumina, leading to a lower amount of back contact recombination. For **an alumina passivation layer with a point contact pitch of 2 µm**, *i.e.* a surface coverage of ~93% by alumina, **a best efficiency of 9.5% and a V_{OC} of 613 mV were achieved**, as compared to 7.9% and 562 mV for the unpassivated reference. Hence, a significant passivation effect was observed, but the co-evaporation of ultrathin absorbers in a 1-stage process leads to much lower performances than in the case of a 3-stage process. As the fabrication of a nano-patterned passivation layer is time-consuming and challenging, it should be of interest to combine a 3-stage co-evaporation process with a passivation layer to determine whether these additional fabrication steps are necessary to achieve an adequate CIGS rear passivation.

Using the aforementioned strategies, the J_{SC} of complete cells generally lie in the 24 – 26 mA/cm^2 range due to the incomplete absorption of the incident light. These J_{SC} are much below the values of ~40 mA/cm^2 of record CIGS cells with standard absorber thicknesses. Light management strategies are thus necessary to enhance the light

absorption in ultrathin solar cells. The main challenge toward this goal remains the introduction of a highly reflective back contact that is compatible with the direct deposition of CIGS at typical temperatures ≥ 500°C. This is why this thesis presents a novel architecture of reflective back contact (RBC) that is stable during the co-evaporation process of CIGS. It includes a silver mirror encapsulated in ZnO:Al layers for thermal stability, and a top ITO layer to provide an ohmic contact with CIGS. The complete stack of this back contact is the following: SLG/ZnO:Al (50 nm)/Ag (150 nm)/ZnO:Al (30 nm)/ITO. Optical simulations indicated that this layer stack can provide an almost perfect double-pass absorption in the ultrathin absorber.

Material characterizations of the sputtered ITO layers showed that ITO is more transparent after a 10-minute annealing in air at a temperature > 500°C. After annealing, the RBCs did not show any sign of Ag diffusion in SEM, which is a necessary prerequisite to be compatible with the direct co-evaporation of CIGS. The annealed RBCs also show a satisfactory reflectance above 90% in the wavelength range between 600 and 1150 nm, as well as sheet resistances of ~0.1 Ω.sq.

Ultrathin CIGS solar cells were fabricated on top of RBCs with ITO thicknesses of 200 nm, 100 nm and 30 nm. Extensive studies in STEM/EDX revealed the growth of a Ga oxide layer at the CIGS/ITO interface. For thinner ITO layers, more Ga oxide was formed inside the grain boundaries of ITO. To mitigate the formation of Ga oxide, the co-evaporation temperature of CIGS was reduced from 550°C to 500°C, and an additional layer of alumina (< 3 nm) was deposited by ALD on ITO. In the case of RBCs with 100 nm of ITO, these strategies were found to lead to a much smoother Ga oxide layer that does not extend into the grain boundaries of ITO. It also avoided a strong consumption of Ga from the CIGS layer, which can result in a reverse and detrimental GGI grading.

In the case of a **RBC with 100 nm of ITO**, the smoother and thinner Ga oxide layer formed at **500°C** and with **3 nm of Al_2O_3** on top of ITO led to an ultrathin cell (500 ± 20 nm of CIGS) with a best **efficiency of 13.5% and a J_{SC} of 28.9 mA/cm²**, which are respectively 1.0% absolute and 2.7 mA/cm² more than the Mo reference. A significant improvement of the J_{SC} was thus achieved, in correlation with an enhancement of the EQE thanks to the highly reflective back contact, as confirmed by optical simulations of the experimental devices. In addition, similar V_{OC} and *FF* values were achieved thanks to the reduced formation of Ga oxide, which preserved the GGI back grading of the CIGS layer.

The impacts of a NaF PDT were also studied with CIGS absorbers co-evaporated at 450°C on a RBC with 30 nm of ITO, as well as a transparent back contact with a 300 nm-thick ITO film. The lower deposition temperature and the addition of Na in a PDT were expected to mitigate the formation of Ga oxide at the CIGS/ITO interface [37], [38], [150]. They indeed resulted in the growth of a thin (< 10 nm) Ga oxide layer, but it extended into the ITO grain boundaries and across the whole ITO layer in the case of the RBC with 30 nm of ITO. As a result, the RBC led to poor cell efficiencies with low *FF* due to a voltage-dependent current collection and a high series resistance. Nevertheless, these cells benefit from a J_{SC} gain of 4.6 mA/cm² as compared to the Mo back contact. In contrast, a transparent back contact with a 300 nm-thick ITO layer led

to the formation of a smooth Ga oxide film and to complete solar cells with a high average *FF* (70.3 ± 0.7%). These cells also exhibited improved average V_{OC} and efficiency values as compared to the Mo reference (*FF* = 71.3 ± 1.6 %, V_{OC} = 581 ± 3 mV and η = 9.3 ± 0.2 %). As a thin Ga oxide layer (< 10 nm) was formed when using a NaF PDT and a CIGS deposition temperature of 450°C, it is expected that incorporating Na through a PDT instead of a NaF precursor layer could improve the efficiencies of cells on RBCs with an ITO thickness ≥ 100 nm.

In an attempt to improve the V_{OC} and *FF* of ultrathin solar cells on RBCs, ACIGS layers were also co-evaporated on RBCs at 550°C and 500°C. However, GD-OES analyses revealed a much stronger formation of Ga oxide at the ACIGS/ITO interface, together with a substantial consumption of Ga from the ACIGS films. It is suggested that this accounts for the low performances of ACIGS solar cells on RBCs, which showed average efficiencies below 7%. In this regard, fabricating ultrathin ACIGS cells on a transparent ITO-based back contact could indicate if the poor performances are intrinsic to the ACIGS/ITO interface. If the co-evaporation of Ag with CIGS actually promotes the formation of Ga oxide, co-evaporating Ag only during the last stages of the process might reduce the production of Ga oxide. Replacing ITO by another TCO at the ACIGS back contact is another solution: for instance, hydrogen-doped In_2O_3 was shown to be a suitable back contact for ACIGS solar cells fabricated at 550°C [192].

In conclusion, an original architecture for flat reflective back contacts was developed. It is compatible with the usual deposition temperatures (≥ 500°C) of CIGS-based absorbers, and exhibits a high reflectivity that enables an almost perfect double-pass absorption in the absorber layer. Using a RBC and an antireflection coating, a J_{SC} of 29.5 mA/cm^2 was measured for a solar cell with 500 nm of CIGS. In addition, it was shown that replacing CIGS by ACIGS absorbers can improve the V_{OC} and *FF* of ultrathin solar cells. A 540 nm-thick ACIGS layer co-evaporated on Mo resulted in a best cell efficiency of 14.9% (without antireflection coating) thanks to a V_{OC} of 741 mV, a *FF* of 81.8% and a J_{SC} of 24.5 mA/cm^2. The fabrication of solar cells including a RBC that is compatible with the deposition of ACIGS is thus expected to further improve the photovoltaic efficiency of ultrathin devices. This work also paves the way toward the fabrication of a nanopatterned RBC that could enhance light absorption in ultrathin solar cells, as proposed recently in CIGS [163] and GaAs [160] photovoltaic devices with nanostructured back mirrors. Based on the planar RBC architecture presented in this work, preliminary optical simulations of nanostructured back contacts were performed with the Reticolo software. In cases close to ideality, the simulated nanopatterned RBCs allowed to reach J_{SC} values of 36.2 mA/cm^2 and 35.4 mA/cm^2, with total volumes of CIGS that respectively correspond to those of 300 nm-thick and 250 nm-thick flat CIGS layers.

At this stage, the main blocking point remains the formation of a Ga oxide layer that is detrimental to photovoltaic performances as it leads to complete solar cells with a degraded collection efficiency. Still, several strategies were shown to mitigate the growth of Ga oxide, like lowering the deposition temperature of CIGS, but also introducing a thin layer of Al_2O_3 at the CIGS back contact or replacing the NaF precursor layer by a PDT of NaF. Other alternatives could also be investigated, such as

using a back contact made of hydrogen-doped In_2O_3, which was reported to be compatible with the ACIGS deposition conditions [192].

Furthermore, the incorporation of heavy alkali should also improve the *p-n* heterojunction of ultrathin cells, and using a more transparent front contact stack would reduce the absorption losses at wavelengths below 550 nm [26], [31], [32]. These additional optimizations should lead to ultrathin CIGS solar cells that are as efficient as standard ones.

Annexe A. Résumé en français

Introduction

Au cours des trois dernières décennies, le Groupe d'Experts Intergouvernemental sur l'évolution du Climat (GIEC) a analysé l'impact des activités humaines sur le climat. En particulier, l'influence néfaste sur le climat des émissions de gaz à effet de serre dues aux activités humaines a été mise en évidence et largement étudiée [1], [2]. La communauté internationale est consciente de l'ampleur du problème, comme le montre la ratification de l'accord de Paris sur le climat qui a été négocié lors de Conférence de Paris de 2015 sur les changements climatiques (COP21) [3]. Cet accord a permis pour la première fois de fixer un objectif commun, consistant à maintenir le réchauffement climatique en dessous de 2°C par rapport aux niveaux préindustriels.

Pour y parvenir, il est impératif que le secteur de la production d'énergie opère une transition vers des sources renouvelables au cours des prochaines décennies. En ce sens, les systèmes photovoltaïques solaires ont un rôle essentiel à jouer étant donné que la ressource solaire est abondante, et que ce mode de production reste moins polluant et dangereux que l'utilisation de ressources fossiles ou nucléaires [2], [4]. Le marché photovoltaïque est largement dominé par les technologies à base de silicium, mais une alternative existe grâce aux technologies dites de couches minces. Notamment celle du $Cu(In,Ga)Se_2$ (CIGS), qui représentait environ 2% de la capacité de production de modules photovoltaïques en 2017 [5]. Avec une épaisseur standard d'absorbeur de 2 à 3 microns, les dispositifs photovoltaïques à base de CIGS ont atteint une efficacité record de 23.4% à l'échelle du laboratoire, et de 17.4% pour un module commercial [6].

Il est encore possible d'améliorer la compétitivité industrielle de ces modules, en réduisant l'épaisseur de l'absorbeur en CIGS tout en maintenant une efficacité photovoltaïque similaire [7]. Ceci représenterait un triple avantage, grâce à (1) une augmentation du débit de production due à un temps de dépôt du CIGS plus court [7], (2) une diminution de la consommation d'indium et de gallium qui sont tous deux identifiés comme des matériaux rares et stratégiques par la commission européenne [8], et (3) une meilleure efficacité photovoltaïque grâce à la réduction des pertes électriques dans une couche d'absorbeur plus fine [9], [10].

Cependant, l'efficacité record pour une cellule solaire fabriquée avec une couche de CIGS ultramince (≤ 500 nm) est limitée à 15.2 % [11]. Les cellules solaires CIGS ultraminces contenant des contacts arrières conventionnels en molybdène montrent de faibles efficacités, principalement du fait de deux types de pertes [12]: la probabilité plus importante de recombinaison des porteurs de charges au niveau du contact arrière, ainsi que l'absorption incomplète de la lumière incidente due à la faible réflectivité de l'interface CIGS/Mo. En conséquence, cette thèse présente différentes stratégies pour dépasser ces limitations de l'efficacité des cellules solaires à base de CIGS ultramince.

Dans une **première partie**, le contexte général de cette étude est exposé. Les marchés de l'énergie et du photovoltaïque y sont brièvement décrits, et la place qu'y occupe la technologie du CIGS est détaillée. Les aspects de physique fondamentale concernant les cellules solaires CIGS sont ensuite présentés, avec un état de l'art des cellules solaires en CIGS ultramince. Il en est conclu que des stratégies de passivation du contact arrière sont nécessaires pour limiter les recombinaisons parasites de porteurs de charge à l'interface arrière du CIGS. De plus, il est essentiel de développer une architecture de contact arrière réfléchissant compatible avec le dépôt de CIGS ultramince afin d'améliorer l'absorption lumineuse de ces cellules solaires. Après avoir présenté les méthodes expérimentales employées au cours de cette thèse, les stratégies pour améliorer les rendements des cellules ultraminces sont abordées. Ainsi, dans une **deuxième partie** trois approches pour améliorer les propriétés électriques des cellules ultraminces sont décrites : le gradient de composition de l'absorbeur, l'incorporation d'argent dans la couche de CIGS et l'ajout d'une couche de passivation en alumine à l'interface arrière du CIGS. Enfin, une **troisième partie** présente l'optimisation d'une nouvelle architecture de contact arrière réfléchissant, stable sous les conditions de co-évaporation du CIGS, et son application aux cellules solaires ultraminces avec environ 500 nm d'épaisseur de CIGS.

Passivation du contact arrière des cellules solaires en CIGS ultramince

Trois approches ont été explorées pour améliorer la tension de circuit ouvert (V_{OC}) et le facteur de forme (*FF*) des cellules solaires ultramince à base de CIGS :

Le gradient de composition du CIGS ultramince déposé par un procédé de co-évaporation en trois étapes a été amélioré. La co-évaporation du CIGS à une température standard du substrat de 550°C a mené à un gradient linéaire du ratio atomique de [Ga]/([Ga]+[In]) (GGI) dans la couche ultramince. La réduction de la température de dépôt du CIGS à 500°C et 450°C a conduit à des gradients de GGI plus importants à l'interface arrière du CIGS avec le Mo, ce qui s'accompagne d'un gradient du minimum de la bande de conduction et donc d'un champ électrique passivant qui contribue à la passivation de l'interface arrière du CIGS en repoussant les électrons vers la jonction *p*-*n* [11], [13]. Ces plus faibles températures de co-évaporation ont aussi affecté la morphologie du CIGS, avec des interfaces plus rugueuses et des grains plus petits. Néanmoins, la cristallinité des couches de CIGS ultraminces déposées à 550°C et 500°C est similaire.

Les cellules solaires complètes avec un empilement standard de CdS/i-ZnO/ZnO:Al et une couche de précurseur de NaF de 15 nm et 8 nm d'épaisseur (Figure A. 1.a) ont été caractérisées. Réduire la température de co-évaporation du CIGS de 550°C à 450°C a diminué l'efficacité des cellules à cause de plus faibles valeurs de V_{OC} et *FF*. Ces pertes ont été attribuées à une quantité plus importante de recombinaisons non-radiatives et une collection des porteurs photogénérés dépendant du potentiel appliqué. Cependant, une température de dépôt du CIGS de 500°C a permis une augmentation de l'efficacité moyenne de 11.5 ± 0.2 % à 12.6 ± 0.4 % (Figure A. 1.b) par rapport à une température de 550°C. Cette amélioration a été établie grâce à une augmentation du

V_{OC} et du courant de court-circuit (J_{SC}) qui a été attribuée au gradient de GGI plus fort à 500°C. En effet, le courant d'obscurité (J_0) plus faible et la réponse spectrale (EQE) (Figure A. 1.c) amélioré pour des longueurs d'onde entre 550 nm et 1100 nm suggèrent une diminution des recombinaisons au contact arrière. Ces performances ont aussi été comparées au cas de cellules avec de plus faibles épaisseurs de couche de précurseur de NaF de 8nm. Pour les deux températures de dépôt, 550°C et 500°C, cette plus faible quantité de NaF a conduit à de moindres rendements à cause d'une baisse du V_{OC}, du *FF* et de l'efficacité de collection des porteurs de charge.

L'incorporation d'Argent (Ag) dans le CIGS ultramince a été étudiée en co-évaporant l'Ag proportionnellement au cuivre durant le dépôt de CIGS en trois étapes, la couche résultante d'(Ag,Cu)(In,Ga)Se_2 (ACIGS) contenant environ 2% at. d'Ag. Contrairement au cas du CIGS, la co-évaporation d'ACIGS à 550°C et 500°C a donné des profils de GGI très similaires. La morphologie des couches d'ACIGS déposées à 500°C a montré de petits grains et une interface avant bien plus rugueuse. Toutefois, les données de diffraction aux rayons X suggèrent que ces couches ont une cristallinité semblable.

Les cellules solaires complètes ont été fabriquées avec 15 nm ou 8 nm de couche de précurseur de NaF. Ces cellules ont eu de meilleures performances avec 8 nm de NaF, grâce à de meilleurs V_{OC}, *FF*, J_0 et facteurs d'idéalité (n). A l'inverse des cellules ultraminces en CIGS, les dispositifs à base d'ACIGS préparés à 500°C plutôt que 550°C ont montré de plus faibles efficacités dues à une diminution des *FF* et V_{OC}. Ceci a été corrélé à une collection du courant dépendante du potentiel appliqué et une augmentation des valeurs de J_0 et n. En conséquence, les meilleures cellules solaires ultraminces ont été obtenues pour une température de co-évaporation de l'ACIGS de 550°C et une couche de NaF de 8 nm. Pour une épaisseur d'ACIGS de 540 ± 20 nm, une efficacité de 14.9% a été mesurée, avec un V_{OC} de 741 mV, un *FF* de 81.8 % et un J_{SC} de 24.5 mA/cm^2 (Figure A. 1.b et c). Cette efficacité est proche du record de 15.2% obtenu dans le cas des absorbeurs en CIGS ultraminces [11]. Elle est aussi remarquablement plus élevée que les rendements obtenus avec nos couches de CIGS ultraminces, grâce notamment à une réduction du déficit de potentiel.

Les meilleures cellules à base de CIGS et d'ACIGS ultraminces fabriquées dans cette étude ont aussi été analysées en cathodoluminescence. Il a été montré que les fluctuations spatiales de la composition ne sont pas significatives. En revanche, les meilleures performances obtenues avec une couche d'ACIGS déposée à 550°C sont corrélées à une luminescence plus intense et une queue d'Urbach plus étroite, ce qui indique une plus faible densité de défauts peu profonds.

Une couche de passivation en alumine de 50 nm d'épaisseur a également été fabriquée sur un contact arrière conventionnel en Mo. Un procédé de nano-impression et une étape de gravure chimique par voie humide ont permis de perforer la couche de passivation afin de créer des contacts localisés entre le CIGS et le Mo. Le diamètre de ces contacts était d'environ 300 nm, et ils étaient espacés d'une période de 1 µm, 2 µm, 3 µm ou 4 µm. Le CIGS ultramince a été déposé en une étape pour éviter la formation d'un gradient de GGI qui contribuerait également à la passivation arrière du CIGS.

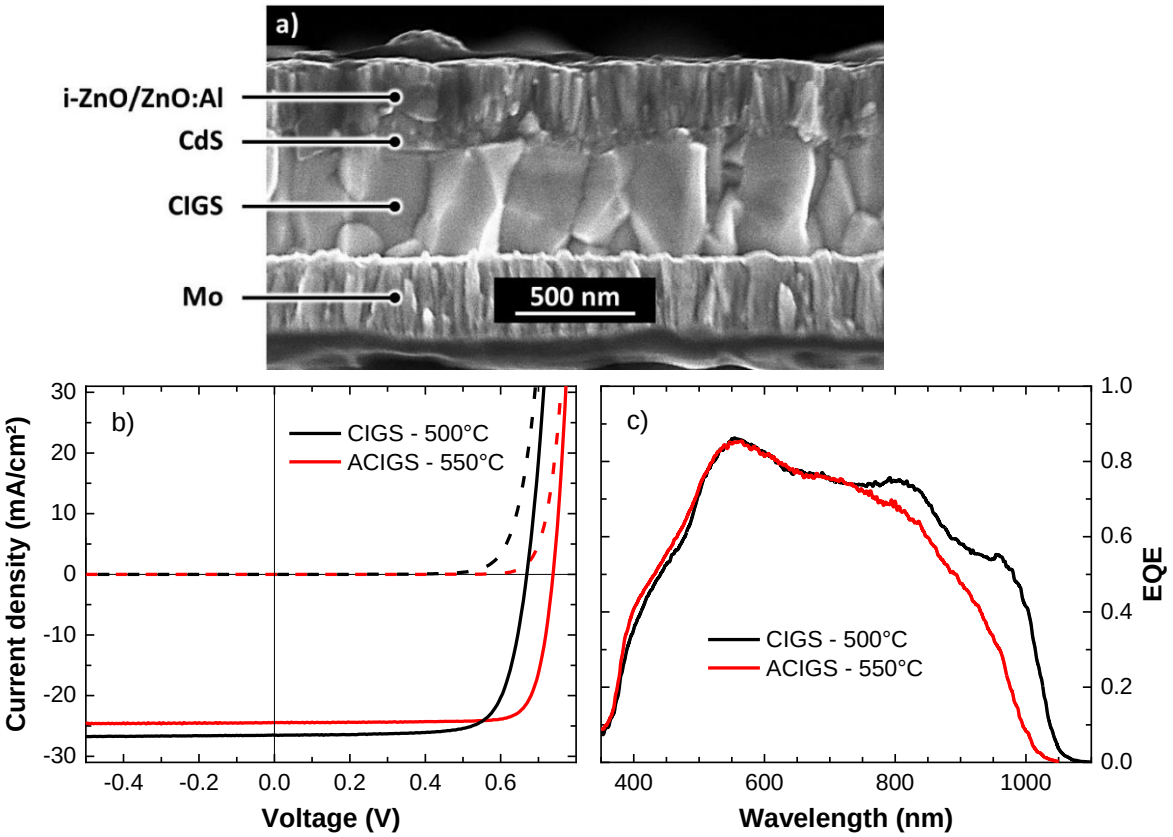

Figure A. 1. (a) Image au microscope électronique à balayage de la tranche d'une cellule solaire à base de CIGS ultramince. (b) Caractéristiques courant-tension et (c) réponses spectrales (EQE) des meilleures cellules ultraminces en CIGS et ACIGS fabriquées au cours de cette étude. La couche de CIGS (resp. ACIGS) a été co-évaporée avec une température de substrat de 500°C (resp. 550°C).

La caractérisation des cellules complètes indique que les périodes de 3 µm et 4 µm entre contacts locaux sont trop grandes par rapport à la longueur de diffusion des porteurs de charge positive (trous), car elles conduisent à de fortes résistances séries et à un effet de « rollover ». En comparaison, les *FF* mesurés pour des périodes de 1 µm et 2 µm ainsi que pour la cellule de référence sans couche passivante sont similaires, avec seulement une faible augmentation de la résistance série due à la couche de passivation. De meilleurs V_{OC} et J_{SC} ont été obtenus avec la couche de passivation. Ceci a été attribué à la passivation de l'interface arrière du CIGS par l'alumine, conduisant à une réduction des recombinaisons au contact arrière. Pour une couche de passivation en alumine avec des contacts espacés de 2 µm, soit une couverture d'environ 93% du contact arrière par l'Al_2O_3, une efficacité de 9.5% et un V_{OC} de 613 mV ont été mesurés avec la meilleure cellule, comparés à 7.9 % et 562 mV pour la meilleure cellule de référence sur Mo. Ainsi, un effet de passivation significatif a été observé, mais la co-évaporation d'absorbeurs ultraminces en une étape a conduit à de plus faibles efficacités que ceux déposés en trois étapes. Étant donné que le procédé de fabrication de contacts localisés à travers la couche de passivation est chronophage mais aussi difficile à réaliser, il serait intéressant de co-évaporer du CIGS ultramince en trois étapes et/ou de l'ACIGS sur une couche de passivation nano-perforée afin de déterminer s'il est nécessaire ou non d'utiliser une telle couche pour passiver l'interface arrière du CIGS.

Contact arrière réfléchissant pour cellules solaires ultraminces en CIGS

En utilisant les approches mentionnées plus haut, les J_{SC} des cellules solaires ultraminces sont généralement compris entre 24 et 26 mA/cm², du fait de leur absorption incomplète de la lumière incidente. Ces valeurs de J_{SC} sont bien inférieures à celles d'environ 40 mA/cm² obtenues dans le cas des cellules solaires record avec des épaisseurs de CIGS standard (de 2 à 3 microns). Des stratégies de piégeage optique sont donc nécessaires pour améliorer l'absorption lumineuse des cellules solaires ultraminces. Le principal obstacle pour atteindre cet objectif reste l'introduction d'un contact arrière hautement réfléchissant, qui soit compatible avec les températures habituelles de dépôt du CIGS à 500°C ou plus. C'est pourquoi une nouvelle architecture de contact arrière réfléchissant, stable sous les conditions de co-évaporation du CIGS, est présentée ici (Figure A. 2). Elle inclut un miroir d'Ag encapsulé dans deux couches de ZnO:Al pour assurer la stabilité thermique de l'empilement, et une couche d'oxyde d'indium dopé étain (ITO) pour créer un contact ohmique avec le CIGS. L'empilement complet est le suivant : SLG/ZnO:Al (50 nm)/Ag (150 nm)/ZnO:Al (30 nm)/ITO (entre 30 et 200 nm). L'impact d'une fine couche de passivation d'Al_2O_3 (1.5 ou 3 nm) à l'interface entre l'ITO et le CIGS a également été étudié. En premier lieu, des simulations optiques ont confirmé que cette architecture permettait un double passage de la lumière presque parfait dans la couche de CIGS.

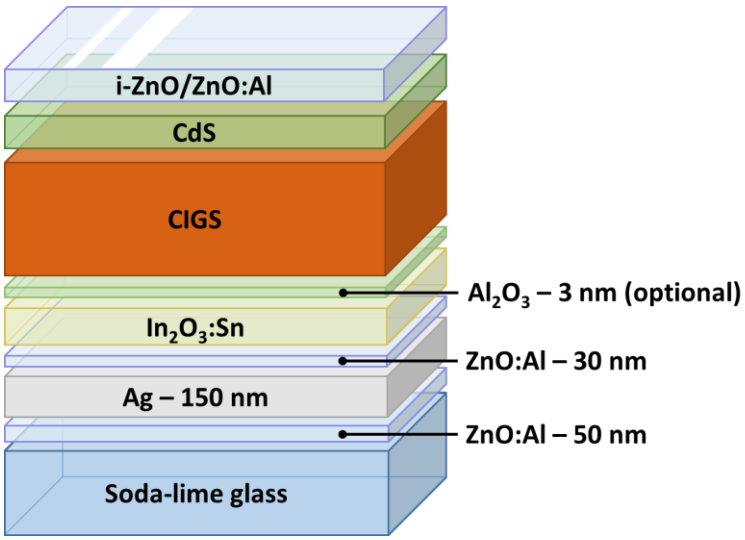

Figure A. 2. Schéma de l'empilement complet d'une cellule solaire à base de CIGS ultramince incluant un contact arrière réfléchissant.

La couche d'ITO a d'abord été caractérisée sur substrat de verre, et il a été observé que celle-ci est plus transparente après un recuit à plus de 500°C pendant 10 minutes à l'air libre. Après recuit, les contacts arrières réfléchissants n'ont pas montré de signe de diffusion de l'Ag au microscope électronique à balayage, ce qui est un prérequis indispensable pour que l'empilement réfléchissant soit compatible avec la co-évaporation de CIGS. Les contacts réfléchissants recuits ont une réflectance satisfaisante de plus de 90% dans la gamme de longueur d'onde comprise entre 600 nm et 1150 nm, ainsi que de faibles résistances de couche d'environ 0.1 Ω.sq.

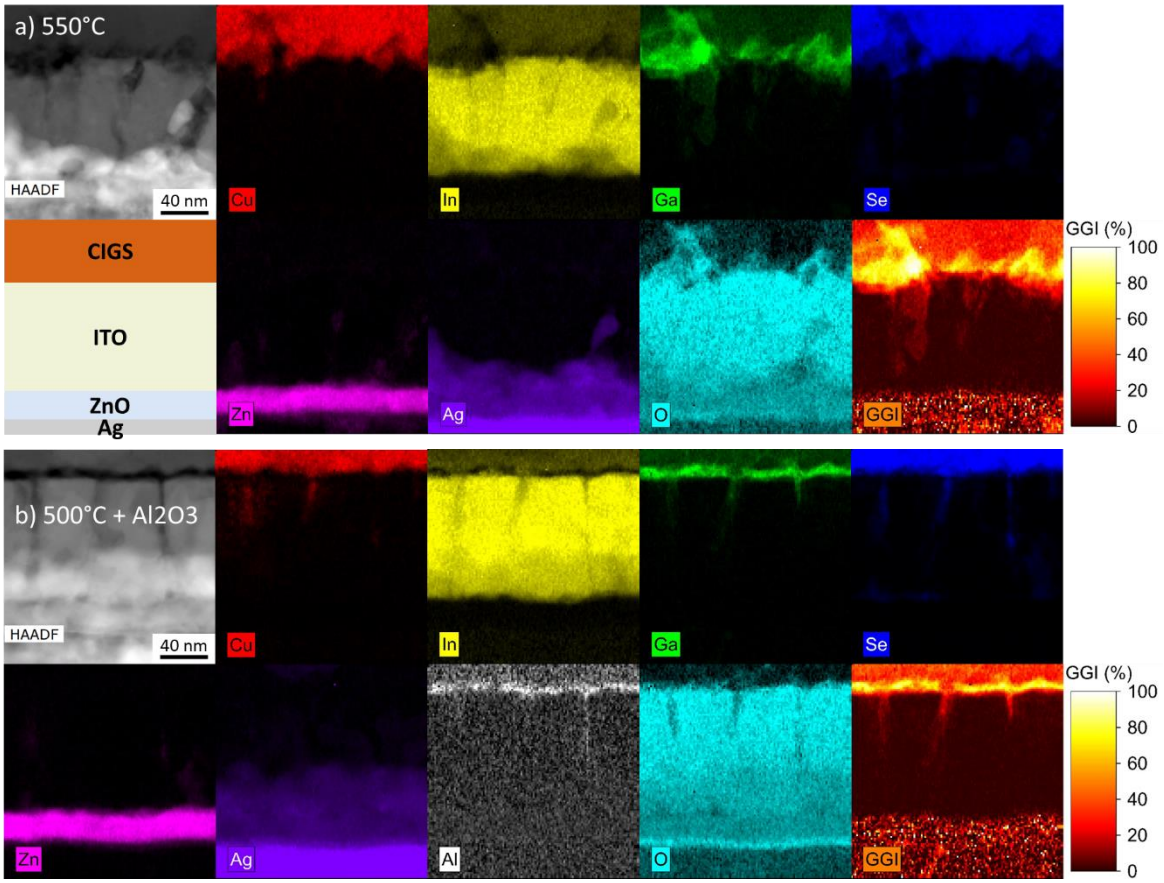

Figure A. 3. Images obtenues au microscope à transmission électronique, avec les cartographies correspondantes de spectroscopie à rayons x à dispersion d'énergie. Le CIGS a été co-évaporé à une température de (a) 550°C ou (b) 500°C, sur un contact arrière réfléchissant (b) avec ou (a) sans couche d'alumine de 3 nm sur l'ITO. Les couches de CIGS, d'ITO, de ZnO:Al et d'Ag sont visibles ici, et représentées schématiquement sur la figure (a) pour plus de lisibilité.

Des cellules solaires en CIGS ultramince ont été fabriquées sur des contacts réfléchissants avec des couches d'ITO de 200 nm, 100 nm et 30 nm. Des études approfondies par microscope électronique en transmission avec spectroscopie à rayons x à dispersion d'énergie (STEM/EDX) ont révélé la croissance d'une fine couche d'oxyde de gallium (Ga) à l'interface entre le CIGS et l'ITO (Figure A. 3). Pour des couches de 30 nm d'ITO, cet oxyde de Ga s'est notamment formé à l'intérieur des joints de grain de l'ITO. Pour limiter la croissance de ce composé, la température de co-évaporation du CIGS a été diminuée de 550°C à 500°C, et une couche additionnelle d'alumine (Al_2O_3) (≤ 3 nm d'épaisseur) a été déposée par ALD (Atomic Layer Deposition) sur l'ITO. Dans le cas d'un contact réfléchissant avec 100 nm d'ITO, ces stratégies ont permis de réduire la rugosité de l'oxyde de Ga, et d'éviter qu'il ne se forme dans les joints de grain de l'ITO (Figure A. 3). Ceci semble également éviter la consommation de Ga contenu dans la couche de CIGS, ce qui peut conduire à un champ électrique opposé à l'extraction des porteurs de charges et diminuer l'efficacité des cellules solaires complètes.

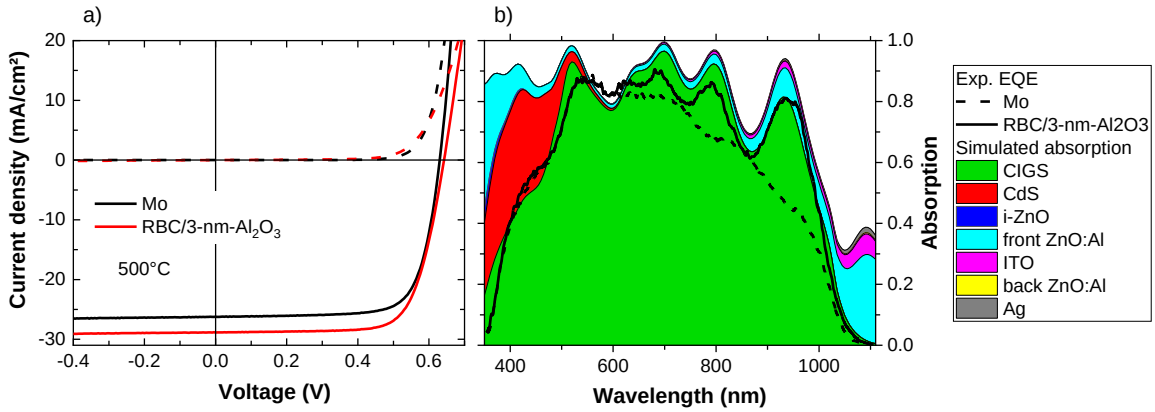

Figure A. 4. Caractéristiques courant-tension, ainsi que (b) réponses spectrales (EQE) et absorptions simulées de cellules solaires CIGS ultraminces sur Mo et contact réfléchissant.

Dans le cas d'un contact réfléchissant avec 100 nm d'ITO et 3 nm d'Al_2O_3, la couche d'oxyde de Ga plus fine et moins rugueuse formée à 500°C a conduit à une cellule ultramince (500 ± 20 nm de CIGS) avec une efficacité de 13.5% et un J_{SC} de 28.9 mA/cm², soit respectivement 1.0% absolu et 2.7 mA/cm² de plus que pour la cellule de référence sur Mo (Figure A. 4). En outre, des V_{OC} et *FF* similaires ont été atteints, grâce à une plus faible formation d'oxyde de Ga et un gradient de GGI préservé.

L'impact du post-dépôt de NaF a aussi été étudié avec des absorbeurs co-évaporés à 450°C sur des empilements réfléchissants contenant 30 nm d'ITO, ainsi que sur des contacts arrières transparents avec 300 nm d'ITO. Il était notamment attendu que cette plus faible température de dépôt du CIGS et l'ajout de Na via un post-dépôt limitent la formation d'oxyde de Ga [37], [38], [150]. Cela a en effet résulté en une couche d'oxyde de Ga très fine (< 10 nm), mais qui s'est également formée dans les joints de grain de l'ITO du contact réfléchissant, et ce sur toute l'épaisseur de l'ITO (30 nm). En conséquence, cet empilement réfléchissant a conduit à de faibles efficacités et *FF* du fait d'une forte résistance série et d'une collection du courant dépendante du potentiel appliqué. Néanmoins, ces cellules ont bénéficié d'un gain de J_{SC} de 4.6 mA/cm² par rapport à un contact arrière en Mo. En comparaison, le contact arrière transparent avec 300 nm d'ITO n'a pas mené à la croissance d'oxyde de Ga dans les joints de grain de l'ITO. Les cellules solaires ont montré en moyenne des *FF* de 70.3 ± 0.7%, et des V_{OC} de 618 ± 3 mV, conduisant à de meilleures efficacités que les cellules de référence sur Mo. En conséquence, puisqu'une couche d'oxyde de Ga de moins de 10 nm s'est formée en utilisant un post-dépôt de NaF, il est attendu que remplacer la couche de précurseur de NaF par un post-dépôt améliore les efficacités des cellules solaires ultraminces sur contacts réfléchissants avec 100 nm d'ITO ou plus.

Dans le but d'améliorer les V_{OC} et *FF* des cellules ultraminces sur contacts réfléchissants, des couches d'ACIGS ont aussi été co-évaporées sur ces empilements à 550°C et 500°C. Cependant, une importante formation d'oxyde de Ga a été détectée, avec une forte consommation de Ga dans les couches d'ACIGS. Les faibles performances de ces cellules, inférieures à 7%, ont été attribuées aux effets de la croissance de l'oxyde de Ga. Si la formation de ce composé est intrinsèque à l'interface ACIGS/ITO, d'autres contacts arrières pourraient être utilisés, comme l'oxyde d'indium dopé hydrogène qui peut former un contact arrière ohmique avec de l'ACIGS déposé à 550°C [192].

Conclusion

En résumé, une architecture originale de contact arrière réfléchissant a été développée. Elle est compatible avec le dépôt de CIGS à des températures habituelles de plus de 500°C, et permet un double passage de la lumière dans la couche d'absorbeur. En utilisant un contact réfléchissant et une couche antireflet, un J_{SC} de 29.5 mA/cm^2 a été mesuré pour une cellule solaire avec 500 nm de CIGS. En outre, l'incorporation d'Ag a permis d'améliorer les V_{OC} et *FF* des cellules ultraminces. Une couche d'ACIGS de 540 nm d'épaisseur a mené à une efficacité de 14.9% (sans couche antireflet), grâce à un V_{OC} de 741 mV, un *FF* de 81.8% et un J_{SC} de 24.5 mA/cm^2. La fabrication de cellules solaires incluant un empilement réfléchissant compatible avec le dépôt d'ACIGS pourrait encore améliorer les rendements des cellules ultraminces.

Ces travaux ouvrent aussi la voie à la fabrication de contacts arrières réfléchissants nanostructurés, comme proposé récemment pour les absorbeurs à base de CIGS [163] ou de GaAs [160]. En perspective, des simulations optiques préliminaires ont aussi été réalisées pour des contacts arrières nanostructurés avec une architecture basée sur l'empilement réfléchissant planaire étudié expérimentalement. Pour des cas proches de l'idéalité, ces architectures nanostructurées permettent d'atteindre des J_{SC} de 36.2 mA/cm^2 et 35.4 mA/cm^2, avec des volumes de CIGS correspondant respectivement à ceux de couches planaires de 300 nm et 250 nm seulement.

À ce stade, le principal point bloquant est la formation d'oxyde de Ga, qui diminue les rendements photovoltaïques à cause d'une dégradation de l'efficacité de collecte des porteurs de charge. Cependant, plusieurs stratégies peuvent limiter la croissance d'oxyde de Ga, comme la réduction de la température de dépôt du CIGS, mais aussi l'introduction d'une fine couche d'Al_2O_3 au contact arrière du CIGS ou l'incorporation de Na via un post-dépôt plutôt qu'une couche de précurseur. D'autres alternatives sont possibles, comme l'utilisation d'un contact arrière en oxyde d'indium dopé hydrogène, qui est compatible avec les conditions de co-évaporation de l'ACIGS à 550°C [192].

Enfin, l'incorporation d'alcalins lourds tels que le potassium (K), le rubidium (Rb) ou le césium (Cs) devrait également améliorer l'hétérojonction des cellules ultraminces. De plus, l'utilisation d'un empilement de contact avant plus transparent devrait réduire l'absorption parasite aux longueurs d'onde de moins de 550 nm [26], [31], [32]. Ces optimisations supplémentaires devraient mener à des cellules solaires à base de CIGS ultramince (≤500 nm) avec des efficacités proches de celles obtenues pour des épaisseurs typiques d'absorbeur entre 2 et 3 microns.

Appendix B.Optimization of the NaF precursor layer thickness on RBCs

The ZnO:Al layers of the RBC architecture presented in Part III are expected to block the diffusion of Na from the SLG during the co-evaporation of CIGS [152], [210]. Besides, as Ag is efficiently encapsulated in ZnO:Al layers, it is reasonable to consider that the RBC stack also prevents the diffusion of Na. This is why an external supply of Na was provided to CIGS layers by thermal evaporation of NaF precursor layers on the RBCs prior to CIGS deposition. In order to determine the optimal NaF quantity for ~500 nm-thick CIGS layers, the thickness of this NaF precursor layer was varied.

A batch of CIGS was prepared with NaF thicknesses of 4 nm, 12 nm and 16 nm on RBCs with 100 nm of ITO covered with a 3 nm-thick alumina layer. As a reference, CIGS was also deposited on a Mo back contact with a 16 nm-thick NaF layer. CIGS was co-evaporated at 500°C, with average composition ratios of CGI = 0.93 ± 0.02 and GGI = 0.40 ± 0.02 determined by XRF, and an average thickness of 560 nm measured with a profilometer. The materials characterization and solar cell performances of this CIGS batch were then compared to samples with RBCs and 8 nm-thick NaF layers, which are described in section III.11.3.

First, the CIGS layers deposited on RBCs with 12 nm and 16 nm-thick precursor layers of NaF partly delaminated during the deposition of the CdS buffer layer by CBD. This delamination is correlated with the NaF thickness as the RBC covered with 16 nm of NaF resulted in a delamination area roughly two times bigger than with 12 nm of NaF. Besides, Rockett *et al.* also showed that CIGS layers with high Na contents have a poor adhesion to Mo back contacts [211]. In order to determine which interface led to delamination, the samples were investigated by top-view SEM/EDX (Figure B. 1).

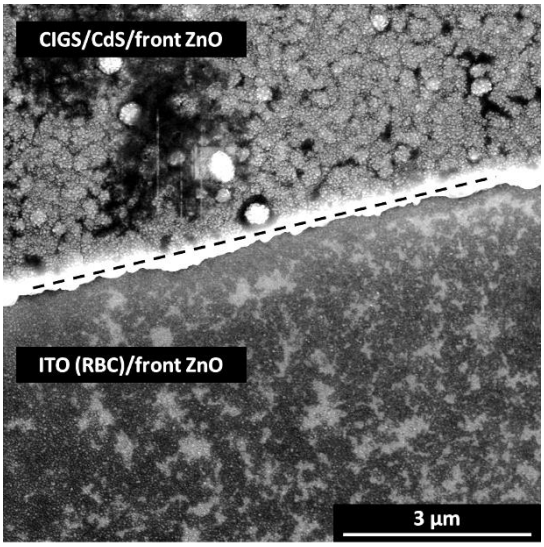

Figure B. 1. Top-view SEM image after completion of all cell fabrication steps, at a delamination edge of the CIGS layer co-evaporated on top of a RBC with a 12 nm-thick NaF precursor layer. A black dashed line indicates the position of the delamination edge. To identify the observed layers, EDX spectra (not shown) were acquired on both sides of the delamination edge.

The EDX spectra (not shown) from both side of the delamination edge reveal that this delamination occurred at the CIGS/ITO interface. A possible explanation to the CIGS delamination could be that thick NaF layers are not completely consumed during CIGS growth and are then dissolved during the CBD process. The excessive NaF content could also lead to chemical reactions with other elements to form other compounds, as it was already shown for example that Na promotes the formation of Ga oxide [38], [153], [191]. However, the SEM/EDX study did not allow to detect any other materials on top of the ITO layer.

Because of this delamination, it is not possible to increase the thickness of the NaF precursor layer above 12 nm in order to incorporate more Na in ultrathin CIGS layers. However, providing NaF through a post-deposition treatment might allow to increase the Na content in CIGS layers while avoiding possible interactions between NaF and the CIGS/ITO back contact.

CIGS layers co-evaporated on RBCs with 4 nm and 8 nm of NaF did not delaminate at all during the CBD process. The CGI, GGI and Na composition profiles of these CIGS films were analyzed in GD-OES, as shown in Figure B. 2. Each CIGS sample exhibit a flat CGI profile and a GGI grading that is steeper at the back contact, as shown previously for a co-evaporation temperature of 500°C.

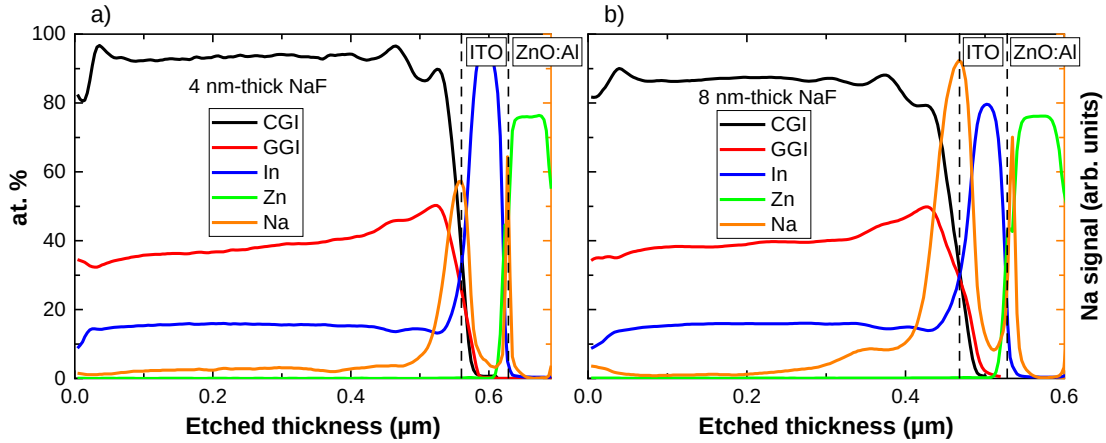

Figure B. 2. GD-OES analysis of ultrathin CIGS layers deposited at 500°C on RBCs with a 100 nm-thick ITO layer. NaF precursor layers were deposited on the RBCs prior to CIGS co-evaporation, with thicknesses of (a) 4 nm and (b) 8 nm. Average values of the CGI, GGI and In ratios were calibrated based on the XRF characterization of CIGS layers on Mo control samples. The thickness of the CIGS films was measured with a profilometer.

The raw GD-OES signal of the Na composition profiles is compared for RBCs with 4 nm and 8 nm of NaF precursor. A strong accumulation of Na is shown at the back interface with ITO, which is increased in the case of the 8 nm-thick NaF precursor layer. Na diffuses through the ITO layer, but is blocked by the ZnO:Al layer as the GD-OES signal of Na drops to zero beyond the ITO/ZnO:Al interface. Based on this GD-OES analysis, the delamination of CIGS layers deposited on RBCs with NaF precursor layers thicker than 8 nm can be attributed to the excessive segregation of Na at the back interface of CIGS.

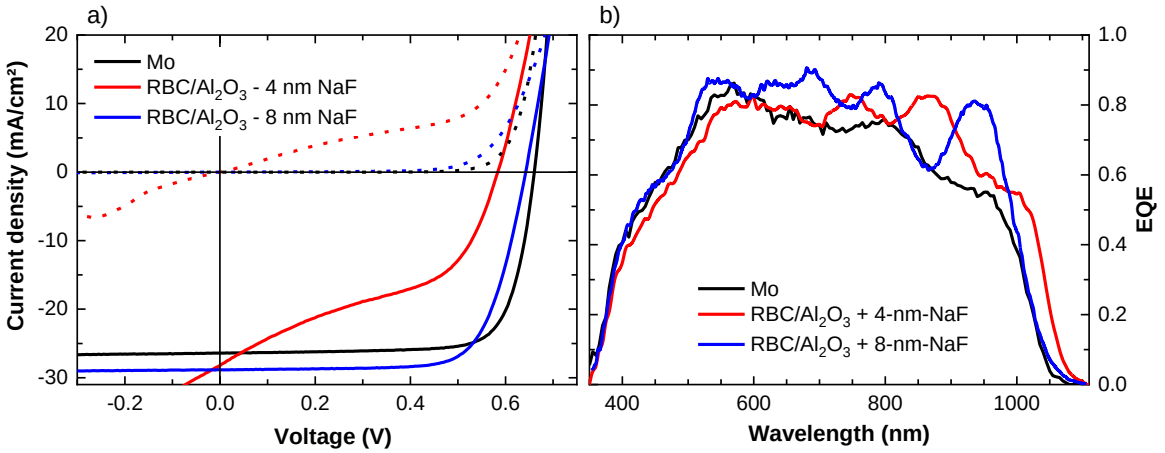

Figure B. 3. (a) I(V) characteristics under one-sum illumination (solid lines) and in the dark (dashed lines), as well as (b) EQE curves of the best solar cells. Back contacts consist of Mo with a 16 nm-thick precursor layer of NaF, as well as RBCs covered with 3 nm of alumina as well as 4 nm and 8 nm of NaF.

		Average / best cell light I(V) parameters			
CIGS batch	Back contact	Eff. (%)	J_{SC} (EQE) (mA/cm²)	V_{OC} (mV)	*FF* (%)
n°1	Mo + 16-nm-NaF	13.2 ± 0.1 / 13.4	26.4	655 ± 4 / 662	76.4 ± 0.3 / 76.8
	RBC/Al_2O_3 + 4-nm-NaF*	7.1	28.2	585	43.2
n°2	RBC/Al_2O_3 + 8-nm-NaF	12.3 ± 1.0 / 13.5	28.9	618 ± 15 / 644	68.8 ± 3.8 / 72.7

Table B. 1. Summary of I(V) parameters under one-sun illumination. CIGS was deposited at 500°C in two different batches. Back contacts consist of Mo with a 16 nm-thick precursor layer of NaF, RBCs covered with 3 nm of alumina as well as 4 and 8 nm of NaF. The average light I(V) parameters and standard deviation were calculated from the 10 best solar cells, except for J_{SC} values which were calculated from the integrated EQE of each respective best cell. *Because of a strong shunting behavior in most cells I(V) parameters are given only for the best cell.

Complete solar cells were fabricated with Mo and RBCs with 4 nm or 8 nm-thick precursor layers of NaF, and their photovoltaic performances were compared. The light and dark I(V) parameters of these samples are detailed in Table B. 1 and Table B. 2, and the light I(V) curves of best solar cells are shown in Figure B. 3 together with their EQE.

The best ultrathin cell fabricated on a RBC with a 4 nm-thick layer of NaF exhibit a low *FF* of 43.2 %, far below the average *FF* of 76.4 ± 0.3 % obtained with a Mo back contact. This poor *FF* is related to a very low shunt resistance of 60 Ω.cm². On the other hand, the best cell on a RBC with 8 nm of NaF shows a high *FF* of 72.7 %, close to the Mo reference. As the 4 nm-thick NaF layer results in an intermediate Na content within the CIGS layer, it seems unlikely that Na is responsible for such low *FF* values. Besides, according to the GD-OES composition profiles, the RBC did not lead to excessive elemental diffusion. This very low *FF* could rather be related to the high CGI composition of this CIGS batch. Indeed, CGI values close to unity have been reported to reduce the shunt resistance of CIGS, possibly through the formation of local shunt paths at defects such as crevices, voids or interfaces [30], [212]. As the substrate

holder does not move during co-evaporation, the Cu content of CIGS is not homogenous and can be estimated to be around 92% in the case of Mo and 94% in the case of the RBC, which could explain why the Mo back contact still achieves high shunt resistance values. The second CIGS batch exhibits a CGI of about 88% and a shunt resistance of 7.10^3 $\Omega.cm^2$, suggesting that the high CGI composition decreased the shunt resistance of complete devices by 2 orders of magnitude.

		Best cell dark I(V) parameters		
CIGS batch	Back contact	J_0 (mA/cm^2)	R_{SH} ($\Omega.cm^2$)	R_S ($\Omega.cm^2$)
n°1	Mo + 16-nm-NaF	2.10^{-5}	$> 1.10^6$	< 0.1
	RBC/Al_2O_3 + 4-nm-NaF	9.10^{-5}	60	1.4
n°2	RBC/Al_2O_3 + 8-nm-NaF	3.10^{-5}	7.10^3	1.5

Table B. 2. Dark I(V) parameters of each best solar cell, fitted with a 1-diode model and an ideality factor of 2 (J_0: saturation currents, R_{SH}: shunt resistance, R_S: series resistance). CIGS was deposited at 500°C in two different batches. Back contacts consist of Mo with a 16 nm-thick precursor layer of NaF, RBCs covered with 3 nm of alumina as well as 4 and 8 nm of NaF.

The best V_{OC} of 585 mV for the RBC with 4 nm of NaF is lower than for the RBC with 8 nm of NaF (644 mV) and the Mo reference (662 mV). It is however difficult to conclude on the origin of this V_{OC} loss that could be related to both the Na and Cu contents of the CIGS layer, as these elements both affect the doping level of CIGS and as high CGI values favor recombination at the hetero-interface [45], [55], [57], [58]. Similarly to RBC samples described in section III.11.3, the improved reflectance of the RBCs results in a J_{SC} increase as compared to the Mo back contact, due to large resonances in the EQE for the 600 – 1050 nm wavelength range (Figure B. 3.b). The EQE curves also show that the RBC with 4 nm of NaF leads to collection losses at wavelengths between 400 nm and 600 nm, as well as a reduction of the bandgap from 1.19 eV to 1.17 eV as compared to Mo, possibly because of Ga oxide formation at the CIGS/ITO interface.

To conclude, a 4 nm-thick precursor layer of NaF deposited on a RBC did not improve the efficiency of ultrathin CIGS solar cells, but the high CGI ratio of this CIGS batch might be the main reason for poor photovoltaic performances. CIGS layers co-evaporated on RBCs with NaF thicknesses of 12 nm and 16 nm delaminated during the CBD process for CdS deposition. This poor adhesion of the CIGS layer has been attributed to the excessive segregation of Na at the back interface of CIGS with ITO. All in all, these findings point out that a NaF post-deposition treatment is required to investigate the effects of higher Na contents in CIGS layers co-evaporated on RBCs. A post-deposition treatment could also result in a Na profile more similar to the case of the Mo back contact, with a higher Na concentration at the front interface of CIGS together with a lower amount of Na at the back contact.

Appendix C. Optical indices used in Reticolo

The list of the optical indices that were used to simulate the absorption of complete solar cells with the Reticolo software [166] is given below, together with their reference. In the case of CIGS, the optical indices take into account the sub-bandgap absorption due to the Urbach tail, which was measured with a Fourier-transform infrared spectrometer in a previous study.

	Mo [213]		CdS [214]		i-ZnO [in-house ellipsometric data]		ZnO:Al [208]		MgF_2 [215]	
λ (nm)	n	k	n	k	n	k	n	k	n	k
320	2.4202	1.9341	2.1243	0.6892	2.3240	0.1208	2.2043	0.2106	1.3904	0.0000
330	2.4670	1.8753	2.2075	0.5394	2.3031	0.0897	2.1783	0.1250	1.3893	0.0000
340	2.4868	1.8332	2.2514	0.4423	2.2897	0.0701	2.1308	0.0763	1.3883	0.0000
350	2.4866	1.8110	2.2668	0.3852	2.2774	0.0552	2.0897	0.0514	1.3874	0.0000
360	2.4816	1.8254	2.2648	0.3554	2.2623	0.0418	2.0569	0.0370	1.3866	0.0000
370	2.4963	1.8674	2.2564	0.3402	2.2388	0.0280	2.0303	0.0277	1.3858	0.0000
380	2.5299	1.9386	2.2520	0.3270	2.2148	0.0178	2.0081	0.0213	1.3851	0.0000
390	2.6040	1.9927	2.2548	0.3121	2.1969	0.0107	1.9891	0.0166	1.3845	0.0000
400	2.6998	2.0273	2.2614	0.3043	2.1747	0.0100	1.9726	0.0132	1.3839	0.0000
410	2.8080	2.0402	2.2685	0.2990	2.1532	0.0095	1.9579	0.0105	1.3833	0.0000
420	2.9200	2.0284	2.2733	0.2865	2.1350	0.0046	1.9446	0.0085	1.3828	0.0000
430	3.0248	1.9998	2.2773	0.2688	2.1218	0.0002	1.9326	0.0070	1.3824	0.0000
440	3.1204	1.9631	2.2874	0.2515	2.1162	0.0000	1.9216	0.0057	1.3819	0.0000
450	3.2087	1.9213	2.3025	0.2395	2.1127	0.0000	1.9114	0.0048	1.3815	0.0000
460	3.3014	1.8774	2.3150	0.2237	2.1034	0.0000	1.9018	0.0041	1.3811	0.0000
470	3.3964	1.8201	2.3275	0.1898	2.0846	0.0000	1.8928	0.0035	1.3808	0.0000
480	3.4952	1.7430	2.3361	0.1368	2.0773	0.0000	1.8843	0.0031	1.3804	0.0000
490	3.5838	1.6455	2.3189	0.1017	2.0746	0.0000	1.8762	0.0027	1.3801	0.0000
500	3.6580	1.5316	2.2943	0.0696	2.0716	0.0000	1.8685	0.0025	1.3798	0.0000
510	3.7136	1.4033	2.2646	0.0329	2.0622	0.0000	1.8610	0.0023	1.3795	0.0000
520	3.7508	1.2663	2.2362	0.0212	2.0496	0.0000	1.8538	0.0022	1.3792	0.0000
530	3.7618	1.1214	2.2181	0.0226	2.0444	0.0000	1.8469	0.0021	1.3790	0.0000
540	3.7473	0.9733	2.2066	0.0213	2.0407	0.0000	1.8401	0.0020	1.3787	0.0000
550	3.7064	0.8318	2.1965	0.0145	2.0375	0.0000	1.8335	0.0020	1.3785	0.0000
560	3.6372	0.7069	2.1822	0.0105	2.0350	0.0000	1.8270	0.0020	1.3783	0.0000
570	3.5488	0.6025	2.1640	0.0095	2.0324	0.0000	1.8207	0.0020	1.3781	0.0000
580	3.4530	0.5175	2.1492	0.0089	2.0288	0.0000	1.8144	0.0021	1.3779	0.0000
590	3.3530	0.4554	2.1401	0.0074	2.0222	0.0000	1.8083	0.0021	1.3777	0.0000
600	3.2519	0.4125	2.1346	0.0056	2.0200	0.0000	1.8022	0.0022	1.3775	0.0000
610	3.1537	0.3839	2.1305	0.0046	2.0197	0.0000	1.7961	0.0023	1.3774	0.0000

	Mo [213]		CdS [214]		i-ZnO [in-house ellipsometric data]		ZnO:Al [208]		MgF_2 [215]	
λ (nm)	n	k	n	k	n	k	n	k	n	k
620	3.0592	0.3718	2.1251	0.0000	2.0161	0.0000	1.7901	0.0024	1.3772	0.0000
630	2.9720	0.3722	2.1165	0.0000	2.0111	0.0000	1.7842	0.0025	1.3770	0.0000
640	2.8954	0.3815	2.1068	0.0000	2.0052	0.0000	1.7783	0.0026	1.3769	0.0000
650	2.8276	0.4051	2.0992	0.0000	2.0001	0.0000	1.7724	0.0028	1.3767	0.0000
660	2.7707	0.4335	2.0951	0.0000	2.0000	0.0000	1.7665	0.0029	1.3766	0.0000
670	2.7285	0.4535	2.0929	0.0000	1.9991	0.0000	1.7606	0.0031	1.3765	0.0000
680	2.7011	0.4622	2.0910	0.0000	1.9945	0.0000	1.7547	0.0032	1.3763	0.0000
690	2.6811	0.4670	2.0885	0.0000	1.9904	0.0000	1.7488	0.0034	1.3762	0.0000
700	2.6607	0.4689	2.0852	0.0000	1.9900	0.0000	1.7429	0.0036	1.3761	0.0000
710	2.6323	0.4685	2.0815	0.0000	1.9900	0.0000	1.7370	0.0038	1.3760	0.0000
720	2.5873	0.4633	2.0778	0.0000	1.9865	0.0000	1.7311	0.0040	1.3759	0.0000
730	2.5307	0.4546	2.0745	0.0000	1.9812	0.0000	1.7251	0.0043	1.3757	0.0000
740	2.4724	0.4465	2.0713	0.0000	1.9800	0.0000	1.7191	0.0045	1.3756	0.0000
750	2.4222	0.4431	2.0679	0.0000	1.9800	0.0000	1.7131	0.0048	1.3755	0.0000
760	2.3854	0.4475	2.0644	0.0000	1.9800	0.0000	1.7070	0.0051	1.3754	0.0000
770	2.3563	0.4577	2.0611	0.0000	1.9800	0.0000	1.7009	0.0053	1.3753	0.0000
780	2.3302	0.4701	2.0586	0.0000	1.9800	0.0000	1.6947	0.0057	1.3752	0.0000
790	2.3027	0.4809	2.0569	0.0000	1.9800	0.0000	1.6885	0.0060	1.3752	0.0000
800	2.2693	0.4865	2.0557	0.0000	1.9792	0.0000	1.6823	0.0063	1.3751	0.0000
810	2.2310	0.4821	2.0549	0.0000	1.9718	0.0000	1.6760	0.0067	1.3750	0.0000
820	2.1911	0.4700	2.0538	0.0000	1.9663	0.0000	1.6696	0.0071	1.3749	0.0000
830	2.1482	0.4563	2.0515	0.0000	1.9617	0.0000	1.6632	0.0075	1.3748	0.0000
840	2.1011	0.4474	2.0475	0.0000	1.9600	0.0000	1.6567	0.0079	1.3747	0.0000
850	2.0483	0.4496	2.0426	0.0000	1.9600	0.0000	1.6502	0.0084	1.3746	0.0000
860	1.9876	0.4683	2.0383	0.0000	1.9600	0.0000	1.6436	0.0089	1.3746	0.0000
870	1.9135	0.5012	2.0362	0.0000	1.9600	0.0000	1.6369	0.0094	1.3745	0.0000
880	1.8302	0.5441	2.0363	0.0000	1.9600	0.0000	1.6302	0.0100	1.3744	0.0000
890	1.7436	0.5937	2.0369	0.0000	1.9600	0.0000	1.6233	0.0105	1.3743	0.0000
900	1.6594	0.6464	2.0364	0.0000	1.9600	0.0000	1.6165	0.0112	1.3743	0.0000
910	1.5835	0.6986	2.0350	0.0000	1.9600	0.0000	1.6095	0.0118	1.3742	0.0000
920	1.5216	0.7471	2.0332	0.0000	1.9600	0.0000	1.6025	0.0125	1.3741	0.0000
930	1.4717	0.7936	2.0316	0.0000	1.9600	0.0000	1.5954	0.0132	1.3740	0.0000
940	1.4296	0.8403	2.0304	0.0000	1.9600	0.0000	1.5882	0.0140	1.3740	0.0000
950	1.3939	0.8873	2.0293	0.0000	1.9600	0.0000	1.5809	0.0148	1.3739	0.0000
960	1.3627	0.9345	2.0281	0.0000	1.9600	0.0000	1.5736	0.0157	1.3738	0.0000
970	1.3346	0.9819	2.0265	0.0000	1.9600	0.0000	1.5661	0.0166	1.3738	0.0000

	Mo [213]		CdS [214]		i-ZnO [in-house ellipsometric data]		ZnO:Al [208]		MgF_2 [215]	
λ (nm)	n	k	n	k	n	k	n	k	n	k
980	1.3078	1.0296	2.0247	0.0000	1.9600	0.0000	1.5586	0.0176	1.3737	0.0000
990	1.2808	1.0774	2.0231	0.0000	1.9600	0.0000	1.5510	0.0186	1.3736	0.0000
1000	1.2533	1.1254	2.0222	0.0000	1.9600	0.0000	1.5433	0.0197	1.3736	0.0000
1010	1.2274	1.1736	2.0219	0.0000	1.9600	0.0000	1.5355	0.0208	1.3735	0.0000
1020	1.2031	1.2218	2.0220	0.0000	1.9594	0.0000	1.5277	0.0220	1.3735	0.0000
1030	1.1804	1.2699	2.0226	0.0000	1.9544	0.0000	1.5197	0.0232	1.3734	0.0000
1040	1.1593	1.3179	2.0235	0.0000	1.9502	0.0000	1.5116	0.0245	1.3733	0.0000
1050	1.1396	1.3656	2.0244	0.0000	1.9500	0.0000	1.5035	0.0258	1.3733	0.0000
1060	1.1215	1.4129	2.0249	0.0000	1.9500	0.0000	1.4952	0.0273	1.3732	0.0000
1070	1.1047	1.4597	2.0243	0.0000	1.9500	0.0000	1.4868	0.0287	1.3732	0.0000
1080	1.0894	1.5059	2.0222	0.0000	1.9500	0.0000	1.4784	0.0302	1.3731	0.0000
1090	1.0755	1.5516	2.0186	0.0000	1.9500	0.0000	1.4698	0.0318	1.3730	0.0000
1100	1.0631	1.5969	2.0146	0.0000	1.9500	0.0000	1.4612	0.0335	1.3730	0.0000
1110	1.0522	1.6417	2.0111	0.0000	1.9500	0.0000	1.4524	0.0352	1.3729	0.0000
1120	1.0424	1.6860	2.0091	0.0000	1.9500	0.0000	1.4435	0.0369	1.3729	0.0000
1130	1.0338	1.7298	2.0091	0.0000	1.9500	0.0000	1.4345	0.0387	1.3728	0.0000
1140	1.0262	1.7731	2.0106	0.0000	1.9500	0.0000	1.4254	0.0406	1.3728	0.0000
1150	1.0195	1.8159	2.0125	0.0000	1.9500	0.0000	1.4161	0.0426	1.3727	0.0000

	Ag [216]		ITO [209]		CIGS (E_g = 1.17 eV), w/ Urbach tail [217]		CIGS (E_g = 1.2 eV), w/ Urbach tail [217]	
λ (nm)	n	k	n	k	n	k	n	k
320	0.1646	2.0502	2.4948	0.1504	2.8129	1.1220	2.8134	1.1221
330	0.1466	2.1943	2.4110	0.1057	2.8320	1.0907	2.8287	1.0908
340	0.1336	2.3350	2.3512	0.0795	2.8431	1.0678	2.8381	1.0678
350	0.1206	2.4737	2.3066	0.0628	2.8457	1.0647	2.8421	1.0647
360	0.1128	2.5809	2.2721	0.0514	2.8476	1.0595	2.8470	1.0595
370	0.1060	2.6862	2.2446	0.0433	2.8599	1.0543	2.8622	1.0543
380	0.0992	2.7888	2.2221	0.0372	2.8931	1.0501	2.8974	1.0501
390	0.0936	2.8908	2.2033	0.0326	2.9513	1.0473	2.9568	1.0474
400	0.0909	2.9935	2.1874	0.0290	3.0282	1.0462	3.0347	1.0463
410	0.0883	3.1007	2.1736	0.0261	3.1075	1.0038	3.1144	1.0038
420	0.0859	3.2087	2.1616	0.0238	3.1714	0.9280	3.1774	0.9281
430	0.0844	3.3145	2.1510	0.0218	3.2102	0.8414	3.2143	0.8414
440	0.0831	3.4005	2.1415	0.0202	3.2252	0.7587	3.2273	0.7587

	Ag [216]		ITO [209]		CIGS (E_g = 1.17 eV), w/ Urbach tail [217]		CIGS (E_g = 1.2 eV), w/ Urbach tail [217]	
λ (nm)	n	k	n	k	n	k	n	k
450	0.0819	3.4830	2.1329	0.0189	3.2227	0.6872	3.2235	0.6872
460	0.0810	3.5655	2.1252	0.0177	3.2092	0.6281	3.2096	0.6281
470	0.0801	3.6469	2.1180	0.0167	3.1899	0.5798	3.1907	0.5799
480	0.0795	3.7276	2.1114	0.0159	3.1682	0.5405	3.1699	0.5405
490	0.0798	3.8071	2.1053	0.0151	3.1461	0.5082	3.1488	0.5082
500	0.0802	3.8826	2.0996	0.0145	3.1247	0.4812	3.1283	0.4813
510	0.0805	3.9580	2.0942	0.0139	3.1043	0.4586	3.1087	0.4586
520	0.0810	4.0335	2.0891	0.0134	3.0854	0.4394	3.0901	0.4394
530	0.0814	4.1087	2.0843	0.0130	3.0679	0.4229	3.0726	0.4229
540	0.0818	4.1835	2.0797	0.0127	3.0518	0.4085	3.0559	0.4085
550	0.0824	4.2584	2.0753	0.0123	3.0370	0.3959	3.0403	0.3959
560	0.0829	4.3332	2.0710	0.0121	3.0235	0.3846	3.0257	0.3846
570	0.0834	4.4164	2.0670	0.0118	3.0113	0.3744	3.0123	0.3744
580	0.0840	4.5174	2.0630	0.0116	3.0005	0.3650	3.0002	0.3650
590	0.0840	4.6133	2.0591	0.0115	2.9909	0.3563	2.9894	0.3563
600	0.0840	4.6702	2.0554	0.0113	2.9826	0.3482	2.9800	0.3482
610	0.0840	4.7221	2.0517	0.0112	2.9754	0.3405	2.9720	0.3405
620	0.0854	4.7740	2.0481	0.0111	2.9692	0.3332	2.9652	0.3332
630	0.0877	4.8345	2.0446	0.0111	2.9640	0.3262	2.9594	0.3262
640	0.0899	4.9232	2.0412	0.0110	2.9596	0.3196	2.9547	0.3196
650	0.0921	5.0136	2.0377	0.0110	2.9560	0.3131	2.9507	0.3131
660	0.0940	5.0989	2.0344	0.0110	2.9530	0.3068	2.9476	0.3068
670	0.0959	5.1806	2.0310	0.0110	2.9505	0.3007	2.9451	0.3007
680	0.0978	5.2624	2.0277	0.0110	2.9487	0.2946	2.9433	0.2946
690	0.0996	5.3400	2.0245	0.0110	2.9472	0.2886	2.9419	0.2886
700	0.1012	5.4160	2.0212	0.0111	2.9462	0.2825	2.9410	0.2825
710	0.1022	5.4921	2.0180	0.0112	2.9456	0.2764	2.9405	0.2765
720	0.1032	5.5681	2.0148	0.0113	2.9453	0.2703	2.9404	0.2703
730	0.1043	5.6409	2.0116	0.0114	2.9453	0.2639	2.9406	0.2640
740	0.1053	5.7028	2.0084	0.0115	2.9456	0.2574	2.9410	0.2574
750	0.1082	5.7647	2.0052	0.0116	2.9461	0.2507	2.9418	0.2507
760	0.1116	5.8266	2.0020	0.0117	2.9469	0.2437	2.9427	0.2437
770	0.1150	5.8888	1.9988	0.0119	2.9478	0.2363	2.9438	0.2363
780	0.1185	5.9561	1.9956	0.0120	2.9489	0.2285	2.9450	0.2285
790	0.1219	6.0246	1.9924	0.0122	2.9501	0.2203	2.9462	0.2203
800	0.1244	6.0931	1.9892	0.0124	2.9514	0.2117	2.9474	0.2117

	Ag [216]		ITO [209]		CIGS (E_g = 1.17 eV), w/ Urbach tail [217]		CIGS (E_g = 1.2 eV), w/ Urbach tail [217]	
λ (nm)	n	k	n	k	n	k	n	k
810	0.1261	6.1640	1.9859	0.0126	2.9527	0.2026	2.9484	0.2026
820	0.1277	6.2449	1.9827	0.0128	2.9538	0.1933	2.9490	0.1933
830	0.1293	6.3260	1.9795	0.0130	2.9548	0.1842	2.9493	0.1843
840	0.1311	6.4071	1.9762	0.0133	2.9557	0.1757	2.9493	0.1757
850	0.1335	6.4814	1.9729	0.0135	2.9564	0.1677	2.9493	0.1677
860	0.1360	6.5403	1.9696	0.0138	2.9568	0.1601	2.9490	0.1601
870	0.1385	6.5990	1.9663	0.0140	2.9567	0.1528	2.9485	0.1528
880	0.1409	6.6577	1.9630	0.0143	2.9557	0.1483	2.9474	0.1456
890	0.1434	6.7238	1.9597	0.0146	2.9534	0.1450	2.9455	0.1382
900	0.1461	6.7945	1.9563	0.0149	2.9510	0.1415	2.9437	0.1310
910	0.1494	6.8653	1.9529	0.0152	2.9490	0.1378	2.9420	0.1267
920	0.1527	6.9407	1.9495	0.0155	2.9473	0.1339	2.9405	0.1223
930	0.1560	7.0178	1.9461	0.0159	2.9460	0.1298	2.9391	0.1175
940	0.1593	7.0922	1.9426	0.0162	2.9449	0.1254	2.9376	0.1123
950	0.1626	7.1610	1.9391	0.0166	2.9438	0.1208	2.9358	0.1068
960	0.1659	7.2295	1.9356	0.0170	2.9427	0.1159	2.9338	0.1009
970	0.1691	7.2950	1.9321	0.0173	2.9413	0.1106	2.9310	0.0945
980	0.1724	7.3592	1.9285	0.0177	2.9397	0.1050	2.9279	0.0874
990	0.1747	7.4233	1.9250	0.0181	2.9379	0.0988	2.9243	0.0795
1000	0.1768	7.4901	1.9213	0.0185	2.9357	0.0922	2.9203	0.0705
1010	0.1789	7.5666	1.9177	0.0190	2.9334	0.0848	2.9162	0.0600
1020	0.1809	7.6434	1.9140	0.0194	2.9304	0.0766	2.9117	0.0469
1030	0.1830	7.7165	1.9103	0.0199	2.9264	0.0671	2.9067	0.0291
1040	0.1851	7.7876	1.9066	0.0203	2.9215	0.0559	2.9011	0.0165
1050	0.1873	7.8590	1.9028	0.0208	2.9142	0.0413	2.8941	0.0094
1060	0.1915	7.9337	1.8990	0.0213	2.9062	0.0243	2.8868	0.0054
1070	0.1963	8.0085	1.8952	0.0218	2.8974	0.0142	2.8791	0.0032
1080	0.2012	8.0828	1.8913	0.0223	2.8889	0.0084	2.8717	0.0019
1090	0.2061	8.1518	1.8874	0.0229	2.8814	0.0050	2.8650	0.0011
1100	0.2110	8.2201	1.8835	0.0234	2.8742	0.0030	2.8586	0.0007
1110	0.2150	8.2879	1.8795	0.0240	2.8679	0.0018	2.8530	0.0004
1120	0.2184	8.3505	1.8755	0.0245	2.8618	0.0011	2.8475	0.0002
1130	0.2219	8.4127	1.8715	0.0251	2.8564	0.0007	2.8426	0.0002
1140	0.2253	8.4748	1.8674	0.0257	2.8512	0.0004	2.8379	0.0001
1150	0.2288	8.5368	1.8633	0.0263	2.8466	0.0003	2.8336	0.0001

Bibliography

[1] "Climate Change 2014: Synthesis Report," Intergovernmental Panel on Climate Change (IPCC), tech. rep., 2015.

[2] D. H. Meadows, D. L. Meadows, and J. Randers, *The limits to Growth, the 30-Year Update*. Earthscan, 2012.

[3] "Paris Agreement," United Nations / Framework Convention on Climate Change (FCCC), Paris, tech. rep., 2015.

[4] *World energy assessment: energy and the challenge of sustainability*. United Nations Development Programme, World Energy Council, 2000.

[5] "Photovoltaics Report," Fraunhofer ISE, tech. rep., 2019.

[6] M. A. Green, E. D. Dunlop, D. H. Levi, J. Hohl-Ebinger, M. Yoshita, and A. W. Y. Ho-Baillie, "Solar cell efficiency tables (version 54)," *Prog. Photovolt. Res. Appl.*, vol. 27, no. 7, pp. 565–575, 2019.

[7] K. A. W. Horowitz, R. Fu, and M. Woodhouse, "An analysis of glass–glass CIGS manufacturing costs," *Sol. Energy Mater. Sol. Cells*, vol. 154, pp. 1–10, 2016.

[8] *Study on the review of the list of critical raw materials: critical raw materials factsheets.* European Commission, 2017.

[9] J. Pettersson, T. Törndahl, C. Platzer-Björkman, A. Hultqvist, and M. Edoff, "The Influence of Absorber Thickness on Cu(In,Ga)Se2 Solar Cells With Different Buffer Layers," *IEEE J. Photovolt.*, vol. 3, no. 4, pp. 1376–1382, 2013.

[10] P. M. P. Salomé *et al.*, "Passivation of Interfaces in Thin Film Solar Cells: Understanding the Effects of a Nanostructured Rear Point Contact Layer," *Adv. Mater. Interfaces*, vol. 5, no. 2, p. 1701101, 2018.

[11] L. M. Mansfield *et al.*, "Efficiency increased to 15.2% for ultra-thin Cu(In,Ga)Se2 solar cells," *Prog. Photovolt. Res. Appl.*, vol. 26, no. 11, pp. 949–954, 2018.

[12] F. Mollica, "Optimization of ultra-thin Cu(In,Ga)Se2 based solar cells with alternative back-contacts," phdthesis, Université Pierre et Marie Curie - Paris VI, 2016.

[13] O. Lundberg, M. Bodegård, J. Malmström, and L. Stolt, "Influence of the Cu (In, Ga) Se2 thickness and Ga grading on solar cell performance," *Prog. Photovolt. Res. Appl.*, vol. 11, no. 2, pp. 77–88, 2003.

[14] "Key World Energy Statistics 2017," International Energy Agency, tech. rep., 2017.

[15] "Renewables 2019 Global Status Report," REN21, tech. rep., 2019.

[16] "iea-pvps.org - Preliminary Market Report." [Online]. Available: http://www.iea-pvps.org/index.php?id=266.

[17] C. Kost, S. Shammugam, V. Jülch, H.-T. Nguyen, and T. Schlegl, "Levelized Cost of Electricity - Renewable Energy Technologies," Fraunhofer ISE, tech. rep., 2018.

[18] "Paris Agreement - Status of Ratification." [Online]. Available: https://unfccc.int/process/the-paris-agreement/status-of-ratification.

[19] "Climate Change 2014: Mitigation of Climate Change," Intergovernmental Panel on Climate Change (IPCC), tech. rep., 2014.

[20] M. Powalla *et al.*, "Advances in Cost-Efficient Thin-Film Photovoltaics Based on Cu(In,Ga)Se2," *Engineering*, vol. 3, no. 4, pp. 445–451, 2017.

[21] "CIGS White Paper 2019," Zentrum für Sonnenenergie- und Wasserstoff-Forschung Baden-Württemberg (ZSW), Helmholtz-Zentrum Berlin für Materialien und Energie (HZB), tech. rep., 2019.

[22] K. A. W. Horowitz and M. Woodhouse, "Cost and potential of monolithic CIGS photovoltaic modules," in *2015 IEEE 42nd Photovoltaic Specialist Conference (PVSC)*, 2015, pp. 1–6.

[23] M. J. (Mariska) de Wild-Scholten, "Energy payback time and carbon footprint of commercial photovoltaic systems," *Sol. Energy Mater. Sol. Cells*, vol. 119, pp. 296–305, 2013.

[24] J. L. Shay, S. Wagner, and H. M. Kasper, "Efficient CuInSe2/CdS solar cells," *Appl. Phys. Lett.*, vol. 27, no. 2, pp. 89–90, 1975.

[25] P. Jackson *et al.*, "New world record efficiency for Cu(In,Ga)Se2 thin-film solar cells beyond 20%," *Prog. Photovolt. Res. Appl.*, vol. 19, no. 7, pp. 894–897, 2011.

[26] M. Nakamura, K. Yamaguchi, Y. Kimoto, Y. Yasaki, T. Kato, and H. Sugimoto, "Cd-free Cu(In,Ga)(Se,S)2 thin-film solar cell with a new world record efficacy of 23.35%," presented at the 46th IEEE PVSC, Chicago, IL, 2019.

[27] P. M. P. Salomé, H. Rodriguez-Alvarez, and S. Sadewasser, "Incorporation of alkali metals in chalcogenide solar cells," *Sol. Energy Mater. Sol. Cells*, vol. 143, pp. 9–20, 2015.

[28] M. Ashby, *Materials and Environment*. Elsevier, 2013.

[29] A. Chirilă *et al.*, "Highly efficient Cu(In,Ga)Se2 solar cells grown on flexible polymer films," *Nat. Mater.*, vol. 10, no. 11, pp. 857–861, 2011.

[30] R. Carron *et al.*, "Advanced Alkali Treatments for High-Efficiency Cu(In,Ga)Se2 Solar Cells on Flexible Substrates," *Adv. Energy Mater.*, vol. 9, no. 24, p. 1900408, 2019.

[31] P. Jackson, R. Wuerz, D. Hariskos, E. Lotter, W. Witte, and M. Powalla, "Effects of heavy alkali elements in Cu(In,Ga)Se2 solar cells with efficiencies up to 22.6%," *Phys. Status Solidi RRL – Rapid Res. Lett.*, vol. 10, no. 8, pp. 583–586, 2016.

[32] T. Kato, J.-L. Wu, Y. Hirai, H. Sugimoto, and V. Bermudez, "Record Efficiency for Thin-Film Polycrystalline Solar Cells Up to 22.9% Achieved by Cs-Treated Cu(In,Ga)(Se,S)2," *IEEE J. Photovolt.*, vol. 9, no. 1, pp. 325–330, 2019.

[33] K. Orgassa, H. W. Schock, and J. H. Werner, "Alternative back contact materials for thin film Cu(In,Ga)Se2 solar cells," *Thin Solid Films*, vol. 431–432, pp. 387–391, 2003.

[34] K.-J. Hsiao, J.-D. Liu, H.-H. Hsieh, and T.-S. Jiang, "Electrical impact of MoSe2 on CIGS thin-film solar cells," *Phys. Chem. Chem. Phys.*, vol. 15, no. 41, p. 18174, 2013.

[35] D. Abou-Ras *et al.*, "Formation and characterisation of MoSe2 for Cu(In,Ga)Se2 based solar cells," *Thin Solid Films*, vol. 480–481, pp. 433–438, 2005.

[36] T. Nakada, Y. Hirabayashi, T. Tokado, D. Ohmori, and T. Mise, "Novel device structure for Cu(In,Ga)Se2 thin film solar cells using transparent conducting oxide back and front contacts," *Sol. Energy*, vol. 77, no. 6, pp. 739–747, 2004.

[37] J. Keller, W.-C. Chen, L. Riekehr, T. Kubart, T. Törndahl, and M. Edoff, "Bifacial Cu(In,Ga)Se2 solar cells using hydrogen-doped In2O3 films as a transparent back contact," *Prog. Photovolt. Res. Appl.*, vol. 26, no. 10, pp. 846–858, 2018.

[38] M. D. Heinemann *et al.*, "Cu(In,Ga)Se2 superstrate solar cells: prospects and limitations," *Prog. Photovolt. Res. Appl.*, vol. 23, no. 10, pp. 1228–1237, 2015.

[39] H. Simchi, B. E. McCandless, T. Meng, J. H. Boyle, and W. N. Shafarman, "MoO3 back contact for CuInSe2-based thin film solar cells," *MRS Online Proc. Libr. Arch.*, vol. 1538, pp. 173–178, 2013.

[40] T. Klinkert, "Comprehension and optimisation of the co-evaporation deposition of Cu(In,Ga)Se2 absorber layers for very high efficiency thin film solar cells," Université Pierre et Marie Curie-Paris VI, 2015.

[41] T. Klinkert, M. Jubault, F. Donsanti, D. Lincot, and J.-F. Guillemoles, "Differential in-depth characterization of co-evaporated Cu(In,Ga)Se2 thin films for solar cell applications," *Thin Solid Films*, vol. 558, pp. 47–53, 2014.

[42] M. I. Alonso, M. Garriga, C. A. Durante Rincón, E. Hernández, and M. León, "Optical functions of chalcopyrite CuGa x In 1-x Se2 alloys," *Appl. Phys. Mater. Sci. Process.*, vol. 74, no. 5, pp. 659–664, 2002.

[43] S. Wei and A. Zunger, "Band offsets and optical bowings of chalcopyrites and Zn-based II-VI alloys," *J. Appl. Phys.*, vol. 78, no. 6, pp. 3846–3856, 1995.

[44] M. A. Contreras *et al.*, "Wide bandgap Cu(In,Ga)Se2 solar cells with improved energy conversion efficiency," *Prog. Photovolt. Res. Appl.*, vol. 20, no. 7, pp. 843–850, 2012.

[45] S. Siebentritt, L. Gütay, D. Regesch, Y. Aida, and V. Deprédurand, "Why do we make Cu(In,Ga)Se2 solar cells non-stoichiometric?," *Sol. Energy Mater. Sol. Cells*, vol. 119, pp. 18–25, 2013.

[46] S. Siebentritt, M. Igalson, C. Persson, and S. Lany, "The electronic structure of chalcopyrites-bands, point defects and grain boundaries," *Prog. Photovolt. Res. Appl.*, vol. 18, no. 6, pp. 390–410, 2010.

[47] T. Nishimura, S. Toki, H. Sugiura, K. Nakada, and A. Yamada, "Effect of Cu-deficient layer formation in Cu(In,Ga)Se2 solar-cell performance," *Prog. Photovolt. Res. Appl.*, vol. 26, no. 4, pp. 291–302, 2018.

[48] M. Morkel *et al.*, "Flat conduction-band alignment at the CdS/CuInSe2 thin-film solar-cell heterojunction," *Appl. Phys. Lett.*, vol. 79, no. 27, pp. 4482–4484, 2001.

[49] D. Hariskos and M. Powalla, "Thermodynamic limitations for alkali metals in Cu(In,Ga)Se2," *J. Mater. Res.*, vol. 32, no. 20, pp. 3789–3800, 2017.

[50] R. A. Mickelsen and W. S. Chen, "Development of a 9.4% efficient thin-film CuInSe2/CdS solar cell," presented at the 15th Photovoltaic Specialists Conference, 1981, pp. 800–804.

[51] R. Klenk, T. Walter, H.-W. Schock, and D. Cahen, "A model for the successful growth of polycrystalline films of CuInSe2 by multisource physical vacuum evaporation," *Adv. Mater.*, vol. 5, no. 2, pp. 114–119, 1993.

[52] M. A. Contreras *et al.*, "High efficiency Cu(In,Ga)Se2-based solar cells: processing of novel absorber structures," in *Proceedings of 1994 IEEE 1st World Conference on Photovoltaic Energy Conversion - WCPEC*, 1994, vol. 1, pp. 68–75.

[53] I. Repins *et al.*, "19.9%-efficient ZnO/CdS/CuInGaSe2 solar cell with 81.2% fill factor," *Prog. Photovolt. Res. Appl.*, vol. 16, no. 3, pp. 235–239, 2008.

[54] T. Dullweber, G. Hanna, U. Rau, and H. W. Schock, "A new approach to high-efficiency solar cells by band gap grading in Cu(In,Ga)Se2 chalcopyrite semiconductors," *Sol. Energy Mater.*, p. 6, 2001.

[55] S.-H. Wei, S. B. Zhang, and A. Zunger, "Effects of Na on the electrical and structural properties of CuInSe2," *J. Appl. Phys.*, vol. 85, no. 10, pp. 7214–7218, 1999.

[56] P. M. P. Salomé *et al.*, "Cu(In,Ga)Se2 Solar Cells With Varying Na Content Prepared on Nominally Alkali-Free Glass Substrates," *IEEE J. Photovolt.*, vol. 3, no. 2, pp. 852–858, 2013.

[57] P. M. P. Salomé *et al.*, "Incorporation of Na in Cu(In,Ga)Se2 Thin-Film Solar Cells: A Statistical Comparison Between Na From Soda-Lime Glass and From a Precursor Layer of NaF," *IEEE J. Photovolt.*, vol. 4, no. 6, pp. 1659–1664, 2014.

[58] D. Rudmann *et al.*, "Efficiency enhancement of Cu(In,Ga)Se2 solar cells due to post-deposition Na incorporation," *Appl. Phys. Lett.*, vol. 84, no. 7, pp. 1129–1131, 2004.

[59] D. Rudmann, D. Brémaud, H. Zogg, and A. N. Tiwari, "Na incorporation into Cu(In,Ga)Se2 for high-efficiency flexible solar cells on polymer foils," *J. Appl. Phys.*, vol. 97, no. 8, p. 084903, 2005.

[60] D. Rudmann *et al.*, "Sodium incorporation strategies for CIGS growth at different temperatures," *Thin Solid Films*, vol. 480–481, pp. 55–60, 2005.

[61] R. Wuerz, A. Eicke, F. Kessler, P. Rogin, and O. Yazdani-Assl, "Alternative sodium sources for Cu(In,Ga)Se2 thin-film solar cells on flexible substrates," *Thin Solid Films*, vol. 519, no. 21, pp. 7268–7271, 2011.

[62] V. Achard *et al.*, "Study of Gallium Front Grading at Low Deposition Temperature on Polyimide Substrates and Impacts on the Solar Cell Properties," *IEEE J. Photovolt.*, pp. 1–6, 2018.

[63] F. Pianezzi *et al.*, "Electronic properties of Cu(In,Ga)Se2 solar cells on stainless steel foils without diffusion barrier," *Prog. Photovolt. Res. Appl.*, vol. 20, no. 3, pp. 253–259, 2012.

[64] R. Wuerz, A. Eicke, F. Kessler, S. Paetel, S. Efimenko, and C. Schlegel, "CIGS thin-film solar cells and modules on enamelled steel substrates," *Sol. Energy Mater. Sol. Cells*, vol. 100, pp. 132–137, 2012.

[65] A. Chirilă *et al.*, "Potassium-induced surface modification of Cu(In,Ga)Se2 thin films for high-efficiency solar cells," *Nat. Mater.*, vol. 12, no. 12, pp. 1107–1111, 2013.

[66] F. Pianezzi *et al.*, "Defect formation in Cu(In,Ga)Se2 thin films due to the presence of potassium during growth by low temperature co-evaporation process," *J. Appl. Phys.*, vol. 114, no. 19, p. 194508, 2013.

[67] P. Reinhard *et al.*, "Features of KF and NaF Postdeposition Treatments of Cu(In,Ga)Se2 Absorbers for High Efficiency Thin Film Solar Cells," *Chem. Mater.*, vol. 27, no. 16, pp. 5755–5764, 2015.

[68] T. Lepetit, S. Harel, L. Arzel, G. Ouvrard, and N. Barreau, "KF post deposition treatment in co-evaporated Cu(In,Ga)Se2 thin film solar cells: Beneficial or detrimental effect induced by the absorber characteristics," *Prog. Photovolt. Res. Appl.*, vol. 25, no. 12, pp. 1068–1076, 2017.

[69] C. P. Muzzillo, J. D. Poplawsky, H. M. Tong, W. Guo, and T. Anderson, "Revealing the beneficial role of K in grain interiors, grain boundaries, and at the buffer interface for highly efficient CuInSe2 solar cells," *Prog. Photovolt. Res. Appl.*, vol. 26, no. 10, pp. 825–834, 2018.

[70] O. Donzel-Gargand *et al.*, "Deep surface Cu depletion induced by K in high-efficiency Cu(In,Ga)Se2 solar cell absorbers," *Prog. Photovolt. Res. Appl.*, vol. 26, no. 9, pp. 730–739, 2018.

[71] F. Pianezzi *et al.*, "Unveiling the effects of post-deposition treatment with different alkaline elements on the electronic properties of CIGS thin film solar cells," *Phys. Chem. Chem. Phys.*, vol. 16, no. 19, p. 8843, 2014.

[72] K. F. Tai, R. Kamada, T. Yagioka, T. Kato, and H. Sugimoto, "From 20.9 to 22.3% Cu(In,Ga)(S,Se)2 solar cell: Reduced recombination rate at the heterojunction and the depletion region due to K-treatment," *Jpn. J. Appl. Phys.*, vol. 56, no. 8S2, 2017.

[73] C. P. Muzzillo, "Review of grain interior, grain boundary, and interface effects of K in CIGS solar cells: Mechanisms for performance enhancement," *Sol. Energy Mater. Sol. Cells*, vol. 172, pp. 18–24, 2017.

[74] E. Cadel, N. Barreau, J. Kessler, and P. Pareige, "Atom probe study of sodium distribution in polycrystalline Cu(In,Ga)Se2 thin film," *Acta Mater.*, vol. 58, no. 7, pp. 2634–2637, 2010.

[75] O. Cojocaru-Mirédin, T. Schwarz, and D. Abou-Ras, "Assessment of elemental distributions at line and planar defects in Cu(In,Ga)Se2 thin films by atom probe tomography," *Scr. Mater.*, vol. 148, pp. 106–114, 2018.

[76] A. Vilalta-Clemente *et al.*, "Rubidium distribution at atomic scale in high efficient Cu(In,Ga)Se2 thin-film solar cells," *Appl. Phys. Lett.*, vol. 112, no. 10, p. 103105, 2018.

[77] N. Nicoara *et al.*, "Direct evidence for grain boundary passivation in Cu(In,Ga)Se2 solar cells through alkali-fluoride post-deposition treatments," *Nat. Commun.*, vol. 10, no. 1, p. 3980, 2019.

[78] D. Abou-Ras *et al.*, "No Evidence for Passivation Effects of Na and K at Grain Boundaries in Polycrystalline Cu(In,Ga)Se2 Thin Films for Solar Cells," *Sol. RRL*, vol. 3, no. 8, p. 1900095, 2019.

[79] U. Rau, K. Taretto, and S. Siebentritt, "Grain boundaries in Cu(In,Ga)(Se,S)2 thin-film solar cells," *Appl. Phys. A*, vol. 96, no. 1, pp. 221–234, 2009.

[80] W. K. Metzger *et al.*, "Recombination kinetics and stability in polycrystalline Cu(In,Ga)Se2 solar cells," *Thin Solid Films*, vol. 517, no. 7, pp. 2360–2364, 2009.

[81] D. Abou-Ras *et al.*, "Grain-boundary character distribution and correlations with electrical and optoelectronic properties of CuInSe2 thin films," *Acta Mater.*, vol. 118, pp. 244–252, 2016.

[82] M. Gloeckler, J. R. Sites, and W. K. Metzger, "Grain-boundary recombination in Cu(In,Ga)Se2 solar cells," *J. Appl. Phys.*, vol. 98, no. 11, p. 113704, 2005.

[83] G. Hanket, J. H. Boyle, and W. N. Shafarman, "Characterization and device performance of (Ag,Cu)(In,Ga)Se2 absorber layers," in *2009 34th IEEE Photovoltaic Specialists Conference (PVSC)*, Philadelphia, PA, USA, 2009, pp. 001240–001245.

[84] M. Edoff *et al.*, "High Voc in (Cu,Ag)(In,Ga)Se2 Solar Cells," *IEEE J. Photovolt.*, vol. 7, no. 6, pp. 1789–1794, 2017.

[85] G. Kim, W. M. Kim, J.-K. Park, D. Kim, H. Yu, and J. Jeong, "Thin Ag Precursor Layer-Assisted Co-Evaporation Process for Low-Temperature Growth of Cu(In,Ga)Se2 Thin Film," *ACS Appl. Mater. Interfaces*, vol. 11, no. 35, pp. 31923–31933, 2019.

[86] J. H. Boyle, B. E. McCandless, W. N. Shafarman, and R. W. Birkmire, "Structural and optical properties of (Ag,Cu)(In,Ga)Se2 polycrystalline thin film alloys," *J. Appl. Phys.*, vol. 115, no. 22, p. 223504, 2014.

[87] P. T. Erslev, J. Lee, G. M. Hanket, W. N. Shafarman, and J. D. Cohen, "The electronic structure of Cu(In1−xGax)Se2 alloyed with silver," *Thin Solid Films*, vol. 519, no. 21, pp. 7296–7299, 2011.

[88] W. Shafarman, C. Thompson, J. Boyle, G. Hanket, P. Erslev, and J. David Cohen, "Device characterization of (Ag,Cu)(In,Ga)Se2 solar cells," in *2010 35th IEEE Photovoltaic Specialists Conference*, Honolulu, HI, USA, 2010, pp. 000325–000329.

[89] C. P. Thompson, Lei Chen, W. N. Shafarman, Jinwoo Lee, S. Fields, and R. W. Birkmire, "Bandgap gradients in (Ag,Cu)(In,Ga)Se2 thin film solar cells deposited by three-stage co-evaporation," in *2015 IEEE 42nd Photovoltaic Specialist Conference (PVSC)*, New Orleans, LA, 2015, pp. 1–6.

[90] A. Luque and S. Hegedus, *Handbook of Photovoltaic Science and Engineering*. John Wiley & Sons, 2011.

[91] N. Naghavi *et al.*, "Buffer layers and transparent conducting oxides for chalcopyrite Cu(In,Ga)(S,Se)2 based thin film photovoltaics: present status and current developments," *Prog. Photovolt. Res. Appl.*, vol. 18, no. 6, pp. 411–433, 2010.

[92] T. Hildebrandt *et al.*, "Fast Chemical Bath Deposition Process at Room Temperature of ZnS-Based Materials for Buffer Application in High-Efficiency Cu(In,Ga)Se2-Based Solar Cells," *IEEE J. Photovolt.*, vol. 8, no. 6, pp. 1862–1867, 2018.

[93] C. Persson, C. Platzer-Björkman, J. Malmström, T. Törndahl, and M. Edoff, "Strong Valence-Band Offset Bowing of ZnO 1 − x S x Enhances p -Type Nitrogen Doping of ZnO-like Alloys," *Phys. Rev. Lett.*, vol. 97, no. 14, p. 146403, 2006.

[94] M. Gloeckler and J. R. Sites, "Efficiency limitations for wide-band-gap chalcopyrite solar cells," *Thin Solid Films*, vol. 480–481, pp. 241–245, 2005.

[95] R. Scheer, L. Messmann-Vera, R. Klenk, and H.-W. Schock, "On the role of non-doped ZnO in CIGSe solar cells," *Prog. Photovolt. Res. Appl.*, vol. 20, no. 6, pp. 619–624, 2012.

[96] M. Powalla, S. Paetel, E. Ahlswede, R. Wuerz, C. D. Wessendorf, and T. Magorian Friedlmeier, "Thin-film solar cells exceeding 22% solar cell efficiency: An overview on

CdTe-, Cu(In,Ga)Se2-, and perovskite-based materials," *Appl. Phys. Rev.*, vol. 5, no. 4, p. 041602, 2018.

[97] Y. Hagiwara, T. Nakada, and A. Kunioka, "Improved Jsc in CIGS thin film solar cells using a transparent conducting ZnO:B window layer," *Sol. Energy Mater. Sol. Cells*, vol. 67, no. 1, pp. 267–271, 2001.

[98] J. S. Ward *et al.*, "Cu(In,Ga)Se2 solar cells measured under low flux optical concentration," in *2014 IEEE 40th Photovoltaic Specialist Conference (PVSC)*, 2014, pp. 2934–2937.

[99] "MiaSolé - Home," *MiaSolé*. [Online]. Available: http://miasole.com/.

[100] M. Stölzel *et al.*, "Absorber Optimization in CIGSSe Modules with a Sputtered ZnOS Buffer Layer at 19% Efficiency," presented at the 36th European Photovoltaic Solar Energy Conference and Exhibition (EU-PVSEC), 2019, p. 7.

[101] J.-F. Guillemoles, T. Kirchartz, D. Cahen, and U. Rau, "Guide for the perplexed to the Shockley–Queisser model for solar cells," *Nat. Photonics*, vol. 13, no. 8, pp. 501–505, 2019.

[102] P. Würfel and U. Würfel, *Physics of Solar Cells: From Basic Principles to Advanced Concepts, 3rd Edition*. Wiley-VCH, 2016.

[103] NREL, "Reference Air Mass 1.5 Spectra." [Online]. Available: https://www.nrel.gov/grid/solar-resource/spectra-am1.5.html.

[104] W. Shockley and H. J. Queisser, "Detailed Balance Limit of Efficiency of p-n Junction Solar Cells," *J. Appl. Phys.*, vol. 32, pp. 510–519.

[105] S. Rühle, "Tabulated values of the Shockley–Queisser limit for single junction solar cells," *Sol. Energy*, vol. 130, pp. 139–147, 2016.

[106] M. Burgelman and J. Marlein, "Analysis of graded band gap solar cells with SCAPS," in *Proceedings of the 23rd European Photovoltaic Solar Energy Conference, Valencia*, 2008, pp. 2151–2155.

[107] "SCAPS download." [Online]. Available: http://scaps.elis.ugent.be/SCAPSinstallatie.html.

[108] W. W. Gärtner, "Depletion-layer photoeffects in semiconductors," *Phys. Rev.*, vol. 116, no. 1, p. 84, 1959.

[109] L. Lombez, D. Ory, M. Paire, A. Delamarre, G. El Hajje, and J. F. Guillemoles, "Micrometric investigation of external quantum efficiency in microcrystalline Cu(In,Ga)(S,Se)2 solar cells," *Thin Solid Films*, vol. 565, pp. 32–36, 2014.

[110] M. Richter, Ms. Hammer, T. Sonnet, and J. Parisi, "Bandgap extraction from quantum efficiency spectra of Cu(In,Ga)Se2 solar cells with varied grading profile and diffusion length," *Thin Solid Films*, vol. 633, pp. 213–217, 2017.

[111] R. Scheer and H.-W. Schock, *Chalcogenide Photovoltaics: Physics, Technologies, and Thin Film Devices*. John Wiley & Sons, 2011.

[112] S. Siebentritt, "What limits the efficiency of chalcopyrite solar cells?," *Sol. Energy Mater. Sol. Cells*, vol. 95, no. 6, pp. 1471–1476, 2011.

[113] "Mineral Commodity Summaries," U.S. Department of the Interior, U.S. Geological Survey, tech. rep., 2019.

[114] "Availability of Indium and Gallium," Indium Corporation, tech. rep., 2019.

[115] V. Bermudez, "Economical and operational issues for CIGS in the future PV panorama," *Sol. Energy*, vol. 146, pp. 85–93, 2017.

[116] W. N. Shafarman, R. W. Birkmire, S. Marsillac, M. Marudachalam, N. Orbey, and T. W. F. Russell, "Effect of reduced deposition temperature, time, and thickness on Cu(InGa)Se2 films and devices," in *Conference Record of the Twenty Sixth IEEE Photovoltaic Specialists Conference - 1997*, 1997, pp. 331–334.

[117] T. Negami, S. Nishiwaki, Y. Hashimoto, and N. Kohara, "Effect of absorber thickness on performance of Cu(In,Ga)Se2 solar cells," in *Proceedings of the 2nd WCPEC*, Vienna, 1998, pp. 1181–1184.

[118] T. Dullweber, O. Lundberg, J. Malmstrom, M. Bodeg, H. W. Schock, and J. H. Werner, "Back surface band gap gradings in Cu(In,Ga)Se2 solar cells," p. 3, 2001.

[119] M. Gloeckler and J. R. Sites, "Potential of submicrometer thickness Cu(In,Ga)Se2 solar cells," *J. Appl. Phys.*, vol. 98, no. 10, p. 103703, 2005.

[120] Z. J. Li-Kao *et al.*, "Towards ultrathin copper indium gallium diselenide solar cells: proof of concept study by chemical etching and gold back contact engineering," *Prog. Photovolt. Res. Appl.*, vol. 20, no. 5, pp. 582–587, 2012.

[121] A. Čampa, J. Krč, J. Malmström, M. Edoff, F. Smole, and M. Topič, "The potential of textured front ZnO and flat TCO/metal back contact to improve optical absorption in thin Cu(In,Ga)Se2 solar cells," *Thin Solid Films*, vol. 515, no. 15, pp. 5968–5972, 2007.

[122] N. Dahan *et al.*, "Optical approaches to improve the photocurrent generation in Cu(In,Ga)Se2 solar cells with absorber thicknesses down to 0.5 μm," *J. Appl. Phys.*, vol. 112, no. 9, p. 094902, 2012.

[123] T. Dullweber, U. Rau, M. A. Contreras, R. Noufi, and H. W. Schock, "Photogeneration and carrier recombination in graded gap Cu(In,Ga)Se2 solar cells," *IEEE Trans. Electron Devices*, vol. 47, no. 12, pp. 2249–2254, 2000.

[124] V. Achard *et al.*, "Study of Cu(In,Ga)Se2 Thin Film Growth at Low Temperature on Polyimide Substrate in a Multistage Coevaporation Process for Photovoltaic Applications," *ACS Appl. Energy Mater.*, vol. 1, no. 10, pp. 5257–5267, 2018.

[125] O. Lundberg, M. Edoff, and L. Stolt, "The effect of Ga-grading in CIGS thin film solar cells," *Thin Solid Films*, vol. 480–481, pp. 520–525, 2005.

[126] T. Klinkert, M. Jubault, F. Donsanti, D. Lincot, and J.-F. Guillemoles, "Ga gradients in Cu(In,Ga)Se2: Formation, characterization, and consequences," *J. Renew. Sustain. Energy*, vol. 6, no. 1, p. 011403, 2014.

[127] G. Yin, V. Brackmann, V. Hoffmann, and M. Schmid, "Enhanced performance of ultra-thin Cu(In,Ga)Se2 solar cells deposited at low process temperature," *Sol. Energy Mater. Sol. Cells*, vol. 132, pp. 142–147, 2015.

[128] A. J. McEvoy, T. Markvart, and L. Castaner, *Practical Handbook of Photovoltaics: Fundamentals and Applications*. Academic Press, 2012.

[129] W.-W. Hsu *et al.*, "Surface passivation of Cu(In,Ga)Se2 using atomic layer deposited Al2O3," *Appl. Phys. Lett.*, vol. 100, no. 2, p. 023508, 2012.

[130] J. Mattheis, P. J. Rostan, U. Rau, and J. H. Werner, "Carrier collection in Cu(In,Ga)Se2 solar cells with graded band gaps and transparent ZnO:Al back contacts," *Sol. Energy Mater. Sol. Cells*, vol. 91, no. 8, pp. 689–695, 2007.

[131] E. Jarzembowski, F. Syrowatka, K. Kaufmann, W. Fränzel, T. Hölscher, and R. Scheer, "The influence of sodium on the molybdenum/Cu(In,Ga)Se2 interface recombination velocity, determined by time resolved photoluminescence," *Appl. Phys. Lett.*, vol. 107, no. 5, p. 051601, 2015.

[132] J. A. Giesecke, M. Kasemann, and W. Warta, "Determination of local minority carrier diffusion lengths in crystalline silicon from luminescence images," *J. Appl. Phys.*, vol. 106, no. 1, p. 014907, 2009.

[133] M. Nerat, "Copper–indium–gallium–selenide (CIGS) solar cells with localized back contacts for achieving high performance," *Sol. Energy Mater. Sol. Cells*, vol. 104, pp. 152–158, 2012.

[134] B. Vermang, V. Fjällström, J. Pettersson, P. Salomé, and M. Edoff, "Development of rear surface passivated Cu(In,Ga)Se2 thin film solar cells with nano-sized local rear point contacts," *Sol. Energy Mater. Sol. Cells*, vol. 117, pp. 505–511, 2013.

[135] R. Kotipalli *et al.*, "Addressing the impact of rear surface passivation mechanisms on ultra-thin Cu(In,Ga)Se2 solar cell performances using SCAPS 1-D model," *Sol. Energy*, vol. 157, pp. 603–613, 2017.

[136] A. Cuevas *et al.*, "Carrier population control and surface passivation in solar cells," *Sol. Energy Mater. Sol. Cells*, vol. 184, pp. 38–47, 2018.

[137] R. Kotipalli, B. Vermang, J. Joel, R. Rajkumar, M. Edoff, and D. Flandre, "Investigating the electronic properties of Al2O3/Cu(In,Ga)Se2 interface," *AIP Adv.*, vol. 5, no. 10, p. 107101, 2015.

[138] F. Mollica *et al.*, "Comparative study of patterned TiO2 and Al2O3 layers as passivated back-contact for ultra-thin Cu(In,Ga)Se2 solar cells," in *2016 IEEE 43rd Photovoltaic Specialists Conference (PVSC)*, Portland, OR, USA, 2016, pp. 2213–2217.

[139] B. Vermang *et al.*, "Employing Si solar cell technology to increase efficiency of ultra-thin Cu(In,Ga)Se2 solar cells," *Prog. Photovolt. Res. Appl.*, vol. 22, no. 10, pp. 1023–1029, 2014.

[140] B. Vermang *et al.*, "Introduction of Si PERC Rear Contacting Design to Boost Efficiency of Cu(In,Ga)Se2 Solar Cells," *IEEE J. Photovolt.*, vol. 4, no. 6, pp. 1644–1649, 2014.

[141] D. Ledinek, O. Donzel-Gargand, M. Sköld, J. Keller, and M. Edoff, "Effect of different Na supply methods on thin Cu(In,Ga)Se2 solar cells with Al2O3 rear passivation layers," *Sol. Energy Mater. Sol. Cells*, vol. 187, pp. 160–169, 2018.

[142] D. Ledinek, J. Keller, C. Hägglund, W.-C. Chen, and M. Edoff, "Effect of NaF pre-cursor on alumina and hafnia rear contact passivation layers in ultra-thin Cu(In,Ga)Se2 solar cells," *Thin Solid Films*, vol. 683, pp. 156–164, 2019.

[143] S. Choi, Y. Kamikawa, J. Nishinaga, A. Yamada, H. Shibata, and S. Niki, "Lithographic fabrication of point contact with Al2O3 rear-surface-passivated and ultra-thin Cu(In,Ga)Se2 solar cells," *Thin Solid Films*, vol. 665, pp. 91–95, 2018.

[144] P. Casper *et al.*, "Optoelectrical improvement of ultra-thin Cu(In,Ga)Se2 solar cells through microstructured MgF2 and Al2O3 back contact passivation layer," *Phys. Status Solidi RRL - Rapid Res. Lett.*, vol. 10, no. 5, pp. 376–380, 2016.

[145] G. Yin *et al.*, "Well-Controlled Dielectric Nanomeshes by Colloidal Nanosphere Lithography for Optoelectronic Enhancement of Ultrathin Cu(In,Ga)Se2 Solar Cells," *ACS Appl. Mater. Interfaces*, vol. 8, no. 46, pp. 31646–31652, 2016.

[146] T. S. Lopes *et al.*, "Rear Optical Reflection and Passivation Using a Nanopatterned Metal/Dielectric Structure in Thin-Film Solar Cells," *IEEE J. Photovolt.*, vol. 9, no. 5, pp. 1421–1427, 2019.

[147] M. Saifullah *et al.*, "Performance and Uniformity Improvement in Ultrathin Cu(In,Ga)Se2 Solar Cells with a WO x Nanointerlayer at the Absorber/Transparent Back-Contact Interface," *ACS Appl. Mater. Interfaces*, vol. 11, no. 1, pp. 655–665, 2019.

[148] H. Simchi, J. K. Larsen, and W. N. Shafarman, "Transparent Back Contacts for Superstrate (Ag,Cu)(In,Ga)Se2 Thin Film Solar Cells," *IEEE J. Photovolt.*, vol. 5, no. 1, pp. 406–409, 2015.

[149] M. D. Heinemann *et al.*, "Advantageous light management in Cu(In,Ga)Se2 superstrate solar cells," *Sol. Energy Mater. Sol. Cells*, vol. 150, pp. 76–81, 2016.

[150] T. Nakada, "Microstructural and diffusion properties of CIGS thin film solar cells fabricated using transparent conducting oxide back contacts," *Thin Solid Films*, vol. 480–481, pp. 419–425, 2005.

[151] M. Terheggen, H. Heinrich, and G. Kostorz, "Ga2O3 segregation in Cu(In,Ga)Se2/ZnO superstrate solar cells and its impact on their photovoltaic properties," *Thin Solid Films*, p. 4, 2002.

[152] F. Mollica *et al.*, "Light absorption enhancement in ultra-thin Cu(In,Ga)Se2 solar cells by substituting the back-contact with a transparent conducting oxide based reflector," *Thin Solid Films*, vol. 633, pp. 202–207, 2017.

[153] Y.-S. Son *et al.*, "Control of Structural and Electrical Properties of Indium Tin Oxide (ITO)/Cu(In,Ga)Se2 Interface for Transparent Back-Contact Applications," *J. Phys. Chem. C*, vol. 123, no. 3, pp. 1635–1644, 2019.

[154] H. Simchi, J. Larsen, K. Kim, and W. Shafarman, "Improved Performance of Ultrathin Cu(InGa)Se2 Solar Cells With a Backwall Superstrate Configuration," *IEEE J. Photovolt.*, vol. 4, no. 6, pp. 1630–1635, 2014.

[155] B. Bissig *et al.*, "Novel back contact reflector for high efficiency and double-graded Cu(In,Ga)Se2 thin-film solar cells," *Prog. Photovolt. Res. Appl.*, vol. 26, no. 11, pp. 894–900, 2018.

[156] J. Goffard *et al.*, "Light Trapping in Ultrathin CIGS Solar Cells with Nanostructured Back Mirrors," *IEEE J. Photovolt.*, vol. 7, no. 5, pp. 1433–1441, 2017.

[157] M. Kovacic *et al.*, "Light management design in ultra-thin chalcopyrite photovoltaic devices by employing optical modelling," *Sol. Energy Mater. Sol. Cells*, vol. 200, p. 109933, 2019.

[158] M. Schmid, "Review on light management by nanostructures in chalcopyrite solar cells," *Semicond. Sci. Technol.*, vol. 32, no. 4, p. 043003, 2017.

[159] H.-L. Chen, "Ultrathin and nanowire-based GaAs solar cells," thesis, Université Paris-Saclay, 2018.

[160] H.-L. Chen *et al.*, "A 19.9%-efficient ultrathin solar cell based on a 205-nm-thick GaAs absorber and a silver nanostructured back mirror," *Nat. Energy*, vol. 4, no. 9, pp. 761–767, 2019.

[161] C. van Lare, G. Yin, A. Polman, and M. Schmid, "Light Coupling and Trapping in Ultrathin Cu(In,Ga)Se2 Solar Cells Using Dielectric Scattering Patterns," *ACS Nano*, vol. 9, no. 10, pp. 9603–9613, 2015.

[162] E. Jarzembowski, B. Fuhrmann, H. Leipner, W. Fränzel, and R. Scheer, "Ultrathin Cu(In,Ga)Se 2 solar cells with point-like back contact in experiment and simulation," *Thin Solid Films*, vol. 633, pp. 61–65, 2017.

[163] G. Yin, M. W. Knight, M.-C. van Lare, M. M. Solà Garcia, A. Polman, and M. Schmid, "Optoelectronic Enhancement of Ultrathin CuIn 1-x Ga x Se2 Solar Cells by Nanophotonic Contacts," *Adv. Opt. Mater.*, vol. 5, no. 5, p. 1600637, 2017.

[164] "Dr. Eberl MBE-Komponenten GmbH." [Online]. Available: https://www.mbe-komponenten.de/.

[165] L. J. van der Pauw, "A Method of Measuring Specific Resistivity and Hall Effect of Discs of Arbitrary Shape," *Philips Res. Rep.*, vol. 13, pp. 1–9, 1958.

[166] P. Lalanne and J. P. Hugonin, "Reticolo software for grating analysis." [Online]. Available: https://www.lp2n.institutoptique.fr/lp2n/Membres-Services/Responsables-d-equipe/LALANNE-Philippe.

[167] C. A. Kaufmann *et al.*, "Depth profiling of Cu(In,Ga)Se2 thin films grown at low temperatures," *Sol. Energy Mater.*, vol. 93, no. 6–7, pp. 859–863, 2009.

[168] L. M. Mansfield *et al.*, "Comparison of CIGS Solar Cells Made With Different Structures and Fabrication Techniques," *IEEE J. Photovolt.*, vol. 7, no. 1, pp. 286–293, 2017.

[169] R. L. Garris, S. Johnston, J. V. Li, H. L. Guthrey, K. Ramanathan, and L. M. Mansfield, "Electrical characterization and comparison of CIGS solar cells made with different structures and fabrication techniques," *Sol. Energy Mater. Sol. Cells*, vol. 174, pp. 77–83, 2018.

[170] J. Moseley *et al.*, "Luminescence methodology to determine grain-boundary, grain-interior, and surface recombination in thin-film solar cells," *J. Appl. Phys.*, vol. 124, no. 11, p. 113104, 2018.

[171] H. Guthrey, J. Moseley, J. Nishinaga, H. Shibata, H. Takahashi, and M. Al-Jassim, "Spatially Resolved Recombination Analysis of CuIn x Ga 1-x Se2 Absorbers With Alkali Postdeposition Treatments," *IEEE J. Photovolt.*, vol. 8, no. 6, pp. 1833–1840, 2018.

[172] "Attolight." [Online]. Available: https://attolight.com/.

[173] D. Drouin, A. R. Couture, D. Joly, X. Tastet, V. Aimez, and R. Gauvin, "CASINO V2.42—A Fast and Easy-to-use Modeling Tool for Scanning Electron Microscopy and Microanalysis Users," *Scanning*, vol. 29, no. 3, pp. 92–101, 2007.

[174] F. Urbach, "The Long-Wavelength Edge of Photographic Sensitivity and of the Electronic Absorption of Solids," *Phys. Rev.*, vol. 92, no. 5, pp. 1324–1324, 1953.

[175] J. D. Cohen, J. T. Heath, and W. N. Shafarman, "Photocapacitance Spectroscopy in Copper Indium Diselenide Alloys," in *Wide-Gap Chalcopyrites*, S. Siebentritt and U. Rau, Eds. Berlin, Heidelberg: Springer, 2006, pp. 69–90.

[176] M. Troviano and K. Taretto, "Urbach Energy In CIGS Extracted from Quantum Efficiency Analysis of High Performance CIGS Solar Cells," *24th Eur. Photovolt. Sol. Energy Conf.*, pp. 2933–2937, 2009.

[177] S. De Wolf *et al.*, "Organometallic Halide Perovskites: Sharp Optical Absorption Edge and Its Relation to Photovoltaic Performance," *J. Phys. Chem. Lett.*, vol. 5, no. 6, pp. 1035–1039, 2014.

[178] A. Cattoni, H. Anne-Marie, D. Decanini, J. Shi, and J. Chen, *Soft UV nanoimprint lithography: a versatile tool for nanostructuration at the 20nm scale*. INTECH Open Access Publisher, 2011.

[179] H. Schmitt *et al.*, "Life time evaluation of PDMS stamps for UV-enhanced substrate conformal imprint lithography," *Microelectron. Eng.*, vol. 98, pp. 275–278, 2012.

[180] M. J. Haslinger, M. A. Verschuuren, R. van Brakel, J. Danzberger, I. Bergmair, and M. Mühlberger, "Stamp degradation for high volume UV enhanced substrate conformal imprint lithography (UV-SCIL)," *Microelectron. Eng.*, vol. 153, pp. 66–70, 2016.

[181] N. Tucher, O. Höhn, H. Hauser, C. Müller, and B. Bläsi, "Characterizing the degradation of PDMS stamps in nanoimprint lithography," *Microelectron. Eng.*, vol. 180, pp. 40–44, 2017.

[182] J. D. Bass, D. Grosso, C. Boissiere, and C. Sanchez, "Pyrolysis, Crystallization, and Sintering of Mesostructured Titania Thin Films Assessed by in Situ Thermal Ellipsometry," *J. Am. Chem. Soc.*, vol. 130, no. 25, pp. 7882–7897, 2008.

[183] T. Bottein *et al.*, "Environment-controlled sol–gel soft-NIL processing for optimized titania, alumina, silica and yttria-zirconia imprinting at sub-micron dimensions," *Nanoscale*, vol. 10, no. 3, pp. 1420–1431, 2018.

[184] O. Dalstein, D. R. Ceratti, C. Boissière, D. Grosso, A. Cattoni, and M. Faustini, "Nanoimprinted, Submicrometric, MOF-Based 2D Photonic Structures: Toward Easy Selective Vapors Sensing by a Smartphone Camera," *Adv. Funct. Mater.*, vol. 26, no. 1, pp. 81–90, 2016.

[185] M. Richter *et al.*, "Comprehensive simulation model for Cu(In,Ga)(Se,S)2 solar cells," *Sol. Energy Mater. Sol. Cells*, vol. 132, pp. 162–171, 2015.

[186] T. Kato, K. Kitani, K. F. Tai, R. Kamada, H. Hiroi, and H. Sugimoto, "Characterization of the Back Contact of CIGS Solar Cell as the Origin of Rollover Effect," *32nd Eur. Photovolt. Sol. Energy Conf. Exhib. 1085-1088*, pp. 4 pages, 4870 kb, 2016.

[187] I. H. Malitson and M. J. Dodge, "Refractive-index and birefringence of synthetic sapphire," *J. Opt. Soc. Am.*, vol. 62, no. 11, pp. 1405–1405, 1972.

[188] N. Naghavi *et al.*, "Ultrathin Cu(In,Ga)Se2 based solar cells," *Thin Solid Films*, vol. 633, pp. 55–60, 2017.

[189] A. Kim, Y. Won, K. Woo, C.-H. Kim, and J. Moon, "Highly Transparent Low Resistance ZnO/Ag Nanowire/ZnO Composite Electrode for Thin Film Solar Cells," *ACS Nano*, vol. 7, no. 2, pp. 1081–1091, 2013.

[190] D. Chen *et al.*, "Thermally Stable Silver Nanowire-Polyimide Transparent Electrode Based on Atomic Layer Deposition of Zinc Oxide on Silver Nanowires," *Adv. Funct. Mater.*, vol. 25, no. 48, pp. 7512–7520, 2015.

[191] M. D. Heinemann *et al.*, "The Importance of Sodium Control in CIGSe Superstrate Solar Cells," *IEEE J. Photovolt.*, vol. 5, no. 1, pp. 378–381, 2015.

[192] J. Keller *et al.*, "Using hydrogen-doped In2O3 films as a transparent back contact in (Ag,Cu)(In,Ga)Se2 solar cells," *Prog. Photovolt. Res. Appl.*, 2018.

[193] G. Yin, P. Manley, and M. Schmid, "Light trapping in ultrathin CuIn1-xGaxSe2 solar cells by dielectric nanoparticles," *Sol. Energy*, vol. 163, pp. 443–452, 2018.

[194] O. Poncelet, R. Kotipalli, B. Vermang, A. Macleod, L. A. Francis, and D. Flandre, "Optimisation of rear reflectance in ultra-thin CIGS solar cells towards 20% efficiency," *Sol. Energy*, vol. 146, pp. 443–452, 2017.

[195] O. Dupré, R. Vaillon, and M. A. Green, "Physics of the temperature coefficients of solar cells," *Sol. Energy Mater. Sol. Cells*, vol. 140, pp. 92–100, 2015.

[196] K. Mullaney, G. M. Jones, C. A. Kitchen, and D. P. Jones, "Infra-red reflective coverglasses: the next generation," in *Conference Record of the Twenty Third IEEE Photovoltaic Specialists Conference - 1993 (Cat. No.93CH3283-9)*, 1993, pp. 1363–1368.

[197] W. Li, Y. Shi, K. Chen, L. Zhu, and S. Fan, "A Comprehensive Photonic Approach for Solar Cell Cooling," *ACS Photonics*, vol. 4, no. 4, pp. 774–782, 2017.

[198] D. C. Paine, T. Whitson, D. Janiac, R. Beresford, C. O. Yang, and B. Lewis, "A study of low temperature crystallization of amorphous thin film indium–tin–oxide," *J. Appl. Phys.*, vol. 85, no. 12, pp. 8445–8450, 1999.

[199] U. Betz, M. Kharrazi Olsson, J. Marthy, M. F. Escolá, and F. Atamny, "Thin films engineering of indium tin oxide: Large area flat panel displays application," *Surf. Coat. Technol.*, vol. 200, no. 20–21, pp. 5751–5759, 2006.

[200] T. S. Sathiaraj, "Effect of annealing on the structural, optical and electrical properties of ITO films by RF sputtering under low vacuum level," *Microelectron. J.*, vol. 39, no. 12, pp. 1444–1451, 2008.

[201] A. M. Gabor *et al.*, "Band-gap engineering in Cu(In,Ga)Se2 thin films grown from (In,Ga)2Se3 precursors," *Sol. Energy Mater. Sol. Cells*, vol. 41–42, pp. 247–260, 1996.

[202] V. G. Hill, R. Roy, and E. F. Osborn, "The System Alumina-Gallia-Water," *J. Am. Ceram. Soc.*, vol. 35, no. 6, pp. 135–142, 1952.

[203] H. Peelaers, J. B. Varley, J. S. Speck, and C. G. Van de Walle, "Structural and electronic properties of Ga2O3-Al2O3 alloys," *Appl. Phys. Lett.*, vol. 112, no. 24, p. 242101, 2018.

[204] J. Keller, F. Gustavsson, L. Stolt, M. Edoff, and T. Törndahl, "On the beneficial effect of Al2O3 front contact passivation in Cu(In,Ga)Se2 solar cells," *Sol. Energy Mater. Sol. Cells*, vol. 159, pp. 189–196, 2017.

[205] S. Niki *et al.*, "Effects of the surface Cu2−xSe phase on the growth and properties of CuInSe2 films," *Appl. Phys. Lett.*, vol. 74, no. 11, pp. 1630–1632, 1999.

[206] J. Kessler, C. Chityuttakan, J. Lu, J. Schöldström, and L. Stolt, "Cu(In,Ga)Se2 thin films grown with a Cu-poor/rich/poor sequence: growth model and structural considerations," *Prog. Photovolt. Res. Appl.*, vol. 11, no. 5, pp. 319–331, 2003.

[207] P. J. Rostan, J. Mattheis, G. Bilger, U. Rau, and J. H. Werner, "Formation of transparent and ohmic ZnO:Al/MoSe2 contacts for bifacial Cu(In,Ga)Se2 solar cells and tandem structures," *Thin Solid Films*, vol. 480–481, pp. 67–70, 2005.

[208] N. Ehrmann and R. Reineke-Koch, "Ellipsometric studies on ZnO:Al thin films: Refinement of dispersion theories," *Thin Solid Films*, vol. 519, no. 4, pp. 1475–1485, 2010.

[209] L. Gouillart *et al.*, "Development of reflective back contacts for high-efficiency ultrathin Cu(In,Ga)Se2 solar cells," *Thin Solid Films*, vol. 672, pp. 1–6, 2019.

[210] F.-J. Haug, D. Rudmann, G. Bilger, H. Zogg, and A. N. Tiwari, "Comparison of structural and electrical properties of Cu(In, Ga)Se2 for substrate and superstrate solar cells," *Thin Solid Films*, vol. 403–404, pp. 293–296, 2002.

[211] A. Rockett *et al.*, "Na in selenized Cu(In,Ga)Se2 on Na-containing and Na-free glasses: distribution, grain structure, and device performances," *Thin Solid Films*, vol. 372, no. 1, pp. 212–217, 2000.

[212] A. Virtuani, E. Lotter, M. Powalla, U. Rau, J. H. Werner, and M. Acciarri, "Influence of Cu content on electronic transport and shunting behavior of Cu(In,Ga)Se2 solar cells," *J. Appl. Phys.*, vol. 99, no. 1, p. 014906, 2006.

[213] F. Erfurth *et al.*, "Mo/Cu(In, Ga)Se2 back interface chemical and optical properties for ultrathin CIGSe solar cells," *Appl. Surf. Sci.*, vol. 258, no. 7, pp. 3058–3061, 2012.

[214] E. Khawaja and S. G. Tomlin, "The optical constants of thin evaporated films of cadmium and zinc sulphides," *J. Phys. Appl. Phys.*, vol. 8, no. 5, p. 581, 1975.

[215] E. D. Palik, *Handbook of Optical Constants of Solids*, Academic Press, Inc. 1985.

[216] Y. Jiang, S. Pillai, and M. A. Green, "Re-evaluation of literature values of silver optical constants," *Opt. Express*, vol. 23, no. 3, p. 2133, 2015.

[217] A. Loubat *et al.*, "Optical properties of ultrathin CIGS films studied by spectroscopic ellipsometry assisted by chemical engineering," *Appl. Surf. Sci.*, vol. 421, pp. 643–650, 2017.

université PARIS-SACLAY

ECOLE DOCTORALE N°575
Electrical, optical, bio : physics and engineering (EOBE)

Titre : Développement de cellules solaires Cu(In,Ga)Se_2 ultraminces incluant un contact arrière réfléchissant

Mots Clés : photovoltaïque, Cu(In,Ga)Se_2, ultramince, passivation, contact arrière réfléchissant

Résumé : Réduire l'épaisseur de l'absorbeur des dispositifs photovoltaïques à base de couches minces est une voie prometteuse pour améliorer leur compétitivité industrielle, via une économie de matières premières et une cadence de production plus élevée. Cela peut aussi accroître leur efficacité en diminuant le parcours des porteurs de charge photogénérés. Cependant, l'efficacité des cellules solaires à base de Cu(In,Ga)Se_2 (CIGS) ultramince avec une épaisseur d'absorbeur d'environ 500 nm, soit environ 5 fois inférieure aux cellules conventionnelles, est limitée par deux phénomènes : les recombinaisons non-radiatives au contact arrière et l'absorption incomplète de la lumière solaire incidente. Différentes stratégies ont été étudiées afin de limiter ces pertes. Dans un premier temps, la composition des couches ultraminces de CIGS a été optimisée pour y créer un gradient du minimum de la bande de conduction. Le champ électrique résultant permet de faciliter la séparation des charges et de limiter les recombinaisons au contact arrière. L'incorporation d'argent dans la composition du CIGS a également amélioré significativement les performances des cellules ultraminces, pour aboutir à une efficacité de 14.9% (avec 540 nm d'ACIGS, sans couche antireflet), proche du record actuel de 15.2% (avec couche antireflet et 490 nm de CIGS). En parallèle, l'ajout d'une couche de passivation en alumine à l'interface entre le CIGS (470 nm) et le Mo a été étudié, et a conduit à une augmentation de la tension de circuit ouvert de 55 mV. Dans un deuxième temps, une nouvelle architecture de contact arrière réfléchissant a été développée. Elle consiste en un miroir d'argent encapsulé dans des couches d'oxydes transparents conducteurs. A l'aide d'observations au microscope électronique en transmission, il a été montré que ce contact arrière est compatible avec la co-évaporation de CIGS à des températures ≥500°C. Grâce à une haute réflectivité et un contact ohmique avec le CIGS, il a mené à une amélioration de l'efficacité de 12.5% à 13.5% et du courant de court-circuit de 26.2 mA/cm^2 à 28.9 mA/cm^2 par rapport à un contact arrière standard en molybdène. Cette nouvelle architecture ouvre la voie à une augmentation du rendement photovoltaïque des cellules solaires à base de CIGS ultramince, ainsi qu'à de nouvelles stratégies de piégeage optique.

Title: Development of ultrathin Cu(In,Ga)Se_2–based solar cells with reflective back contacts

Keywords: photovoltaics, Cu(In,Ga)Se_2, ultrathin, rear passivation, reflective back contact

Abstract: Reducing the absorber thickness of thin-film photovoltaic devices is a promising way to improve their industrial competitiveness, thanks to a lower material usage and an increased throughput. It can also increase their efficiency due to a shorter pathway for the separation of photogenerated charge carriers. Still, the efficiency of ultrathin Cu(In,Ga)Se_2-based (CIGS) solar cells , which have an absorber thickness ≤500 nm that is approximately 5 times thinner than standard devices, is limited by two phenomena: the non-radiative recombination of charge carriers at the back contact and the incomplete absorption of the incident light. Several strategies were studied in order to mitigate those losses. First, the composition of ultrathin CIGS layers was optimized to create a grading of the semiconductor's conduction band minimum. The resulting electric field contributes to a better charge carrier separation and a lower back contact recombination rate. The incorporation of silver in the CIGS composition greatly improved the performances, leading to an efficiency of 14.9% (540 nm of ACIGS, without antireflection coating [ARC]), close to the current record of 15.2% (490 nm of CIGS, with ARC). Besides, the addition of an alumina passivation layer at the interface between CIGS (470 nm) and Mo was also investigated, and resulted in an improvement of the open-circuit voltage of 55 mV. Second, a novel architecture of reflective back contacts was developed. It consists of a silver mirror that is encapsulated with layers of transparent conductive oxides. Based on a transmission electron microscopy study, this back contact was shown to be compatible with the co-evaporation of CIGS at 500°C or more. Thanks to a high reflectivity and an ohmic contact with CIGS, it led to an increase of the efficiency from 12.5% to 13.5% and of the short-circuit current from 26.2 mA/cm^2 to 28.9 mA/cm^2 as compared to cells with a standard molybdenum back contact. This reflective back contact paves the way toward higher photovoltaic efficiencies as well as novel strategies for further light trapping.

Université Paris-Saclay
Espace Technologique / Immeuble Discovery
Route de l'Orme aux Merisiers RD 128 / 91190 Saint-Aubin, France